CELL-TYPE-SPECIFIC EPIGENETICS OF ORGAN-DERIVED NEURONS AND ADIPOCYTES

by

PING YU

(Under the Direction of Richard B. Meagher)

ABSTRACT

Epigenetics has been the study of cell-type-specific differences in chromatin structure(s) (defined herein as epitype) among cells with the same genotype. The "Holy Grail" of current epigenetic is the cell-type-specific analyses of epitype within a complex tissue. Yet most of the publications on epigenetics examine the epitype of whole organs or parts of organs, which are comprised of dozens if not hundreds of cell types. In this dissertation, two technologies are developed, the first inspects the nuclei of specific cell types, Fluorescence Nuclear Cytometry (FNC), while the second both inspects and enriches the nuclei of specific cell types for further analyses, Fluorescence-Activated Nuclear Sorting (FANS). Two different mammalian organs were examined. FANS and FNC were employed to study subsets of neuronal nuclei from mouse brain and subsets of adipocyte nuclei from pig adipose depots. In all studies of this dissertation, cell-type-specific differences were observed in those subpopulations fractionated by FANS. The first study (Chapter 3) determined that a significant subpopulation of adult mouse brain nuclei (NeuN-High) had highly decondensed chromatin, expressed elevated levels of chromatin modifying machinery, and expressed high levels of transcripts encoding markers of neurogenesis, learning and memory, multipotency and cell cycle activity. The surprising

discovery is the co-expression of multipotency and neuronal activity markers in the same subpopulation. In chapter 4, 5-hydroxymethylcytosine (5hmC), the first product in the demethylation of 5-methylcytosine (5mC), levels were evaluated among NeuN-High, NeuN-Low and NeuN-Neg mouse brain nuclei. Tet-assisted bisulfite sequencing (TAB-seq) demonstrated that 5hmC levels in NeuN-High nuclei were significantly higher compared to NeuN-low and NeuN-Neg nuclei. The third study (chapter 5) identified a previously unknown subset of visceral adipose tissue (VAT) nuclei (PPARg2-Positive) that expressed significantly higher levels of transcripts encoding both mature adipocyte markers and chromatin-remodeling factors, and also had higher levels of 5hmC. Collectively, the studies of this dissertation provide further evidence that epigenetic reprogramming is a cell-type-specific process and advance nuclear cytometry for the analysis of brain and adipose tissues. Future epigenetics analyses will be enhanced by using the full potential of FANS and FNC technologies along with the wide variety of new and well-characterized immunological markers.

INDEX WORDS: epigenetics, cell-type-specific, fluorescence-activated nuclear sorting (FANS), fluorescence nuclear cytometry (FNC), Isolation of Nuclei Tagged in specific Cell Types (INTACT), 5-hydroxymethylcytosine (5hmC).

CELL-TYPE-SPECIFIC EPIGENETICS OF ORGAN-DERIVED NEURONS AND ADIPOCYTES

by

PING YU

B.S., East China Normal University, China, 2010

M.S., University of Georgia, 2012

A Dissertation Submitted to the Graduate Faculty of The University of Georgia in Partial Fulfillment of the Requirements for the Degree

DOCTOR OF PHILOSOPHY

ATHENS, GEORGIA

2017

CELL-TYPE-SPECIFIC EPIGENETICS OF ORGAN-DERIVED NEURONS AND ADIPOCYTES

by

PING YU

Major Professor:	Richard B. Meagher
Committee:	Jonathan Eggenschwiler Jianfu Chen Hang Yin Nathan T. Jenkins

Electronic Version Approved:

Suzanne Barbour
Dean of the Graduate School
The University of Georgia
May 2017

DEDICATION

I would like to dedicate this work to my parents, Guoqing Yu and Hongyun Tu, and my fiancé Jun Xu. My work on this dissertation could not have been possible without their support, encouragement and love.

ACKNOWLEDGMENTS

I would like to express my utmost gratitude to my Major Professor, Dr. Richard Meagher for the research direction and opportunity to progress in his laboratory. I am greatly inspired by his passion into science and his leadership. Without his guidance and encouragement, I would never have grown into an independent geneticist.

I would like to express my sincere gratitude for the guidance from all my committee members, Dr. Jonathan Eggenschwiler, Dr. Jianfu Chen, Dr. Hang Yin and Dr. Nathan Jenkins. I would also like to thank Dr. Clifton Baile for his recommendation and encouragement to pursue my PhD study in Meagher's lab.

I would like to thank previous and current members of the Meagher lab including Suresh Ambati, Shivangi Nath, Natalie Hohos, Emily England, Colette Miller, Elizabeth Mckinney, Muthugapatti Kandasamy and Diane Hartzell.

I want to thank our collaborators, Dr. Robert Schmitz for providing computation resources for data analysis.

Last but not least, I want to thank my fiancé Jun Xu and my parents Guoqing Yu and Hongyun Tu, for their constant support and love to complete this challenging journey.

TABLE OF CONTENTS

Page

CHAPTER 1

INTRODUCTION

Epigenetic controls function at the level of specific cell types. The "Holy Grail" of epigenetics is the ability to rapidly analyze chromatin structures from single cell types within an organ or tissue. Examining mixed populations of cell types compromises epigenetic data and may render it "unintelligible" (Deal and others, 2010a; Reinius and others, 2012b). Yet the majority of studies have been examining epigenetic profiles from samples derived from whole tissue or mixed cell types. These aggregated results from mixtures of cell types do not accurately capture the real biology of specific cell types, which is essential to understand for designing improved therapies. For example, DNA methylation profiles (methylation epitype) of seven purified individual blood leukocyte cell types are found to be significantly different from that of whole blood (Reinius and others, 2012b). Pairwise comparisons of the seven leukocyte types revealed that they varied at 9.5% to 40% of the 485,000 cytosine methylation sites assayed. Because the epitype of whole blood cells is the weighted average of methylation differences among all cell types, whole blood data has relatively weak statistical significance. Therefore, cell-type-specific epigenetic analysis makes it possible to obtain more biologically relevant data on chromatin structures.

The diversity of cell types in organs complicates attempts of epigenetic analysis at cell-type-specific level. For brain tissue, due to the interdigitation of neuronal and glial processes within and between other cells and tissues, it is nearly impossible to isolate subpopulations of

adult neurons from within the brain away from multipotential precursor cells, glia, leukocytes, and endothelium. For Adipose tissue, in addition to various classes of preadipocytes as well as maturing and mature adipocytes, adipose tissue is rich with blood vessels, endothelial cells and numerous lymphoid cell types (e.g. T cells, neutrophils, and natural killer cells) (Deiuliis and others, 2011b; Lumeng and others, 2011b; Lumeng and Saltiel, 2011b; Wozniak and others, 2009a). Mature white adipocytes can be enzymatically dissociated from adipose tissue, but they are difficult to be isolated because they are large (50 to 200 μm) and easily lysed during manipulation (Wei and others, 2013). Fluorescence activated cell sorting (FACS) has been used to fractionate dissociated adipocytes, but the large cell sizes require special instrumentation to prevent cell breakage, clogging and slow flow rates (Song and others, 2015). As an alternative, Fluorescence-Activated Nuclear Sorting (FANS) and Fluorescence Nuclear Cytometry (FNC) were used herein to study cellular nuclei as surrogates for isolated cells by fractionating nuclei into different subpopulations. These technologies are relatively simple to employ for "problematic tissues" and have the potential to reveal a great deal about epigenetically and transcriptionally distinct cell populations within tissues.

It was proposed by Sir Francis Crick 30 years ago that cellular memory was recorded as reversible modifications to DNA and proteins (Meagher, 2014). Only in the last decades has it become clear that changes to the epigenome, modifications to chromatin (such as methylation of DNA cytosine) and the post-translational modifications of nucleosomal histones (for example, acetylation, methylation, phosphorylation) play essential roles in memory formation and maintenance (Kramer, 2013; Rudenko and Tsai, 2014; Sweatt, 2013; Zovkic and others, 2013). We hypothesize that different cell types within a tissue have distinct epigenetic profiles, which are differentially potentiated to record cellular memories. Of particular interest is the recently

identified DNA cytosine modification 5-hydroxymethylcytosine (5hmC) which may define genes poised to change their expression through localized loss of 5mC (Lister and others, 2013a; Pastor and others, 2011). Because 5hmC may be the rate-limiting step in removing 5mC at CG dinucleotides, and hence, rate limiting to the turnover of modified cytosine, I examined 5hmC levels among distinct subpopulations of brain and adipose tissue nuclei by FANS.

I began the first study of my dissertation by developing techniques to rapidly isolate mouse brain nuclei and pig adipose tissue nuclei from formalin fixed tissues such that both nuclear structure and chromatin modification would be preserved. In chapter 3, FANS was applied to fractionate mouse brain nuclei into three different subpopulations, NeuN-High, NeuN-Low and NeuN-Negative (-Neg) based on the level of NeuN protein. NeuN is a neuronal nuclear localized RNA processing protein. I found a surprisingly large NeuN-High population that had decondensed chromatin and expressed significantly higher levels of transcripts encoding chromatin remodeling machinery and markers of learning and memory (*ARC, BDNF, ERG1, HOMER1, NFL/NEF1, SYT1*), chromatin remodeling (*SIRT1, HDAC1, HDAC2, HDAC11, KAT2B, KAT3A, KAT3B, KAT5, DNMT1, DNMT3A, Gadd45a, Gadd45b*) and multipotency and cell cycle activity (*BRN2, FOXG1, KLF4, c-MYC, OCT4, PCNA, SHH, SOX2*). In chapter 4, I explored the 5hmC levels among these three different subpopulations and found that NeuN-High nuclei had elevated levels of 5hmC and expressed higher levels of factors promoting modified cytosine turnover (*TET1, TET2, TDG, MBD2, MBD4*) relative to the balance of neuronal (NeuN-Low) or non-neuronal (NeuN-Neg) nuclei. In chapter 5, I extended FANS and FNC to the analysis of adipocyte nuclei within visceral adipose tissue. Nuclear sorting based on the expression of the adipocyte-specific nuclear receptor protein PPARg2 (peroxisome proliferator-activated receptor gamma 2) identified subpopulations of adipocyte and non-adipocyte nuclei

that differentially expressed a significant fraction of the epigenetic machinery assayed. Adipocyte nuclei were identified that had highly elevated levels of factors involved in the regulation of histone methylation (*KDM4A, KMT2C, SETDB1, ARID1A, JMJD6, PRMT5*) and DNA cytosine modification (*DNMT1, DNMT3A, TET1, TET2, TET3, AICDA)*, and in particular displayed widely divergent levels of 5hmC across the gene body of different groups of genes. Collectively, these studies all provide evidence of the importance and necessity of performing cell-type-specific epigenetics within a tissue or mixed cell types.

CHAPTER 2

LITERATURE REVIEW

To provide a basis for this dissertation, my literature review will focus on providing a relevant background on epigenetics, DNA methylation, 5-hydroxymethylcytosine, roles of DNA demethylation in neural development, cell-type-specific epigenetic analysis using FANS, decondensed chromatin and multipotency.

Epigenetics

The term “epigenetics” was used to refer the events that could not be explained by genetic principles and from its various inceptions and reincarnations has generally referred to the development of cells, tissues, and organs. Aristotle described epigenesis as the process by which organized organs and organisms developed from unorganized structures (Aristotle, 1984). Conrad Waddington defined epigenetics as “the branch of biology which studies the causal interactions between genes and their products, which bring the phenotype into being” (Waddington, 1942). In a subsequent publication when describing epigenetics Waddington begins with “at some early stage in development certain major discontinuities between tissues or organs become established” (Waddington, 1957). In an apparently independent inception of epigenetics, David Nanney states that after cell division the two daughter cells may be epigenetically different and states “The term "epigenetic" is chosen to emphasize the reliance of these systems on the genetic systems” and goes on to say “epigenetic systems regulate the expression of the genetically determined potentialities” (Haig, 2004; Nanney, 1958). Today,

Epigenetics is commonly defined as the heritable changes in gene expression or cellular phenotype that occur without changing the underlying DNA sequence (Campion and others, 2009; Dupont and others, 2009; Goldberg and others, 2007; Perez-Cornago and others, 2014). Epigenetic changes include DNA modification, histone and other protein modifications and microRNAs (Barter and others, 2012). Modifications to DNA and histone tails can alter chromatin structure and gene accessibility to transcriptional machinery and thus regulating patterns of gene expression (Handy and others, 2011). Here, I will briefly introduce the core molecular actors that play important role in epigenetic mechanisms.

DNA methylation

DNA methylation typically refers to the covalent attachment of a methyl group to the C5 position of cytosine residues in CpG-dense sequences (termed CpG islands (CGIs)), although methylation in non-CG contexts has also been reported in both humans and mice(Ichiyanagi and others, 2013; Lister and others, 2009; Ramsahoye and others, 2000). 5-methylcytosine (5mC) occurs predominantly in the context of CGIs in the genome (Goll and Bestor, 2005b). 5mC accounts for ~1% of the nucleotides in the human genome and is referred to as the fifth DNA base (Lister and Ecker, 2009).

Genomic DNA methylation patterns are donated by *de novo* or maintenance DNA methyltransferases (DNMTs). Currently, there are five known mammalian DNMTs: DNMT1, DNMT2, DNMT3A, DNMT3B and DNMT3L (Robertson, 2002). In mammals, new DNA methylation patterns are established by *de novo* DNA methyltransferases, DNMT3A and DNMT3B. Their activity can be modulated by a catalytically inactive family member, DNMT3L (Goll and Bestor, 2005a). During mitosis, the methylation patterns are maintained by DNMT1,

an enzyme that copies DNA methylation patterns from parent to daughter stand during DNA replication (Gibney and Nolan, 2010; Jones and Liang, 2009). Such inheritability of DNA methylation suggests a role for 5mC in long-term epigenetic regulation required for various biological functions, such as stable silencing of gene expression, maintenance of genome stability and establishment of genomic imprinting (Bird, 2002).

Typically DNA methylation is associated with condensed heterochromatin, resulting in the repression of gene expression (Siegfried and Simon, 2010). DNA methylation in gene promoter regions usually serves as a transcriptional "OFF" switch, which associated with transcriptional repression. However, gene body methylation has a less clear relationship with gene expression (Suzuki and Bird, 2008). In early embryogenesis, methylation is erased throughout the genome and then reestablished in all but CGIs. CGIs become methylated in later development and they are associated with transcriptional repression, especially when these methylated sites involve promoter or other gene regulatory regions (Bird, 1986; Illingworth and Bird, 2009; Weber and others, 2007). CGIs methylation suppress transcription by directly block DNA recognition and binding by some transcription factors. For instance, studies have shown that transcription activation at GC-boxes is inhibited by methylation which blocks the binding of Sp1 and Sp3 transcription factors at promoter contexts (Aoyama and others, 2004; Nomura and others, 2007). Alternatively, other factors may bind to methylated DNA and block the access of transcription factors. For example, Methyl-CpG-binding protein 2 (MeCP2) bind to methylated DNA and lead to transcriptional repression by recruiting histone deacetylases (HDACs), and HDACs promote chromatin condensation, further repressing transcription (Fuks and others, 2003).

5-hydroxymethylcytosine

Although DNA methylation pattern in somatic cells is stably maintained, genome-wide loss of 5mC is observed in developing primordial germ cells (PGCs) and early embryos (Hajkova and others, 2010; Mayer and others, 2000). Global DNA demethylation is essential for erasing parental-origin imprints in developing PGCs and resetting pluripotent states in early embryos (Feng and others, 2010b). There is evidence showing that the rapid erasure of 5mC during these two stages of epigenetic reprogramming cannot be fully explained by replication-dependent passive loss of 5mC, suggesting the existence of enzymatic process that actively remove methyl groups on cytosines (Wu and Zhang, 2010).

Recently, 5-hydroxymethylcytosine (5hmC) was identified as another epigenetic mark that arose from oxidation of 5mC by ten eleven translocation (TET) (Ito and others, 2010; Kriaucionis and Heintz, 2009; Tahiliani and others, 2009; Williams and others, 2011a; Xu and others, 2011). Evidence has shown that dynamic regulation of DNA methylation is mainly achieved through a cyclic enzymatic cascade. First, DNA methyltransferase (DNMTs) methylate DNA cytosine to 5mC, while TETs catalyze its conversion to 5hmC and to other more oxidized forms (5fC, 5caC). Although, 98% of TET activity is restricted to modified cytosine residues in the CG dinucleotide context. Thymine-DNA glycosylase (TDG) acts on 5fC or 5caC to generate an abasic site (-OH). The base excision repair pathway (BER) and factors like the GADD45s recognize a G residue in the antiparallel DNA strand and restore cytosine (Wu and Zhang, 2014).

5hmC has been proposed to be not only an intermediate of the demethylation of 5mC, but is associated with gene expression changes. Genome-wide mapping of 5hmC in several mouse brain regions showed an enrichment of 5hmC in intragenic regions (gene bodies) as well as in proximal upstream and downstream regions relative to the transcription start site (TSS) and was

associated with more highly expressed genes, namely developmentally activated genes. Approximately 70% of mammalian promoters are associated with short CpG-dense sequences (Deaton and Bird, 2011). CpG-rich promoters are generally unmethylated and transcriptionally active. The lack of 5mC at CpG-rich promoters predicts that TET-mediated oxidation of 5mC is minimal at these promoters, in other word, there is minimal levels of 5hmC on promoters. Indeed, studies have shown that regions surrounding the transcriptional start site (TSS) of active promoters are generally devoid of 5hmC in mouse ESCs (Shen and others, 2013; Song and others, 2013; Yu and others, 2012c). However, enrichment of 5hmC within intragenic regions, particularly at 3' portion of gene bodies, is found to be a hallmark of active transcription in virtually all cell types that have been studied, including mouse/human embryonic stem cells (Szulwach and others, 2011b; Tahiliani and others, 2009; Williams and others, 2011b; Wu and others, 2011; Yu and others, 2012b), neuronal cells (Kriaucionis and Heintz, 2009; Lister and others, 2013b; Mellen and others, 2012) and adipocytes (Serandour and others, 2012a). Also despite their scarcity in the genome, 5fC and 5caC also seem to accumulate within active transcribed gene bodies (Shen and others, 2013; Song and others, 2013). In mouse ESCs, 5hmC are found to be enriched at poised tissue-specific enhancers (H3K4me1-positive, H3K27ac-negative), indicating that these poised enhancers are pre-marked by 5hmC for subsequent demethylation during later development (Shen and others, 2013; Song and others, 2013), suggesting that hydroxymethylation might be an early event in enhancer activation. The exact role of intragenic 5hmC/5fC/5caC in transcriptional regulation has not been fully investigated.

Besides acting as an intermediates of active DNA demethylation, there is evidence suggesting that 5hmC is relatively stable in the genome and may influence transcription by recruiting or repelling specific DNA binding proteins. For example, several methyl-CpG-binding

domains (MBD) proteins, including MBD3, MeCP2, and MBD4 are reported to bind to fully hydroxymethylated CpG sites, and regulate 5hmC marked genes (Mellen and others, 2012; Otani and others, 2013; Yildirim and others, 2011). Recently, mass spectrometry has identified a large number of candidate proteins that bound selectively to or repelled by 5hmC containing sequences from mouse ESC and mouse brain lysate (Spruijt and others, 2013).

Role of DNA demethylation in neural development

The development of mammalian brain is a finely orchestrated spatiotemporally by precisely controlled gene regulation to generate diverse, functionally distinct populations of neurons and glia. Brain-specific deletion of DNA methylation results in postnatal neurodevelopment abnormalities and neuronal function defects (Chahrour and Zoghbi, 2007; Nguyen' and others, 2007; Wu and others, 2010), suggesting that the precise control of DNA methylation pattern is required for proper brain development and maturation. Major parts of mammalian brains, frontal cortex, hippocampus and cerebellum, all displayed an increase of 5hmC levels with an increase of age (Lister and others, 2013b; Munzel and others, 2010; Song and others, 2011b; Szulwach and others, 2011c). In fact, the adult mammalian brain contains the highest levels of 5hmC compared to other tissues such as kidney, lung and liver, accounting for about 40% of methylated CG sites in cerebellar Purkinje cells (Globisch and others, 2010a; Kriaucionis and Heintz, 2009). Given the evidence that 5hmC is an intermediate in an active DNA demethylation pathway, it suggests that DNA demethylation and 5mC turnover may be functionally important in neuronal development. It may be worth noting at this point that along with my collaborators I discovered surprisingly high levels of 5hmC in adipose tissue (Chapter

4), considering that we conceive of this tissue as much less active in functions concerning molecular memory.

TET enzymes are dioxygenases capable of oxidizing 5mC into 5hmC. The Tet protein family includes three members: Tet1, Tet2 and Tet3. All three Tet genes are expressed at detectable levels in developing mouse brains. Knockdown of Tet1 significantly increased apoptosis of cerebellar granule cells in mouse brain (Xin and others, 2015). Mice lacking Tet1 exhibited impaired hippocampal neurogenesis which affected cognitive brain functions such as learning and memory (Zhang and others, 2013). Similarly, knockdown of Tet2 and Tet3 led to neuronal differentiation deficits (Hahn and others, 2013). In contrast, overexpression of Tet2 and Tet3 seems to promote mouse embryonic neurogenesis (Hahn and others, 2013). In addition, Tet 3 has been reported to be essential in early eye and neural development in Xenopus (Xu and others, 2012). Future studies elucidating the effect of TET depletion should be a key contribution to better understand how the absence of these enzymes influence brain development and function.

Cell-type-specific epigenetics

There is a critical need to perform cell-type-specific epigenetic analyses of cells derived from organs or tissues if we are to obtain significant data defining their developmental state. For example, adipose tissue is not the same as adipocytes and brain is not the same as neurons, even if we conceive of the latter as the dominant and critical cell types to organ function. Although it is now accepted that epigenetic controls function at the level of specific cell types, most of the epigenetic studies published examine chromatin structures of whole organs or tissues and most commonly whole blood (Yu and others, 2016). These averaged results from mixtures of cell

types do not accurately capture the real biology or epigenetics of specific cell types, which is essential to understand for designing improved cell therapies. It was found in healthy male blood donors there is huge variation in the DNA methylation profiles of whole blood, mononuclear cells, granulocytes, and cells from seven purified leukocytes (Reinius and others, 2012a). Reinius et al. found that the CD4+ T cells and the CD8+ T cells differed in ~45,000 sites of the ~485,000 sites assayed in methylation levels (Reinius and others, 2012a). Because the epitype of whole white blood cells is the weighted- average of the methylation differences among all cell types, whole blood data has relatively weak statistical significance.

The brain is a particularly good example of highly specialized and diverse functions from the same genetic program. One of the important epigenetic mechanisms, DNA methylation has been shown to contribute to memory formation (Miller and Sweatt, 2007), synaptic plasticity (Feng and others, 2010a) and developmental visual cortical plasticity (Maya-Vetencourt and Origlia, 2012). Despite its importance, the epigenetic profile of the brain has not yet been explored in depth due to brain region and cell-type heterogeneity. Recent studies have indicated that DNA methylation significantly varied between different brain regions as well as between white and gray matter of the same region (Davies and others, 2012; Gibbs and others, 2010; Ladd-Acosta and others, 2007). The brain is composed of a heterogeneity of cell types including neurons and glia among different brain regions. A study has shown that neurons and glia from human and mouse frontal cortex differed significantly in the composition and patterning of mCG and mCH (H=A, T, C). Neurons were globally enriched for mCH compared with glia (Lister and others, 2013a).

White adipose tissue (WAT) contains many different cell types of which adipocytes comprise only 20-40% (Benton and others, 2015). Thus, differences in the DNA methylome of

non-fat cells within adipose tissue mask differentially DNA methylated sites in fat cells (e.g., adipocytes). Changes in the adipose tissue DNA methylome may therefore reflect altered cellular composition rather than altered DNA methylated sites in a specific cell type. And in fact, the cellular composition of adipose tissue varies dramatically in response to high fat diet, inflammation, and hypoxia. A study of the DNA methylome of isolated adipocytes from WAT reported bigger absolute difference in methylation at specific CpG sites between obese women and non-obese women compared to previous studies using whole WAT pieces (Arner and others, 2015; Benton and others, 2015; Nilsson and others, 2014).

In brain tissue, the interdigitation of axons and dendrites extending from adult neurons prevents the isolation of large populations of adult neurons from within the brain away from glia, leukocytes, and endothelium and from other classes of neurons. In other words cell sorting can't be used to separate intact fully adult neuronal cells because they are so damaged during isolation. Although sorting has been used in neuroscience, its use is limited to embryonic brain tissue, stem cells cultured cells, or synaptosomes as these cells or organelles lack or have fewer extensive processes and connections than adult neurons (Arlotta and others, 2005; Maric and Barker, 2005; Wolf and Kapatos, 1989a; Wolf and Kapatos, 1989b; Wolf and Kapatos, 1989c). In visceral adipose tissue, mature white adipocytes may be enzymatically dissociated from adipose tissue, but they are difficult to be isolated because they are large (50 to 200 μm) and easily lysed during manipulation (Wei and others, 2013). Among the approaches used to improve cell-type specificity, laser capture microdissection recovers only small amounts of brain tissue (Craven and Banks, 2002; Merbs and others, 2012b). Isolation of nuclei tagged in specific cell types (INTACT) is easily scalable, but requires the expensive genetic engineering of a target cell type in a model organism (Deal and others, 2010b; Henry and others, 2012). Fluorescence nuclear

cytometry (FNC) and fluorescence activated nuclear sorting (FANS) have been used in just a few studies to reduce the complexity of brain cell transcriptomes, epigenomes, and proteomes (Bilsland and others, 2006b; Dammer and others, 2013b; Okada and others, 2011a). The transcription profile in the nucleus is essential the same as that in the cells. A genome-wide study of 22,000 transcripts showed that nuclear RNA levels correlated linearly and strongly with total cellular RNA levels [r=0.94; see supplement to (Deal and others, 2010a)]. That is to say, for the majority of transcripts, but not all transcripts, nuclear RNA levels reflect total cellular RNA levels. A recent analysis of human brain cell nuclei demonstrated that the proteome and methylome of NeuN-positive nuclei is quite distinct from that of NeuN-negative nuclei (Dammer and others, 2013b; Lister and others, 2013a). However, the manipulation of cellular nuclei derived from a tissue as a surrogate for isolated cells is still in its infancy.

Decondensed chromatin and multipotency

Chromatin is the state in which DNA is packaged within the cells. The nucleosome is the fundamental unit of chromatin and it is composed of an octamer of the four core histones (H3, H4, H2A, H2B) around which 147 base pairs of DNA are wrapped (Kouzarides, 2007). Emil Heitz made the distinction between the two varieties of chromatin, heterochromatin and euchromatin in 1928. Heterochromatin represented the more densely stained, compacted areas, while euchromatin represented the sparsely stained less compacted chromatin. On the basis of predominantly histological evidence, many stem cells and progenitor cells have been classically described as having an open chromatin conformation nearly devoid of heterochromatin (Gaspar-Maia and others, 2011). Neural progenitor cells (NPCs) is a type of stem/progenitor cell which are defined as “undifferentiated cells which are capable to self-renew and display neuronal and

glial differentiation potential". NPCs appear early in development and remain active within the central nervous system for the whole life duration of the organism (Park and others, 2013b).

The evidence of the association of open chromatin with pluripotency first came from directly visualizing chromatin in embryonic stem (ES) cells under electronic microscopy. What was observed is the prevalent heterochromatin in differentiated cells, but much less so in undifferentiated ES cells (Park and others, 2004). ChIP-seq analysis showed that the repressive histone modification marks H3K9me3 and H3K27me3 increased from 4% genome coverage in ES cells to 12%-16% in differentiated cells (Hawkins and others, 2010). On the other hand, H3K9 acetylation, an epigenetic mark associated with open chromatin, has been shown to be decreased globally along with the endoderm-like differentiation of human ES cells (Krejci and others, 2009). Also, there is indirect evidence that supports the open chromatin state in pluripotent stem cells. Studies have shown that the chromatin in ES cells contains loosely bound architectural chromatin proteins, such as core and linker histone, and heterochromatin protein 1, which however, was not observed in differentiated cells (Bhattacharya and others, 2009; Meshorer and others, 2006). Moreover, the genome of the ES cells is transcriptionally globally hyperactive in which case it transcribes normally silenced repetitive elements as well as coding and non-coding regions resulting in increased levels of total RNA, whereas the transcription landscape becomes more discrete as differentiation proceeds (Efroni and others, 2008). Taken together, these data indicate that chromatin in pluripotent cells is globally decondensed compared to differentiated cells.

Well-characterized multipotent cells have enlarged nuclei. This apparently results from decondensed chromatin and large amounts of chromatin remodeling and transcriptional machinery that is associated with elevated epigenetic and transcriptional activities readying them

to enter the cell cycle and to differentiate (Hezroni and others, 2011b; Ram and Meshorer, 2009a). This property of having enlarged nuclei has been described as associated with the "chromatin plasticity of pluripotent cells" (Melcer and Meshorer, 2010a). Examples of multipotent cell types with decondensed chromatin come from various sources including large adult retinal pyramidal neurons (Davis and Dyer, 2010a), embryonic or induced PSCs (Hezroni and others, 2011a; Morey and others, 2007b; Ram and Meshorer, 2009b), and somatic cells after nuclei transplantation just prior to embryo development (Ostrup and others, 2009a). The connection between decondensed chromatin and multipotency has not been elucidated in most studies of multipotent neural progenitor/precursor cells (NPCs).

Recent lineage tracing studies demonstrate that some adult highly differentiated postmitotic neuronal and glial cells are potentiated to reenter the cell cycle, produce certain classes of progenitor cells, and contribute to the genesis of new adult neurons and glia (Bonaguidi and others, 2012b; Ladewig and others, 2013a). This stands in complete opposition of the earlier view that cells in most adult organs and neurons and glia in the brain in particular were in a state of hypertrophy and developmentally incapable of hyperplasia (e.g., cell division) (Goss, 1966). There are now examples of post-mitotic neuronal cells reentering the cell cycle include adult mouse retinal horizontal neurons producing multipotent retinal progenitor cells (Davis and Dyer, 2010b), adult mouse hippocampal quiescent glia-like cells generating proliferative precursors which give rise to neuroblasts and then immature neurons (Dranovsky and Leonardo, 2012), and mouse Sox2 expressing radial glial cells from subgranular zone of the hippocampal dentate gyrus apparently developing into NSCs and then into glial and neural cells (Suh and others, 2007). Neural progenitor/precursor cells (NPCs), in the broadest sense, the numbers and the types of

multipotential NPCs including cells derived from “postmitotic” neurons are far greater than previously anticipated.

CHAPTER 3

CHARACTERIZATION OF BRAIN CELL NUCLEI WITH DECONDENSED CHROMATIN[1]

[1]Yu P, Mckinney EC, Kandasamy MM, Albert AL, Meagher RB. Accepted by *Developmental Neurobiology*.

Reprinted here with permission of the publisher, 10/30/14.

Abstract

Although multipotent cell types have enlarged nuclei with decondensed chromatin, this property has not been exploited to enhance the characterization of neural progenitor cell (NPC) populations in the brain. We found that mouse brain cell nuclei that expressed exceptionally high levels of the pan neuronal marker NeuN/FOX3 (NeuN-High) had decondensed chromatin relative to most NeuN-Low or NeuN-Neg (negative) nuclei. Purified NeuN-High nuclei expressed significantly higher levels of transcripts encoding markers of neurogenesis, neuroplasticity, and learning and memory (ARC, BDNF, ERG1, HOMER1, NFL/NEF1, SYT1), subunits of chromatin modifying machinery (SIRT1, HDAC1, HDAC2, HDAC11, KAT2B, KAT3A, KAT3B, KAT5, DMNT1, DNMT3A, Gadd45a, Gadd45b) and markers of NPC and cell cycle activity (BRN2, FOXG1, KLF4, c-MYC, OCT4, PCNA, SHH, SOX2) relative to neuronal NeuN-Low or to mostly non-neuronal NeuN-Neg nuclei. NeuN-High nuclei expressed higher levels of HDAC1, 2, 4, and 5 proteins. The cortex, hippocampus, hypothalamus, thalamus, and nucleus accumbens contained high percentages of large decondensed NeuN-High nuclei, while the cerebellum, and pons contained very few. NeuN-High nuclei have the properties consistent with their being derived from extremely active neurons with elevated rates of chromatin modification and/or NPC-like cells with multilineage developmental potential. The further analysis of decondensed neural cell nuclei should provide novel insights into neurobiology and neurodegenerative disease.

Key words: sorting, nuclei, cytometry, pluripotency, cell-cycle, epigenetics

Introduction

New models have emerged recently to explain the roles and relationships among various hyperplastic multipotential neural cells contributing to neurogenesis (Bonaguidi and others, 2012b; Ladewig and others, 2013a). In the adult brain, neural stem cells (NSCs), pluripotent stem cells (PSCs), and neural progenitor/precursor cells (NPCs) all may develop into neurons and glia (Ehninger and Kempermann, 2008; Ladewig and others, 2013b; Taupin, 2009). Unexpectedly, lineage tracing studies demonstrate that some adult highly branched and differentiated postmitotic neuronal and glial cells are also potentiated to reenter the cell cycle, produce certain classes of progenitor cells, and contribute to the genesis of new adult neurons and glia (Bonaguidi and others, 2012a; Ladewig and others, 2013b). Examples of postmitotic neuronal cells reentering the cell cycle include large adult mouse retinal horizontal neurons producing multipotent retinal progenitor cells (Davis and Dyer, 2010b), adult mouse radial glial cells from the dentate gyrus showing multilineage potential and producing new neurons and glia (Bonaguidi and others, 2011; Dranovsky and Leonardo, 2012), "postmitotic" quiescent mouse progenitor cells in the hippocampus undergoing asymmetric and symmetric cell divisions to produce stem cell-like cells that developed into new "postmitotic" neurons and astrocytes (Encinas and others, 2011; Lugert and Taylor, 2011) and mouse Sox2 expressing radial glial cells from subgranular zone of the hippocampal dentate gyrus apparently developing into NSCs and then into glial and neural cells (Suh and others, 2007). Using the phrase, NPCs, in the broadest sense, the numbers and types of multipotential NPCs including cells derived from "postmitotic" neurons is far greater than previously anticipated.

Well-characterized multipotent cells have enlarged nuclei with decondensed chromatin that is associated with elevated epigenetic and transcriptional activities readying them to enter the

cell cycle and/or to differentiate (Hezroni and others, 2011a; Melcer and others, 2012b; Ram and Meshorer, 2009b). This property has been variously described as the "chromatin plasticity of pluripotent cells" (Melcer and Meshorer, 2010a). Examples of multipotent cell types with decondensed chromatin come from various sources including large adult retinal pyramidal neurons (Davis and Dyer, 2010a), embryonic or induced PSCs (Hezroni and others, 2011a; Morey and others, 2007b; Ram and Meshorer, 2009b), and somatic cells after nuclei transplantation just prior to embryo development (Ostrup and others, 2009a). The connection between decondensed chromatin and multipotency has not been addressed in most studies of multipotent NPCs. The interdigitation of axons and dendrites extending from adult neurons prevents the isolation of large populations of adult cells with decondensed chromatin from brain tissue and direct analysis of their pluripotency. However, populations of nuclei are relatively easy to isolate directly from brain tissue and may be characterized directly, circumventing the difficulties of manipulating adult brain cells (Bilsland and others, 2006a; Dammer and others, 2013a; Okada and others, 2011b).

We focused on characterizing neuronal nuclei with decondensed chromatin from young mouse brain to make an assessment of multipotent NPC populations independent of the growth properties of isolated brain cells. We hypothesized that exceptionally large decondensed neural cell nuclei from brain define a broad class of NPCs. Surprisingly, we found that brain cell nuclei expressing the highest levels of the pan-neuronal marker NeuN, represented a large fraction of the brain cell nuclei with decondensed chromatin. These decondensed NeuN-High nuclei showed elevated expression of markers for neuronal cell types and neuronal plasticity and for epigenetic, cell cycle, and pluripotent activities. Decondensed neuronal nuclei were found in particularly high concentrations in some regions of the brain, but were nearly absent from others.

Methods

Mice

Mice (BALB cJ) weighed between 25 and 30 g and were handled according to AUP approved protocols (project AUP number: A3437-01). Live mice were obtained from UGA's animal facility and flash frozen mice were obtained from Rodent Pro (Evansville, IN).

Protocol for Isolating Brain Cell Nuclei

The following rapid protocol for isolating brain cell nuclei combined and simplified the general methods described previously for higher plant and vertebrate nuclei. The main difference in this protocol over those published previously is combining a prefiltration with Miracloth to sort out nuclei from debris, a brief centrifugation through a sucrose cushion at low speed instead of longer periods using ultracentrifugation, and an additional filtration through a small pore Swinnex filter (Kandasamy and others, 2010; Lopez-Sanchez and Frade, 2013; Luthe and Quatrano, 1980; Westra and others, 2010a). Freshly dissected and minced mouse brain tissue was treated for 1 h to 2 months in 4 volumes (w/v) of 0.3SPBSTA (0.3 M Sucrose, 20 mM KH2PO4, 20 mM Na_2HPO4, pH 57.2, 137 mM NaCl, 3.0 mM KCl, 0.1% Triton X-100, 0.1% sodium azide), plus 3.7% freshly added formalin. Fresh, fixed, or flash frozen brain tissue was homogenized in a Polytron (Fischer Sci) for 2.5 min at a setting of 6.5 in 16 volumes (w/v) of 0.3SPBSTA (1 g/16 ml). The homogenate was filtered through large pieces (10 in. sq.) of Miracloth (Calbiochem, #475855) stretched loosely over a funnel. This prevented nuclei from being trapped with large pieces of cytoplasm during the subsequent centrifugation and increased the yield of nuclei 8-fold to 10-fold. Nuclei were centrifuged through a sucrose cushion (1.4 M sucrose, in 1.4SPBSTA) in a swinging bucket rotor in a refrigerated centrifuge (4 °C) at 3000g

for 20 min instead of 3 h at 82,000g in an ultracentrifuge as described previously (Korfali and others, 2009). The nuclear pellet was gently resuspended in 20 volumes of 0.3 M SPBSTA and pressed slowly through a 25-mm diameter Swinnex Nylon Net Filter with a 41 μm pore size (EMD Millipore). The yield of nuclei from fresh fixed mouse brain tissue was approximately 80 x 10^6 nuclei/g of brain tissue and several-fold less from frozen brain tissue fixed subsequent to thawing. Nuclei were stored for up to 1 year at 4 °C in PBSTBA (PBS + 0.1% Triton X-100 + 5% BSA + 0.02% Azide) and 4% formaldehyde. All reagents were purchased from Thermo Fisher (Waltham, MA), unless stated otherwise.

Isolated Brain Cell Nuclei were Examined by IFM, FNC, and FANS

The following protocols were conducted at room temperature. Samples of 0.4 x 10^6 to 20 x 10^6 nuclei were pelleted in 1.5-mL microfuge tubes in a horizontal rotor at 800g for 2 min, washed once in 0.5 mL 50% methanol in PBS, washed twice in PBSTBA, and blocked for 1 h in PBSTBA on a neutator. For FNC 400,000 nuclei were incubated in 100 mL with primary antibodies (**Supplemental Table 2.S1**) at dilutions of 1:100 to 1:500 for 1 h at room temperature. For FANS, where as many as 100-times more total nuclei were labeled in small volumes, antibody concentrations was estimated based on the number of nuclei being examined (>0.75 ug antibody per 10^6 nuclei) and not the volume of buffer. In a typical FANS experiment, 15 mg of labeled Alexafluor conjugated anti-NeuN antibody was incubated with 20 x 10^6 nuclei in 500 uL for 1 hour on a neutator at room temperature. Anti-NeuN antibodies were chemically conjugated with DyLight488 (Thermo Scientific, #46403) or AlexaFluor488 (Life Technologies, A20181). In FNC experiments unconjugated rabbit polyclonal HDAC antibodies bound to nuclei were reacted in semidarkness with fluorescent secondary anti-rabbit antibody. After three washes

samples were co-stained with DAPI 0.1 mg/mL for 30 min. Photographic images of nuclei and tissue sections were made on a confocal microscope (Zeiss SM710) using ZEN 2011 software or on a Leica TR600 epifluorescence microscope using Hamamatsu SimplePCI Image Analysis software to process images and measure nuclear areas and fluorescence intensities.

NeuN-High nuclei appear to have a higher nuclei acid content based on DAPI or Hoechst staining than the balance of nuclei. However, it should be noted neither DAPI nor Hoechst are completely DNA specific. For example, using the common emission filters to detect DAPI fluorescence (em440 to em480), the signal from RNA is approximately 20 to 30% as strong as that for an equivalent amount of DNA (Tanious et al., 1992). Therefore, in very large nuclei with significantly more RNA, a considerable fraction of the fluorescent signal may come from RNA and not from an increased DNA content. Propidium iodide (PI) staining appeared to reduce the NeuN-antibody staining intensity, and hence, PI was not used in these experiments.

Nuclei to be examined by FNC or FANS were prefiltered in 0.5 mL aliquots by centrifugation at 300g into a polystyrene tube with 35-μm cell-strainer cap (BD Falcon, REF352235). FNC and FANS were conducted on a Cyan ADP and a MoFlo XDP, respectively (Beckman Coulter Miami, Florida). Nuclei were gated for 2C or greater DNA content and forward (FS) and side (SS) light scattering to eliminate the analysis of small particulate contamination (**Supplemental Figure 2.S1A**). Pulsed width gating did not detect a significant number of doublets (**Supplemental Figure 2.S1C**) nor did the application of a pulse-width gate significantly alter the relative populations of sorted nuclei. Furthermore, a pulse-width gate was not applied, because of the concern that it might eliminate some very large decondensed nuclei that were of interest to this research. Figures of FNC and FANS data were prepared using FlowJo Software version 9.7.6 (Treestar, Ashland, OR).

RNA and qRT-PCR

RNA from formalin fixed nuclei was prepared using RNeasy FFPE kit (Qiagen). A heat treatment of 90°C for 1 h was included, after the proteinase K digestion, to hydrolyze off the formalin (Fraenkel-Conrat and Olcott, 1948). RNA was quantified using a Qubit RNA Assay Kit (Life Technologies). The yield of RNA from 500,000 fixed sorted nuclei varied from 0.5 to 3 µg. 250 ng samples of RNA were reverse transcribed (RT) into cDNA using qScript cDNA SuperMix (Quanta BioSciences). After RT, 0.5 µl of RNase H at 5 units/µL (New England Biolabs) was added to the 20 µL reaction and incubated at 37°C for 20 min. cDNA yield was quantified using the Qubit ssDNA (single strand DNA) Assay Kit. 1.5 ng of cDNA was used per reaction in qRT-PCR assays. Primers are described in **Supplemental Table 2.S2**. Four commonly used control transcripts (b-actin, a-tubulin, RPL13, GAPDH) (Vandesompele and others, 2002) were not equivalently expressed in the three nuclear fractions, when qRT-PCR assays were normalized for equivalent cDNA input, and hence, were not suitable as controls. Each assay was run in triplicate and the Relative Quantity of transcript was calculated based on the ddCT method including the standard deviation from the mean (Livak and Schmittgen, 2001). The properties of the marker genes assayed are described in **Supplemental Table 2.S3**.

Western Blotting

Protein blotting experiments were performed as described previously with minor modifications (Kandasamy and others, 2002). Protein extracts from total brain and purified nuclei were prepared by heating homogenates in Laemmli SDS sample buffer at 95°C for 5 min and centrifuging out the insoluble material. Antibodies are described in **Supplemental Table 2.S1.**

Tissue Fixation, Cryosections, Immunohistochemistry

Mice were anesthetized with inhaled isoflurane (project AUP number: A3437-01) and quickly sacrificed via decapitation according to AUP approved protocols. The brains were rapidly dissected out, and immediately placed into ice-cold 4% formalin in PBS at 4℃ overnight. Alternatively, mice were deeply anesthetized by injection with ketamine (Lloyd, NADA 139–236) and aylazine (Vedco, NDC 50989-996-06) and transcardially perfused with 4% formaldehyde in PBS before dissection (Ohira and Miyakawa, 2011). The brains were then transferred into 30% sucrose-PBS at 4 ℃ and incubated until they were completely submerged. Each brain was embedded in OCT (#14–373-65 Fischer Scientific), and frozen in dry ice for cryosectioning. Sagittal or coronal sections (10 μm) were taken on a Leica cryostat (CM305) and collected on poly-L-lysine coated microscope slides (Polysciences, Inc. #2224). Slides were stored at -80 ℃. Slides were thawed, rinsed with PBS, and incubated for 5 min with PBST (PBS+ 0.1% Triton X100). Small 1.5 cm areas on slides were encircled with a Dako pen (Dako S200230) to contain antibody solutions. Sections on slides were blocked with PBST + 5% BSA+ 2% goat serum for 1 hour. Two different mouse monoclonal antibodies to NeuN (Millipore A60 MAB377, Abcam ab104224) (**Supplemental Table 2.S1**) were used at 1:200 dilutions into PBS and treating tissue sections 1 hour to overnight. Slides were washed three times with PBST and incubated with Alexafluor488 conjugated goat anti-mouse antibody (Life Technologies A11001) at 1:500 dilution in PBS for 1 h. Slides were washed three times with PBST, co-stained with DAPI and photographed on a Leica TR600 epifluorescent microscope.

Results

Isolating Brain Cell Nuclei

We developed a simple rapid method of purifying mouse brain cell nuclei (3-month-old mice) in less than 3 h that is summarized in **Figure 2.1A**. The relative purity and recovery of isolated nuclei was routinely examined by combined DIC and IFM imaging on a hemocytometer (**Figure 2.1B**). To further test the enrichment of nuclei, we compared nuclear proteins in the crude homogenates to proteins in purified nuclei using Western blotting. The nuclear fraction contained very little of the predominantly cytoplasmic proteins NSE and actin and was highly enriched for nuclear protein histone H3 (**Figure 2.1C**). Because of our long-term interest in epigenetic alterations to chromatin structure in NPCs, we focused on nuclei isolated from formalin fixed fresh tissue, yet this isolation protocol worked similarly, but with lower yield, for fresh unfixed or flash frozen tissue that was subsequently fixed (Materials and Methods).

The widely used pan-neuronal marker NeuN (Neuronal Nuclei) is an RNA splicing factor (Dredge and Jensen, 2011b) that is essential to brain development and the differentiation of most postmitotic neurons (Gehman and others, 2012; Kim and others, 2013a). We found that a significant portion of the nuclear population (15 to 20%) from young mouse brain stained exceptionally strongly for NeuN (NeuN-High) using the mouse mAb 1B7. The NeuN-High nuclei appeared much larger (see arrows) than nearly all of the nuclei that were weakly immune-stained or unstained with NeuN antibodies as shown in (**Figure 2.1E**). A similar population of decondensed NeuN-High nuclei were also observed (**Supplemental Figure 2.S2**) using the classical mAb for NeuN, A60 (Mullen and others, 1992a).

Sorting Isolated Nuclei

Nuclei from formalin fixed mouse brain were labeled with Alexafluor488 conjugated NeuN antibodies and examined by fluorescent nuclear cytometry (FNC) and fluorescence activated nuclear sorting (FANS) (Dammer and others, 2013a). Nuclear populations were gated to include 2C and 4C nuclei after DAPI staining for DNA (**Figure 2.2A**). A histogram revealed three populations: non-neuronal NeuN-Neg (negative) nuclei, neuronal NeuN-Low nuclei (weakly immunostained main peak), and a shoulder of neuronal NeuN-High nuclei, those stained most strongly for NeuN (**Figure 2.2B**). We used FANS to isolate these three populations of nuclei. The sorted NeuN-Neg, -Low, and -High nuclei were reanalyzed by cytometry to confirm that these fractions indeed represented three distinct nonoverlapping populations based on NeuN staining levels (**Figure 2.2C–E**). IFM after sorting and without restaining (**Figure 2.2F–H**) revealed that the NeuN-Neg and NeuN-Low populations were primarily composed of small nuclei with diameters of 6 to 7 μm, typical of mammalian 2C nuclei, although the NeuN-Low population did contain some very large nuclei (Arrow, **Figure 2.2G**). By contrast the NeuN-High population was highly enriched for very large nuclei with decondensed chromatin (Arrows, **Figure 2.2H-I**), displaying diverse nuclear morphologies including oval, triangular, trapezoid, spindle, and kidney shaped nuclei. Many of the large NeuN-High nuclei had average diameters exceeding 14 μm, twice that of typical 2C nuclei. Nuclear area was quantified for the three sorted populations (**Figure 2.2J**). NeuN-High nuclei from different experiments had areas that averaged 1.85 to 2-times larger than the other two populations, and hence, their volumes were predicted to be several times larger than typical interphase nuclei. We presume that most of the NeuN-Neg nuclei are from leukocyte, glial and endothelial cells.

Analysis of these cytometric data for nuclei with exceptionally strong DAPI staining, revealed that essentially all of the NeuN-High nuclei came from what might be presumed to be the greater than 2C (">2C") class of nuclei, while only a small fraction of NeuN-Neg or NeuN-Low nuclei belonged to the ">2C" class. This relationship may be seen by comparing the red ">2C" population of nuclei in **Figure 2.2A** to that in **Figure 2.2B**. Because DAPI and Hoechst (not shown) also fluoresce modestly well when bound to RNA (see Materials and Methods) and because these large nuclei likely contain a lot more RNA, the actual DNA content or ploidy level of most of ">2C" NeuN-High nuclei was not clear from our analysis (see Materials and Methods). Within this background of ">2C" nuclei with high nucleic acid content, a small peak of tetraploid nuclei representing a few percent of the total population of brain cell nuclei is apparent in **Figure 2.2A** (located at 204 fluorescence units on the DAPI scale) as has been reported previously for human, mouse, and chicken brain (Lopez-Sanchez and Frade, 2013; Mosch and others, 2007; Westra and others, 2010b). A further examination of **Figure 2.2B** and a comparison of **Figure 2.2F-I** also revealed a second smaller population of strongly DAPI staining decondensed ">2C" nuclei in the NeuN-Neg nonneuronal population, which are probably from glial, leukocyte, and/or endothelial cells.

NeuN-High Nuclei had an Exceptional Transcript Expression Profile

Quantitative real time PCR of RT nuclear transcripts (qRT-PCR) was used to characterize the cells from which the NeuN-High, NeuN-Low, and NeuN-Neg nuclei were enriched. A genome-wide study of 22,000 transcripts shows that nuclear RNA levels correlated linearly and strongly with total cellular RNA levels [r = 0.94; see supplement to (Deal and others, 2010a)]. That is to say, for the vast majority of transcripts, but not all transcripts, nuclear RNA levels

reflect total cellular RNA levels. RNA was prepared from the formalin fixed and sorted brain cell nuclei, reverse transcribed into cDNA, and the amount of cDNA produced was quantified (Materials and Methods). We screened for appropriate endogenous RNA controls that could be used to normalize the relative quantities (RQ) of transcript levels among the three nuclear fractions in qRT-PCR assays (see Materials and Methods). Transcript levels for succinate dehydrogenase complex subunit A (SDHA) transcript and ribosomal protein large subunit 13A (RPL13A) did not vary significantly among the NeuN-High, -Low, and -Neg nuclear RNA samples, when the qRT-PCR assays were controlled to contain equivalent amounts of input cDNA (e.g., 1.5 ng per assay). SDHA and RPL13A transcripts were shown previously to be reasonable endogenous controls for brain tissue (Vandesompele and others, 2002).

We screened for appropriate endogenous RNA controls that could be used to normalize the relative quantities (RQ) of transcript levels among the three nuclear fractions in qRT-PCR assays (see Materials and Methods). Transcript levels for succinate dehydrogenase complex subunit A (SDHA) transcript and ribosomal protein large subunit 13A (RPL13A) did not vary significantly among the NeuN-High, -Low, and -Neg nuclear RNA samples, when the qRT-PCR assays were controlled to contain equivalent amounts of input cDNA (e.g., 1.5 ng per assay). SDHA and RPL13A transcripts were shown previously to be reasonable endogenous controls for brain tissue (Vandesompele and others, 2002).

To characterize the properties of the cell types from which the three nuclear fractions were enriched we examined the RQ of several transcripts reported to have cell type specificity and/or reflect neuronal activity in the brain (**Supplemental Table 2.S3**) using SDHA as the endogenous control. The NeuN-High nuclei expressed 2- to 20-times higher levels of cell type marker transcripts for neuron-specific factors involved in learning and memory and neuronal plasticity,

including ARC, BDNF, ERG1, HOMER1, NFL/NEF1, and SYT1, than NeuN-Low or NeuN-Neg nuclei (**Figure 2.3A**). NeuN-Low nuclei expressed 1.5 to 4.5-fold higher levels of these same neuronal markers than the NeuN-Neg nuclei. The leukocyte marker IKAROS was 25-fold and endothelial marker ETB was 80-fold more highly expressed in non-neuronal NeuN-Neg nuclei, than in the two NeuN positive nuclear fractions. NeuN-Neg nuclei expressed 5- and 14-fold higher levels of glial-specific markers BLBP and PDGFR, respectively (**Figure 2.3A**). OLIG2 and GLAST were higher in both the NeuN-High nuclei and NeuN-Neg nuclei than in NeuN-Low nuclei. Both are widely considered glial-specific developmental markers, but are also expressed in NPCs with the potential to develop into both neurons and glia (Bonfanti and Peretto, 2011; Dromard and others, 2007; Molyneaux and others, 2007). Hence, the NeuN-High and NeuN-Low nuclei were enriched from neural cells, with the NeuN-High nuclei enriched from cells with differentiation potential and/or more neural activity. As expected, NeuN-Neg nuclei were enriched from non-neuronal cell types, including glia, leukocytes, and endothelial cells.

Because cells with decondensed chromatin commonly associated with a high level of epigenetic potentiation (Davis and Dyer, 2010b; Hezroni and others, 2011b; Melcer and Meshorer, 2010b; Morey and others, 2007a; Ostrup and others, 2009b; Ram and Meshorer, 2009a), we examined transcripts for subunits of chromatin modifying machines controlling the lysine acetylation of nucleosomal histones and the cytosine methylation of DNA (**Supplemental Table 2.S3**). Histone hyperacetylation and DNA hypomethylation are most commonly associated with transcriptionally more active decondensed chromatin. Transcripts for four of the seven histone deacetylases assayed (SIRT1, HDAC1, HDAC2, HDAC11) were 3- to 10 times more highly expressed in the NeuN-High nuclei than in either of the other nuclear classes

(**Figure 2.3B**). HDAC4 and HDAC5 transcript levels were not distinguishable among the three nuclear fractions. We were unable to reproducibly detect HDAC3 transcripts in sorted nuclei (not shown). The four histone acetyltransferase transcripts assayed [KAT2B (PCAF), KAT3A (CBP, CREBBP), KAT3B (p300), KAT5 (TIP60)] were 2.5 to 7-times more highly expressed in the NeuN-High nuclei than the other two classes of nuclei (**Figure 2.3B**). Transcripts for the DNA cytosine methyltransferases DNMT1 and DNMT3A and repair proteins involved in DNA demethylation Gadd45a and Gadd45b were 3- to 14-times more highly expressed in the NeuN-High nuclei, than in the NeuN-Low or NeuN-Neg nuclei (**Figure 2.3C**). Hence, the population of NeuN-High nuclei appeared to be from more epigenetically activated cells. However, in the balance, these epigenetic activities did not reflect any general increase in histone lysine transacetylation activity or decrease DNA cytosine methylation activities as might have been expected for cells that were more transcriptionally activated.

Fourth, we assayed the level of markers for cell cycle activity and pluripotency reported in other studies of neural cells (**Supplemental Table 2.S3**) (Bardet and others, 2012; Davis and Dyer, 2010b; Faiz and Nagy, 2013; Lujan and others, 2012). The NeuN-High nuclei were again quite distinct, showing approximately 25-, 20-, 17- 18-, 8-, 12-, 9-, and 30-fold higher transcript levels for SHH, Sox2, Oct4, Klf4, PCNA, BRN2, FOXG1, and MYC, respectively, than the NeuN-Low neuronal nuclei and were in many cases even more highly expressed than in the NeuN-Neg brain cell nuclei (**Figure 2.3D**).

Thus, the population of NeuN-High neuronal nuclei expressed elevated levels of transcripts for markers of neuronal cell type specificity and of epigenetic, cell cycle, and pluripotent activities relative to NeuN-Low or NeuN-Neg nuclei. Three, independent biological replicates

gave similar quantitative results for the four classes of transcripts, with the exception of SIRT1 levels, which were highly variable among RNA samples.

Expression of Histone Deacetylase Proteins in the NeuN-High Decondensed Nuclei

We wished to determine if the exceptional nuclear RNA profiles for epigenetic factors assayed in NeuN-High nuclei were reflected in the levels of nuclear proteins. The expression of the non-sirtuin family of HDACs is well-characterized in the rodent brain (Broide and others, 2007; Darcy and others, 2010; Liu and others, 2008; Yao and others, 2013). Therefore, we performed FNC on total mouse brain cell nuclei immunostained for NeuN and co-immunostained with antibodies to six different histone deacetylases, HDAC1, 2, 3, 4, 5, and 11. Nuclei examined by FNC (**Figure 2.4**) were gated for size and shape and DNA content as described for FANS. NeuN-High neuronal nuclei were more strongly immunostained for HDAC1, 2, 4, and 5 than nuclei staining weakly for NeuN (**Figure 2.4A,B,D,E**). Taking into account the fluorescence background from the secondary antibody used to detect the HDACs (dotted line histogram on the horizontal access), significant levels of HDAC3 and 11 were not detected in any class of nuclei (**Figure 2.4C,F**).

NeuN-High Decondensed Nuclei are Concentrated in Particular Regions of the Brain

The neurons most active in learning and memory and neuronal plasticity and development are more highly concentrated in some regions of the brain than others, and hence decondensed NeuN-High nuclei might be associated with these more dynamic cells. We used two approaches to examine the distribution of decondensed NeuN-High neuronal nuclei in the cortex, hippocampus, cerebellum, and pons. First, to quantify the numbers of NeuN-High nuclei

with decondensed chromatin we examined unfractionated tissue homogenates from the dissected cortex, hippocampus, cerebellum, and pons. We followed the "Isotropic Fractionator" method used previously to quantify the numbers of NeuN-positive neuronal nuclei in crude homogenates of mouse, rat, and human brain (Azevedo and others, 2009; Herculano-Houzel and Lent, 2005; Herculano-Houzel and others, 2006). Extracts from the cortex and hippocampus contained a significant fraction of large decondensed nuclei and these were also the nuclei that stained most strongly for NeuN (DAPI red, anti-NeuN green), while the cerebellum and pons did not (**Figure 2.5A–D**). Interestingly, the cerebellum contained a very high percentage of nuclei staining modestly with NeuN relative to DAPI staining levels (yellow nuclei in **Figure 2.5C**). To quantify these data we defined decondensed nuclei as those having DAPI stained area 1.5X greater than the smallest 40% of nuclei in a sample. The latter defined typical 2C nuclei that had diameters of 6 to 7 μm. Based on this metric, the cortex, hippocampus, cerebellum, and pons contained approximately 44, 43, 2.9, and 5.9% NeuN-High decondensed nuclei, respectively (**Figure 2.5E**).

To extrapolate our results to another mammalian species we isolated nuclei from young pig (Sus scrofa) brain and also found significant numbers of large decondensed NeuN-High nuclei (**Supplemental Figure 2.S3**). Some the NeuN-High pig brain cell nuclei were even larger in diameter than those from mice. A future analysis of NeuN-High nuclei from human brain tissue should prove interesting.

Second, fixed whole young mouse brain was sagittally cryosectioned, stained with DAPI and fluorescent NeuN mAb (Mullen and others, 1992b), and examined by IFM. Again, the cortex and hippocampus were rich in strongly stained NeuN-High nuclei. NeuN-High nuclei were interspersed among NeuN-Low and NeuN-Neg nuclei throughout the cortex as shown for the

somatosensory region (**Figure 2.6A**). In the hippocampus contained the majority of NeuN-High nuclei were in the pyramidal and granular cell layer (**Figure 2.6B**). An expanded view from the CA1 region from the hippocampus (**Figure 2.6C**) further confirmed the exceptionally large size and decondensed status of the DNA in NeuN-High nuclei (white arrows indicate examples), relative to the NeuN-Neg nuclei that were generally of normal small size and showed dense DAPI staining (red arrows). The cerebellum and pons contained few NeuN-High nuclei (**Figure 2.6D,E**). As in the tissue homogenates from the cerebellum (**Figure 2.5E**), the neuronal nuclei in sections of the cerebellum stained only moderately with antibodies to NeuN (yellow nuclei **Figure 2.6D** right panel) and were relatively small in size.

We expanded our analysis of brain cell nuclei to coronal cryosections of the thalamus, hypothalamus, and nucleus accumbens (**Supplemental Figure 2.S4**). While the concentration of decondensed NeuN-High nuclei was modestly high in the thalamus (**Supplemental Figure 2.S4A**), the hypothalamus displayed a gradient of decondensed NeuN-High nuclei with a very high concentration in the ventral region to almost none in the dorsal region (**Supplemental Figure 2.S4B**). The nucleus accumbens revealed very high concentrations of NeuN-High nuclei dispersed throughout (**Supplemental Figure 2.S4C**).

Discussion

We began testing a hypothesis stating that exceptionally large decondensed neural cell nuclei from brain define a broad class of neural progenitor-like cells. While our data provide support for this theory, some results from our investigation are unexpected and complex, or do not fully support this working hypothesis, and warrant discussion. These include the ability of NeuN staining intensity to detect decondensed chromatin for a large population of nuclei, the

epigenetic and multipotential nature of decondensed brain cell nuclei, the relationship between the turnover of chromatin modifications, neuroplasticity and memory in neurons, and the future application of FNC and FANS to the study of neurobiology and neurodegenerative disease.

Strong NeuN Staining Identified Brain Cell Nuclei with Decondensed Chromatin

NeuN (a.k.a., Fox3, RbFox3, Hexaribonucleotide Binding Protein-3) was originally identified as panneuronal nuclear marker antigen, based on the reaction of the mAb A60 with neuronal nuclei (Foudah and others, 2013; Lind and others, 2005b; Mullen and others, 1992b; Sarnat and others, 1998; Weyer and Schilling, 2003; Wolf and others, 1996). Although, there are a few specialized classes of neurons that do not react with NeuN-antibodies such as Purkinje cells (Mullen and others, 1992b), the exceptions are rare. Therefore, counting NeuN immune-positive neuronal nuclei in crude tissue homogenates gives the best estimates of the number of neurons in the brains of rodents and primates (Herculano-Houzel, 2009; Herculano-Houzel, 2012; Herculano-Houzel and others, 2006). It was only recently discovered that antibodies to NeuN recognized the protein product of Fox3, a gene whose function had been well characterized (Kim and others, 2009). NeuN/Fox3 is required to promote neuronal differentiation of cultured neuronal precursors including the production of phosphorylated neurofilaments and axon-like structures and the development of postmitotic neurons from cultured chicken neural tubes (Gehman and others, 2012; Kim and others, 2013a). NeuN binds RNA and is a regulator of alternative splicing and nonsense mediated decay in neuronal cells (Dredge and Jensen, 2011b; Kim and others, 2009). In RNA silencing experiments, NeuN-dependent alternative splicing of *Numb* transcripts is shown to limit neuronal cell differentiation (Kim and others, 2013b). Due to its RNA splicing and binding activity NeuN is more concentrated in regions of the nucleoplasm

with high mRNA concentrations then in regions with less mRNA (Lind and others, 2005a). Hence, our data showing that NeuN staining levels are proportional to the expression of transcript and protein markers of neuronal activity are consistent with previous information about NeuN.

However, it was perhaps not obvious that these activities would be associated with decondensed nuclei and that there would be such a large fraction of decondensed nuclei in the brain. Previous studies have identified that within the nucleus, NeuN was preferentially localized in areas of low chromatin density and virtually excluded from areas containing densely packed DNA by co-immunofluorescence staining of NeuN and propidium iodide (PI, DNA stain) (Lind and others, 2005a). They found within cultured cortical neuron nuclei, intensely PI-stained areas/ speckles showed much weaker NeuN staining then does the rest of the nucleus, and highly condensed nucleus had no co-staining with NeuN (Lind and others, 2005a). This is consistent with what we have found in our study which mouse brain cell nuclei expressing the highest levels of NeuN (NeuN-High) had largest nuclei size and decondensed chromatin.

NeuN is preferentially localized to the nucleoplasm, but some protein is distributed to the cytoplasm proximal to the nucleus (Lind and others, 2005a; Mullen and others, 1992a). This distribution results in part from the differential localization of NeuN-splice variant isoforms (Dredge and Jensen, 2011a). Isoforms corresponding to variant #1 NP_001034256 and #2 NP_001034257 are concentrated in the nucleus, while variant #3 NP_001020102 is more cytoplasmic. The two distinct mouse anti-NeuN mAbs we used in this study (A60 Millipore, 1B7 Abcam, **Supplemental Table 2.S1**) reacted with protein isoforms in isolated brain cell nuclei and migrating at approximately 45 and 50 kDa (**Figure 2.1D**), the sizes recognized as the major splice variants of NeuN (Dredge and Jensen, 2011b; Maxeiner and others, 2014). Both mAbs are

specific to epitopes within the first 100 residues of the N terminus (**Supplemental Table 2.S1**), and hence, we expected them to react with the same protein isoforms in the same cellular locations. In fact, in tissue sections, while A60 and 1B7 both stained cellular nuclei (**Figure 2.5**), in tissue sections 1B7 stained perinuclear regions more strongly relative to A60 (not shown).

NeuN Intensity Identified Neuronal Cell Nuclei with Elevated Histone Deacetylase Activity

Decondensed chromatin is positively correlated with the epigenetically potentiated state of multipotent cells (Mattout and others, 2011; Melcer and others, 2012a; Melcer and Meshorer, 2010a; Yang and others, 2012). Therefore, as an initial test of our hypothesis, we assayed the three nuclear fractions for transcripts encoding chromatin-modifying enzymes controlling histone acetylation and DNA cytosine methylation. 12 out of 14 of these markers of epigenetic activity were the most highly expressed in NeuN-High nuclei (**Figure 2.3B,C**). As an example, transcripts for non-sirtuin histone lysine deacetylases HDAC1, HDAC2, and HDAC11 were significantly more highly expressed in the NeuN-High nuclei than NeuN-Low or -Neg nuclei. FNC demonstrated that a HDAC1, HDAC2, HDAC4, and HDAC5 proteins were more highly expressed in NeuN-High nuclei.

These results are supported by previous studies showing that although NeuN expression varies widely among neurons in different regions of the brain, histone deacetylases are in general most strongly expressed in regions rich in neuronal nuclei. For example, NeuN nuclear protein staining levels are reported to be at the highest in layers of neurons within the cortex and the layer of pyramidal neurons in the hippocampus (regions CA1–4 and dentate gyrus) and distinct, but weaker, throughout the granule cell layer of the cerebellum and in the pontine nucleus of the brain stem (Gong and others, 2011; Mullen and others, 1992b; Weyer and Schilling, 2003).

Based on in situ RNA hybridization experiments, the non-sirtuin histone lysine deacetylases HDAC2, HDAC3, HDAC4, HDAC5, and HDAC11 and the sirtuin deacetylase SIRT1 are highly expressed in neurons in the cortex and hippocampal regions and with few exceptions more weakly expressed in other cell types in the brain (Broide and others, 2007; Huang and others, 2011). A comprehensive semi-quantitative analysis of the relative levels of HDAC2 protein by immunofluorescence revealed some of the highest levels in the piriform region within the cortex, in the pyramidal cell layers CA1 to CA4 and the granular cell layer of the dentate gyrus within the hippocampus, the granular and purkinje cell layers of the cerebellum (Yao and others, 2013). This study only reported weak to moderate staining for HDAC2 in the brain stem. So far as these comparisons may be made across the literature, most previous data are consistent with our results suggesting that the NeuN-High nuclei are concentrated in bands of neurons in the hippocampus and cortex, where histone deacetylases are also highly expressed, with a few notable exceptions.

There is then a potential discrepancy with our data on HDAC4 and HDAC5 RNA levels not reflecting previous in situ mRNA data showing staining neuronal nuclei in the hippocampus (Broide and others, 2007; Huang and others, 2011). It is certainly possible nuclear RNA levels of these two deacetylases do not reflect total cellular mRNA levels as was observed for a small percentage of transcripts in a comparison of nuclear and total RNA levels [see supplement to (Deal and others, 2010a)]. In addition, previous evidence suggests there is strong expression of HDAC2 levels in the large Purkinje neurons of cerebellum, neurons that do not stain with NeuN (Mullen and others, 1992b). However, we did not observe large decondensed nuclei in the cerebellum and saw only modest intensity NeuN staining. However, FNC did reveal a population of NeuN-Neg nuclei staining for HDAC2 and this fraction might contain, among other things, nuclei from Purkinje cells (**Figure 2.4B**). Taking these exceptions into account most previous

evidence supports a positive correlation between strong NeuN staining and elevated histone deacetylase activity.

NeuN Intensity Correlates with Expression Levels of Markers for Multipotent Progenitor Cells

The NeuN-High nuclei contained much higher levels of transcripts for common markers of cell cycle activity and of developmental potential than the NeuN-Low or NeuN-Neg nuclei (**Figures 2.3 and 2.4, Supplemental Table 2.S3**). None of the marker genes assayed act alone to maintain pluripotency and many have activities besides those involved in pluripotency. Nevertheless, the molecular activities of the individual genes, which are upregulated in NeuN-High nuclei, lend support for the working hypothesis that these nuclei are enriched from pluripotent neural progenitor-like cells. For example, expression of SHH shortens the G1 and G2 phases of the cell cycle and helps to control the development of new NPCs (Alvarez-Medina and others, 2009; Lai and others, 2003; Oh and others, 2009). Sox2 is expressed in most embryonic and adult NSC and its levels of expression are likely responsible for maintaining essential stem cell activities including stem cell identity, self-renewal, proliferation and neurogenesis (Agathocleous and others, 2009; Ellis and others, 2004; Surzenko and others, 2013; Taranova and others, 2006). Although less specific for any cell type, PCNA expression parallels BrdU incorporation and is a frequently used indicator of active cell proliferation, entry into the cell cycle, and of multipotent NPCs in the brain (D'Amico and others, 2013; Marschallinger and others, 2014; Marz and others, 2010; Nguyen and others, 2014). OCT4 expression is essential to cell fate determination, neurogenesis, and pluripotency and widely accepted as prognostic of NPCs and stem cells (Archer and others, 2011; Luo and others, 2013; Shi and others, 2008; Yamada and others, 2013). MYC is a regulator of epigenetic activities essential to self-renewal

and neurogenesis of NPCs (Smith and Dalton, 2010; Varlakhanova and others, 2010). KLF4 expression in conjunction with OCT4, cMYC, and SOX2 can induce somatic cells to become PSCs (Shi and others, 2008). BRN2 (Pou3f2) expression influences multiple stages of neurogenesis and its overexpression in the neonatal mouse brain cortex is sufficient to trigger the development of new neurons (Dominguez and others, 2013). Finally, treating mouse embryonic fibroblasts with FoxG1 generates NPCs that give rise to astrocytes and neurons (Lujan and others, 2012). In summary, based on the major activities of few moderately well-characterized markers that showed elevated expression levels, the NeuN-High nuclear population may be enriched from NPC-like pluripotent cells with the potential to reenter the cell cycle. Our results are also consistent with the existence of numerous different NPC types in the adult brain (Lugert and others, 2010). However, some aspects of our results do not fully support our working hypothesis or confound simple interpretation. For example, we found it seems too large a fraction of brain cell nuclei in the decondensed NeuN-High population (15 to 20%) for them all to be from NPC-like cells poised for cell cycle reentry.

An Alternate Hypothesis Concerning the Activity of NeuN-High Nuclei in Neuronal Development and The Turnover of Chromatin Modifications

Second and perhaps equally surprising is our evidence that transcripts for two complementary pairs of factors controlling chromatin modification are highest in NeuN-High nuclei relative to either the NeuN-Low or NeuN-Neg populations (**Supplemental Table 2.S3**). These data are not intuitively consistent with an epigenetically determined general increase in transcriptional activity in decondensed multipotent nuclei. NeuN-High nuclei showed increased transcript levels for four histone lysine acetyltransferases [*KAT2B (PCAF), KAT3A (CBP),*

KAT3B (p300), and KAT5 (TIP60)] expected to increase overall levels of transcription, but this was balanced by increased transcript levels for several histone deacetylases expected to dampen transcription (**Figure 2.3B**). Similarly, in NeuN-High nuclei there was an increase in the levels of two DNA repair proteins involved in demethylation *Gadd45a* and *Gadd45b* (**Figure 2.3C**) expected to increase overall transcriptional activity, but this was countered by an increase in transcripts for two DNA methyltransferases *DNMT1* and *DNMT3A* with the potential to silence transcription. In short, there are higher expression levels of complementary histone acetyltransferases with histone deacetylases and of complementary DNA cytosine methyltransferases with DNA cytosine demethylating activities in NeuN-High nuclei. These data suggest an increase in the turnover rates of these two chromatin modifications, ^{5Me}C on DNA and acetylated histones on nucleosomes.

Thirty years ago Sir Francis Crick put forward the idea that short- and long-term memory and associated synaptic strength would be controlled by variations in molecular turnover rates of DNA and protein modifications in the brain (Crick, 1984). We now accept that epigenetic modifications to chromatin are critical to memory formation and many neurogenic functions. Concerned that the rapid turnover rates of most biomolecules and their modifications was incompatibility with the maintenance of memories that might last “tens of years,” Crick proposed a model for the long-term upkeep of modifications on hemimodified symmetrical molecules like the anti-parallel strands of DNA or multi-subunit protein complexes (i.e., today we might think of nucleosomes). The cyclic activity of complementary enzymes adding, removing, and readding chromatin modifications fits well into Crick’s turnover model. Therefore, based on our results and extending on Crick’s model it seems reasonable to propose an alternative hypothesis for the further examination of different classes of neuronal nuclei, stating that: decondensed NeuN-High

nuclei are derived from the most active neurons involved in more rapid turnover of chromatin modifications required for neuroplasticity and memory formation. The outcome of balanced changes to complementary chromatin modifying machinery and increased turnover rates are hard to predict. However, in NeuN-High nuclei these activities may result in the observed increases in the levels of transcripts important to neurogenesis and to learning and memory (*ARC, BDNF, ERG1, HOMER1*), to synaptic plasticity (*ARC, BDNF, ERG1, NFL, SYT1*) and to long-term potentiation (*ARC, BDNF, HOMER1*; **Figure 2.3A**, **Supplemental Table 2.S3**). These data suggest NeuN-High nuclei may be from the most active neurons.

Further support for this alternative hypothesis comes from other less-well recognized roles played by several of the marker genes initially assayed for evidence of cell cycle activity and multipotency (*PCNA, KLF4, SHH, BRN2, FOXG1, MYC*; **Figure 2.3D**). Of direct relevance to this second model, PCNA binds DNA just beyond the replication fork and associates with histone chaperons in assembling new nucleosomes, thus participating directly in and essential to nucleosomal histone turnover (Margueron and Reinberg, 2010). Our PCNA data are not trivial, because recent evidence suggests that nucleosomal histones in gene regions have half-lives measured in minutes (Deal and Henikoff, 2010a). Among several "alternate" functions, KLF, SHH, BRN2, and FOXG1 are involved in axonal outgrowth, guidance and/or axon regeneration (Dominguez and others, 2013; Moore and others, 2009; Pratt and others, 2004; Qin and others, 2013; Tian and others, 2008; Yam and Charron, 2013). MYC was recently shown to participate not only in the differentiation of NPCs, but also in neurogenesis (Wittmann and others, 2014; Zinin and others, 2014). MYC activates gene expression associated with cell growth and development through its interaction with the acetyltransferases KAT5 (TIP60) machinery or through its binding to DNA methyltransferase DNMT3a and its association with DNA

methylation activity (Brenner and others, 2005). Finally, SSH and FOXG1 have reported roles in learning and memory (Shen and others, 2006; Sylvester and others, 2013). Hence, the alternate activities of these markers suggest that NeuN-High nuclei may be derived from highly active neurons.

Whether or not there is actually more rapid turnover of histone lysine acetylation and DNA cytosine methylation in NeuN-High nuclei or that increased turnover rates significantly affect memory or neuronal development remains to be determined experimentally, but these ideas have additional support. In the hippocampus, memory formation is associated with rapid reprogramming of histone acetylation (Bousiges and others, 2013; Dyrvig and others, 2012; Lopez-Sanchez and Frade, 2013; Park and others, 2013a) and long-term potentiation and memory consolidation are associated with DNA methylation (Lubin and others, 2008; Sultan and others, 2012). As particular examples of the important role for the turnover and the removal of chromatin modifications, deletion of *Gadd45b* increases gene-specific DNA methylation, and enhances synaptic plasticity and long-term memory formation (Sultan and others, 2012). Similarly, HDAC2 knockout mice have increased H4K5, H4K12 and H2B acetylation and increased short term and spatial memory (Guan and others, 2009). The idea that NeuN-High nuclei are epigenetically potentiated for or involved in more active memory formation than NeuN-Low nuclei seems worthy of further study. Additionally, and as discussed in the Introduction, recent evidence suggests that large postmitotic neurons are in fact potentiated to reenter the cell cycle, and under certain circumstances proliferate (Bonaguidi and others, 2012a; Davis and Dyer, 2010b; Ladewig and others, 2013b). In other words, the two hypotheses presented are not mutually exclusive and may apply to some of the same NeuN-High neuronal cells.

Cell-Type-Specific Analyses of Disease Models Using FNC and FANS

Epigenetic reprogramming is a cell-, cell-type-, and tissue-specific process. Therefore examining mixed populations of cell types compromise epigenetic data and may render it "unintelligible" (Deal and others, 2010a; Reinius and others, 2012a). Due to the interdigitation of neuronal and glial processes within and between other cells and tissues it is nearly impossible to isolate subpopulations of adult neurons from within the brain away from glia, leukocytes, and endothelium and from other classes of neurons. Laser capture microdissection recovers only small amounts of brain tissue (Merbs and others, 2012a). Isolation of nuclei tagged in specific cell types (INTACT) is easily scalable, but requires the expensive genetic engineering of a target cell type in a model organism (Deal and Henikoff, 2010a; Henry and others, 2012). FNC and FANS have been used in just a few studies to reduce the complexity of brain cell transcriptomes, epigenomes, and proteomes (Bilsland and others, 2006b; Dammer and others, 2013b; Okada and others, 2011a). A recent analysis of human brain cell nuclei demonstrates that the proteome and methylome of NeuN-Positive nuclei is quite distinct from that of NeuN-Neg nuclei (Dammer and others, 2013b; Lister and others, 2013a). However, the manipulation of brain cell nuclei as a surrogate for isolated cells is in its infancy. We have extended FNC and FANS technologies a bit further and characterized the NeuN-High subpopulation of neuronal nuclei and show that it is enriched from highly potentiated cells with exceptional properties.

Some human neurodegenerative diseases such as Alzheimer's and mouse models of neurodegenerative diseases show increased frequencies of postmitotic neurons in the brain reentering the cell cycle and increased expression of cell cycle and epigenetic factors (Arendt, 2012; Busser and others, 1998; Folch and others, 2012; Graff and others, 2012; Harrison and Dexter, 2013; Hernandez-Ortega and others, 2011; Kim and others, 2008; Li and others, 2011;

Pirooznia and others, 2012; Seo and others, 2013; Wang and others, 2009). Clearly, large numbers of neurons have the potential to reenter the cell cycle, supporting our working hypothesis. However, in the degenerative brain these cells generally arrest in the G2 stage of the cell cycle before completing DNA replication, and undergo apoptotic cell death. The end result is the loss of neurons. Developing therapeutic treatments to block the cell cycle-apoptosis pathway, to appropriately stimulate existing progenitor cells, or to transplant progenitor cells to replace dead neurons all depend upon our having a deeper understanding the existence and behavior of the various multipotent cell populations with replicative and neurogenic capacity. Almost a decade ago, FNC of bromodeoxyuridine (BrdU) labeled mouse hippocampal nuclei was used to demonstrate the ability of therapeutics (e.g., imipramine) to double cell proliferation rates (Bilsland and others, 2006b). However, BrdU labeling has its limitations and may be a better predictor of DNA repair, underestimating both the number of cells undergoing normal DNA replication based cell proliferation and cells with neurogenic potential (Morte and others, 2013; Zheng and others, 2011). Our work suggests that cell proliferation assays based on the analysis of populations of brain cell nuclei should be revisited as a powerful approach to examine neurodegenerative diseases and therapeutics. However, future analyses will be enhanced by using the full potential of FNC and FANS technologies along with the wide variety of well-characterized markers now available.

Acknowledgements

Drs. Mary Anne Della-Fera, Clifton Baile, Jonathan Eggenschwiler, Jianfu Chen, Jim Lauderdale, and Steve Dalton at the University of Georgia and Nicholas Seyfried at Emory University offered helpful advice and encouragement as this project developed. Julie Nelson

provided invaluable assistance with the cytometry at UGA's Center for Tropical and Emerging Global Diseases Flow Cytometry Core facility. Confocal images were taken at UGA's Biomedical Microscopy Core facility. Ryan Crow assisted us in obtaining fresh pig brain from UGA's Abattoir.

Figure 2.1. Purifying brain cell nuclei. A. Protocol for the rapid purification of brain cell nuclei. B. Combined DIC & fluorescent DAPI DNA (blue) stained images in a hemocytometer show purity at the end of the purification protocol (A) and quantify the recovery. C. Western blot comparing the levels of NSE, actin, and histone H3 in total mouse brain homogenate (H) and purified nuclear protein extracts (N). Approximately 15 ug of total protein was loaded in each lane (see Materials and Methods). Equal loading was further estimated by the electrophoresis of equivalent samples for only a brief period followed by Coomassie blue staining. D. Western showing the reactivity of 1B7 and A60 NeuN-specific mAbs with protein in total mouse brain homogenate (H) and purified nuclei (N). E. Confocal microscopic images of purified nuclei DAPI stained for DNA (blue) and immunostained for NeuN (red, AlexaFluor488 conjugated mAb 1B7). The strongest staining for NeuN is in large decondensed nuclei indicated by white arrows. Antibodies are described in Supplemental Table 2.S1.

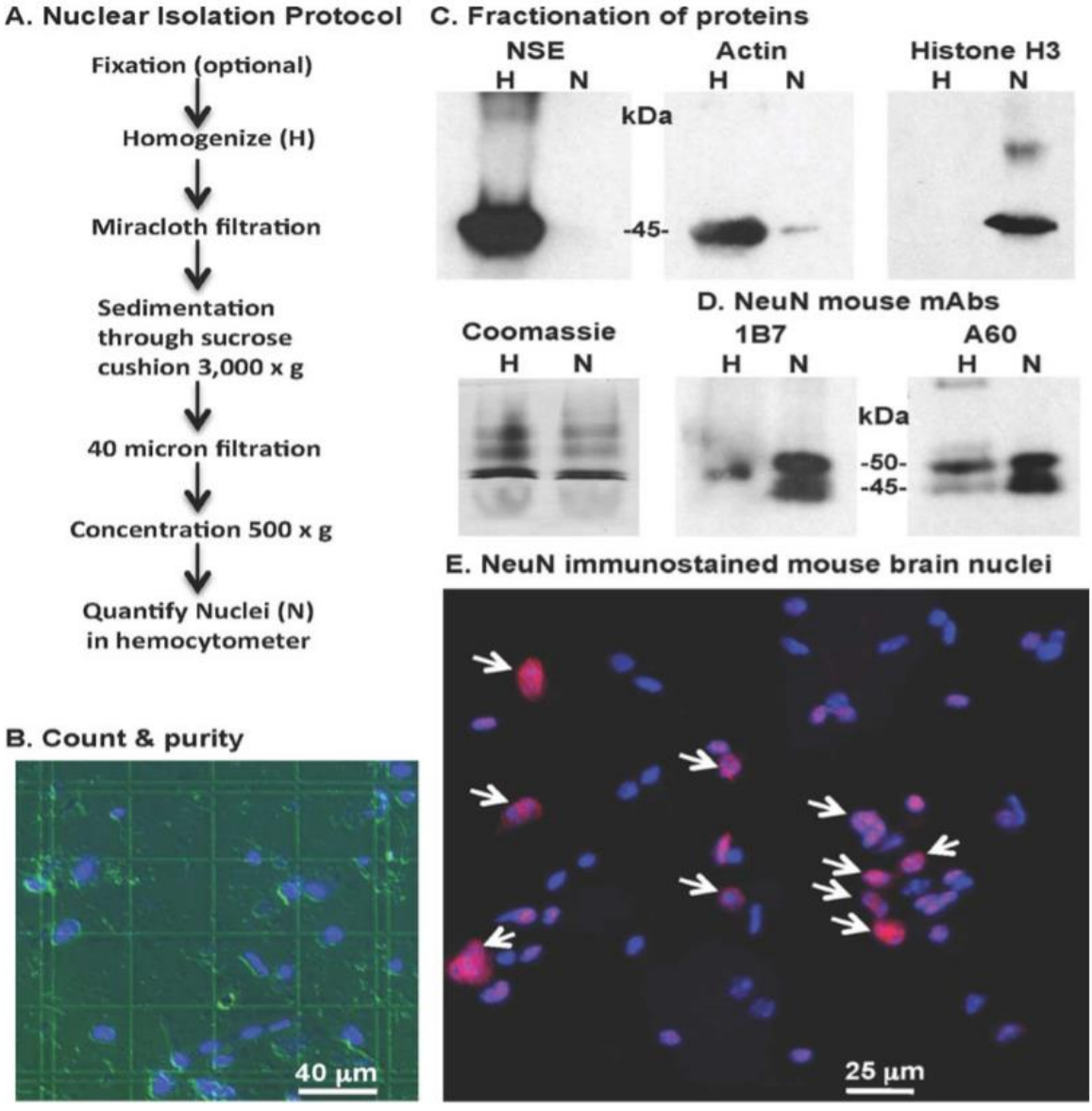
A. Nuclear Isolation Protocol
Fixation (optional)
Homogenize (H)
Miracloth filtration
Sedimentation through sucrose cushion 3,000 x g
40 micron filtration
Concentration 500 x g
Quantify Nuclei (N) in hemocytometer
B. Count & purity
40 µm
C. Fractionation of proteins
NSE
Actin
Histone H3
H N
kDa
-45-
D. NeuN mouse mAbs
Coomassie
1B7
A60
-50-
-45-
E. NeuN immunostained mouse brain nuclei
25 µm

Figure 2.2. FANS of three classes of mouse brain cell nuclei. A. Cytometric histogram (linear scale) of mouse brain cell nuclei stained with DAPI for nucleic acids. R2 defines the gate used to include 2C + 4C peaks of nuclei. The red area defines nuclei staining more strongly than 2C (R6, ">2C") re-examined in Figure 2B. B. Histogram of NeuN-Neg, -Low and -High stained nuclei from sorting experiment (log scale) gated for DNA content (R2 in A) and forward and side light scattering (not shown). NeuN antibody mAb 1B7 was conjugated with AlexaFluor488. The distribution of nuclei with exceptionally strong DAPI staining (red, ">2C" from 2A) relative to the profile of anti-NeuN immunostaining intensity are indicated. C–E. Histograms of three sorted nuclear fractions reexamined by cytometry to confirm their relative NeuN staining levels. F–H. Merged immunofluorescence microscope images of three isolated fractions of nuclei stained with DAPI (red) and anti-NeuN (green). I. NeuN-High nuclei from image H showing the DAPI staining alone to reveal decondensed nuclei. J. Comparison of the average nuclear area for the three fractions from one experiment (N5100). The NeuN-High nuclei averaged 1.85-times larger in their cross sectional area than NeuN-Low or NeuN-Neg nuclei. The histogram in 2A was not gated for light scattering to show the level of small particulate contamination in nuclear preparations, most of which was not visible by light microscopy (Figure 2.1B).

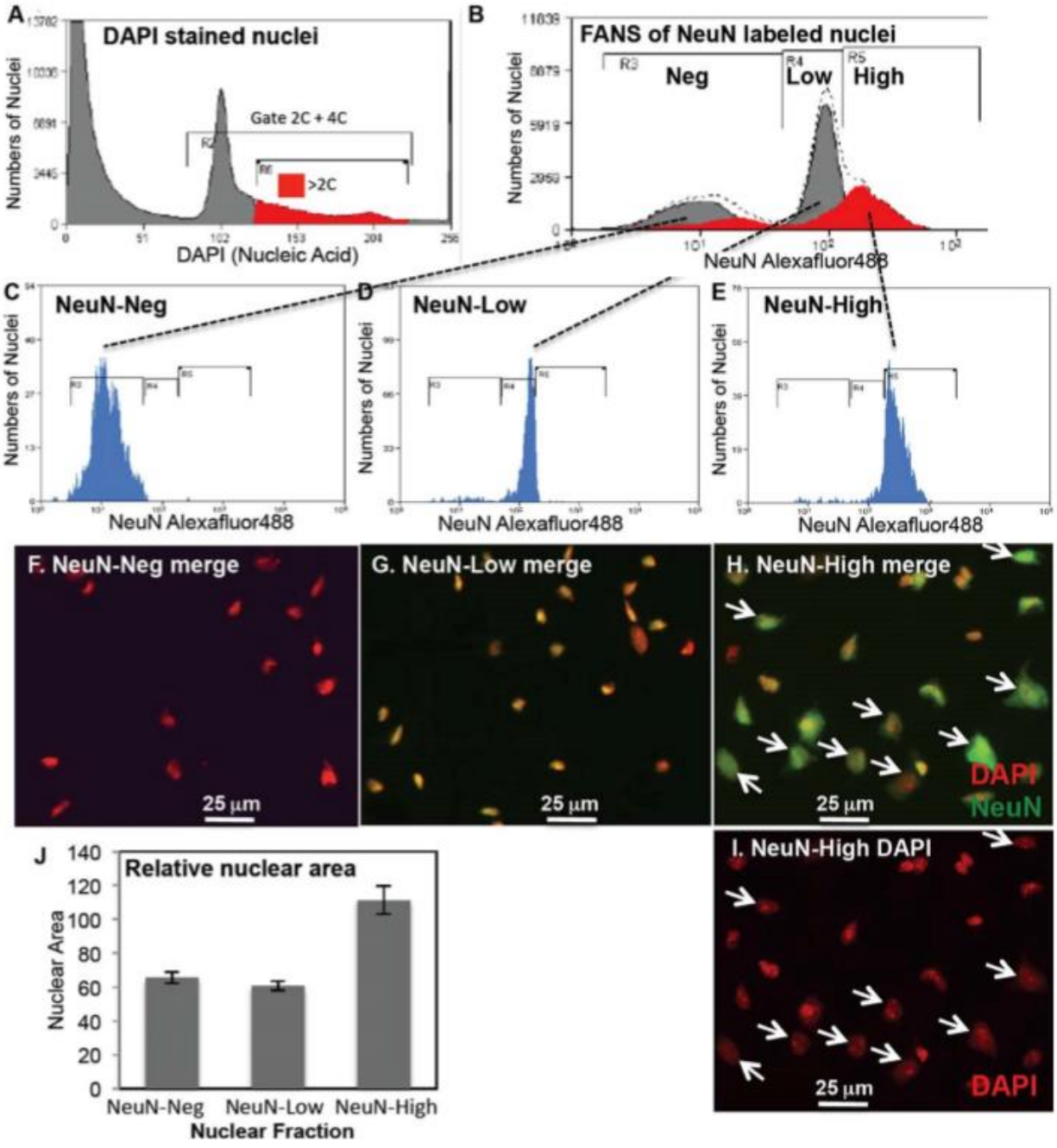
A
DAPI stained nuclei
Numbers of Nuclei
Gate 2C + 4C
>2C
DAPI (Nucleic Acid)
B
FANS of NeuN labeled nuclei
Neg
Low
High
Numbers of Nuclei
NeuN Alexafluor488
C
NeuN-Neg
D
NeuN-Low
E
NeuN-High
F. NeuN-Neg merge
G. NeuN-Low merge
H. NeuN-High merge
25 µm
DAPI
NeuN
I. NeuN-High DAPI
J
Relative nuclear area
Nuclear Area
NeuN-Neg
NeuN-Low
NeuN-High
Nuclear Fraction

Figure 2.3. Transcript expression in three classes of brain cell nuclei isolated by FANS. The Relative Quantity of marker transcripts were determined by qRT-PCR. A. Transcripts for markers of cell type specificity, learning and memory and neuronal plasticity. The values for IKAROS were increased 10-fold so that they might be viewed on the same scale with the other markers in this figure. B Transcripts for factors controlling acetylation levels on nucleosomal histones (Histone deacetylases Sirt1, HDAC1, 2, 3, 4, 5, 11 and histone lysine transacetylases KAT2B, 3A, 3B, 5). C. Transcripts for factors controlling the levels of 5-methylcytosine modification of DNA (DNMT1, DNMT3A and Gadd45a and Gadd45b). D. Transcripts for factors involved in pluripotency and cell cycle activity. SHDA was used as the endogenous control in A-D. Assays were run in triplicate and standard errors are shown. Oligonucleotide primers for marker gene transcripts and the properties of maker genes are described in Supplemental Tables 2.S2 and 2.S3, respectively.

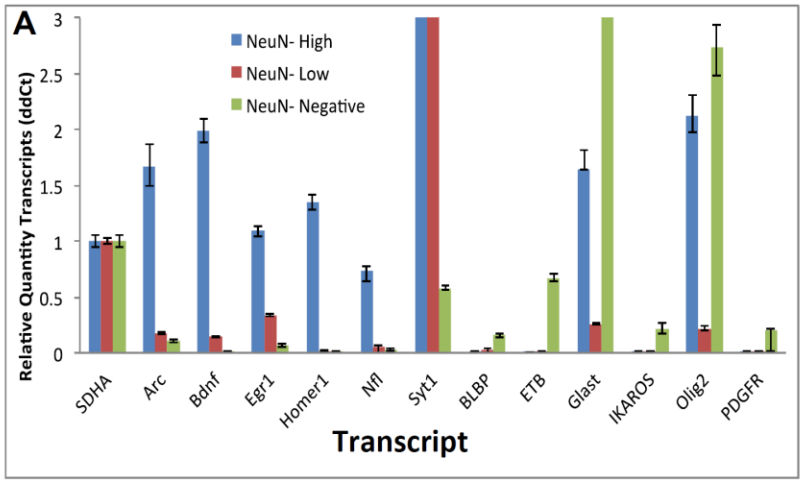
A
NeuN- High
NeuN- Low
NeuN- Negative
Relative Quantity Transcripts (ddCt)
3
2.5
2
1.5
1
0.5
0
SDHA
Arc
Bdnf
Egr1
Homer1
Nfl
Syt1
BLBP
ETB
Glast
IKAROS
Olig2
PDGFR
Transcript

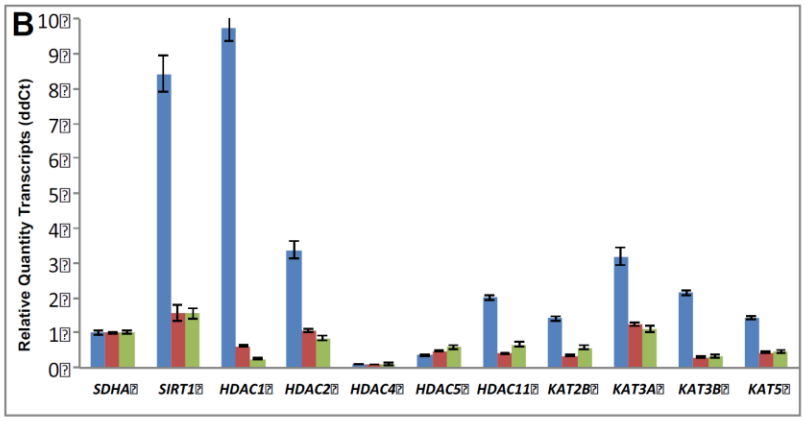
B
Relative Quantity Transcripts (ddCt)
10
9
8
7
6
5
4
3
2
1
0
SDHA
SIRT1
HDAC1
HDAC2
HDAC4
HDAC5
HDAC11
KAT2B
KAT3A
KAT3B
KAT5

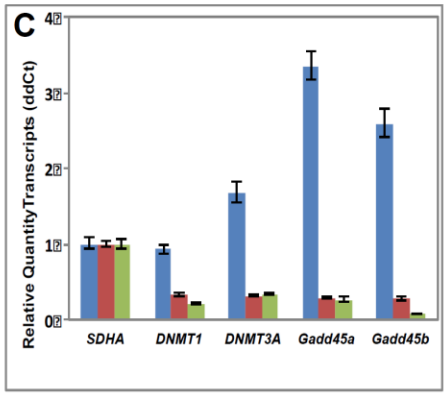
C
Relative QuantityTranscripts (ddCt)
4
3
2
1
0
SDHA
DNMT1
DNMT3A
Gadd45a
Gadd45b

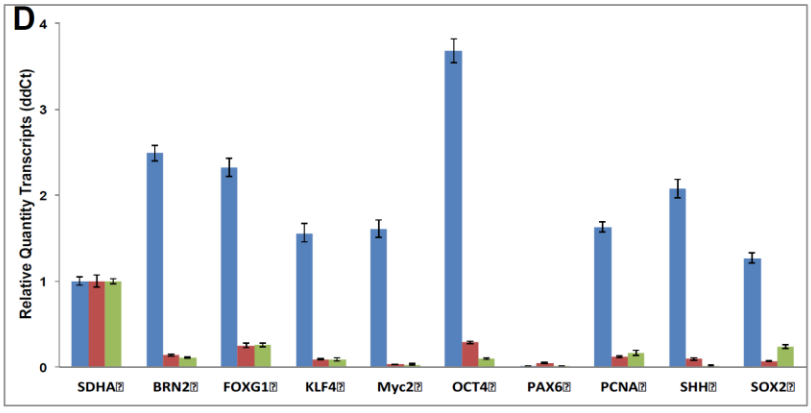
D
Relative Quantity Transcripts (ddCt)
4
3
2
1
0
SDHA
BRN2
FOXG1
KLF4
Myc2
OCT4
PAX6
PCNA
SHH
SOX2

Figure 2.4. Fluorescence nuclear cytometric (FNC) examination of histone lysine deacetylase protein expression in anti-NeuN immunostained brain cell nuclei. A. HDAC1, B. HDAC2, C. HDAC3, D. HDAC4, E. HDAC5, and F. HDAC11. Vertical axis examines NeuN nuclear fluorescence levels in nuclei using the NeuN mAb described in 1E. Approximate locations of NeuN-High, -Low, and Neg nuclei are indicated. Horizontal axis examines the levels of six histone deacetylases using distinct HDAC rabbit polyclonal antibodies, which are detected with goat anti-rabbit Cy5 secondary antibody (Supplemental Tables 2.S1 and 2.S3). The dotted line shows a histogram of the background staining of nuclei with peak height measured in numbers of nuclei plotted against Cy5 fluorescence intensity produced by secondary antibody alone. 50,000 nuclei were sorted in each experiment.

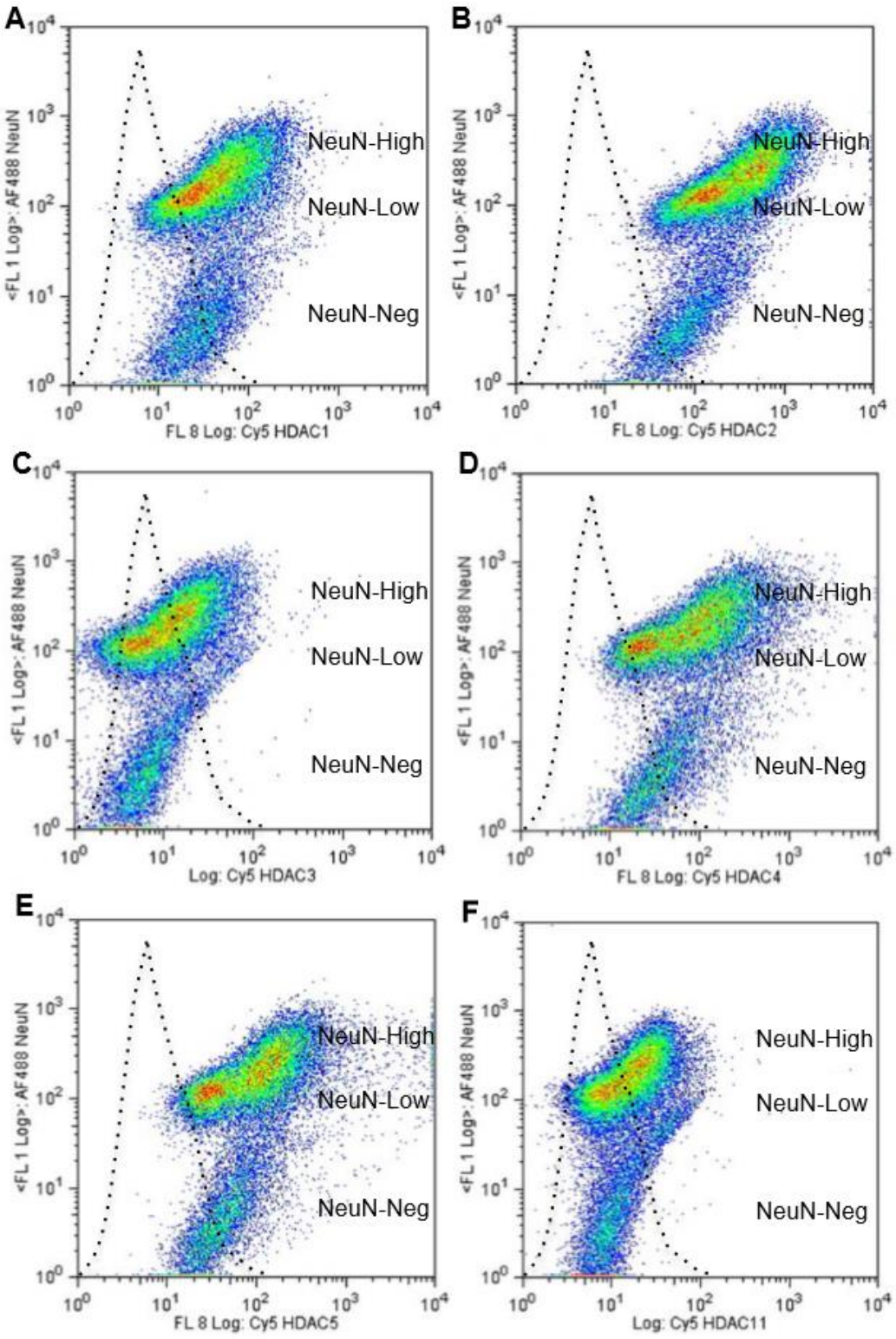
A
B
C
D
E
F
NeuN-High
NeuN-Low
NeuN-Neg
<FL 1 Log>: AF488 NeuN
FL 8 Log: Cy5 HDAC1
FL 8 Log: Cy5 HDAC2
Log: Cy5 HDAC3
FL 8 Log: Cy5 HDAC4
FL 8 Log: Cy5 HDAC5
Log: Cy5 HDAC11

Figure 2.5. Anti-NeuN immunostaining and morphology of nuclei in tissue homogenates of cortex, hippocampus, cerebellum and pons. A–F. Brain tissue homogenates unfractionated, costained with DAPI (red) and anti-NeuN conjugated to AlexaFluor488 (green), and examined by IFM. A. Cortex. B. Hippocampus. C & D. Expanded view of a small number of hippocampal nuclei from 5B stained with DAPI alone and with DAPI and anti-NeuN, respectively, reveals the smaller size of the NeuN-Neg nuclei. E. Cerebellum. F. Pons. The anti-NeuN mAb (A-F) is mAb 1B7. G. Quantification. The fraction of the nuclei that both had highly decondensed chromatin and strong NeuN immunostaining as defined in the text was quantified for each brain region. Three bins of nuclei for each region of the brain (N=40 to 100 per bin) were assayed separately and used to calculate the standard deviation from the mean.

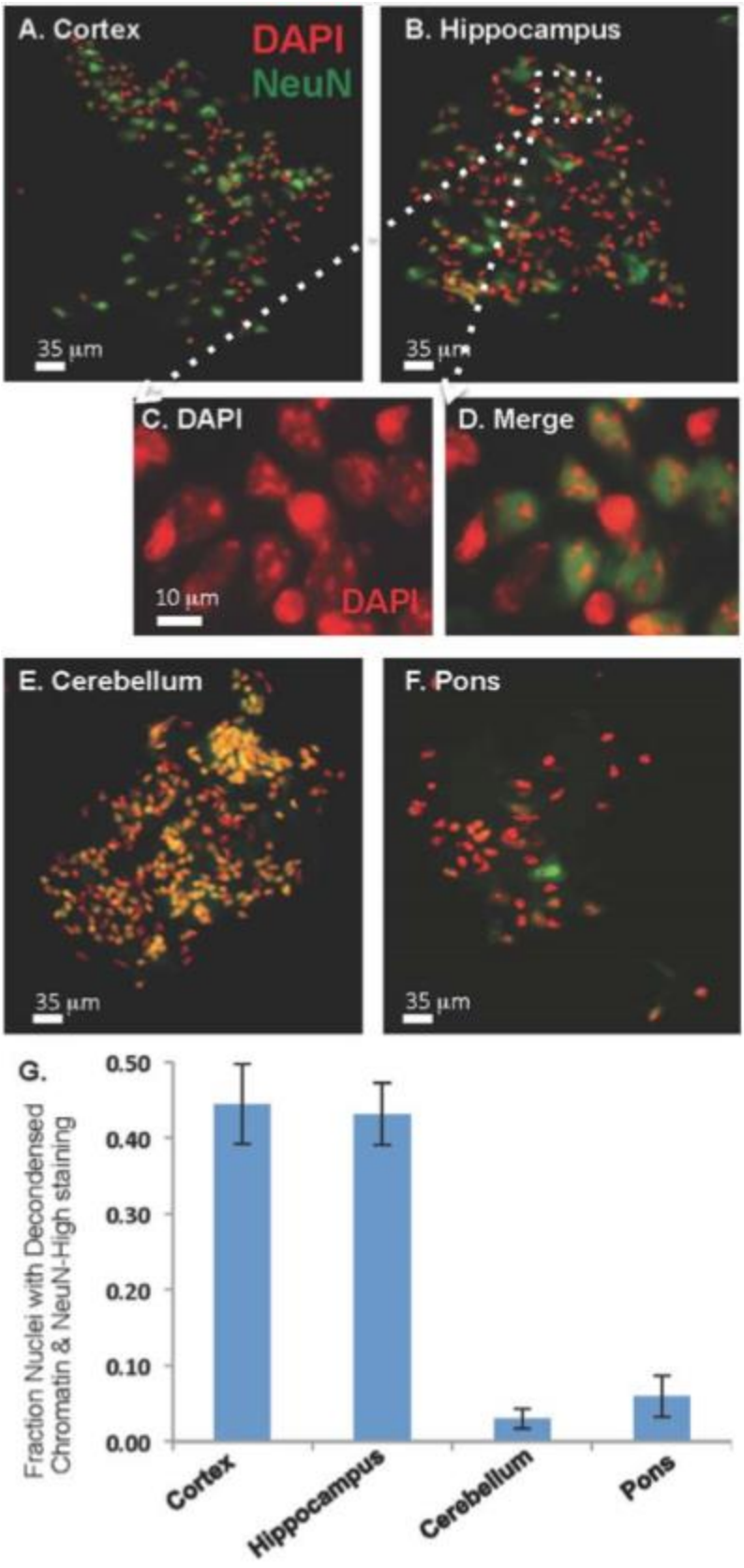
A. Cortex
DAPI
NeuN
35 µm
B. Hippocampus
35 µm
C. DAPI
10 µm
DAPI
D. Merge
E. Cerebellum
35 µm
F. Pons
35 µm
G.
Fraction Nuclei with Decondensed Chromatin & NeuN-High staining
0.50
0.40
0.30
0.20
0.10
0.00
Cortex
Hippocampus
Cerebellum
Pons

Figure 2.6. Morphology of NeuN-High nuclei in cryosections of the cortex, hippocampus, cerebellum, and pons. Frozen sagittal sections of young mouse brain were stained with DAPI and anti-NeuN (mAb A60, Supplemental Table 2.S1) and secondary goat anti-mouse antibody conjugated with Alexafluor488. A. Cortex, B. Hippocampus CA1 region. C. Expanded region from the hippocampus outlined in dotted line from merged image B. White arrows indicate decondensed NeuN-High nuclei, while red arrows indicate smaller densely DAPI stained NeuN-Negative nuclei. D. Cerebellum. E. Pons. Left panels show DAPI stained nuclei (red). Right panels show merged images of DAPI (red) + anti-NeuN fluorescence (green).

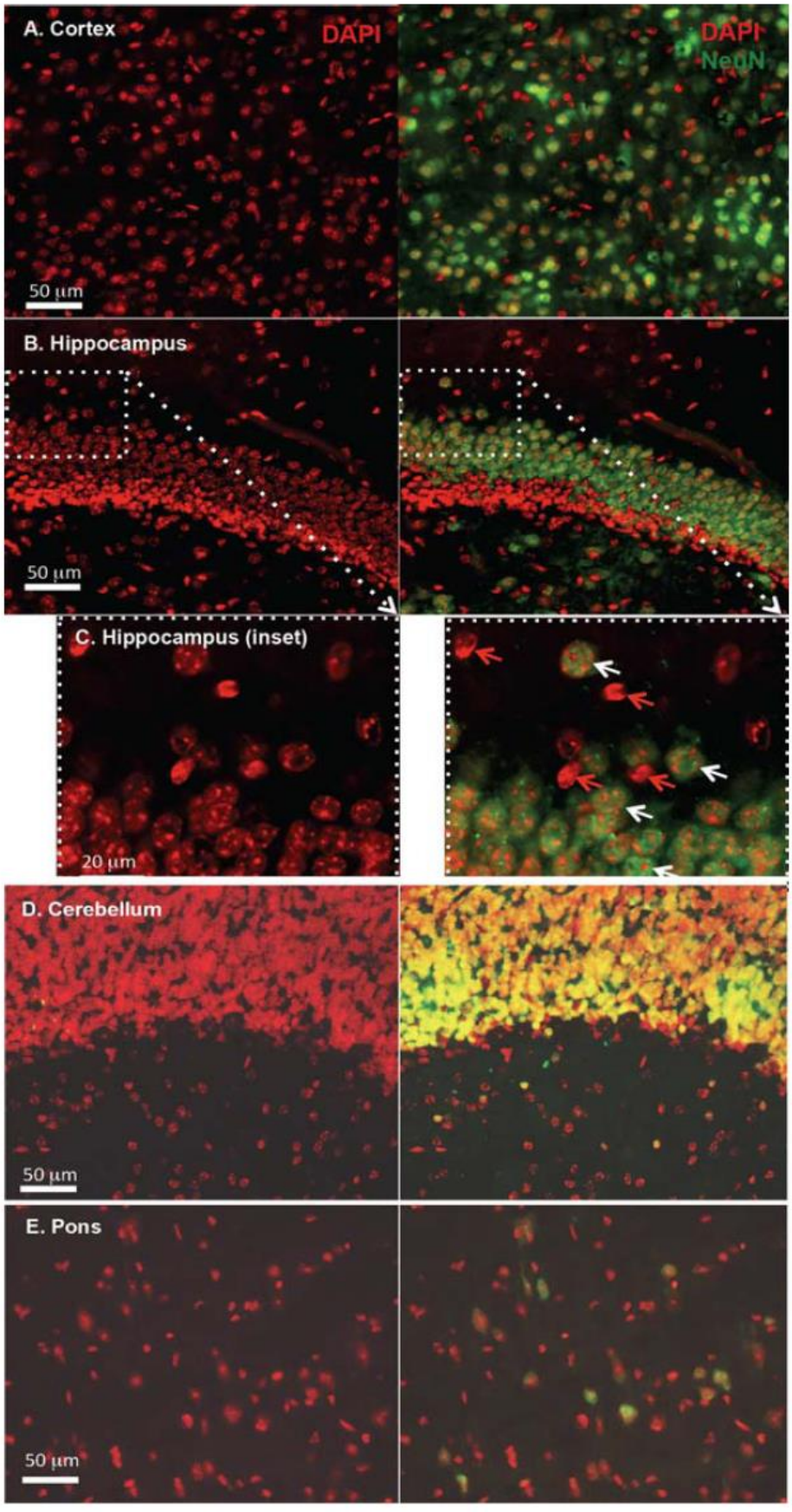
A. Cortex
DAPI
DAPI
NeuN
50 µm
B. Hippocampus
50 µm
C. Hippocampus (inset)
20 µm
D. Cerebellum
50 µm
E. Pons
50 µm

Supplemental Figure 2.S1. FNC and FANS were conducted on a Cyan ADP and a MoFlo XDP, respectively. Nuclei were gated for 2C or greater DNA content and forward (FS) and side (SS) light scattering to eliminate the analysis of small particulate contamination (Supplemental Figure 2.S1A). Pulsed width gating did not detect a significant number of doublets (Supplemental Figure 2.S1C) nor did the application of a pulse-width gate significantly alter the relative populations of sorted nuclei (Compare % of NeuN-High nuclei in Figure 2.S1B,D).

A. Scatter gate

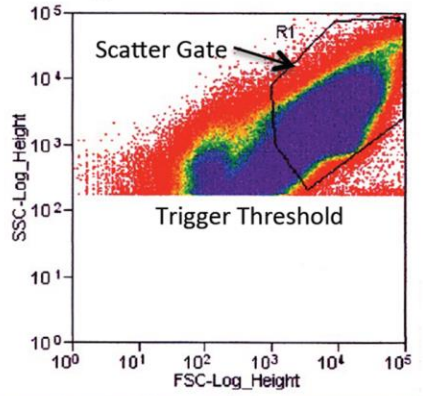

Region	Count	% Hist	Median
Total	1000000	100.00	3540.13, 143...
R1	699936	69.99	6085.75, 215...

B. NeuN histogram with gating for scatter & DAPI

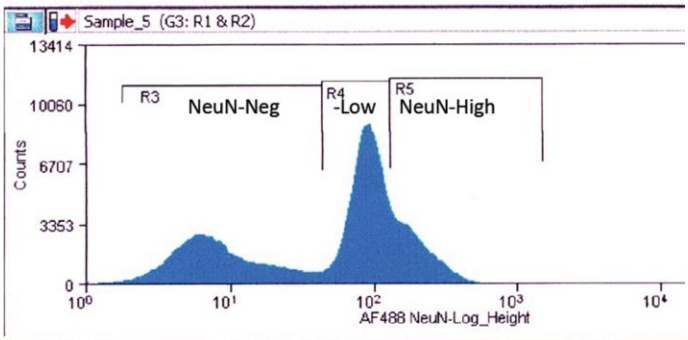

Region	Count	% Hist	Bounds	Median
Total	268635	100.00	(1.00,100000.04)	79.79
R3	95515	35.56	(1.80,44.37)	7.63
R4	119826	44.61	(44.37,131.11)	91.37
R5	56982	21.21	(131.11,1501.31)	188.15

C. Pulse width

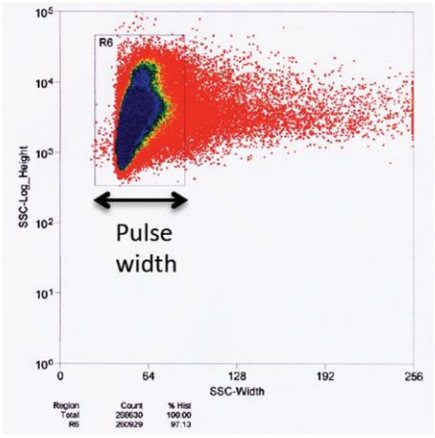

D. NeuN histogram with gating for scatter, DAPI, and pulse width

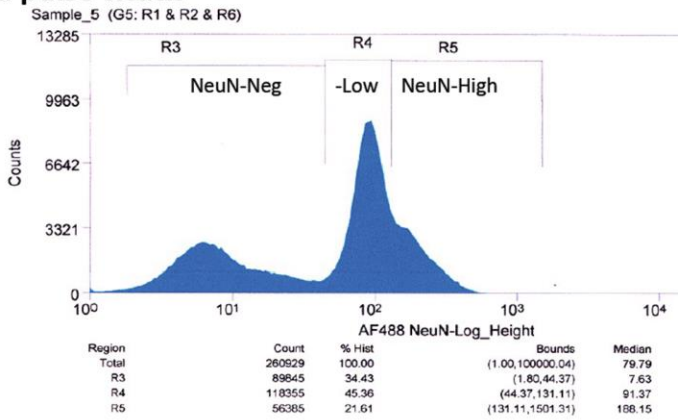

Region	Count	% Hist	Bounds	Median
Total	260929	100.00	(1.00,100000.04)	79.79
R3	89845	34.43	(1.80,44.37)	7.63
R4	118355	45.36	(44.37,131.11)	91.37
R5	56385	21.61	(131.11,1501.31)	188.15

Supplemental Figure 2.S2. Fluorescent microscopic images of purified mouse brain cell nuclei stained for DNA with DAPI (red) and immunostained for NeuN (mAb A60) with goat anti-mouse conjugated with AlexaFluor488 (green). This image is a companion to Figure 2.1E in which mAb 1B7 was used. A60 antibody is described in **Supplemental Table 2.S1**. This figure shows that decondensed NeuN-High nuclei are easily identified with two different NeuN monoclonal antibodies.

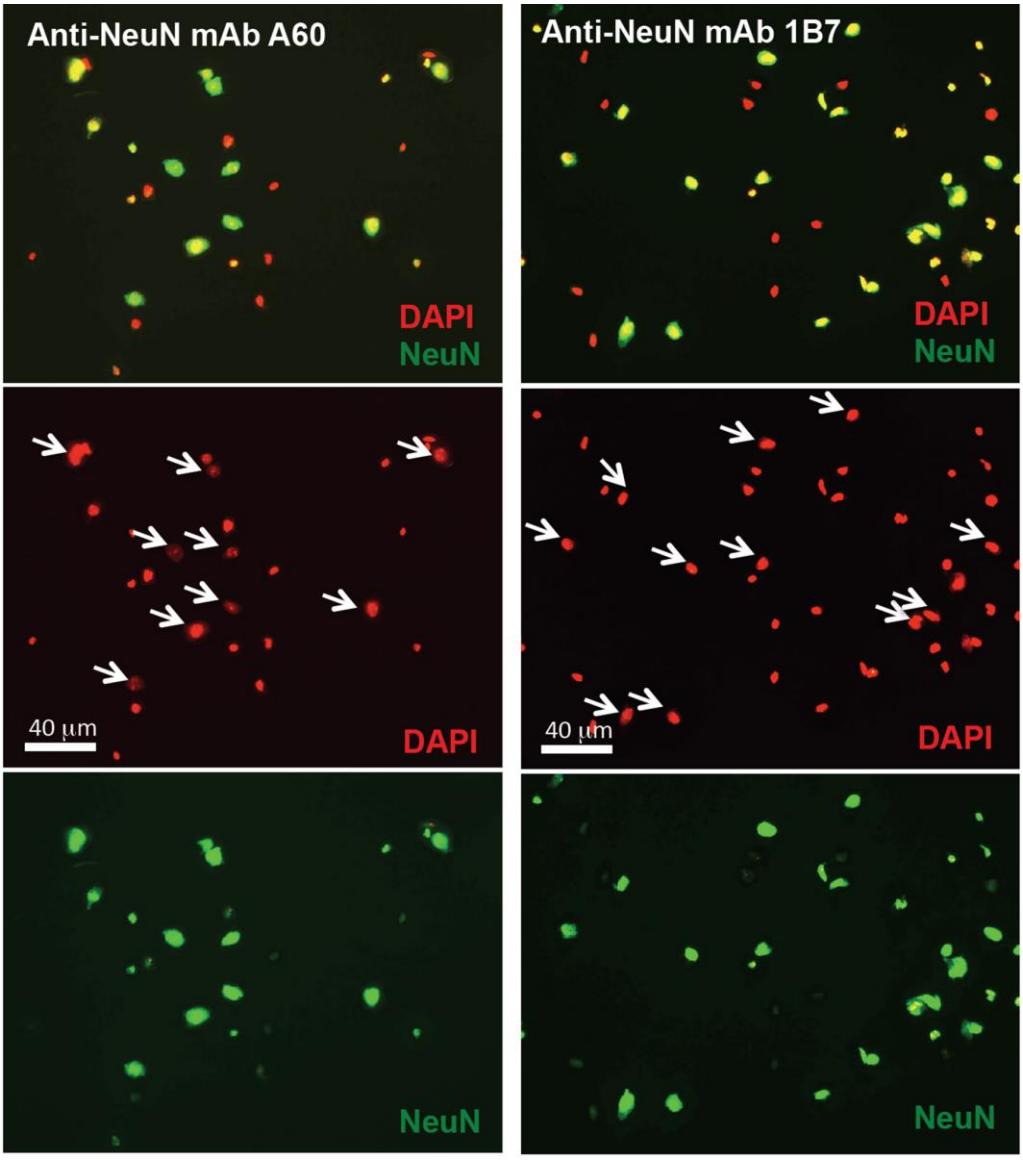

Supplemental Figure 2.S3. Microscopic images of purified young pig brain cell nuclei stained with DAPI for DNA (red) and immunostained for NeuN (green) with mouse mAb A60 and goat anti-mouse antibody conjugated to AlexaFluor488). The strongest staining for NeuN is observed in the large decondensed nuclei indicated by white arrows in the DAPI image. The antibody is described in Supplemental Table 2.S1. The brain (95 g) from 6-mo-old pig was minced, fixed in PBSTBA plus 4% paraformaldehyde (Materials and Methods), and nuclei were prepared as described in the text for mouse brain cell nuclei. This figure shows that large decondensed NeuN-High nuclei may be identified in a second vertebrate species.

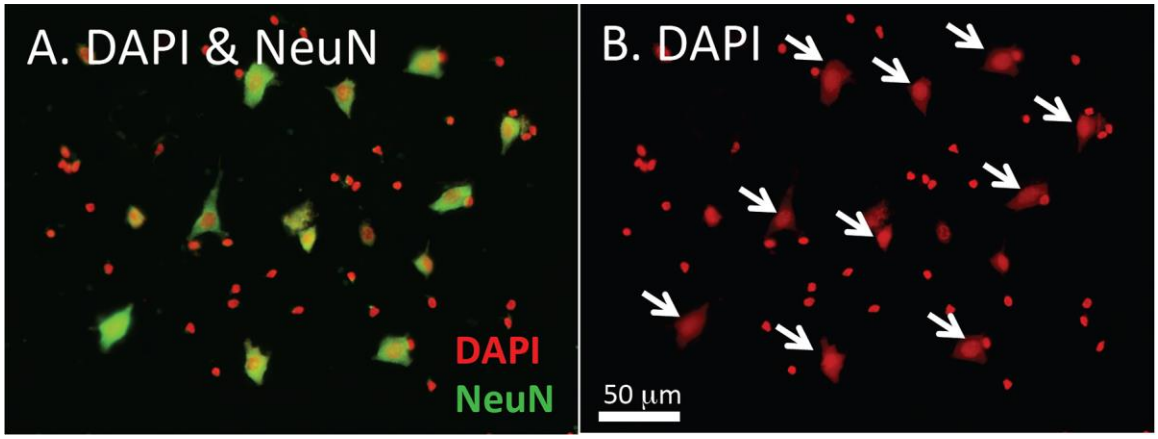

Supplemental Figure 2.S4. Morphology of NeuN-High nuclei in cryosections of the hypothalamus, thalamus, and nucleus accumbens. Frozen coronal sections of young mouse brain were prepared as described for sagittal sections in Figure 2.6. A. Hypothalamus. B. Thalamus. C. Nucleus accumbens. Left panels show DAPI stained nuclei (red). Middle panels show merged images of DAPI (red) + anti-NeuN fluorescence (green). Right panels show an expanded view.

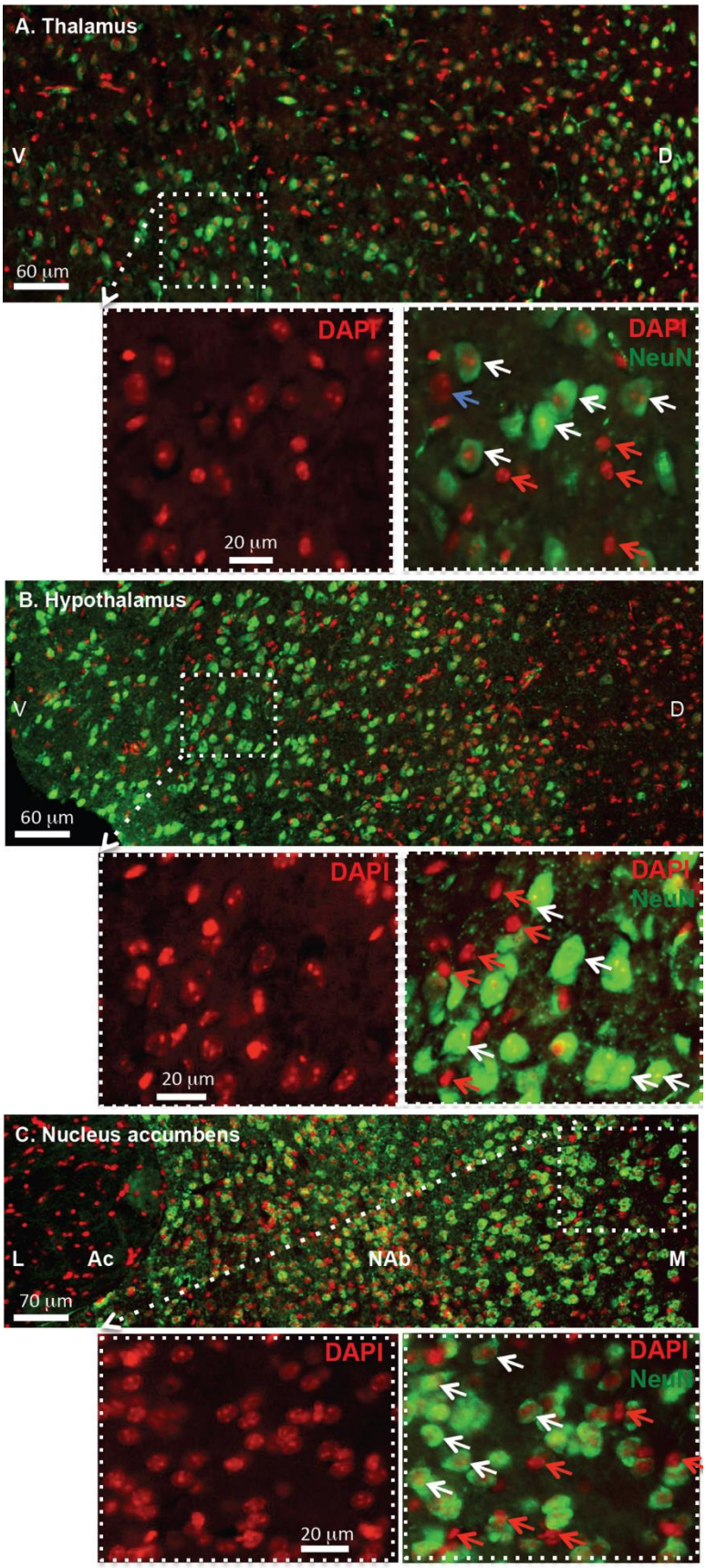
A. Thalamus
V
D
60 μm
DAPI
20 μm
DAPI
NeuN
B. Hypothalamus
V
D
60 μm
DAPI
20 μm
DAPI
NeuN
C. Nucleus accumbens
L
Ac
NAb
M
70 μm
DAPI
20 μm
DAPI
NeuN

Supplemental Table 2.S1. Antibody reagents used in this study.

Antibody	Known Species Reactivity	Source	Cat#
Primary Antibodies			
Anti-Actin mouse monoclonal GEAmAb	All plant and animal actins, some protist actins	Thermo Scientific	MA1-744
Anti-HDAC1 Mouse Monoclonal 10E2 mouse, rat human	mouse, rat, human	Abcam	ab46985
Anti-HDAC1 rabbit polyclonal	mouse, rat, human	Abcam	ab19845
Anti-HDAC2 mouse monoclonal HDAC2-62	Mouse, Rat, Chicken, Cow, Dog, Human	Abcam	ab12169
Anti-HDAC2 rabbit polyclonal	Mouse, Rat, Human	Abcam	ab16032
Anti-HDAC3 mouse monoclonal Y415	Mouse, Rat, Human	Abcam	ab32369
Anti-HDAC3 rab polyclonal	Mouse, Rat, Human, Indian Muntjac, Zebrafish	Abcam	ab16047
Anti-HDAC4 mouse monoclonal HDAC-144	Mouse, Rat, Human	Abcam	ab12171
Anti-HDAC4 rab polyclonal	Mouse, Rat, Human	Abcam	ab1437
Anti-HDAC5 mouse monoclonal HDAC5-35	Mouse, Rat, Human	Abcam	ab50001
Anti-HDAC5 rab polyclonal	Mouse, Human	Abcam	ab55403
Anti-HDAC11 rab polyclonal	Mouse, Human	Abcam	ab135492
Anti-Histone H3 mouse monoclonal	Mouse, Rat, Human, Fruit fly, Monkey	Abcam	ab10799
Anti-NeuN mouse mAb – the original A60 clone made to nuclei. IgG1. Specific for residues 6-15 PPAQYPPPPQ	Avian, chicken, ferret, mouse, human	EMD Millipore	MAB377
Anti-NeuN mouse mAb 1B7 clone (Fox-3) IgG2a. Prepared against a synthetic peptide antigen -residues 1-100.	Mouse, Rat,Cow, Human, Pig	Abcam	ab104224
Anti-NSE Neuron specific enolase (NSE) 5G10 IgG2b Abcam	Mouse, Rat, Sheep, Goat, Cat, Dog, Human, Zebrafish	Abcam	ab8324
Secondary Fluorescent Antibodies			
Anti-mouse (H+L) from goat AlexaFluor488 conjugated	Mouse	Life Technologies	A11059 A11001

Anti-mouse from goat R-PE phycoerythrin IgG	Mouse	Life Technologies	P852
Anti-mouse from goat Cy5 488/679 far red	Mouse	Abcam	Ab6563
Anti-rabbit from goat AlexaFluor 488/530 green	Mouse	Abcam	Ab150077
Anti-rabbit from goat PE (phycoerythrin) 488/575 red	Rabbit	Abcam	Ab97070
anti-Rabbit IgG H&L from goat (Cy5) secondary antibody	Rabbit	Abcam	Ab97077
anti-rabbit from goat conjugated with AlexaFluor633	Rabbit	Life Technologies	A21070

Supplemental Table 2.S2. qRT-PCR Primers for RNA from Mouse Brain Nuclei.

Endogenous Controls	**Forward Sense Primers**		**Reverse Sense Primers**
Name	Sequence	Name	Sequence
ACTB-S2	5 ´ACCTTCCAGCAGATGTGGAT 3´	ACTB-A2	5 ´TAGAAGCACTTGCGGTGCACGA 3´
B2M-S2	5 ´GAGAATGGGAAGCCGAACATA 3´	B2M-A2	5 ´CCGTTCTTCAGCATTTGGATTT 3´
GAPDH-S2	5 ´AACAGCAACTCCCACTCTTC 3´	GAPDH-A2	5 ´CCTGTTGCTGTAGCCGTATT 3´
RPL13-S3	5 ´GAAACAAGTCCACGGAGTCA 3´	RPL13-A3	5 ´GCAGAACTGTCTCCCTTCTTC 3´
RPL13A-S1	5 ´CCAAGATGCACTATCGGAAGAA 3´	RPL13A-A1	5 ´CTTGAGGACCTCTGTGAACTTG 3´
SDHA-S3	5 ´CTCTTTCCTACCCGATCACATAC 3´	SDHA-A3	5 ´CCATCTCCAGTTGTCCTCTTC 3´
TBP-S2	5 ´CTACCGTGAATCTTGGCTGTAA 3´	TBP-A2	5 ´GTTGTCCGTGGCTCTCTTATT 3´
TUBA-S2	5 ´ATGGAGGAGGGTGAGTTCT 3´	TUBA-A2	5 ´AATCCACACCAACCTCCTCA 3´
UBC-S5	5 ´CCCAGTGTTACCACCAAGAAG 3´	UBC-A5	5 ´CCCATCACACCCAAGAACAA 3´
YWHAZ-S2	5 ´TGAAGCAGAAGCAGGAGAAG 3´	YWHAZ-A2	5 ´GGACAGCATGGATGACAAATG 3´
Figure 2.3A			
Arc-S1	5 ´GAAGTGGTGGGAGTTCAAGC 3´	Arc-A1	5 ´CTCCTCAGCGTCCACATACA 3´
BDNF-S2	5 ´CTGAGCGTGTGTGACAGTATTA 3´	BDNF-A2	5 ´CTTTGGATACCGGGACTTTCTC 3´
Egr1-S2	5 ´AACAACCCTATGAGCACCTG 3´	Egr1-A2	5 ´GAGTCGTTTGGCTGGGATAA 3´
Homer1-S1	5 ´CATAGCCAAAAGCCGGTCTA 3´	Homer1-A1	5 ´ATCATTGCCAACCTTGTTCC 3´
Nfl-S1	5 ´GACAGCCTGATGGACGAGAT 3´	Nfl-A1	5 ´GGCTCTTGAACCACTCTTCG 3´
Syt1-S2	5 ´GAGGGAAGAACGCCATTAACA 3´	Syt1-A2	5 ´CTCCATCAGTCAGTCCAGTTTC 3´
BLBP-S2	5 ´CAGAAGTGGGATGGCAAAGA 3´	BLBP-A2	5 ´TAACAGCGAACAGCAACGATA 3´
ETB-S2	5 ´GGTGGCTGTTCAGTTTCTACT 3´	ETB-A2	5 ´ATCTGCATACCGCTCTTCTTC 3´
Glast-S2	5 ´CAAGATGTAGACGGACAGAGAAG 3´	Glast-A2	5 ´CCTATCAGAGTAGGGAGGAAAGA 3´
IKAROS-S2	5 ´AAGAGCGATGCCACA	IKAROS-A2	5 ´

	ACTAC 3´		GGACCTCTCTGCTCCTATCT T 3´
Olig2-S3	5´CGAAGCAATGGGAGC ATTTG 3´	Olig2-A3	5´TGGAGTGTTCAGCCAAAG AG 3´
PDGFRa-S2	5´CTCGTGCTTGGTCGGA TTT 3´	PDGFRa-A2	5´TCTTCACAGCCACCTTCAT TAC 3´
Figure 2.3B			
SIRT1-S2	5´CTCAGCACCGTGGAAT ATGTAA 3´	SIRT1-A2	5´GGCCTAATAGACTTGCAA AGGA 3´
HDAC1-S1	5´GCTGCTCAACTATGGT CTCTAC 3´	HDAC1-A1	5´CACTGTGGTACTTGGTCA TCTC 3´
HDAC2-S2	5´CGAGCATCAGACAAAC GGATAG 3´	HDAC2-A2	5´CCTAGCCTTCTTTGCTCCT TTC 3´
HDAC4-S1	5´CTCTACGGCACAAATC CTCTC 3´	HDAC4-A1	5´ATTCCATATGGTGTCGCTA TCC 3´
HDAC5-S1	5´TGCAGGAGAGCTCAAG AATG 3´	HDAC5-A1	5´GATGGCTACGGAGTTGAA GAA 3´
HDAC11-S1	5´GGCATTGTGAAGAGGG ATGAA 3´	HDAC11-A1	5´AGGATGGAGTCGGCGATA ATA 3´
KAT2B-S1	5´CCGTGTCATTGGTGGT ATCT 3´	KAT2B-A1	5´GGTTCCATAGCCCTTGACT T 3´
KAT3A-S1	5´TCAAGCCATCTTCCCA ACTC 3´	KAT3A-A1	5´CCCTCCACTTTCTTAGCAT AGG 3´
KAT3B-S1	5´ACAGAACAGCCCTGGA TTAAG 3´	KAT3B-A1	5´GACTGAGTAGGACCCTGA TTTG 3´
KAT5-S2	5´TGACGGAGTATGACTG CAAAG 3´	KAT5-A2	5´TAGGGAGGCAGAGTCAAG AT 3´
Figure 3C			
DNMT1-S1	5´CCATCTTCTTGTCTCCC TGTATG 3´	DNMT1-A1	5´GGTGCTTTGTCCTTCTCCT T 3´
DNMT3a-S2	5´GTCTCAACAGCACCAT TCCT 3´	DNMT3a-A2	5´TGTGGTAGGCACCTGAAA TAC 3´
Gadd45a-S2	5´GATGACTTTGCAGAGG GAGAG 3´	Gadd45a-A2	5´CTTTCTTGCAGTGCTTTGT AGTT 3´
Gadd45b-S1	5´GTGAAGAGAGCAGAG GCAATAA 3´	Gadd45bA1	5´CGACAGTTGCTTTAGATGT TTGG 3´
Figure 3D			
BRN2-S2	5´AGTGAAGCAATCCAG AGAAGG 3´	BRN2-A2	5´GCCTAAGAGAGCAAGAG AGAAC 3´
FOXG1-S2	5´AATAGTGACTGCTTTG CCATTTC 3´	FOXG1-A2	5´CCACCAGATAGCTCCATG ATAAC 3´
Klf4-S1	5´GACCTCCTGGACCTAG ACTTTA 3´	Klf4-A1	5´GAAGACGAGGATGAAGCT GAC 3´
Myc-S2	5´CTGGAGATGATGACCG AGTTAC 3´	Myc-A2	5´GAGAAACCGCTCCACATA CA 3´
Oct4-S1	5´GAAGGATGTGGTTCGA	Oct4-A1	5´CCCTGTAGCCTCATACTCT

	GTATGG 3´		TCT 3´
Pax6-S3	5´AGTGAATGGGCGGAGT TATG 3´	Pax6-A3	5´GAACTGACACTCCAGGTG AAA 3´
PCNA-S1	5´GGCTCTCAAAGACCTC ATCAA 3´	PCNA-A1	5´GAGTAAGCTGTACCAAGG AGAC 3´
SHH-S1	5´CCTTTAGCCTACAAGC AGTTTATTC 3´	SHH-A1	5´GTTCCTTAAATCGTTCGGA GTTTC 3´
Sox2-S2	5´CGCTCTGCACATGAAG GA 3´	Sox2-A2	5´CCGGGAAGCGTGTACTTA TC 3´

Supplemental Table 2.S3. Cell Type Specificity and Particular Functional Associations of Marker Genes and Proteins.

Gene	**Full Name**		**Cell Type Specificity in Brain**				**Function**				
Cell type markers		**Acticvity NeuN-High nuclei**	Neuron	Glia	Endothelial	Leukocyte	Learning memory	Epigenetic	Cell differentiation	Cell cycle	Pluripotency
ARC	Activity-regulated cytoskeletonassociated protein	H	✓				✓		✓		
BDNF	brain-derived neurotrophic factor	H	✓				✓		✓	✓	
BLBP	Brain lipid binding protein	L		✓							
BRN2/POU3F2	Brain-specific 2/N gene, POU domain class 3 homeobox 2	H	✓								✓
CDK5	cyclin-dependent kinase 5	H	✓				✓		✓	✓	
cMYC	Myc family of transcription factors	H							✓	✓	✓
DNMT1, 3A, 3B	DNA methyltransferase 1, 3A, 3B	H						✓		✓	
EGR1	early growth response protein 1	H	✓				✓				
ETB, EDNRB	Endothelin-B receptor	L			✓						
FOXG1	Forkhead box G1	H	✓								✓
GADD45 α	Growth Arrest DNA Damage Inducible Protein 45a, DNA cytosine demethylases	H						✓		✓	
GADD45 β	Growth Arrest DNA Damage Inducible Protein 45b, DNA cytosine demethylases	H						✓		✓	
GLAST	Glutamate Aspartate Transporter	C	✓	✓							
HDAC1, 2, 4, 5, 11	Histone Lysine Deacetylases	H					✓	✓			
HOMER 1	homer protein homolog 1	H	✓				✓		✓		
IKAROS, IKZF1	Ikaros family zinc finger protein 1	L				✓					
KAT2B, 3A, 3B, 5	Lysine (K) acetyltransferases (PCAF, CBP/CREBBP,	H					✓	✓			

	P300, Tip60, respectively)										
KLF4	Kruppel-like factor 4	H							✓		✓
NFL/NEF1	Neurofilament 1	H	✓				✓				
OCT4, POU5F1	Octamer-binding transcription factor 4, POU domain, class 5, transcription factor 1	H								✓	✓
OLIG2	Oligodendrocyte transcription factor 2	C	✓	✓							
PAX6	Paired Box 6	C	✓						✓		✓
PCNA	Proliferating cell nuclear antigen	H						✓	✓	✓	
PDGFR-α	Platelet-derived growth factor receptor alpha	L		✓							
SHH	Sonic hedgehog	H							✓	✓	✓
SIRT1	Sirtuin 1, deacetylase						✓	✓			
SOX2, SRY	Sex determining region Y-box 2	H							✓	✓	✓
SYT1	Synaptotagmin 1	H	✓				✓		✓		

CHAPTER 4

A SUBSET OF MOUSE NEURONAL CELL NUCLEI WITH EXCEPTIONALLY HIGH LEVELS OF HYDROXYMETHYLCYTOSINE[2]

[2] Ping Yu, Lexiang Ji, Kevin J. Lee, Miao Yu, Chuan He, Emily R. Trunnell, Natalie M Hohos, Richard B. Meagher, and Robert J. Schmitz. To be submitted.

Abstract

5-methylcytosine (5mC) in many transcriptionally active gene regions turns over rapidly. The rate-limiting step in turnover of 5mCs in the CG dinucleotide context appears to be the Ten-eleven translocation enzyme (TET)-catalyzed oxidation of 5mC to 5-hydroxymethylcytosine (5hmC). Recent studies on the distribution of 5hmC in mouse brains suggest a model in which the high levels of 5hmC in neurons reflect a highly poised or activated transcriptional state for "on demand gene regulation". We recently reported that a significant subpopulation of adult mouse brain cellular nuclei (NeuN-High) had highly decondensed chromatin and expressed elevated levels of factors promoting neurogenesis, learning and memory, cell cycle, pluripotency and of complementary factors promoting more rapid turnover of DNA cytosine modification. Herein, we explore the idea that the NeuN-High subset of neurons from mouse brain might also have exceptionally high levels of 5hmC reflecting elevated rates of modified cytosine turnover and a greater potential for rapid changes in neurogenesis and learning and memory. NeuN-High nuclei have elevated levels of 5hmC and express higher levels of factors promoting modified cytosine turnover relative to the balance of neuronal or non-neuronal nuclei. Tet-assisted bisulfite sequencing (TAB-seq) demonstrated that 5hmC levels in NeuN-High nuclei reached nearly 40% of total CG dinucleotides at the start of gene regions for the most highly transcribed neuron-specific genes, and were variably distributed in well-defined gene regions among different functional gene categories. The extremely high level of 5hmC found in mouse brain and in NeuN-High nuclei in particular suggest a model in which more rapid turnover of cytosine modification potentiates more rapid learning and memory.

Introduction

Sir Francis Crick proposed 30 years ago that active learning and memory are controlled by secondary modifications to DNA and proteins (Crick, 1984; Meagher, 2014). However there is a dominant and generally overlooked theme of his proposal. All known secondary modifications to these biomolecules turn over rapidly, which accommodates synaptic plasticity, but does not allow for long-term memory storage. He proposed that biomolecules recording memories must have symmetrical structures such as 5 ´methylation of DNA cytosine within the 5 ´-^{5m}CG/3 ´-G^{5m}C paired double-stranded dinucleotide context. Symmetry provides a mechanism by which these modifications might maintain long-term memories in the face of rapid molecular turnover. Symmetrical structures enable recognition of the stored information in hemi-modified sites (e.g., 5 ´-^{5m}CG/3 ´-GC) and restoration of chemical modification to a symmetrically modified site (5 ´-^{5m}CG/3 ´-G^{5m}C). 5-methylcytosine (5mC) in many transcriptionally active gene regions in certain cell types turnover rapidly with half-lives generally measured in tens of minutes (Meagher, 2014). The cyclic turnover of 5mC residues is summarized in Figure 1. A rate-limiting step in this cycle appears to be the *Ten-eleven translocation* (*TET*) enzymes-catalyzed oxidation of 5mC to 5-hydroxymethylcytosine (5hmC) (Wu and Zhang, 2014; Xu and Walsh, 2014). 5hmCG levels are reported to be the highest in the adult brain of any organ, but vary widely in other organs and may be as much as 40-fold lower (Globisch and others, 2010b; Guz and others, 2014; Li and Liu, 2011; Lister and others, 2013a; Nestor and others, 2012; Szulwach and others, 2011a; Terragni and others, 2012). The TET enzymes with their associated machinery have strong specificity for 5mCG dinucleotides, and hence, 98% of 5hmC residues are found in the 5hmCG dinucleotide context (Lister and others, 2013a; Yu and others, 2012a). The three TET enzymes (TET1, TET2 and TET3) have the potential to further oxidize 5hmC to 5-

formylcytosine (5fC) and 5-carboxylcytosine (5caC). At this point the base-excision-repair (BER) pathway takes over. The latter two oxidized bases may be removed by thymine DNA glycosylase (TDG) making an abasic site with a hydroxyl group (-OH) substituted for the missing base. The 5 ´-abasic ribose residue is aligned with a 3 ´-G residue in the complementary strand of DNA and may be restored to a cytosine (C) by other activities in BER, which includes the activities of GADD45A, B, and G (Barreto and others, 2007; Ma and others, 2009; Rai and others, 2008; Schmitz and others, 2009). BER is active even in post-mitotic neurons (Gavin and others, 2013). DNA methyltransferases (DNMT1, DNMT3A, DNMT3B) may re-methylate these cytosines to maintain a moderately constant steady-state level of 5mC at most sites as the cytosine modification cycle begins again. Although, DNMT3A and 3B are responsible for most gene body *de novo* methylation (Baubec and others, 2015), and the maintenance methyltransferase DNMT1 carries out symmetrical methylation of hemi-methylated sites, all three methyltransferase may participate at some level in gene body maintenance methylation (Baubec and others, 2015; Gonzalez-Bosquet and others, 2014; Hahn and others, 2011). One emerging view is that dynamic transient changes in 5hmC levels regulate the transient removal of 5mC to potentiate and/or maintain gene induction (Hahn and others, 2014; Neri and others, 2015; Wen and Tang, 2014).

Most studies on chromatin remodeling in the brain have utilized dissected tissues that contain mixtures of cell types each with their own epitype, such that the resulting data represent a weighted average of those cell type (Yu and others, 2015). Among the approaches used to improve cell-type specificity, three recent studies have used fluorescence activated nuclear sorting (FANS) to examine the epigenetics of distinct classes of mouse brain neuronal cell nuclei and show the following. NeuN-positive neuronal nuclei have higher levels and a different

distribution of 5mC and 5hmC than NeuN-Neg non-neuronal brain nuclei (Li and others, 2014; Lister and others, 2013a). The NeuN-Positive population is comprised of extremely different NeuN-High and NeuN-Low sub-populations, which represent ~20 and ~50%, respectively, of adult brain nuclei (Yu and others, 2015). In this manuscript we take the analysis of chromatin in these two classes of neuronal cell nuclei further and revealed that NeuN-High neuronal nuclei had exceptionally high levels of gene body 5hmC compared to NeuN-Low and NeuN-Neg sub-populations of nuclei.

Multipotent cell types commonly have enlarged nuclei with decondensed chromatin (Davis and Dyer, 2010b; Hezroni and others, 2011b; Melcer and others, 2012a; Morey and others, 2007a; Ram and Meshorer, 2009a). As compared to compacted heterochromatic DNA, decondensed euchromatic DNA is marked with higher levels of 5hmC and lower levels of 5mC (Kubiura and others, 2012). As mouse brain development progresses from embryonic to the adult stages, 5hmC levels increase several fold and these increases are most concentrated in euchromatic regions and are directly proportional to transcript expression levels (Lister and others, 2013a). By contrast there is not a strong correlation between gene body 5mC levels and gene expression levels. Based on a limited number of studies, 5hmC levels are highest in regions of the brain most active in learning and memory such as the hippocampus (Chen and others, 2014; Hahn and others, 2013; Lister and others, 2013a; Szulwach and others, 2011a). More significantly 5hmCG dinucleotides in mouse fetal brain cortex mark 5mCG sites that are poised to lose all modification later in the adult brain, concurrent with gene activation (Lister and others, 2013a).

We recently reported that a large fraction of adult mouse brain neuronal cell nuclei, those expressing the highest levels of the pan-neuronal marker, NeuN (e.g., NeuN-High nuclei) have

significantly decondensed chromatin, with nuclear volumes averaging several times those of most NeuN-Low neuronal cell nuclei or NeuN-Neg mostly non-neuronal brain cell nuclei (e.g., those from glia, astrocytes, endothelial cells, leukocytes) as well as Purkinje neurons(Yu and others, 2015). Herein, we explore possible relationships between decondensed NeuN-High neuronal nuclei and gene potentiation or activation by hydroxymethylation. NeuN-High nuclei represent approximately 20% of total adult mouse brain cell nuclei. However, the percentage of NeuN-High nuclei ranges from as high as 50% in the hippocampus, nucleus accumbens, and cortex, to as little as a few percent in the pons and cerebellum. Relative to other isolated brain cell nuclei NeuN-High nuclei express 3- to 100-fold higher levels of transcripts for a remarkable variety of functions, including multipotency, cell cycle activity, histone acetylation and deacetylation, DNA cytosine methylation, base-excision-repair, neurogenesis, and learning and memory (**Supplemental Table 3.S1**) (Yu and others, 2015).

We wished to begin to explore the hypothesis that *the cytosine modification cycle (Figure 3.1) runs more rapidly in the brain than in other organs to accommodate rapid learning and memory* (Crick, 1984; Meagher, 2014; Yu and others, 2015). The exceptionally high levels of neuronal 5hmC, one possible limiting intermediate in the cycle, might lend support for this idea. Using independent assays we showed that several sub-populations of brain neuronal cellular nuclei have distinctly different 5hmC content and distribution. A *de novo* genome sequence analysis (Sims and others, 2014) of 5hmC levels demonstrated that 5hmC levels were significantly higher across gene regions of the most highly expressed genes. The levels and gene-region distribution of 5hmC varied among functionally different gene categories. For NeuN-High nuclei, in general, the 5hmC level drops to the lowest directly following the transcriptional start site, but immediately increased to nearly 40% of the CG dinucleotides at the start of the gene

body in the most actively transcribed gene regions, as compared NeuN-Low and NeuN-Neg nuclei, which exhibited significantly lower and with less dynamic variation in the levels of 5hmC.

Materials and Methods

Mice

Approximately 3-month-old adult mice (BALB cJ) weighing between 25 and 30 g and post-natal day 1 (PND1) mice were used. Live mice were obtained from UGA's animal facility and flash frozen mice were obtained from Rodent Pro (Evansville, IN). Entire mouse brain tissue was used to isolate mouse brain nuclei. All institutional and national guidelines for the care and use of laboratory animals were followed. All protocols for this experiment were approved by the University of Georgia Institutional Animal Care and Use Committee (AUP # A3437-01) prior to the start of this experiment.

RNA and qRT-PCR

Mouse brain nuclei were isolated from entire mouse brain tissue and sorted according to previously published FANS protocol (Yu and others, 2015) summarized briefly here. 20 X 10^6 isolated nuclei were labeled with 15 μg of Alexafluor 488 conjugated anti-NeuN antibody and sorted using fluorescent activated nuclear sorting (FANS) into NeuN-High, NeuN-Low and NeuN-Negative populations (**Figure 3.2A**) (Yu and others, 2015). RNA was isolated from sorted formalin fixed nuclei using RNeasy FFPE kit (Qiagen #73504). A heat treatment of 90°C for 1 h was included, after the proteinase K digestion, to hydrolyze off the remaining formalin. RNA was quantified using Qubit 2.0 Fluorometer (Invitrogen) with the Qubit RNA Assay Kit (Life

Technologies # Q32855). 500ng RNA was reverse transcribed into cDNA using qScriptc DNA SuperMix (Quanta BioSciences). cDNA yield was quantified using the Qubit ssDNA Assay Kit (Life Technologies # Q10212). 5 ng of cDNA was used per reaction in qRT-PCR assays. SDHA (Succinate dehydrogenase complex subunit A) was used as the endogenous control. Each assay was run in triplicate and the Relative Quantity (RQ) of transcript level was calculated based on the dCT method including the standard deviation from the mean. *TET* and *TDG* transcript expression levels in three classes of nuclei determined herein were compared to other previously published marker transcript levels in **Supplemental Table 3.S1**. Primer sequences used in this study can be found in **Supplemental Table 3.S2**.

Immunohistochemistry

Mice were anesthetized with inhaled isoflurane (project AUP number: A3437-01) and quickly sacrificed via decapitation according to AUP approved protocols. The brains were rapidly dissected out, and immediately placed into ice-cold 4% formalin in PBS at 4°C overnight. Alternatively, mice were deeply anesthetized by injection with ketamine (Lloyd, NADA 139–236) and xylazine (Vedco, NDC 50989-996-06) and transcardially perfused with 4% formaldehyde in PBS before dissection (Ohira and Miyakawa, 2011). The brains were then transferred into 30% sucrose-PBS at 4°C and incubated until they were completely submerged. Each brain was embedded in OCT (Fischer Scientific #14-373-65), and frozen on dry ice for cryosectioning. Coronal sections (30 μm) were taken on a Leica cryostat (CM305) and collected on poly-lysine-coated microscope slides (Polysciences, Inc #2224). Slides were stored at -80°C. Slides were thawed, rinsed with PBS, and incubated in PBST (PBS + 0.4% Triton X100) for 1h. Antigen retrieval was performed by treating tissue sections with 10mM sodium citrate at 100°C

for 15 min. Small 1.5 cm areas on slides were encircled with a Dako pen (Dako S200230) to contain antibody solutions. Sections on slides were blocked with PBST + 5% BSA + 2% goat serum for 1 h. Anti-NeuN (Millipore A60 MAB377) and anti-5hmC (Active Motif # 39769) antibodies were used at 1:200 dilutions into PBST and incubated with tissue sections at 4℃ overnight. Slides were washed three times with PBST and incubated with Alexa Fluor633 goat anti-rabbit IgG and Alexa Fluor488 goat anti-mouse IgG (Life technologies) for 1 hour at dilution factor 1:500. Slides were washed three times with PBST, co-stained with DAPI and photographed on a Leica TR600 epifluorescent microscope.

For immunostaining of isolated brain cellular nuclei, 1-10 X 10^5 mouse brain nuclei were labeled with antibodies to NeuN, 5hmC, TET1, TET2 and/or TET3. Mouse brain nuclei were washed with 50% methanol in PBS to remove the residual formalin. Nuclei were then blocked with PBSTBA (PBS+ 0.1% tween + 5% BSA + 0.02% Azide) for 1 h. Double-labeling was performed by adding mouse monoclonal NeuN (Millipore A60 MAB377) and rabbit polyclonal 5hmC (Active Motif # 39769) primary antibodies to blocked nuclei and incubated for 1 hour at dilution factor 1:200. Nuclei were washed three times with PBSTBA and incubated with secondary antibodies Alexa Fluor633 goat anti-rabbit IgG and Alexa Fluor488 goat anti-mouse IgG (Life technologies) for 1 hour at dilution factor 1:500. Nuclei were washed three times with PBST, co-stained with DAPI and photographed on a Leica TR600 epifluorescent microscope. The following TET antibodies were used: anti-TET1 (Origene TA309902), anti-TET2 (Abcam ab94580), and anti-TET3 (Abcam ab139805). For anti-TET2 and anti-TET3 antibodies, overnight incubation was needed for efficient immunostaining.

Quantification of DNA hydroxymethylation by ELISA

Quantification of total 5hmC in NeuN-High, Low and Neg mouse brain nuclei was performed using Quest 5-hmC DNA ELISA Kit (Zymo Research Quest Kit #D5425), following the manufacturer's instructions with the following modifications. DNA was isolated from sorted NeuN-High, NeuN-Low and NeuN-Neg mouse brain nuclei (2 to 5 x 10^6 nuclei) using DNeasy kit (Qiagen, Frederick, MD, USA #69504) according to the manufacturer's recommendations. A heat treatment of 90℃ for 1 h was included, after the proteinase K digestion, to hydrolyze off the formalin. DNA was quantified using Qubit 2.0 Fluorometer (Invitrogen) with the Qubit dsDNA Assay Kit (Life Technologies # Q32853). 200ng of genomic DNA isolated from sorted NeuN-High, Low and Neg mouse brain nuclei were used in each assay. As controls we examined total brain DNA from post-natal day 1 (PND1) and 3-month-old (3-mon) adult mice (**Supplemental Figure 3.S1**). 5hmC levels are reported to increase 3 to 5-fold from fetal and early post-natal brain to adult brain (Szulwach and others, 2011a). We also attempted to measured 5hmC levels in isolated CD4+ and CD16+ human leukocytes, whose DNA was reported to have 0.03% 5hmC per nucleotide (Guz and others, 2014). Although the relative levels of 5hmC among brain DNA samples were reasonably reproducible, we observed significant day-to-day variation in quantification of absolute 5hmC levels, relative to standards provided with this kit.

Analysis of DNA hydroxymethylation levels by fluorescence nuclear cytometry (FNC)

1-10 X 10^5 mouse brain nuclei were washed with 50% methanol in PBS to remove the residual formalin. Nuclei were then blocked with PBSTBA for 1 h. Double-labeling was performed by adding mouse monoclonal NeuN (Millipore A60 MAB377) and rabbit polyclonal 5hmC (Active Motif # 39769) primary antibodies to blocked nuclei and incubated for 1 hour at

dilution factor 1:200. Nuclei were washed three times with PBSTBA and incubated with secondary antibodies Alexa Fluor633 goat anti-rabbit IgG and Alexa Fluor488 goat anti-mouse IgG (Life technologies) for 1 hour at dilution factor 1:500. Nuclei were washed three times with PBST, co-stained with DAPI and pre-filtered in 0.5ml aliquots by centrifugation at 300g into a polystyrene tube affixed with a 35-μm cell-strainer cap (BD Falcon, REF352235). FNC was conducted on a Cyan ADP (Beckman Coulter Miami, Florida). Nuclei were gated for 2C or greater DNA content and forward (FS) and side (SS) light scattering to eliminate the analysis of small particulate contamination (**Supplemental Figure 3.S2**).

TAB-seq

DNA from NeuN-High, NeuN-Low and NeuN-Neg nuclei (1 ug each) was prepared as for ELISAs. A heat treatment of 90°C for 1 h was included, after the proteinase K digestion, to hydrolyze off the formalin. DNA was quantified using a Qubit 2.0 Fluorometer (Invitrogen) with the Qubit dsDNA Assay Kit (Life Technologies # Q32853). TET-enzyme assisted bisulfite sequencing (TAB-seq) was performed as described previously (Yu and others, 2012b). Methyltransferase *M. Sss*I methylated lambda DNA (0.5 ng) and 0.25 ng of hydroxymethylated pUC19 DNA were added per 1ug of mouse DNA prior to treatment as C/5mC and 5hmC controls, respectively. Sequencing libraries were prepared following the MethylC-Seq protocol (Urich and others, 2015). *De novo* genome sequencing was performed using an Illumina NextSeq500 Instrument at the University of Georgia's Genomics Facility, with coverage estimated to range from 0.37 to 0.4 genome equivalents among the various samples (**Supplemental Table 3.S3**) (Popp and others, 2010). This level of coverage is deep enough

(Sims and others, 2014) to obtain information about gene region distribution of 5hmC among genes in diverse of gene expression categories.

TAB-seq data analysis

The raw sequence data were trimmed for adapters, preprocessed to remove low quality reads, and aligned to the *Mus musculus* GRCm38 reference genome as previously described in (Yu and others, 2012b). The 5mCG sites on the methylated lambda DNA sequence were used to calculate the 5mC non-conversion rate upon TET and bisulfite treatment. Non-CG sites were used to compute the non-conversion rate of unmodified cytosines upon bisulfite treatment (**Supplemental Table 3.S3**). The 5hmC sites in pUC19 were used to evaluate the protection rate of 5hmCs. For this analysis, only cytosines in the CG context were considered.

For quintile expression data, we grouped approximately 12,500 genes into five gene expression categories based on the rank of their transcript levels assayed on arrays of whole mouse brain transcripts, averaging the expression data from two different mouse lines presented in a previous study (Bhave and others, 2006). For each quintile of transcripts (2497 or 2498 genes represented in each), the level of 5hmC was determined using weighted methylation level calculation (Schultz and others, 2012) for each of 20 bins upstream, 20 bins within genes (between annotated TSS and TTS), and 20 bins downstream of genes. Each of the upstream and downstream bins spanned 5kb for a total of 100kb spanned in each direction. The within-gene regions, no matter what their length, were evenly divided among the 20 bins. We then examined the levels of 5hmC for neuronal and non-neuronal Gene Ontology (GO) term categories (**Figure 3.6 and Supplemental Figure 3.S3**). The genes in each GO term category were extracted and all CG sites within a 100bp window of the relevant locations were used to determine the fraction of

5hmC. A table describing the GO terms used and the number of genes in teach term is provided (**Supplemental Figure 3.S4**). Figures were prepared using ggplot2 (Wickham, 2009).

Data Availability

The authors state that all data necessary for confirming the conclusions presented in the article are represented fully within the article. TAB-seq data set supporting the results of this article is available in NCBI GEO repository with accession number (GSE72432). A unique persistent identifier and hyperlink to our dataset is http://www.ncbi.nlm.nih.gov/geo/query/acc.cgi?token=svelsssolfgnfql&acc=GSE72432.

Results

NeuN-High nuclei had higher levels of TETs, TDG and 5hmC

Nuclei isolated from 3-month-old mouse brain were labeled with Alexafluor488 conjugated NeuN antibodies and sorted by FANS as previously reported (Yu and others, 2015). A histogram of the cytometry revealed three populations of nuclei: non-neuronal NeuN-Neg (negative), neuronal NeuN-Low (weakly immunostained main peak), and neuronal NeuN-High (those stained most strongly for NeuN) (**Figure 3.2A, Supplemental Figure 3.S2**). The nuclear transcript levels of *TET1*, *TET2*, *TET3*, *TDG*, *MBD2*, *MBD3 and MBD4* were determined using quantitative real time PCR of reverse transcribed transcripts (qRT-PCR) (Deal and Henikoff, 2011). TETs and TDG are central to the active demethylation of 5mCG dinucleotides (Figure 1) (Song and others, 2012). The validity of assaying nuclear transcripts is supported by previous work showing that the vast majority of transcripts are proportionally expressed in the cytoplasmic and nuclear compartments (see supplemental data in Deal and Henikoff (2010b)).

NeuN-High nuclei expressed modestly higher levels of *TET1*, *TET2* and *TDG* transcripts relative to levels in NeuN-Low or NeuN-Neg nuclei (**Figure 3.2B**). Some methyl CG binding domain proteins, MBD4 in particular, contains a glycosylase domain and is capable of repairing mismatches in symmetrically methylated CGs, and hence, also might impact the turnover cycle (Du and others, 2015). We found transcripts for *MBD2*, *MBD3* and *MBD4* all slightly more highly expressed in NeuN-Positive neuronal nuclei. Although the ~2-fold higher levels of these transcripts in NeuN-High nuclei relative to NeuN-Neg nuclei are consistent with more rapid turnover, the results seemed unremarkable, when compared to the order or magnitude higher expression of other factors involved in regulating various chromatin structures (**Supplemental Table 3.S1**).

Considering their central importance to the cycle, we went on to assay TET1, TET2, and TET3 proteins by IFM. Substantially higher levels of all three TETs were found concentrated in the larger NeuN-High nuclei, compared to the nuclei that immunostained weakly or remained unstained with antibodies to NeuN (**Figure 3.2C, D, E**). The levels of TET proteins in NeuN-High nuclei assayed by IFM appeared greatly enhanced relative to the only slightly higher levels of *TET* RNAs assayed by qRT-PCR.

Assays of 5hmC levels in isolated nuclei

These data supported the view that decondensed NeuN-High nuclei might be more active in the TET catalyzed oxidation of 5mC to 5hmC and perhaps the turnover of 5mC (**Figure 3.1**). Four independent approaches were used to assay 5hmC levels among the NeuN-High, NeuN-Low, and NeuN-Neg subpopulations of mouse brain nuclei. First, immunostaining of mouse brain nuclei with antibodies to 5hmC showed that the large, decondensed NeuN-High nuclei had much higher levels of 5hmC compared to NeuN-Low and NeuN-Neg nuclei (**Figure 3.3A**).

Second, fluorescent nuclear cytometry (FNC) of NeuN/5hmC co-immunostained nuclei was performed to better quantify the relative levels of NeuN and 5hmC. FNC showed that there was a general coordinate expression between NeuN and 5hmC. Further, FNC resolved several subpopulations of brain cell nuclei (i.e., A, B, C, D) differing in their relative levels of NeuN and 5hmC (**Figure 3.3B**). Notice that the immunofluorescent signal for the strongest staining 5hmC nuclear population is several-fold higher than that of 5hmC-Low population, in agreement with the wide dynamic range of 5hmC immunostaining observed by IFM. Third, the levels of 5hmC in DNA of NeuN-High, Low, and Neg mouse brain nuclei were measured using a commercial ELISA assay. The percent 5hmC relative to total nucleotide (nt) content of NeuN-High, Low and Neg nuclei were ~ 0.81%, 0.54%, and 0.34%, respectively (**Figure 3.3C**).

Fourth, we performed a Tet-Assisted Bisulfite sequencing (TAB-seq) on DNA isolated from each class of sorted nuclei. We calculated the percent 5hmCG (% 5hmCG) in three classes of nuclei determined by TAB-seq by dividing total 5hmCG by total CG (**Table 3.1**). Also, the scaled percent 5hmCG was determined by correcting for non-conversion and protection-rates (see Methods). NeuN-High nuclei had the highest level of scaled % 5hmCG, wherein an average of 25% of the CG dinucleotide sites assayed were 5hmCG. NeuN-Low and NeuN-Neg had lower and similar levels of 5hmCG, 16.30% and 16.61%, respectively. These levels are much higher than observed for other tissues such as leukocytes (Hohos and others, Submitted for publication). These values were based on the analysis of approximately $10x10^6$ different CG dinucleotides from each class of cellular nuclei.

There are a few simple explanations for the differences among measurements made by qRT-PCR for TET RNAs, immuno-detection of 5hmC, and TAB-seq analysis of 5hmC. First, differential stability of TET proteins might favor the accumulation of TETs in the NeuN-High

subset of cells, while RNA levels might not reflect this relationship. Second, 5hmC is most concentrated in euchromatin in regions with decondensed structure (Chen and others, 2014; Kubiura and others, 2012). We had observed previously that NeuN-High nuclei were extremely large and decondensed (Yu and others, 2015) and a decondensed chromatin structure should greatly favor accessibility of antibody reagents in fixed tissues. While this potential artifact might prevent absolute quantitative interpretation of our immunochemical data, it may have contributed to the wide dynamic ranges of NeuN and 5hmC staining observed and aided in separating classes of NeuN stained nuclei by FANS.

NeuN-High, 5hmC-High decondensed nuclei are enriched in hippocampus

We have previously shown that decondensed NeuN-High nuclei are enriched in mouse regions most active in learning and memory such as cortex, hippocampus, and nucleus accumbens, whereas the cerebellum and pons contain few NeuN-High nuclei (Chen and others, 2012; Yu and others, 2015). We therefore assessed the abundance of 5hmC in NeuN-High nuclei in the mouse hippocampus. Fixed whole young mouse brain was coronally cryosectioned, stained with antibodies to NeuN and 5hmC, co-stained with DAPI for DNA and secondary fluorescent antibodies, and examined by IFM. We found enrichment of 5hmC positive cellular nuclei (**Figure 3.4**) in the neuron-rich regions of the hippocampus in agreement with the previously published data (Chen and others, 2012). Consistent with the results observed by nuclei immunostaining, a substantial colocalization of 5hmC with decondensed NeuN-High nuclei in hippocampus was observed. The majority of large, decondensed NeuN-High nuclei in the hippocampus were highly enriched for 5hmC, whereas, small, condensed NeuN-Neg nuclei were essentially negative for 5hmC (white arrows, **Figure 3.4C-G**).

Gene-region-specific 5hmCG distribution relative to transcriptional activity

We have presented our TAB-seq data as a percent of the total CG dinucleotides, because essentially all 5hmC residues are in the 5hmCG context (Lister and others, 2013a; Yu and others, 2012a). To assess the gene-region-specific 5hmCG profile of three classes of nuclei, we plotted the percent 5hmCGs relative to total CG dinucleotide composition by gene region (100 kilobases (kb) upstream of the transcriptional start site (TSS), gene body (GB), and 100kb downstream of the TTS (transcriptional termination site)) as mapped in **Figure 3.5A**. The data were further analyzed by quintiles of transcript expression level among 12,488 gene-specific transcripts detected in mouse whole brain samples, where 5 of 5 represents the gene set with highest quintile of expressed transcripts and 1 of 5 represents the gene set with lowest quintile expression (Bhave and others, 2006) (**Figure 3.5**). Normalized expression data used to assign genes to quintiles were obtained from a previously performed microarray study (Accession Number GSE2502) of whole brain tissue from male C57BL/6 and DBA/2 mice, in which 12,488 genes passed quality control thresholds for expression (Bhave and others, 2006). NeuN-High, NeuN-Low and NeuN-Neg nuclei had roughly the same relative pattern of 5hmCG across and flanking the gene region (**Figure 3.5B**). There is a valley of low 5hmCG just after the transcriptional start site (TSS), immediately followed by the highest 5hmCG peak for each class of nuclei and transcript quintile at the beginning of the gene body, then a plateau of 5hmCG that gradually decreases (**Figure 3.5B**). This pattern is quite distinct from the pattern reported for CD4+ T cells, where the 5 ´peak is not followed by a plateau, but rather a rapid decline in 5hmC ending at the TTS and immediately and rapidly increasing downstream of the TTS (Ichiyama and others, 2015). Although the highest expressed transcript quintile had the highest level of 5hmCG for all classes of nuclei, the peak level of 5hmCG was different for each class of nuclei, with the NeuN-High

nuclei having the highest peak of 5hmCG at 38.5% (5th quintile), NeuN-Low nuclei having an intermediate peak 5hmCG at 31.5%, and NeuN-Neg nuclei having the lowest 5hmCG peak at 28.7% (**Figure 3.5B**). NeuN-High nuclei have substantially higher 5hmCG levels than the other two classes of nuclei for all quintiles of transcripts. The lowest level of gene region 5hmCG was 14% for NeuN-Low nuclei in the 1st quintile gene set. Notice also that the relative levels of 5hmCG in the gene body are higher in NeuN-Low than NeuN-Neg nuclei in the 5th quintile of expressed genes, although this order is switched for the most weakly expressed 2nd and 1st quintile data, where the 5hmCG levels are higher in the NeuN-Neg population. 5hmCG levels were the highest for the 5th quintile of highly expressed genes and progressively lower down to the 1st quintile of lowest expressed genes for all three classes of nuclei. This relationship of descending 5hmCG level among the five descending quintile groups of expressed genes is quantitatively summarized for the NeuN-High class of nuclei (**Figure 3.5C**).

Gene-region-specific distribution of 5hmCG among different classes of genes

The level of gene-region-specific 5hmCG for each class of nuclei was plotted for genes collated based on gene ontology (GO) terms both specific and not specific to brain or neuronal functions (**Figure 3.6 and Supplemental Figure 3.S3**). A detailed description of each GO gene list and the number of genes in each are presented (**Supplemental Table 3.S4**). Again, each gene region was divided into 100kb upstream of TSS, the gene body, and 100kb downstream of TTS (see map in **Figure 3.5**). Generally, there is a valley of low 5hmCG just after the transcriptional start site (TSS), immediately followed by the highest 5hmCG peak for each class of nuclei in the region of gene body, and another valley of low 5hmCG at the TTS site. For brain-specific gene clusters related to neuronal function (neuronal, synaptic transmission, synaptic plasticity, leaning

& memory), the three types of nuclei showed same pattern with NeuN-High nuclei having the highest level of 5hmCG in the gene body, NeuN-Low nuclei having significantly lower levels of 5hmCG, and NeuN-Neg having a significantly lower level still. Comparatively, for most gene lists specific to non-neuronal cell types (stem cell maintenance, astrocyte, angiogenesis, glial cell differentiation), NeuN-Neg nuclei had slightly higher levels of 5hmCG than NeuN-Low nuclei (**Figure 3.6**). These results are easily explained by the fact that enrichment of nuclei from these non-neuronal cell types in the NeuN-Neg fraction gives greater resolution to the higher levels of 5hmC in non-neuronal cell-type-specific genes. When GO-term-based gene lists not specific to brain function were examined (**Supplemental Figure 3.S3**), there was no difference in 5hmCG levels among NeuN-Low and NeuN-Neg nuclei, yet NeuN-High nuclei continued to show~30% higher 5hmCG levels.

Discussion

Cell-type-specific enrichment of 5hmCG in actively transcribed genes

We isolated three sub-populations of mouse brain nuclei by FANS (Yu and others, 2015) and used TAB-seq data to profile 5hmCG levels and distribution across gene regions for 12,488 genes expressed in the brain as a function of expression level. 5hmCG dropped to a very low level right after the TSS, but immediately increased to the highest level at the beginning of gene body, which is reasonably consistent with the evidence that gene region 5hmCG is inversely correlated with PolII binding at the TSS (Choi and others, 2014; Mellen and others, 2012; Szulwach and others, 2011a). Genes in the highest expression quintile (5 of 5) had the highest 5hmCG levels across the whole gene region among all three classes of nuclei. Yet, the peak level of 5hmCG was different for each class of nuclei. NeuN-High nuclei had the highest peak of 5hmCG, generally 25% higher than the 5hmCG levels in NeuN-Low or NeuN-Neg for all

quintiles of transcript. Our data demonstrated that the relationship between genomic distribution of 5hmCG and gene expression is neuronal cell-type-specific and that the majority of neuronal nuclei, the relatively inactive NeuN-Low nuclei (Yu and others, 2015), have comparatively low 5hmCG levels, generally indistinguishable from NeuN-Neg non-neuronal nuclei.

Three recent papers examined gene-region 5hmC levels in neurons isolated from brain. Mellen et al (2012) performed a quantitative, genome-wide analysis of 5hmCG and gene expression in granule cells and Bergmann glial (BG) cells based on their each being fluorescently tagged in the brain of distinct transgenic mouse lines. Their data for granule cells on the relative levels of 5hmCG among genes grouped by quintiles of transcript expression level resembled ours: with a narrow valley at the TSS and increasing rapidly in the gene body for the most highly expressed transcripts. However, their data showed progressively a less dramatic change for more weakly expressed transcripts (Mellen and others, 2012). Granule cells are NeuN-positive neurons that have relatively small cell bodies, but their nuclei are large and decondensed, and may be represented within the NeuN-High fraction. As compared to granule cells, BGs are a terminally differentiated NeuN-Neg non-neuronal cell type with smaller nuclei. BGs had lower 5hmCG levels that were less dynamic as a function of gene region and gene expression levels resembling best our NeuN-Neg fraction data (Mullen and others, 1992b). Two of the papers enriched for NeuN-Positive brain cell neuronal nuclei by FANS, although neither examined subsets of neuronal nuclei. When Lister et al. (2013a) compared NeuN-Positive and NeuN-Neg nuclei in fetal and adult mouse frontal cortex, they found 5hmCG was enriched throughout the gene bodies of the more highly transcribed genes. Their data on these two cell categories in the adult brain resembled ours for NeuN-High and NeuN-Neg nuclei, respectively. However, the differences in 5hmCG levels appear much less dramatic. This is as would be

expected from mixing the NeuN-High and NeuN-Low nuclei into a NeuN-Positive category, weight averaging 5hmCG data toward the predominant less active NeuN-Low class of nuclei (Yu and others, 2015). When Wen et al (2014) compared NeuN-Positive and NeuN-Neg nuclei they actually observed a drop in 5hmC in NeuN-positive nuclei for the highest quintile of expressed neuronal genes. This most likely results from the low level of 5hmC levels in what we defined as NeuN-Low nuclei representing the predominant population of NeuN-positive nuclei.

Cell-type-specific 5hmC distribution in functionally relevant gene clusters

It has been suggested that precisely conserved, cell-type-specific DNA methylation patterns may be related to specific neuronal and glial cellular processes (Lister and others, 2009; Maunakea and others, 2010). Given that 5hmCG is an intermediate in the dynamic cycle of DNA cytosine methylation and demethylation (**Figure 3.1**), it is reasonable to hypothesize that conserved, cell-type-specific 5hmCG patterns may be related to specific neuronal or non-neuronal cellular functions. We therefore plotted the pattern of 5hmCG for genes collated based on GO terms both specific and not specific to brain and neuronal cell functions. For some subsets of GO-term gene lists each type of nuclei had a relatively distinct 5hmCG profile.

For most of the brain specific gene clusters, the three classes of brain nuclei showed the same general pattern across the gene body, except that NeuN-High nuclei had by far the highest level of 5hmCG, and in general NeuN-Low nuclei had a much lower but intermediate level of 5hmCG, whereas NeuN-Neg had the lowest level of 5hmCG. The exceptions to this pattern were observed for the two lowest quintiles of transcripts, where the NeuN-Neg class of nuclei had higher 5hmCG levels than the NeuN-Low class. Similarly, for GO-term based gene lists for stem cells, angiogenesis, astrocytes, and glial cells NeuN-Neg nuclei had higher 5hmCG levels than

NeuN-Low. This appears to be the logical outcome, considering that the NeuN-Neg population contains nuclei from glial and endothelial cells, astrocytes, and some classes of progenitor cells (Yu and others, 2015), each with their own expression programs. These cell types are dramatically under-represented in total brain RNA samples. NeuN-Neg nuclei comprise only 25% of nuclei in a healthy 3-mo-old mouse brain, and nuclei from each of the mentioned cell types is highly enriched in the NeuN-Neg population (Yu and others, 2015). However, for most gene lists, even those not related to brain specific function, NeuN-Low and NeuN-Neg nuclei had similar lower levels of 5hmCG, whereas NeuN-High always had the highest levels of 5hmCG. Our data support the view that cell type has the biggest impact on 5hmCG patterns and levels, but that 5hmC also demarcates functionally relevant gene clusters based most significantly on expression level.

Relevance of 5hmC level in the brain to gene expression programs and health

Early in the exploration of the importance of 5hmCG to a healthy brain, higher 5hmCG levels in gene bodies were statistically correlated with higher levels of gene transcription (Jin and others, 2011b; Song and others, 2011a; Szulwach and others, 2011a). There are other examples connecting 5hmC levels and the turnover of modified cytosine to normal or aberrant brain activity. First, 5hmCG levels in the brain correlate with rates of neurogenesis and synaptogenesis, increasing 4- and 6-fold as the brain develops from fetal to prenatal and then to adult stages, respectively (Chouliaras and others, 2012; Lister and others, 2013a; Szulwach and others, 2011a). 5hmC levels may increase further with advancing age (Chen and others, 2012; Dzitoyeva and others, 2012). By contrast to normal function, lower than normal 5hmC or TET1 protein levels are associated with brain tumors and gliomas (Jin and others, 2011a; Muller and

others, 2012). Second, 5caC is considered an unstable intermediate in the turnover cycle, slowly formed from 5hmC by TET activity and at order-of-magnitude lower levels than 5hmC in most cells. Yet, during differentiation of neural stem cells, 5caC accumulation peaks to more significant levels 12 to 13 days post-conception and co-localizes with 5hmC in euchromatin (Wheldon and others, 2014). TDG is capable of removing 5caC and 5fC (**Figure 3.1**). Knocking down TDG leads to increased 5caC levels in the brain, confirming TDG's relative position in this cycle and its likely importance in maintaining normal levels of intermediates in this cycle (Hashimoto and others, 2012; Wheldon and others, 2014). Third, the notch receptor gene, *NOTCH1* and its ligand encoding genes, *JAG2* and *DLL1*, have roles in the maintenance and development of various types of progenitor cells including those in the brain. All three genes contain exceptionally high levels of 5hmC (30 to 45% of CGs) at gene-specific CG sites in the brain as compared to barely detectable 5hmC levels at these sites in leukocytes (Terragni and others, 2014). Fourth, mice subjected to prenatal stress linked to a schizophrenia-like phenotype show elevated levels of BDNF and increases in 5mCG and 5hmCGs in *BDNF* gene regulatory regions (Dong and others, 2015). Fifth, increases in 5hmCG in euchromatic gene regions are associated with increases in nucleosomes containing the histone modification H3K4me2 and loss of H3K27Me3 in neural tissue, both of which are associated with gene activation (Chen and others, 2014; Hahn and others, 2013).

Evidence more strongly supporting a cause-and-effect relationship, where TET-catalyzed oxidation of 5mCG to 5hmCG or beyond (**Figure 3.1**) may direct changes in gene expression and brain function, is now emerging, but remains very limited. The outstanding issue is whether or not TET-catalyzed formation of 5hmCG directs essential changes in gene expression, or if changes in 5hmC result, for example, from increased transcription caused by independent forces.

Here are examples of the relevant genetic studies, all of which support a high-level causal-role for 5hmCG in gene activation and brain function. First, TET1 overexpression in the hippocampus causes increases in 5hmCG, decreases in 5mC, and reduces long-term memory formation (Kaas and others, 2013). Second, TET1 knockout mice show reduced expression of genes essential to neuronal activation (*Npas4, c-Fos, Arc*) and are impaired in hippocampal functions including a significant loss of both normal fear and spatial memory extinction (Rudenko and others, 2013). Loss of memory extinction would be expected if TET1-catalyzed turnover of modified cytosine in highly active neurons is required for normal rate of loss of recorded memories. In other words, when the rate of molecular turnover is reduced, normally extinguished memories are retained. This implies molecular turnover would is required for memory extinction, a natural extension of Crick's model. Our data showing the highest levels of TETs and 5hmC in NeuN-High nuclei are consistent with this view, if indeed NeuN-High nuclei are the most active in learning and memory as gene expression data imply. Third, at the time of eye opening in mice (2 to 3-weeks) in the retinal neuronal ganglion cell layer (GCL) there is a dramatic increase in TET3 expression and 5hmC in thousands of predominantly neuronal gene regions (Perera and others, 2015). TET3 is highly expressed in the brain, but the *TET2* mRNA splice variant that is expressed most strongly in brain, lacks the domain encoding its own CXXC DNA binding domain recognizing CGs. TET3 appears to be recruited to corresponding CG-rich gene regions by direct binding to transcription factors such as REST. Most significant to this discussion of potential causation, TET3 overexpression increases the expression of transcripts from a significant fraction of REST bound gene targets. Fourth, *TET3* expression is minimal in embryonic stem cells (ESCs), but rapidly increases by an order of magnitude during neuronal differentiation (Li and others, 2015). ESC cell lines derived from *TET3*-knockout mice are

capable of self-renewal and maintenance and differentiate into neural progenitor cells (NPC). However, derived NPCs have lower levels of 5hmC, are less efficient at neuronal differentiation, and have higher rates of apoptosis (Li and others, 2015). In other words, it appears TET3 activity is essential for the normal differentiation of ESCs into NPCs. Fifth, Lister et al. (2013a) show that of the differentially methylated regions (DMRs) that normally become 5mC hypomethylated in the frontal cortex during the fetal to adult transition, 20% remain hypermethylated in adult *TET2* knockout mice. Hence, TET2 activity plays an essential role in the loss of 5mCG at a significant fraction of the differentially methylated CGs. Although total levels of 5hmCG are lower in the fetal brain, many of these fetal DMRs were also disproportionally enriched for 5hmC. Therefore, the authors go on to suggest that 5hmCG "*creates pre-modified sites that are poised for subsequent demethylation and activation at a later developmental stage.*" The finding that 5hmC is preferentially enriched within gene bodies of neuronal function-related gene clusters in NeuN-High neuronal nuclei suggests that a higher rate of 5hmCG-dependent turnover of 5mCG occurs in this subset representing the most active neuronal cells.

A model

If the TET enzyme catalyzed oxidation of modified cytosine residues is rate limiting to the cytosine modification cycle (**Figure 3.1**), our data showing extremely elevated levels of 5hmC and factors involved in NeuN-High nuclei might be interpreted as supporting our working hypothesis that *the cytosine modification cycle runs more rapidly in the brain than in other organs to accommodate rapid learning and memory.* It has been proposed previously, that more rapid turnover of 5mCG via oxidation to 5hmCG creates the poised, activated state for "*on demand gene regulation*" (Irier and others, 2014). We propose a model in which, maintaining a

high idling speed for the cycle in all brain cells enables better performance, such as greater neuronal plasticity. A high idling speed would ensure a more rapid response of cellular and molecular memory systems. As an analogy to illuminates the model, formula one F1 racecar engines maintaining extremely high idling speeds for maximum performance, while tractor trailer truck engines maintain low idling speeds for maximum efficiency. In this model concerning the brain, we are likening the brain to a F1 racecar designed for performance to maintain this poised responsive state. As evidence for a more direct parallel to a high performance racecar engine, the adult brain accounts for only 2% of human body weight, but consumes 20% of resting oxygen levels (Raichle and Gusnard, 2002). Other organs and tissues that have lower levels of TET oxidized products like 5hmC might run the cytosine modification cycle at a lower idling speed. Continuing the analogy, resting muscle, might maintain low idling speed for efficiency like the truck engine, and have slower less-responsive system of cellular and molecular memory. Muscle represents about 40% of body mass, but only consumes 18% of resting oxygen levels (Durnin, 1981), further supporting this analogy. TET catalyzed increases in both 5hmCG and the turnover of modified cytosine may enable accelerated activity of molecular memory systems via their combined impact on overall chromatin structure and transcriptional machinery. According to this model, the decondensed chromatin state in NeuN-High neuronal nuclei, created by an elevated cytosine modification cycle and elevated levels of 5hmC within large gene sets, maintains an exceptional subsets of neuronal cells in an even higher potentiated state than other NeuN-Low neuronal cells (Yu and others, 2015). Further evidence for this high idling speed is the exceptionally high relative levels of relevant transcripts in NeuN-High nuclei (**Supplemental Table 3.S1**). The subset of poised genes that are initially induced or repressed "*on demand*" would be dependent upon the spectrum of transcription factors and signaling

molecules expressed in that cell type (Dogan and others, 2015; Ptashne, 2007) and the influence of the external environment. This model may be tested initially, by inhibiting TET enzyme catalyzed oxidation of modified cytosine in different organs and tissues and then measuring the decay rate of 5hmC levels.

Conclusions

A high-resolution map of 5hmCG differences across gene regions for different brain cell types was achieved by separating NeuN-High neuronal cell nuclei from NeuN-Low neuronal nuclei and all classes of NeuN-Neg non-neuronal nuclei. We showed that the decondensed NeuN-High subset of neuronal cell nuclei have a valley of very low levels of 5hmCG right after the TSS followed by exceptionally high levels of 5hmCG in the rest of the gene body and in flanking regions relative to other brain cell nuclei. The valley and peak in 5hmCG levels at the start of the gene region are 22% and 39% of all GCs, respectively, for the most highly expressed quintile of ~2,500 genes. Perhaps surprisingly, although the total level of 5hmCG dropped dramatically from the strongest to weakest quintile of expressed genes, the higher level of 5hmCGs for NeuN-High nuclei from the others classes of nuclei persisted in all quintiles even for the most weakly-expressed quintile. Differences were strongest among brain-related gene categories (Figures 6 & 7). The difference between NeuN-Low neuronal and NeuN-Neg non-neuronal nuclei were generally small and unremarkable. In summary, there are significant advantages in examining chromatin structures in sub-fractions of neuronal cell nuclei. Perhaps the higher level of 5hmCG in the NeuN-High most active subset of nuclei reflects higher rates of turnover of cytosine modification. More rapid turnover may create a poised activated state enabling this subset of neuronal cells to respond more rapidly to learning and memory and/or

initiate neurogenesis (Yu and others, 2015). Combining molecular turnover models for various chromatin modifications (Meagher, 2014) with the cell type resolution afforded by sorting nuclei or isolating affinity tagged nuclei (Deal and Henikoff, 2011) should enhance our understanding of cellular memory (Deal and Henikoff, 2011; Lister and Mukamel, 2015; Meagher, 2014; Mo and others, 2015) .

Authorship

PY, RBM and RJS conceived of the project. PY performed dissections, prepared nuclei by FANS, purified DNA and RNA samples, and performed qRT-PCR, IFM and ELISAs. ERT and NMH contributed to the ELISAs. RJS, MY, and CH collaborated on the TAB-seq analysis of DNA. LJ and KJL performed the computational analysis of the sequence data and prepared the first drafts of related figures. RBM and PY prepared the major drafts of the manuscript and final figures, while all the authors contributed to revising the manuscript.

Acknowledgements

Julie Nelson provided invaluable assistance with the cytometry at UGA's Center for Tropical and Emerging Global Diseases Flow Cytometry Core facility. The work was funded by grants from the National Institutes of Health NIDDK Grants DK096300 and DK100392 and UGA's Research Foundation to RBM, NHGRI HG006827 to CH, the National Institutes of Health grant R00GM100000 to RJS. CH is an investigator of the Howard Hughes Medical Institute. MY is an international pre-doctoral fellow of the Howard Hughes Medical Institute.

Table 3.1. Percent 5hmCG in three classes of nuclei determined by TAB-seq and averaged across all sequences.

Nuclei	Total 5hmCG	Total CG	% 5hmCG	Scaled % 5hmCG
NeuN-High	1,083,110	8,104,772	13.36%	25.10%
NeuN-Low	789,538	9,246,699	8.54%	16.30%
NeuN-Neg	696,096	9,867,503	7.05%	16.61%

Based on these TAB-seq data, we calculated the percent 5hmCG (% 5hmCG) in three classes of nuclei by dividing total 5hmCG assayed by total CG. Also, scaled percent 5hmCG (scaled % 5hmCG) was presented after correction for non-conversion and protection-rates (see Methods).

Figure 3.1. A model for dynamic turnover of DNA cytosine modification. This diagram for the cyclic turnover of modified cytosine (C) residues emphasizes that TETs catalyze the rate-limiting step of removing 5mC by oxidation to 5-hydroxymethylcytosine (5hmC). TET activity further oxidizes 5hmC to 5-formalcytosine (5fC) and 5-carboxycytosine (5caC). The essential roles of other factors include DNMTs in the methylation of C to 5-methylcytosine (5mC), thymine DNA glycosidase (TDG) in the excision of 5fC or 5caC creating a single nucleotide gap, and gap repair back to a C residue by base excision repair (BER) machinery such as the GADD45s. The gene-region-specific balance of these activities determines the levels of C, 5mC and 5hmC. Enzymes are in square boxes and nucleotide bases in ovals. The diagram was redesigned from those published previously (Kohli and Zhang, 2013; Meagher, 2014; Wu and Zhang, 2014).

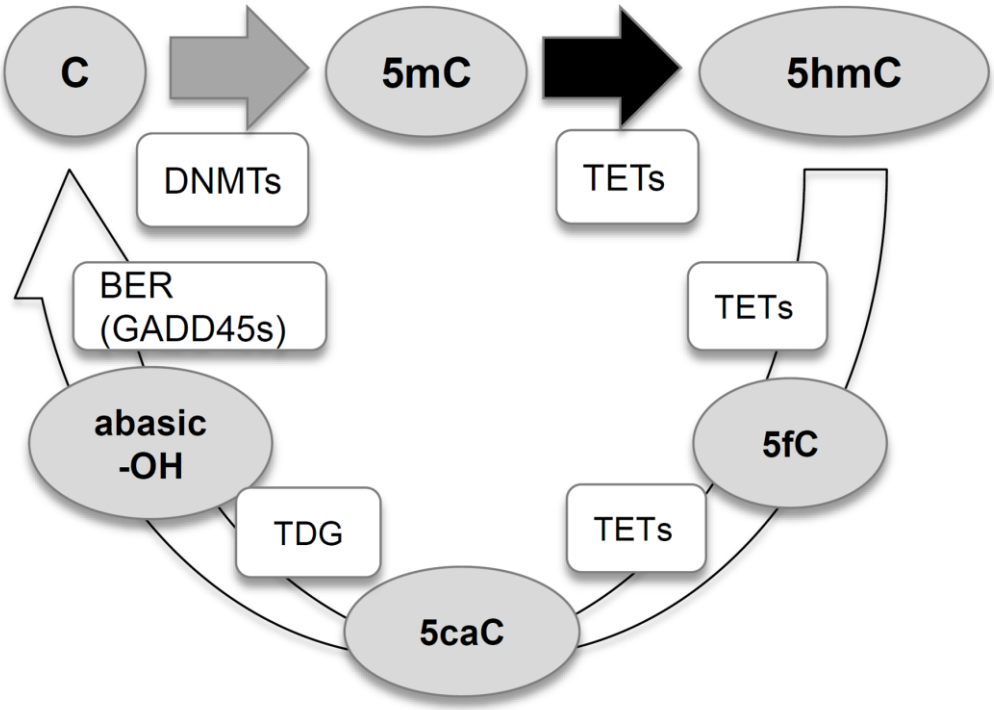
C
5mC
5hmC
DNMTs
TETs
BER
(GADD45s)
TETs
abasic
-OH
5fC
TDG
TETs
5caC

Figure 3.2. FANS of three classes of nuclei and expression of factors involved in DNA cytosine turnover. A**.** Cytometric histogram of NeuN-Neg, -Low and –High stained brain cell nuclei from one sorting experiment (log scale), pre-gated for DNA content and forward and side light scattering (See Supplemental Figure 3.S2). NeuN antibody mAb 1B7 was conjugated with AlexaFluor488. B. qRT-PCR analysis of the relative transcript expression was performed on cDNA prepared from three classes of brain cell nuclei. The Relative Quantity (RQ) of transcript level was calculated based on the dCT method including the standard deviation from the mean. SHDA was used as the endogenous control. C, D, E. Immuno-fluorescent analysis of mouse brain nuclei revealed decondensed NeuN-High mouse brain nuclei contained exceptionally high levels of TET1 (C), TET2 (D), and TET3 (E), relative to NeuN-Low and NeuN-Neg non-neuronal cell nuclei.

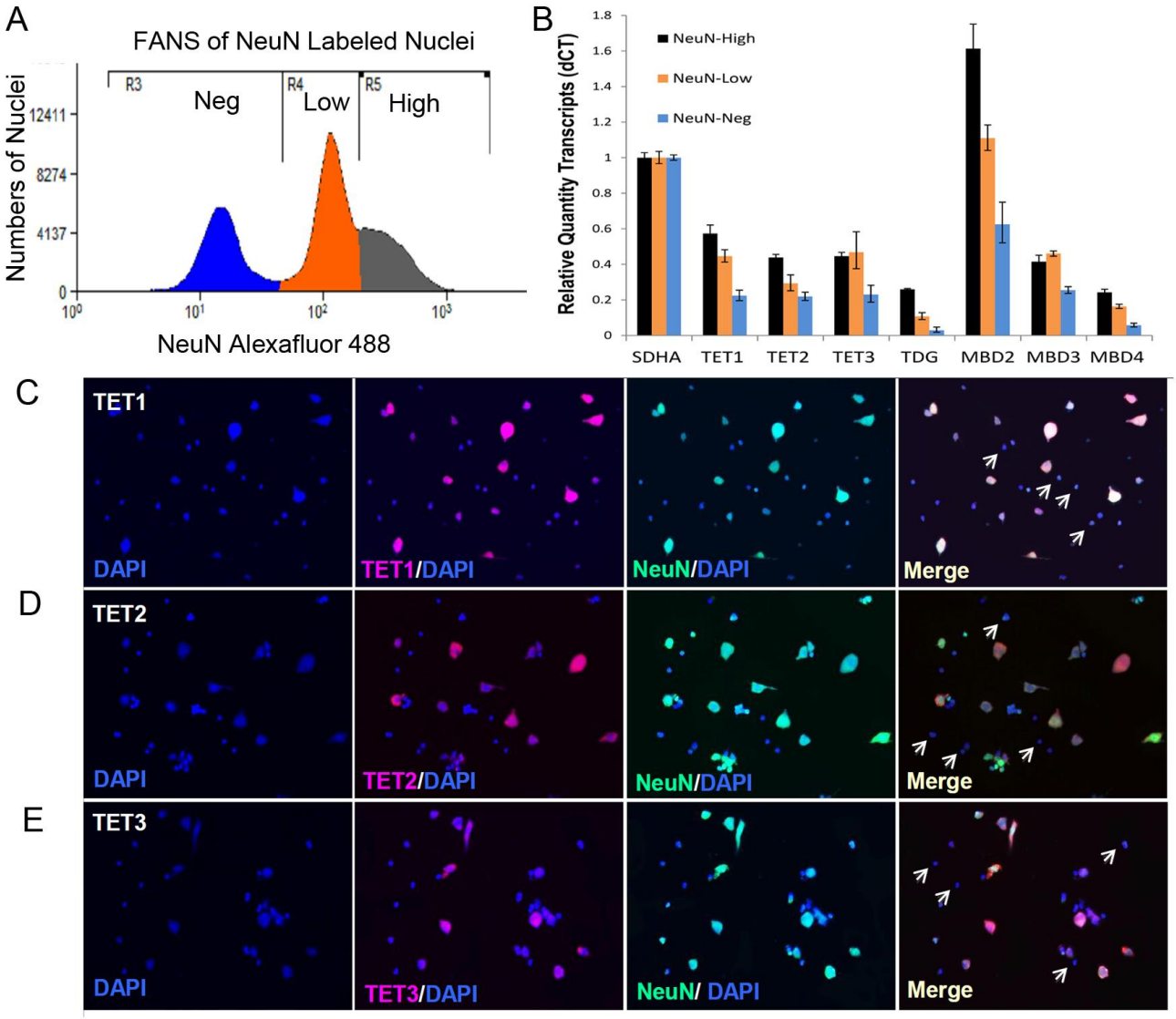
A
FANS of NeuN Labeled Nuclei
Numbers of Nuclei
12411
8274
4137
0
R3
Neg
R4
Low
R5
High
NeuN Alexafluor 488
B
Relative Quantity Transcripts (dCT)
NeuN-High
NeuN-Low
NeuN-Neg
SDHA
TET1
TET2
TET3
TDG
MBD2
MBD3
MBD4
C
TET1
DAPI
TET1/DAPI
NeuN/DAPI
Merge
D
TET2
DAPI
TET2/DAPI
NeuN/DAPI
Merge
E
TET3
DAPI
TET3/DAPI
NeuN/ DAPI
Merge

Figure 3.3. 5hmC is concentrated in the NeuN-High subset of mouse brain nuclei. A. Immunostaining of total mouse brain nuclei for 5hmC revealed that decondensed NeuN-High nuclei contained exceptionally high levels of 5hmC relative to NeuN-Low and NeuN-Neg non-neuronal cell nuclei. B. Fluorescent nuclear cytometry (FNC) identified four subpopulations of brain cellular nuclei (A, B, C, D) differing in their relative levels of NeuN and 5hmC immunostaining. We were unable to detect the levels of 5hmC in most NeuN-Neg nuclei (lower left hand quadrant). C. The percent 5hmC as a fraction of total nucleotides assayed in NeuN-Neg, NeuN-Low and NeuN-High mouse brain nuclei was measured using a commercial ELISA Kit (Zymo, Sci.).

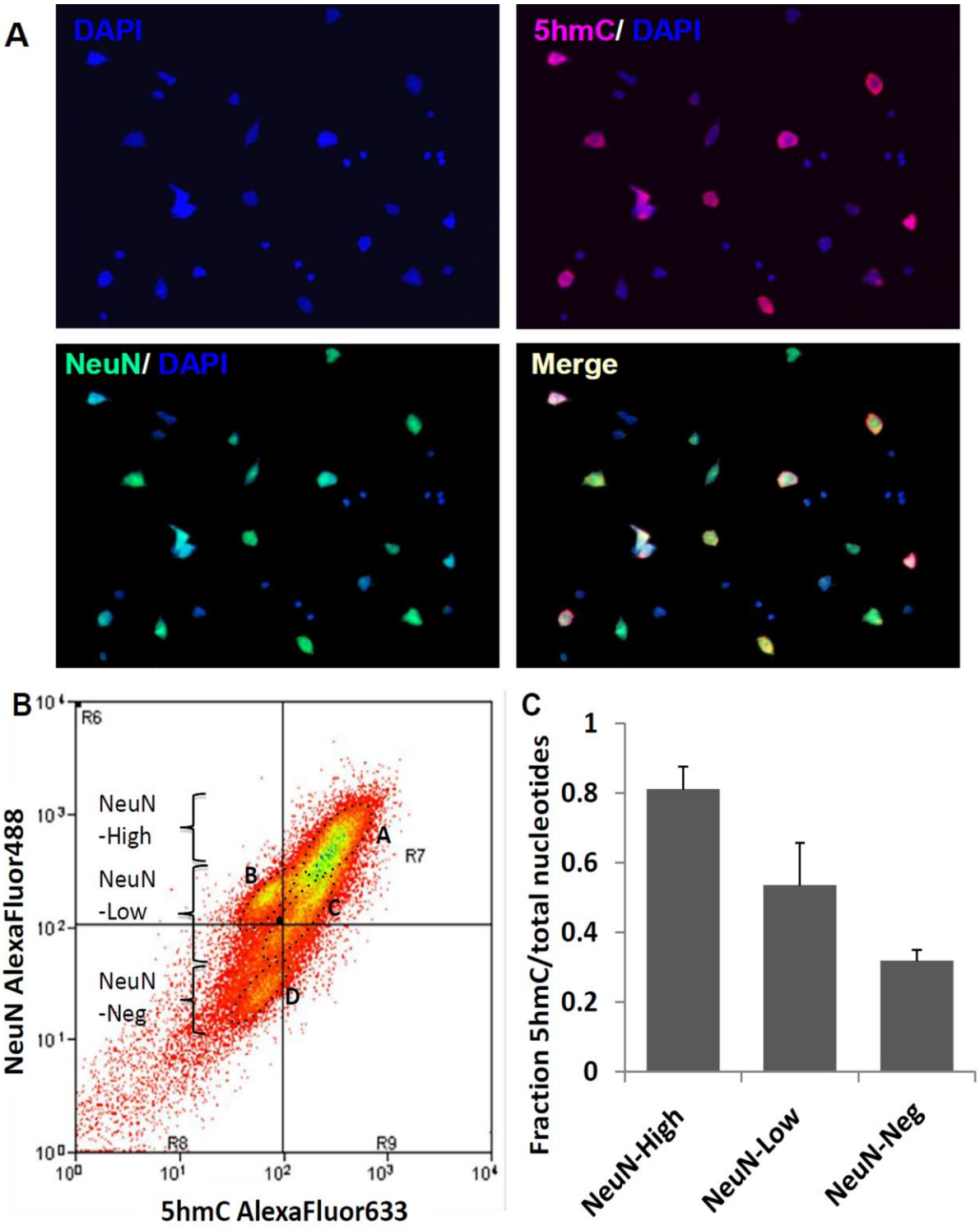
A
DAPI
5hmC/ DAPI
NeuN/ DAPI
Merge
B
R6
NeuN
-High
NeuN
-Low
NeuN
-Neg
A
B
C
D
R7
R8
R9
NeuN AlexaFluor488
5hmC AlexaFluor633
C
Fraction 5hmC/total nucleotides
NeuN-High
NeuN-Low
NeuN-Neg

Figure 3.4. Analysis of 5hmC and NeuN in the hippocampal region of the brain. Frozen coronal sections of mouse brain were co-immunostained with fluorescent antibodies to NeuN and 5hmC and examined by IFM. A & B. Overview of mouse hippocampus observed under low magnification. A. Stained with DAPI for DNA. B. Immunostained for 5hmC (see Methods). C-G. Expanded region from the hippocampus CA3 region revealed decondensed, NeuN-High mouse brain nuclei contained exceptionally high levels of 5hmC, whereas no 5hmC signal was detected in the condensed, NeuN-Neg nuclei (white arrows).

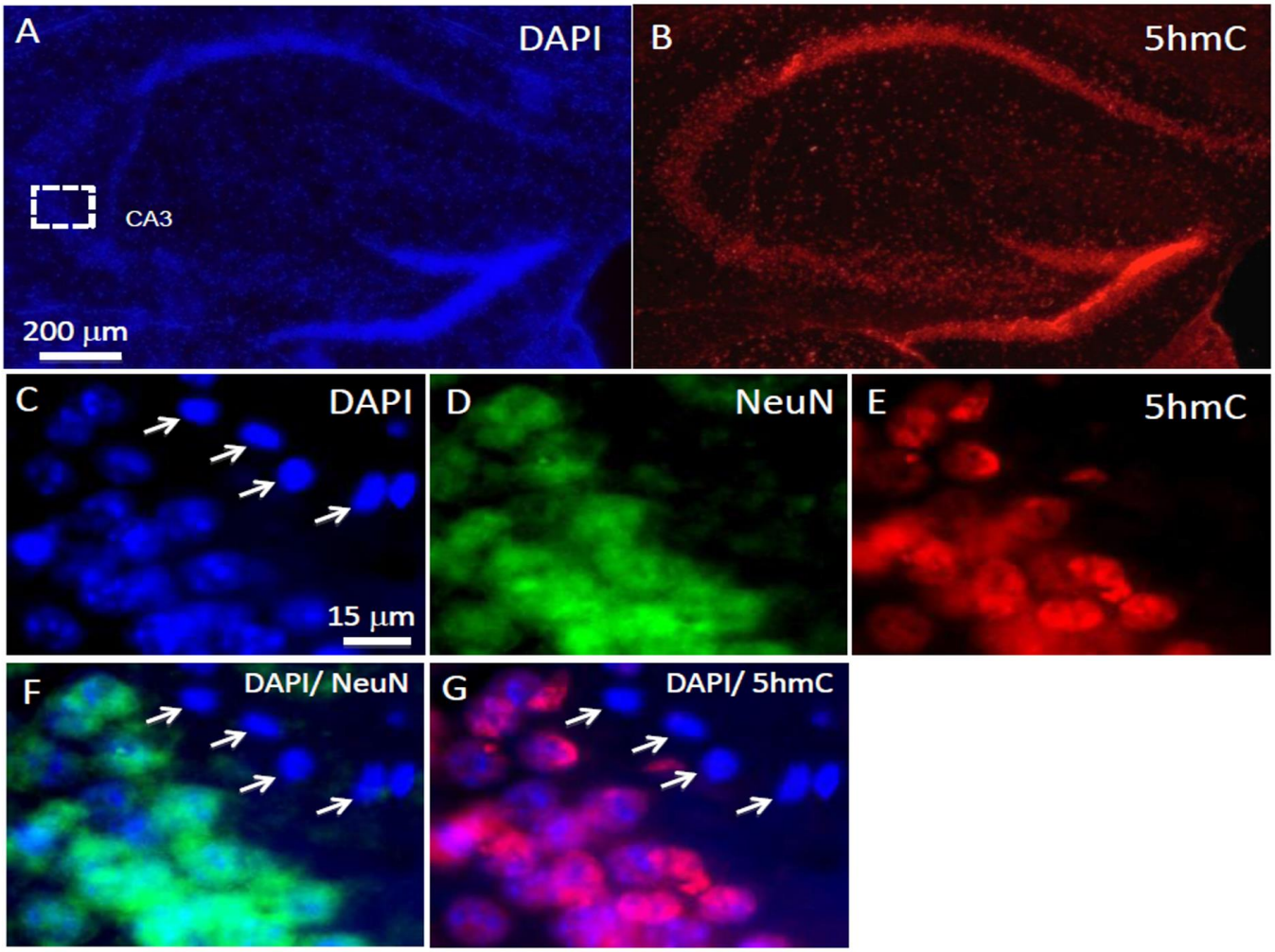
A
DAPI
CA3
200 μm
B
5hmC
C
DAPI
15 μm
D
NeuN
E
5hmC
F
DAPI/ NeuN
G
DAPI/ 5hmC

Figure 3.5. NeuN-High nuclei expressed the highest levels of 5hmC in the most highly expressed genes. **A**. Map of the DNA sequences examined. Each gene was divided into three parts: 100 kb upstream of the TSS (UTSS), gene body (GB), and 100 kb downstream of the TTS (DTTS) as defined previously (Lister and others, 2013a). Each of the three regions was divided into 20 equal-sized bins. **B**. Approximately 12,500 brain transcripts were subdivided into equal quintiles of expression level (5 of 5 the highest expression, 1 of 5 the lowest). Five plots of 5hmC levels across the 3 regions (**A**) were presented, one for each quintile of transcripts, for the three classes of mouse brain nuclei NeuN-High, -Low, and -Neg. **C.** 5hmC levels were presented for the five quintiles of transcript expression across the three gene regions (**A**) for just the NeuN-High class of nuclei.

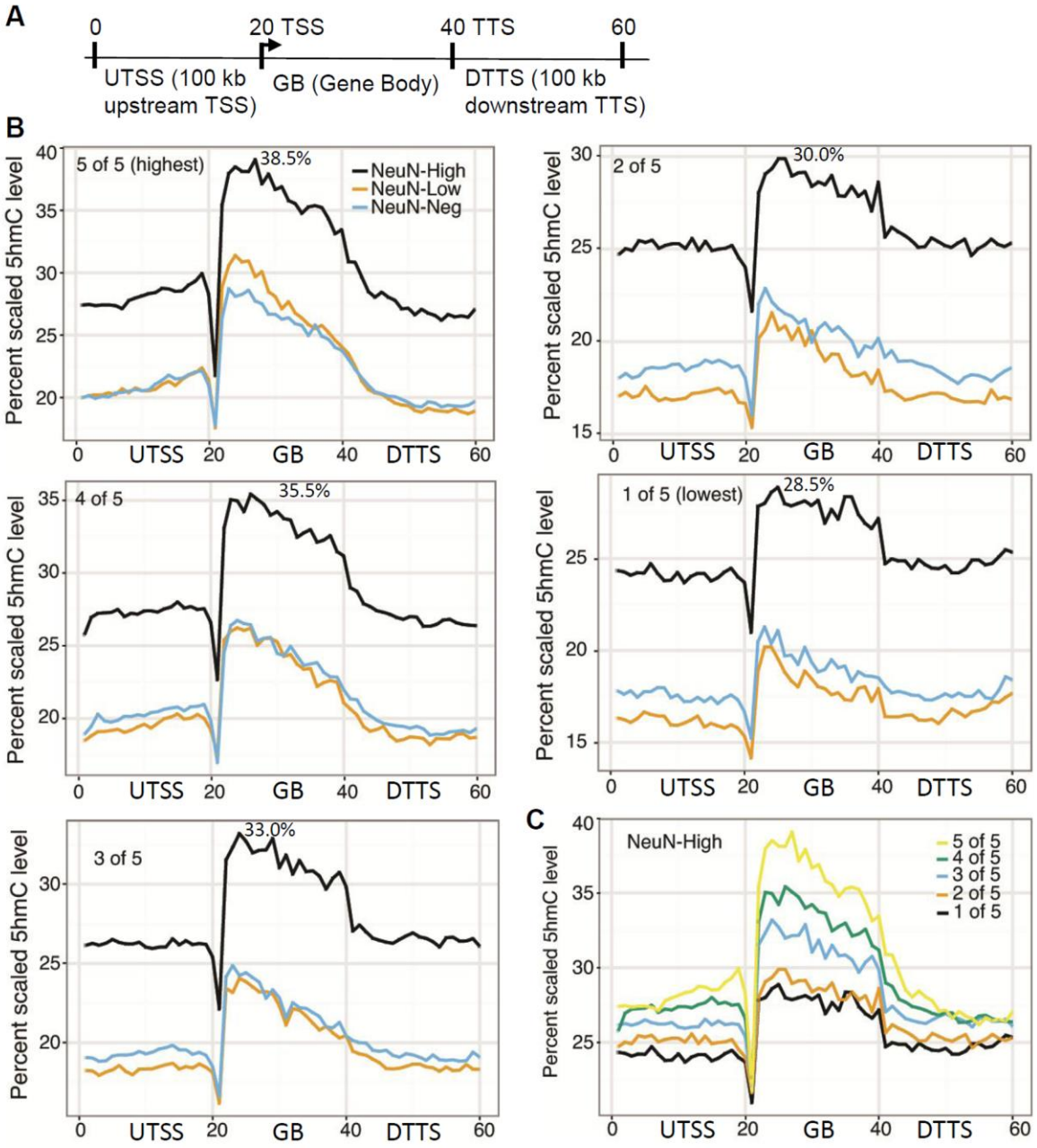
A
0
20 TSS
40 TTS
60
UTSS (100 kb upstream TSS)
GB (Gene Body)
DTTS (100 kb downstream TTS)
B
5 of 5 (highest)
38.5%
NeuN-High
NeuN-Low
NeuN-Neg
2 of 5
30.0%
4 of 5
35.5%
1 of 5 (lowest)
28.5%
3 of 5
33.0%
Percent scaled 5hmC level
UTSS
GB
DTTS
C
NeuN-High
5 of 5
4 of 5
3 of 5
2 of 5
1 of 5

Figure 3.6. Gene-region-specific distribution of 5hmCG levels for relevant GO term gene lists. The fraction of 5hmCG relative to all CG dinucleotides for three gene sequence locations (see map in Figure 3.5A) were plotted for eight GO term-based brain-specific gene lists related to neuronal and non-neuronal cell functions. Similarly plotted data for two other brain-specific gene lists and six gene lists not specific for brain function were presented in Supplemental Figure 3.S3.

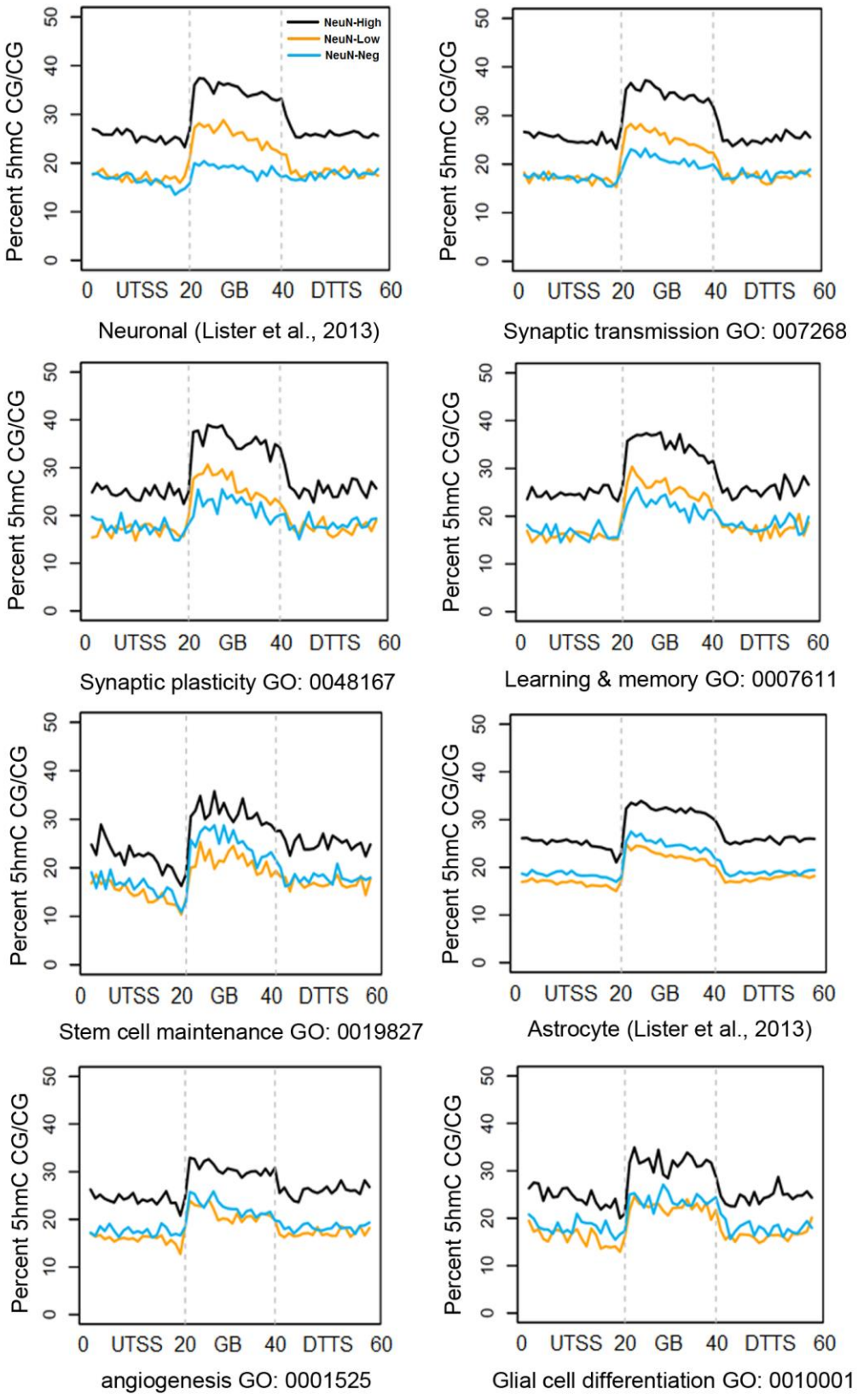
NeuN-High
NeuN-Low
NeuN-Neg
Percent 5hmC CG/CG
0 10 20 30 40 50
0 UTSS 20 GB 40 DTTS 60
Neuronal (Lister et al., 2013)
Synaptic transmission GO: 007268
Synaptic plasticity GO: 0048167
Learning & memory GO: 0007611
Stem cell maintenance GO: 0019827
Astrocyte (Lister et al., 2013)
angiogenesis GO: 0001525
Glial cell differentiation GO: 0010001

Supplemental Figure 3.S1. Validation of the commercial ELISA kit for measuring 5hmC. The fraction of 5hmC out of total nucleotides was measured using a commercial ELISA Kit (Z5411, Zymo, Sci.) in PND1 (post-natal day 1), 3-mon (3-month-old) mouse cortex, CD4+, and CD16+ human leukocytes. The kit was sensitive enough to reproducibly detected the expected difference between PND1 and 3-mon brain, but did not detect the several-fold lower levels expected in leukocytes.

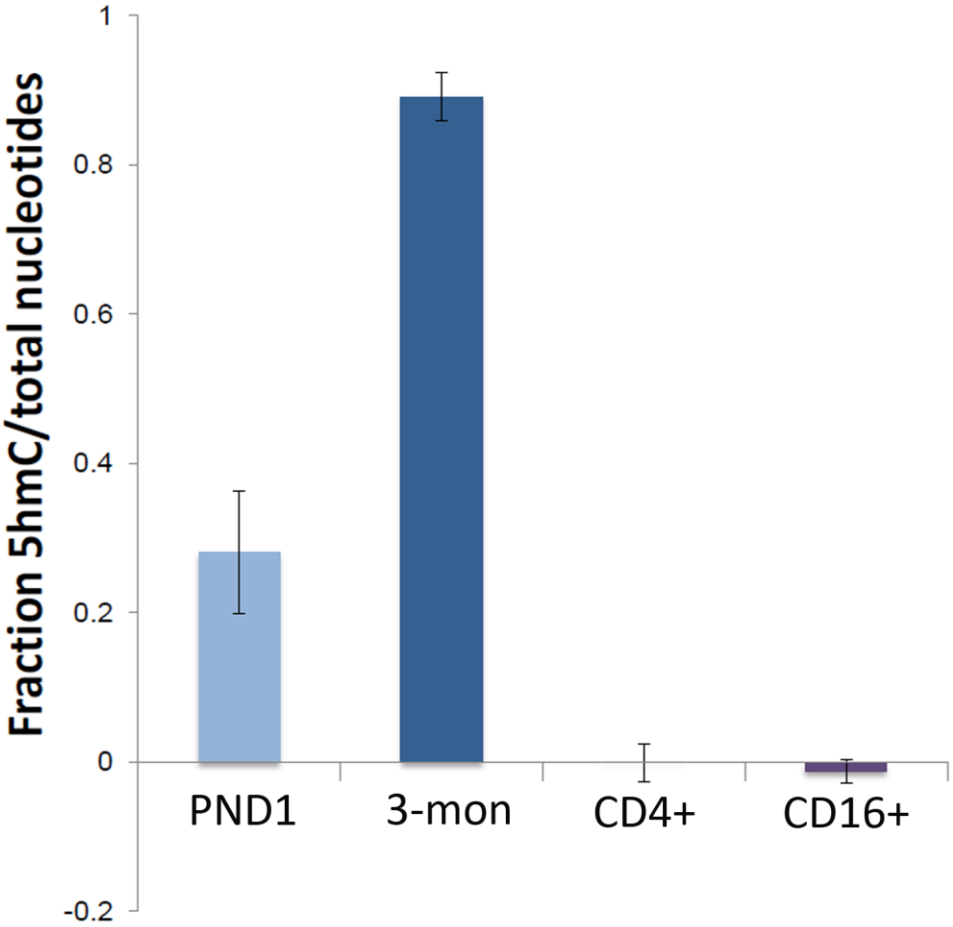

Supplemental Figure 3.S2. FANS of brain nuclei was gated for size, shape, and DNA content. During the sorting of NeuN-High, -Low and -Neg fractions of mouse brain cell nuclei. Samples were stained with DAPI for DNA content (B, gate R2) and gated for size and shape (A, forward FSC and side SSC scatter light) to eliminate small debris contaminating the nuclear preparation.

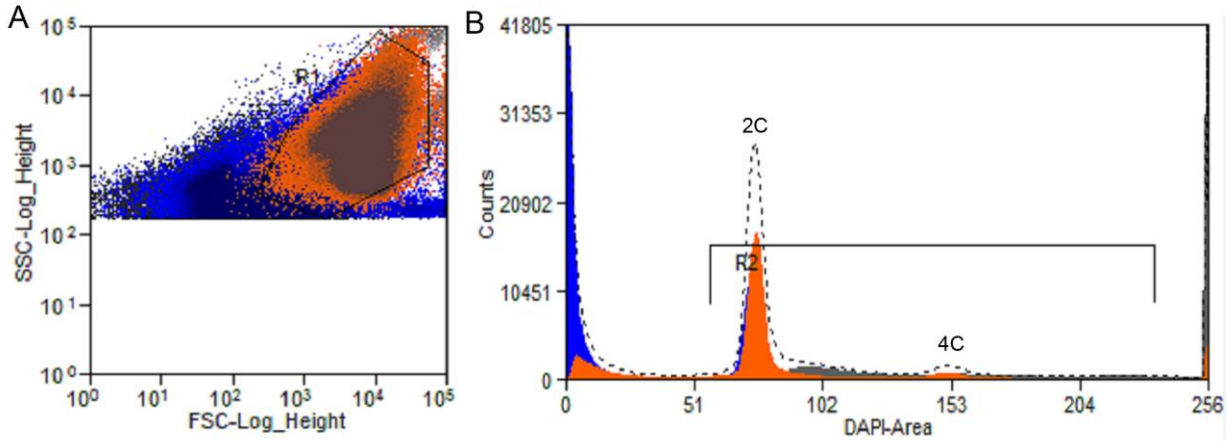

Supplemental Figure 3.S3. Gene-region-specific distribution of 5hmCG levels for additional GO term gene lists. Plotted data for two brain-specific gene lists and six gene lists not specific for brain function were presented. See legends to Figures 3.5 and 3.6.

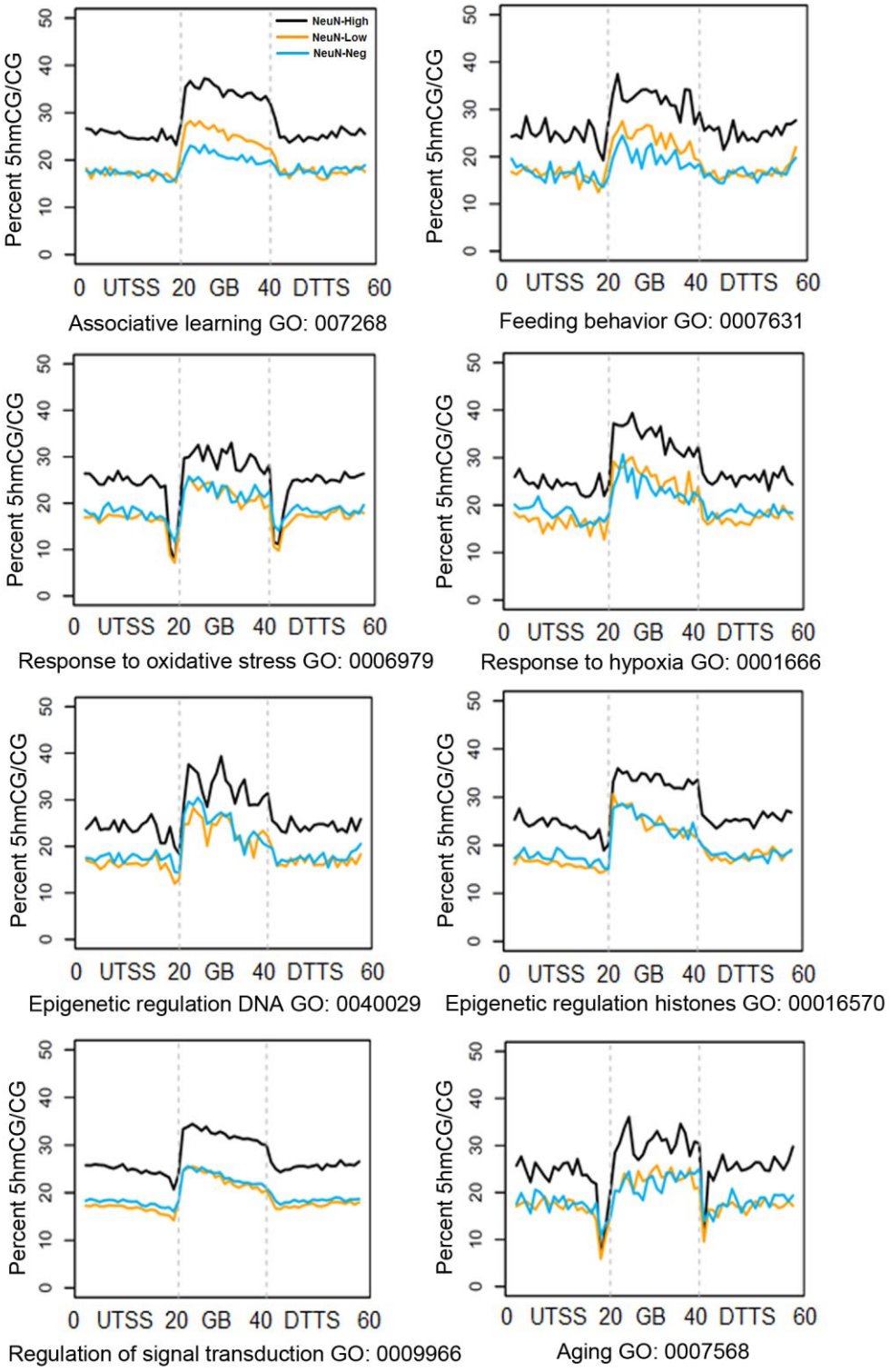
NeuN-High
NeuN-Low
NeuN-Neg
Percent 5hmCG/CG
0 10 20 30 40 50
0 UTSS 20 GB 40 DTTS 60
Associative learning GO: 007268
Feeding behavior GO: 0007631
Response to oxidative stress GO: 0006979
Response to hypoxia GO: 0001666
Epigenetic regulation DNA GO: 0040029
Epigenetic regulation histones GO: 00016570
Regulation of signal transduction GO: 0009966
Aging GO: 0007568

Supplemental Table 3.S1. Relative transcript expression levels among NeuN-High, -Low, and -Neg nuclei for factors involved in chromatin modification and brain activity.

GENE FUNCTION	RATIO of TRANSCIPT LEVELS (NeuN-High: -Low: -Neg)
Central metabolism-Endogenous control	SDHA (1:1:1) used to normalize qRT-PCR data
Chromatin-modification of DNA cytosine (this study)	TET1 (1:0.78:0.39), TET2 (1:0.76:0.51), TET3 (1:1.04:0.54)
DNA cytosine methylation	DNMT1 (1:0.33:0.22), DNMT3A (1:0.17:0.20)
Base excision repair	TDG (1:0.38:0.076), Gadd45a (1:0.08:0.07), Gadd45b (1:0.08:0.02)
Chromatin-modification of histones	SIRT1 (1:0.18:0.18), HDAC1 (1:0.05:0.02), HDAC2 (1:0.28:0.25), HDAC11 (1:0.15:0.25), KAT2B (1:0.21:0.36), KAT3A (1:0.38:0.35), KAT3B (1:0.12:0.14), KAT5 (1:0.20:0.28)
Neurogenesis & synaptogenesis	SOX2 (1:0.08:0.20), OCT4 (1:0.07:0.03), MYC (1:0.05:0.04), KLF4 (1:0.06:0.07), ARC (1:0.12:0.06), BDNF (1:0.09:0.04), EGR1 (1:0.30:0.09), HOMER1 (1:0.06:0.02)
Learning & Memory	ARC (1:0.12:0.06), BDNF (1:0.09:0.04), EGR1 (1:0.30:0.09), HOMER1 (1:0.06:0.02), NEFL (1:0.10:0.03), SYT1 (1:0.70:0.07)
Pluripotency	SOX2 (1:0.08:0.20), OCT4 (1:0.07:0.03), KLF4 (1:0.06:0.07), SHH (1:0.05:0.01), BRN2 (1:0.06:0.04), FOXG1 (1:0.11:0.12)
Cell cycle	SHH (1:0.05:0.01), PCNA (1:0.07:0.12), MYC (1:0.05:0.04)
Non-neuronal glial, lymphoid, & endothelial cell types	BLBP (1:3.10:10.25), EDNRB (1:1.35:94.02), IKZF1 (1:1.13:28.31), PDGFR (1:1.65:23.67)

TET and TDG transcripts levels compared to other marker transcripts involved in modifying DNA cytosine in three classes of brain nuclei. SDHA was the normalization control for determining relative quantities (RQ). Then the data were renormalized to the levels of transcript in NeuN-High nuclei. The ratio of transcript levels is expressed in the right hand column. The bulk of these data come from Yu et al., 2015 (Yu and others, 2015).

Supplemental Table 3.S2. qRT-PCR primers used in this study.

sense		antisense	
SDHA	CTCTTTCCTACCCGATCACATAC	SDHA	CCATCTCCAGTTGTCCTCTTC
TET1	CTGAAGATGACAAGCAGCAAAC	TET1	GGTGTGTGTCAGTGGGTAAA
TET2	CTCATGCCTCGGGTTCATATT	TET2	CTGGCACACTCCCATTGTAT
TET3	CTTCCCTCCTTTGGCTACTATG	TET3	GAGGTCTGGCTTCTTCTCAAA
TDG	CCACGAATAGCGGTGTTTAATG	TDG	GAGTTTCTGTGTCTGGGATCTT
MBD2	TGGCAAGATACCTGGGAAATG	MBD2	GGAGTCTCTGCTTGTTCTTCTG
MBD3	CACAACTGGCACGTTACCT	MBD3	CACGCTGGCGACTCTTATT
MBD2	AGACACGAAGCAAGTGGAAA	MBD2	AAGCAAGCCGAGTTAGAGTTAG

Sense and antisense primer sequences used in qRT-PCR were presented.

Supplemental Table 3.S3. Additional data on TAB-seq analysis and an estimate of genome coverage.

Sample	Mapped reads		Lambda						pUC19 (5hmC)			Genome coverage
			CpG sites (5mC)			Non-CpG sites						
	number	%	methylated Cs	mapped Cs	%	methylated Cs	Mapped Cs	%	methylated Cs	mapped Cs	%	
NeuN-High	8,548,790	39.28%	2,943	301,536	0.98%	6,623	928,338	0.71%	1,172	2,201	53.2%	0.37
NeuN-Low	8,987,367	42.93%	4,180	413,257	1.01%	9,126	1,239,697	0.74%	1,519	2,900	52.4%	0.39
NeuN-Neg	9,353,292	41.66%	4,163	414,985	1.00%	9,341	1,236,783	0.76%	946	2,228	42.5%	0.40

The genome coverage achieved by our TAB-seq analysis was listed in the last column as a fraction of coverage of the mouse genome (GRCm38).

Supplemental Table 3.S4. GO terms used and the number of genes in each term.

GO Term	GO Number	Number of Genes	Definition
Aging	GO:0007568	138 genes	Age-dependent behavioral decline, age-dependent general metabolic decline, cell aging, multicellular organismal aging, organ senescence
angiogenesis	GO:0001525	400 genes	Angiogenesis involved in coronary vascular morphogenesis or wound healing, glomerular capillary function, negative and positive regulation of, patterning of blood vessels, sprouting angiogenesis, etc.
associative learning	GO:0008306	82 genes	Conditioned place preference, conditioned taste aversion, olfactory learning, visual learning
cell cycle	GO:0007049	1374 genes	Cell cycle process, meiotic cell cycle, mitotic cell cycle
DNA replication	GO:0006260	254 genes	Cell cycle DNA replication, DNA synthesis involved in, DNA-dependent, negative and positive regulation of, RNA-dependent, etc.
feeding behavior	GO:0007631	115 genes	Adult feeding behavior, conditioned taste aversion, drinking and eating behavior, larval feeding behavior, negative and positive regulation of, etc.
glial cell differentiation	GO:0010001	175 genes	Astrocyte differentiation, glial cell development and fate commitment, microglia differentiation, oligodendrocyte differentiation, positive and negative regulation of, Schwann cell differentiation, etc.
histone modification	GO:0016570	374 genes	Histone acetylation, biotinylation, citrullination, deacetylation, demethylation, dephosphorylation, deubiquitination, H3-K9 modification, methylation, peptidyl-prolyl isomerization, phosphorylation, ubiquitination; negative and positive regulation of, etc.
learning or memory	GO:0007611	219 genes	The acquisition and processing of information and/or the storage and retrieval of this information over time.
neurogenesis	GO:0022008	1377 genes	Generation of neurons, gliogenesis, negative and positive regulation
neuron differentiation	GO:0030182	1166 genes	Differentiation of many cell types, negative and positive regulation of, neuron development, neuron fate commitment, etc.
regulation of gene expression, epigenetic	GO:0040029	222 genes	DNA methylation and demethylation, negative and positive regulation of, posttranscriptional gene silencing, etc.
regulation of signal	GO:0009966	2313 genes	Many signaling pathways, adaptation of signaling pathways, negative and positive

transduction			regulation of, etc.
regulation of synaptic plasticity	GO:0048167	141 genes	Long term synaptic depression and potentiation, positive and negative regulation of, regulation by chemical substance, etc.
response to hypoxia	GO:0001666	169 genes	Any process that results in a change in state or activity of a cell or an organism (in terms of movement, secretion, enzyme production, gene expression, etc.) as a result of a stimulus indicating lowered oxygen tension.
response to oxidative stress	GO:0006979	311 genes	Age-dependent and cellular responses to oxidative stress, detection of, positive and negative regulation of, response to hydroperoxide, response to photooxidative stress, response to ROS.
stem cell maintenance	GO:0019827	146 genes	Germ-line stem cell maintenance, negative and positive regulation of, neuronal stem cell maintenance, somatic stem cell maintenance, etc.
synaptic transmission	GO:0007268	528 genes	Negative and positive regulation of; neuron-neuron, neuromuscular, and cholinergic synaptic transmission; neurotransmitter receptor metabolic process; regulation of postsynaptic membrane potential; regulation of synapse maturation; synaptic vesicle transport; etc.
Neuronal*		461 genes	
Astrocyte*		2249 genes	

GO terms used in this study and detailed information can be found at Mouse Genome Informatics database at **(**http://www.informatics.jax.org).

* Neuronal and Astrocyte GO Terms contains 461 genes and 2249 genes, and the gene list can be found in (Lister and others, 2013a).

CHAPTER 5

SUBSETS OF VISCERAL ADIPOSE TISSUE NUCLEI WITH DISTINCT LEVELS OF 5-HYDROXYMETHYLCYTOSINE[3]

[3] Ping Yu, Lexiang Ji, Kevin J. Lee, Miao Yu, Chuan He, Suresh Ambati, Elizabeth C. Mckinney, Crystal Jackson, Clifton A. Baile, Robert J. Schmitz, Richard B. Meagher. Accepted by *PLoS ONE*. Reprinted here with permission of publisher, 04/28/16.

Abstract

The reprogramming of cellular memory in specific cell types, and in visceral adipocytes in particular, appears to be a fundamental aspect of obesity and its related negative health outcomes. We explored the hypothesis that *adipose tissue contains epigenetically distinct subpopulations of adipocytes that are differentially potentiated to record cellular memories of their environment*. Adipocytes are large, fragile, and technically difficult to efficiently isolate and fractionate. We developed fluorescence nuclear cytometry (FNC) and fluorescence activated nuclear sorting (FANS) of cellular nuclei from visceral adipose tissue (VAT) using the levels of pan-adipocyte protein, peroxisome proliferator-activated receptor gamma-2 (PPARg2), to distinguish classes of PPARg2-Positive (PPARg2-Pos) adipocyte nuclei from PPARg2-Negative (PPARg2-Neg) leukocyte and endothelial cell nuclei. PPARg2-Pos VAT nuclei showed 2- to 50-fold higher levels of transcripts encoding most of the chromatin-remodeling factors assayed, which regulate the methylation of histones and DNA cytosine (e.g., *DNMT1, TET1, TET2, KDM4A, KMT2C, SETDB1, PAXIP1, ARID1A, JMJD6, CARM1, and PRMT5*). PPARg2-Pos nuclei have a large decondensed chromatin structure. TAB-seq demonstrated 5-hydroxymethylcytosine (5hmC) levels were remarkably dynamic in gene bodies of PPARg2-Pos nuclei, dropping 3.8-fold from the highest quintile of expressed genes to the lowest. In short, VAT-derived adipocytes appear to be more actively remodeling their chromatin than non-adipocytes.

Key words: cytometry, 5hmC, TAB-seq, epitype, chromatin, cell-type-specific

Introduction

There is a critical need to perform cell-type-specific epigenetic analyses of adipocytes within adipose tissues, because of their likely direct role in obesity and its comorbidities, including tissue inflammation, many cancers, cardiovascular disease, Type II Diabetes, and Alzheimer's. Epigenetic controls function at the level of specific cell types, and yet, the vast majority of published epigenetic studies examine chromatin structures (i.e., epitypes) of whole organs or tissues (e.g., adipose tissue) and most commonly whole blood. These aggregated results from mixtures of cell types, however, do not accurately capture the real biology of specific cell types, which is essential to understand for designing improved therapies. For example, Reinius et al., 2012 (Reinius and others, 2012a) examined the DNA cytosine methylation profiles for seven purified blood leukocyte cell types in healthy individuals. They found that the DNA methylation profile (epitype) of each cell type varied significantly from that of whole blood. Pairwise comparisons of the seven leukocyte types varied at 9.5% to 40% of the 485,000 cytosine methylation sites assayed. Because the epitype of peripheral white blood cells is the weighted average of methylation differences among cell types, whole blood data has relatively weak statistical significance. The results from two studies examining the link between gene-specific DNA cytosine methylation at CG dinucleotides and systemic lupus erythematosus (SLE) highlight the need for cell- type-specific analyses. While whole blood DNA produced median p values of 10^{-3} for some methylation sites associated with SLE, the methylation data from CD4+ T cells resulted in median p values of 10^{-7} for numerous sites associated with SLE (Javierre and others, 2010; Jeffries and others, 2011). Hence, most of these latter data are statistically and most likely biologically significant. Our technical goal herein was to *enable the*

cell-type-specific epigenetic analysis of adipocyte populations from within adipose tissues, and thereby obtain more biologically relevant data on chromatin structures.

The diversity of cell types in adipose tissue complicates attempts at cell-type-specific analysis. In addition to various classes of preadipocytes as well as maturing and mature adipocytes, adipose tissue is rich with blood vessels, endothelial cells and numerous lymphoid cell types (e.g., T cells, neutrophils, and natural killer cells) (Deiuliis and others, 2011a; Elbatarny and others, 2007; Lumeng and others, 2011a; Lumeng and Saltiel, 2011a; Spencer and others, 2011; Wozniak and others, 2009b). Furthermore, obese adipose tissue cell populations are different from lean ones. The pathology of obesity results in more mesenchymal stem cells (MSCs) being directed to develop into white adipocytes and the enlargement of existing adipocytes (Catalan and others, 2012; Cristancho and Lazar, 2011; Rocha and Folco, 2011; Schipper and others, 2012; Spencer and others, 2011). Larger numbers of T lymphocytes and neutrophils infiltrate adipose tissue in obese individuals relative to lean individuals (Bourlier and others, 2008; Hagman and others, 2012; Kintscher and others, 2008). Immunocytochemistry reveals individual obese adipocytes surrounded by several-fold larger numbers of inflammatory leukocytes than surrounding lean adipocytes (Deiuliis and others, 2011a; Lumeng and others, 2011a; Lumeng and Saltiel, 2011a). Because any analysis of chromatin modification from adipose tissue would represent a weighted average of the various cell types, changes in the ratios of adipocyte subpopulations and non-adipocyte cell types would compromise conclusions about epigenetic reprogramming and disease.

White adipocytes may be enzymatically dissociated from adipose tissues, but they are difficult to isolate efficiently because of their large size (50 to 200 μm) and tendency to lyse rapidly during manipulation or brief storage (Wei and others, 2013). Fluorescence activated cell

sorting (FACS) has been used to fractionate dissociated adipocytes, but the large cell sizes require special instrumentation to prevent clogging and slow flow rates (Song and others, 2015). Furthermore, very few immunochemical surface markers are available that distinguish subsets of adipocytes. Several technical approaches have been applied to increasing the cell-type-specificity of epigenetic studies for cell types that are difficult to isolate, but these too have their limitations. For example, great improvements have been made in laser-capture micro-dissection (LCM) technologies, yet, relatively small numbers of cells are recovered and tissue processing can be time consuming and expensive (Arend and others, 2013; Hackler and others, 2012; Merbs and others, 2012a). Model organisms may be engineered for the Isolation of Nuclei Tagged in Specific Cell Types (INTACT), but transgenic animals are expensive to make and maintain and INTACT cannot be applied diretly to isolate human cellular nuclei (Deal and Henikoff, 2010b; Henry and others, 2012). As an alternative, Fluorescent Nuclear Cytometry (FNC) and Fluorescence Activated Nuclear Sorting (FANS) have been used to compare the transcriptome, epigenome, and proteome among classes of brain cellular nuclei (Bilsland and others, 2006b; Chen and others, 2013; Dammer and others, 2013b; Okada and others, 2011a). For example, using FANS we recently characterized a subset of neuronal cellular nuclei that were decondensed and expressed exceptionally high levels of stem cell and cell cycle neurotrophic, synaptotropic, and chromatin modifying factors markers, relative to the majority of neuronal and non-neuronal nuclei (Yu and others, 2015). Overexpression of this machinery may be associated with the rapid turnover of chromatin modifications in cell types most likely to be potentiated to respond to their environment and more rapidly record cellular memories (Meagher, 2014). Using FNC and FANS to study cellular nuclei as surrogates for isolated cells is still in its infancy, but these technologies are relatively simple to employ for “problematic tissues” and

have the potential to reveal a great deal about epigenetically distinct cell populations within adipose tissues.

There is mounting evidence that adipocytes within adipose tissues may be epigenetically programmed in response to obesity, obesity-related diseases, exercise, diet, and sleep, as well as when adipocytes exit from the cell cycle and proceed through adipogenesis (Inagaki and others, 2015; Keller and others, 2014; Khalyfa and others, 2014; Lewis and others, 2013; Ronn and others, 2013; Wang and others, 2013; Zhang and others, 2011). Our long-term working hypothesis is that *adipose tissue contains epigenetically distinct subpopulations of adipocytes, which are differentially potentiated to record cellular memories*. However, there is currently limited information about subpopulations of adipocytes from within tissue or their mechanisms of cellular memory. A number of nucleosomal histone side chain modifications as well as modifications to DNA cytosine residues are correlated with the adipogenic program and postulated to play a role in programming preadipocytes and mature adipocytes (see Discussion). Of particular interest is the recent evidence that gene-region- and enhancer-region-specific 5-hydroxymethylcytosine (5hmC) at CG dinucleotides may define genes poised to change their expression or already having increased expression in part through localized loss of 5mC (Lister and others, 2013a; Pastor and others, 2011). During the *in silico* differentiation of 3T3-L1 preadipocytes to adipocytes there is 2-fold increase in 5hmC levels in activated vs. repressed gene regions and as much as a 10-fold increase in 5hmC in the fatty acid binding protein 4, *FABP4* gene (Serandour and others, 2012b). Hence, the oxidation of 5mC to 5hmC is strongly associated with adipogenesis.

The cyclic turnover of 5 ´-modified cytosine is summarized in **Figure 4.1**. DNA methyltransferases (DNMTs) methylate DNA cytosine to 5mC, while Ten-eleven translocation

methylcytosine dioxygenases (TETs) catalyze its conversion to 5hmC and to other more oxidized forms (5fC, 5caC). Thymine-DNA glycosylase (TDG) acts on 5fC or 5caC to generate an abasic site (-OH). The base excision repair pathway (BER) and factors like the GADD45s recognize a G residue in the antiparallel DNA strand and restore cytosine. In general, 5hmCG dinucleotides mark a small subset of antiparallel CGs, which may or may not also be 5mC modified (5mCGs) in the antiparallel strand, such that increases in one of these two modifications at a site is not always correlated with the loss of the other. TET dioxygenase-catalyzed oxidation of 5mC to 5hmC at constitutive CTS (CTCF binding sites) and PPARg enhancers (PPAREs) appears to be part of and perhaps may be essential to adipogenesis (Dubois-Chevalier and others, 2014; Dubois-Chevalier and others, 2015). The ADP-ribose polymer attached to parylated-PPARg binds TET enzymes to catalyze the localized conversion of 5mC to 5hmC (Fujiki and others, 2013), which begins to outline a mechanism connecting 5hmC modification and adipogenesis. Enhancer cytosine hydroxymethylation appears to be tissue-specific, where it acts on adipocyte-specific enhancers during a 3T3-L1 cell's differentiation to an adipocyte and on neuronal-specific enhancers during neurogenesis in a cultured neural progenitor cell type (Serandour and others, 2012b). Little is known about the precise role of gene-region distribution and changes in 5hmC in adipocytes, although in neurons it has been proposed that high levels of gene-region 5hmC "*creates pre-modified sites that are poised for subsequent demethylation and activation at a later developmental stage*" prepared for "*on demand gene regulation*" (Irier and others, 2014; Lister and others, 2013a).

Initial pioneering studies suggested that large-scale gene silencing by DNA methylation might be essential to the commitment to adipogenesis. The differentiation to lipid body-rich mature adipocytes proceeds after preadipocytes exit the cell cycle (Guo and others, 2009). Two

days after the differentiation of 3T3-L1 cells begins global DNA cytosine methylation levels increase, as do 5mC levels at the C/EBP alpha promoter region (Guo and others, 2009). DNA methyltransferase DNMT1 levels increase rapidly during the first 24 hours after inducing differentiation (Londono Gentile and others, 2013) and decline later as mature adipocytes are formed. But DNMT1 is defined as a maintenance enzyme, not a de novo methyltransferase. Hence, DNMT1 levels may account for the increase in 5mC by more efficiently maintaining methylation and by supporting increases in de novo methylation. Small interfering RNA silencing of the de novo cytosine methyltransferase DNMT3a in 3T3-LI preadipoctyes significantly blocks adipogenesis (Guo and others, 2009) again emphasizing a positive role for DNA methylation. However, additional work stands against this simple positive role for increased global 5mC levels in adipogenesis. Small RNA silencing of the maintenance methyltransferase DNMT1 in 3T3-L1 preadipocytes accelerates adipogenesis (Londono Gentile and others, 2013). In addition, treating bone marrow derived MSCs, a normal precursor of adipocytes, with 5-azacytidine (5-azaC), a cytidine analog and inhibitor of methyltransferases, decreases both cell proliferation and differentiation into adipocytes and results in concomitant down-regulation of PPARg (Zych and others, 2013). Finally, treating atrial cardiac cells with 5-azaC, an inhibitor of all DNMT activity, reduces 5mC to produce an interesting outcome, wherein these cells trans-differentiate into lipid body-containing adipocytes (Kaur and others, 2014). Among the likely possibilities that might explain these complex results, the starting epitype of the progenitor cell undoubtedly affects their developmental potential, as does their existing chromatin modification machinery. Additionally, the C-residue sequence specificity and regulation of the cytosine modification cycle will affect the genes being altered and the developmental outcome. Hence, the role of the DNA cytosine modification cycle appears distinct

during stem cell differentiation into preadipoctyes, during adipogenesis, and in mature adipocytes. The roles of 5mC are more complex than simply removing its silencing effects on appropriate adipogenic gene-regions and enhancers. In any case, we focused on the formation of 5hmC, because it appears to be the rate-limiting step in removing 5mC at CG dinucleotides and hence rate limiting to the turnover of modified cytosine.

Herein, we extend FNC and FANS to the analysis of adipocyte nuclei within adipose tissue. We developed techniques to rapidly isolate cellular nuclei from fixed adipose tissue, such that both nuclear structure and chromatin modification would be preserved. We showed that cytometry was easily applied to characterize subpopulations of adipose tissue nuclei. Nuclear sorting identified subpopulations of adipocyte and non-adipocyte nuclei that differentially expressed a significant fraction of the epigenetic machinery we assayed. Adipocyte nuclei were identified that had highly elevated levels of factors involved in the regulation of histone methylation and DNA cytosine modification, and in particular displayed widely divergent levels of 5-hydroxymethylcytosine (5hmC) across the gene body of different groups of genes.

Materials and Methods

Sus scrofa tissues

Animals (*Sus scrofa* 6 month old, 220-280 lbs) were slaughtered at UGA's abattoir. UGA abattoir was USDA licensed and collection at UGA abattoir had IACUC approval. All institutional and USDA guidelines for the care and use of animals were followed. Fresh kidney-associated visceral adipose tissue (VAT) was harvested and chilled on ice for no more than 2 h prior to being processed to purify nuclei or flash frozen in liquid nitrogen and stored at -80°C.

Protocol for isolating cellular nuclei from adipose tissue

The following rapid protocol for isolating cellular nuclei from adipose tissue is an extension of the simplified method described recently for brain cell nuclei (Yu and others, 2015). Freshly dissected and minced adipose tissue was treated for 1 hour at RT to 2 months at 4°C in four volumes (w/v) of 0.3SPBSTA (0.3 M Sucrose in PBSTA, 20 mM KH_2PO_4, 20 mM Na_2HPO_4, pH = 7.2, 137 mM NaCl, 3.0 mM KCl, 0.1% Triton X 100, 0.1% sodium azide), plus 3.7% freshly added formalin. The protocol works on fresh tissue, but the yield of nuclei is lower than for fixed. The fixed tissue is heated briefly to 60°C to solubilize the fat (5 to 10 min depending upon the sample size). Typically 50 g of tissue was homogenized in a prewarmed (60°C water) Polytron (Fischer Sci) for 2.5 min at a setting of 6.5 in 8 volumes (w/v) of 0.3SPBSTA. The homogenate was filtered through large pieces (10 in. sq.) of Miracloth (Calbiochem, #475855) stretched loosely over a funnel. This filtration step prevented nuclei from being trapped with large pieces of cytoplasmic debris during the subsequent centrifugation and increased the yield of nuclei several fold. The filtrate was placed in centrifuge bottles or tubes and under-layered with 0.25 volumes of 1.4 M sucrose in SPBSTA. Nuclei were centrifuged in a pre-chilled rotor (4°C) through the sucrose cushion at 3,000xg for 20 min. The supernatant was removed gently by pouring it out from one of two holes made through the hardened fat layer. The nuclear pellet under the fat floatation pellet was gently re-suspended in with 0.3M SPBSTA. 3-5 ml aliquots were pressed slowly through 25 mm diameter Swinnex Nylon Net Filters with a 41-μm pore size (EMD Millipore). The yield of nuclei from freshly fixed VAT tissue was approximately 1.0 x 10^6 nuclei/g tissue and a few-fold less from frozen tissue fixed subsequent to thawing. Nuclei were stored for up to one year at 4°C in PBSTBA (PBS + 0.1% Triton X-100 + 5% BSA + 0.02% Azide) and freshly added 4% formaldehyde. Storage did not seem to alter the

quality of immunofluorescence staining for several markers assayed, but storage for more than three months did lower the yield of RNA. All reagents were purchased from Thermo Fisher (Waltham, MA), unless stated otherwise. In various experiments, this protocol has been scaled from 50 g to 50 mg of VAT, and these differed only in that the heat treatment may be omitted prior to homogenizing very small samples. This isolation protocol worked similarly, but with slightly lower yield than when using fresh unfixed or -80°C frozen adipose tissue that was immediately fixed after thawing. The protocol has worked as well with rat and mouse VAT, SAT, and BAT as it did with porcine VAT and SAT.

IFM, FNC, and FANS analysis of nuclei

Immunochemical labeling of nuclei followed exactly the protocol used for brain nuclei (Yu and others, 2015). For FNC 100,000 to 400,000 nuclei were incubated in 200µl blocking solution with primary antibodies (**Supplemental Table 4.S1**) at dilutions of 1:100 to 1:500 w/v for 1 h at room temperature. For FANS, where as many as 100-times more total nuclei were labeled in small volumes, the antibody concentration was much higher and was estimated based on the number of nuclei being examined (0.5 to 1.0 ug antibody per 10^6 nuclei) and not based on the volume of buffer. In a typical FANS experiment, 15 µg of rabbit polyclonal antibody to PPARg2 (ab45036) was incubated with 20 x10^6 nuclei in 500 ul blocking solution for 1 hr. After 3 washes with PBSTBA samples were co-stained with DAPI or propidium iodide (PI) at 20 µg/ml for 30 min. Photographic images of nuclei and tissue sections were made on a Leica TR600 epifluorescence microscope using a Hamamatsu ORCA-CR camera and Hamamatsu SimplePCI Image Analysis software to process images and measure nuclear areas and fluorescence intensities.

FNC and FANS were conducted as described previously (Yu and others, 2015). The nuclear population was first gated for size and shape (**Supplemental Figure 4.S1A**) and DNA content (**Supplemental Figure 4.S1B**) to reduce the number of contaminating particles sorted. The fraction of 4C nuclei appeared low to undetectable in most VAT nuclear preparations, but there was a large percentage of nuclei that showed higher than 2C staining with DAPI. This signal may result from decondensed nuclei that have a very high RNA content, because DAPI has a modest fluorescence enhancement with dsRNA (Tanious and others, 1992) as was observed for decondensed brain nuclei (Yu and others, 2015). No significant population of doublet nuclei was detected during sorting (**Supplemental Figure 4.S1C**), and therefore, a doublet gate was not applied so as not to discriminate against large decondensed nuclei (Yu and others, 2015). Furthermore, a pulse-width gate was not applied because of the concern that it might eliminate some very large decondensed nuclei that were of interest to this research. Figures of FNC and FANS data were prepared using FlowJo Software version 9.7.6 (Treestar, Inc. Ashland, Oregon).

RNA, cDNA, and qRT-PCR

RNA from formalin-fixed nuclei was prepared and reverse transcribed into cDNA for qRT-PCR analysis as described previously (Yu and others, 2015). Primers are listed in **Supplemental Table 4.S2**. Multiple primer pairs were designed and assayed for each porcine target RNA and only those showing efficient amplification of product from total VAT RNA were selected. The primer pairs selected also had a product dissociation curve with only one peak (i.e., only one cDNA was amplified). Among several commonly used control transcripts that were examined (Vandesompele and others, 2002), *β-actin* and *RPL13* were found to be relatively equivalently expressed among the four nuclear fractions, when qRT-PCR assays were normalized for

equivalent cDNA input. Hence, these two were suitable as endogenous controls. Each assay was run in triplicate and the Relative Quantity (RQ) of transcript was calculated based on the dCT method, including the standard deviation from the mean (Livak and Schmittgen, 2001). We were unable to find *bona fide MBD4* or *TDG* sequences in the porcine genome database, and hence their transcripts were not assayed by qRT-PCR.

TAB-seq and Quintile Expression Data

DNA sample preparation. DNA was isolated from sorted PPARg2-High, pooled PPARg2-Med & -Low, and PPARg2-Neg porcine kidney VAT nuclei (~2 to 4 x 10^6 nuclei per sample) using a DNeasy kit (Qiagen, Frederick, MD, USA #69504) according to the manufacturer's recommendations. A heat treatment of 90°C for 1 h was included, after the proteinase K digestion, to hydrolyze off the formalin. DNA was quantified using a Qubit 2.0 Fluorometer (Invitrogen) with the Qubit dsDNA Assay Kit (Life Technologies # Q32853). TET-assisted bisulfite sequencing (TAB-seq) was performed as we previously described (Yu and others, 2012a). 0.5 ng of methyltransferase M. SssI methylated lambda DNA was added per 1ug of DNA prior to treatment as a C/5mC control. After βGT-mediated glucosylation and Tet-mediated oxidation, the sequencing libraries were then prepared following the MethylC-seq protocol (Urich and others, 2015). DNA sequencing was performed using an Illumina NextSeq500 Instrument at the University of Georgia's Genomics Facility, with coverage estimated to range from 0.35 to 0.41 genome equivalents among the various samples (**Supplemental Table 4.S3)** (Popp and others, 2010). Due to high cost associated with deep coverage of the pig genome using WGBS, we chose an alternative strategy to look at 5hmC metagene plots for hundreds to thousands of genes (groups of genes). To demonstrate that

metagene analysis do not require high coverage, we downloaded a published high-coverage 5hmC dataset (Lister et al., 2013) in all genes in mouse frontal cortex and then subsampled number of reads ranging from 0.2X to 13X to plot 5hmC distribution for six gene groups. As can be seen in **Supplemental Figure 4.S5**, coverage didn't affect the patterns of metagene plots, even for coverage as low as 0.2X.

TAB-seq data analysis. The raw sequence data were trimmed for adapters, preprocessed to remove low quality reads, aligned to the *S.scrofa* reference genome Sscrofa10.2 (GCA_000003025.4, http://www.ensembl.org/Sus_scrofa/) and analyzed as we described previously for TAB-seq analysis of 5hmC (Yu and others, 2012b). The control 5mC modified lambda DNA sequence was used to calculate the 5mC non-conversion rate upon Tet and bisulfite treatment. Non-CG dinucleotide sites were used to compute the non-conversion rate of unmodified cytosines upon bisulfite treatment (**Supplemental Table 4.S3**). For this analysis, only cytosines in the CG context were considered.

Quintiles expression data. We obtained extensive transcript expression data for porcine adipose tissue based on RNA-seq, covering a large dynamic range of expression levels (Pilcher and others, 2015). Expression levels from the 16 adipose tissue samples presented were averaged to obtain a list of 25,321 expressed transcripts. Because in RNA-seq, the number of reads mapped to a gene is also a function of the total exonic length, the average expression level was divided by this exonic length of each gene to normalize expression levels. This list was broken into quintiles based on exon-normalized mRNA expression levels, resulting in "quintile of expression" gene lists with 5,064 to 5,065 genes in each list.

For each quintile of transcripts, the level of 5hmC was determined using weighted methylation level calculation (Schultz and others, 2012) for each of 20 bins upstream, 20 bins

within genes (between annotated TSS and TTS) and 20 bins downstream of genes. Each of the upstream and downstream bins spanned 5kb for a total of 100kb spanned in each direction. The within-gene regions, no matter what their length, were evenly divided among the 20 bins. Figures were prepared using ggplot2 (Wickham, 2009).

Availability of supporting data

The TAB-seq data set supporting the results of this article is available in NCBI GEO repository, accession number **GSE73684.**

Statistical analysis

Hamamatsu SimplePCI Image Analysis software was used to process images and measure nuclear areas and fluorescence intensities. The data of nuclear area and qRT-PCR results were analyzed by one-way ANOVA with post hoc Tukey's HSD test using Statistica software 7.1 (StatSoft; Tulsa, OK, USA). A value of $p<0.01$ is denoted with * while a value of $p<0.001$ is denoted with **.

Results

Isolating and sorting adipocyte nuclei from adipose tissue

We considered possible nuclear protein markers that could be used to identify subsets of adipocyte nuclei. Members of the peroxisome proliferator-activated receptor (PPAR) subfamily of nuclear receptor transcription factors positively control transcription, the metabolism of glucose and lipids, and ultimately cell division and differentiation (Mulero and others, 2013). One of the three PPAR subtypes, PPAR gamma (PPARg) is induced during and is essential to adipogenesis, and it cooperates with many other factors in the process. PPARg binds to PPAR-

enhancers and activates genes involved in adipocyte differentiation, lipid synthesis, and lipid storage (Oger and others, 2014). While the best characterized subtype of PPARg protein, PPARg1, is strongly expressed in the nuclei of maturing and mature adipocytes (MMAs), it is also expressed in other cell types in adipose tissues including mesenchymal adipocyte lineage-committed cells, dedifferentiated fat cells, endothelial cells, and leukocytes (e.g., T-cells, neutrophils) (Matsumoto and others, 2008; Reddy and others, 2012; Reddy and others, 2008; Wohlfert and others, 2007). Because of its essential roles in adipogenesis and lack of quantitative evidence to the contrary, we considered the possibility that PPARg1 protein might be most highly expressed in the most active adipocytes and therefore a good marker to quantitatively distinguish highly active adipocyte nuclei from the nuclei of other cell types.

A protocol for the rapid isolation of adipocyte nuclei was developed as outlined in **Figure 4.2A** and detailed in Materials and Methods. Phase contrast microscopy image of isolated *Ss*VAT nuclei and DAPI staining of nuclei showed that the enriched preparation of nuclei contained very little cellular debris (**Figure 4.2B**). The method required only minor modifications from that for brain cellular nuclei (Yu and others, 2015). To further test the enrichment of nuclei, we compared proteins in crude VAT homogenate to proteins in purified nuclei using Western blotting (**Figure 4.2C**, H & N). The nuclear fraction (N) was highly enriched for nuclear protein histone H3 and the total VAT homogenate (H) was greatly enriched for the cytoplasmic protein actin. Equal loading of total protein amounts was predetermined by Coomassie blue staining of equivalent samples electrophoresed into the end of stacking gel for a brief period. Our long-term interest was in the epigenetic alterations to chromatin structure, therefore, we focused on nuclei isolated from formalin-fixed fresh tissue.

We characterized nuclei that had been sorted based on PPARg1 levels. A relatively large fraction of all VAT nuclei stained strongly with antibodies to PPARg1, but there was a wide dynamic range in the staining consistent with the differential expression of PPARg1 among cell types (**Supplemental Figure 4.S2A**). Using qRT-PCR assays for cell-type-specific transcripts, we found that nuclei with higher levels of PPARg1 were not significantly enriched for adipocyte transcripts relative to transcripts marking other cell types (**Supplemental Figures 4.S3 and 4.S4**). For example, PPARg1-High nuclei had high levels of transcripts encoding IKAROS, a leukocyte-specific marker, higher than the levels in PPARg1-Neg nuclei. Note that the levels of most nuclear transcripts are strongly linearly correlated with their levels in total cellular RNA (R correlation coefficient = 0.94, supplementary data in Deal et al (2010b)). Hence, neither the cell-type-specificity nor the relative levels of PPARg1 protein expression were sufficient to identify subsets of adipocyte nuclei within adipose tissues.

An alternate upstream promoter and alternate RNA splicing produce a slightly longer isoform of PPARg, PPARg2, with a 28-amino-acid extension on the N-terminus relative to PPARg1 (Zhu and others, 1995). Although less well characterized than the shorter PPARg1 isoform, PPARg2 appears to be an essential adipose tissue-specific enhancer of adipocyte development that is produced throughout adipogenesis (Tontonoz and others, 1994). Ectopic overexpression of PPARg2 alone is sufficient to induce pluripotent stem cells to differentiate into adipocytes (Ahfeldt and others, 2012), making PPARg2 both necessary and sufficient for adipogenesis. We used antibodies targeting the distinct amino terminus of PPARg2 to identify subsets of adipocyte nuclei from non-adipocyte nuclei prepared from adipose tissue.

A small subset of VAT nuclei was strongly stained with PPARg2 antibodies and there were also populations of intermediately stained and unstained nuclei as well (**Supplemental Figure**

4.S2B). Examination of the highly stained PPARg2-High nuclei for DAPI staining morphology revealed that many were larger and more decondensed with diameters exceeding twice that of the smallest PPARg2 negative nuclei (**Supplemental Figure 4.S2C**). We previously defined decondensed to mean that the nuclei had a larger DAPI staining area with less intense staining per unit area as compared to the intensely staining normal-sized 2C nuclei (Yu and others, 2015). FNC showed that there was an approximately 100-fold dynamic range in the PPARg2 immuno-fluorescence staining intensity among VAT nuclei (**Figure 4.3**) above the background staining observed with secondary antibody alone (**Supplemental Figure 4.S1D**).

VAT nuclei were subjected to FANS based on the levels of PPARg2 immuno-staining (**Figure 4.3**). Four populations of nuclei were sorted (PPARg2-Neg, -Low, -Med and -High) based on PPARg2 staining, each having an approximately 5-fold increase in PPARg2 immuno-staining intensity above background staining (**Figure 4.3A**). The low background staining from the secondary antibody alone was used to define the PPARg2-Neg class of nuclei (**Supplemental Figure 4.S1D**)**.** In repeated FANS experiments, we gated to collect approximately 20%, 40%, 30%, and 10% of the nuclei in each category, -High, -Med, -Low, and -Neg, respectively. The sorted nuclear fractions were re-photographed without re-staining (**Figures 4.3C-F**)**.** Besides the obvious difference in PPARg2 staining intensities, there is variation in nuclear morphologies. The PPRG2-Neg nuclei are mostly spherical, while the PPARg2-Med and -Low fractions contained many ovoid- and spindle-shaped nuclei typical of nuclei in the thin cytoplasmic layer surrounding the lipid body in mature adipocytes. The PPARg2-High nuclei are generally oval or round, and were predominantly larger and more decondensed relative to the other populations. However, it is worth noting that some strongly stained PPARg2-High nuclei are small, reflecting some heterogeneity in morphology (**White**

Arrows Figures 4.3F and H). The PPARg2-Neg nuclei in **Figure 4.3C** had a diameter of approximately 6.5 μm, typical of 2C mammalian nuclei (Dammer and others, 2013b). By comparing PPARg2-Neg nuclei (**Figure 4.3C**) to PPARg2-High nuclei (**Figure 4.3H**), where the PPARg2-High nuclei are viewed for DAPI staining alone, the larger diameters of these nuclei were easily seen. When the average two-dimensional cross-sectional area of the original images of DAPI stained PPARg2-Neg nuclei were set to 1.0, the nuclear areas of the PPARg2-High, -Med, and -Low populations were 2.8-, 2.0-, and 1.6-fold larger, respectively (**Figure 4.3G**). There were statistical significant differences between any of the two fractions of nuclear areas except for between PPARg2-Low and PPARg2-Neg fractions (* $p<0.01$; ** $p<0.001$). Hence, the nuclear volumes of adipocyte nuclei may be computed to vary over a 20-fold range. Transcript levels of PPARg2 were assayed among the four fractions of nuclei by qRT-PCR. PPARg2 was expressed at significantly higher levels in PPARg2-High and PPARg2-Med classes of nuclei, relative to PPARg2-Neg fraction (* $p<0.01$, **Figure 4.3B**).

Transcript profile of sorted visceral adipocyte nuclei

Approach. Considering that neither FANS or PPARg2 staining has not been implemented to separate and characterize adipose tissue nuclei previously, we profiled the relative levels of a few sets of transcripts, which were potentially informative as to the phenotypes of these four classes of nuclei.

Transcripts encoding cell-type-specific markers. The four classes of adipose tissue nuclei were assayed for the relative quantity (RQ) of transcripts encoding proteins that were reasonably specific markers of adipocytes, endothelial cells, and leukocytes and their potential for cell cycle activity. Among the four fractions, *beta actin (ACTB)* mRNA was determined to bean

equivalently expressed endogenous control relative to total cDNA input. Therefore, the expression levels of various marker transcripts were compared to actin set to 1 (Materials and Methods). For most of the cell type markers, significant difference in transcript expression levels were found distinguishing the PPARg2-Pos classes of nuclei (PPARg2-High, -Med, -Low) from PPARg2-Neg class of nuclei (* $P<0.01$, ** $P<0.001$, **Figure 4.4**). Adipocyte specific transcripts *ADIPOQ, SREBF1,* and *FABP4* were approximately 4- to 20-fold more highly expressed in most of the PPARg2-Pos classes of nuclei, relative to PPARg2-Neg fraction, as shown in **Figure 4.4**. The leukocyte and progenitor cell markers *IKZF1* and *IHH* were estimated to be 10- to 100-fold more highly expressed in the PPARg2-Neg fraction of nuclei than in the PPARg2-Pos fractions (**Figure 4.4**). IHH, a suppressor of adipocyte development, was extremely highly expressed in PPARg2-Neg nuclei. Thus, the PPARg2-Neg fraction appears enriched for some nuclei from progenitor cell types not committed to adipocyte development. Interestingly, transcripts for the transcription factor GATA2, which promotes the differentiation of MSCs into adipocytes (Kamata and others, 2014), and ERG3, a sterol C5-desaturase involved in cholesterol biosynthesis (Acimovic and others, 2011), were more highly expressed in the PPARg2-Low and -Med classes of nuclei than either the PPARg2-Neg or PPARg2-High nuclei. Perhaps, the cells from which PPARg2-High nuclei were derived have finished their development from MSCs and are no longer synthesizing as much lipids. In summary, the PPARg2-Pos nuclei appear to be derived from adipocytes, and the PPARg2-Neg nuclei from non-adipocytes. Summary information and references on the properties of the marker genes assayed is given in **Supplemental Table 4.S4.**

Transcripts encoding factors involved in multipotency and the cell cycle. Three markers of cellular multipotency, proliferation, and cell cycle activity were examined (*KLF4*, *MYC*, and

PCNA as defined in **Supplemental Table 4.S4**). They were 2- to 6-fold more highly expressed in most of the PPARg2-Pos adipocyte fractions relative to the PPARg2-Neg non-adipocyte fraction of nuclei. Thus, although there was significant variation in the expression of these markers, they were in general more highly expressed in PPARg2-Pos nuclei.

Transcripts encoding chromatin-remodeling proteins. To begin testing the first part of our hypothesis, *adipose tissue contains epigenetically distinct subpopulations of adipocytes,* we analyzed transcripts encoding factors responsible for programming a range of chromatin modifications (**Figure 4.5).** Highly decondensed nuclei are associated with an elevated transcription level of chromatin remodeling machinery and genes of multipotency and in the brain with elevated expression of markers for learning and memory (Yu and others, 2015). Therefore, although the cellular memory of adipocytes might be biochemically quite different from that of neurons, subsets of adipocyte nuclei still might have different capacities to record cellular memories, and hence, be distinctly potentiated to respond to their tissue environment. We performed qRT-PCR assays on transcripts from 19 genes encoding chromatin-remodeling factors, which are broken into four sets. First we assayed factors involved in DNA cytosine modification including two DNA cytosine methyltransferases, DNMT1 and DNMT3A, which catalyze the synthesis of DNA 5mC and three ten-eleven translocation methylcytosine dioxygenases, TET1, TET2, and TET3, which catalyze the oxidation of 5mC to 5hmC (**Figure 4.5A** and **Supplemental Table 4.S4**). TETs are the major enzymes controlling the removal and turnover of 5mC (**Figure 4.1**) (Wu and Zhang, 2014). Of these *DNMT1*, *DNMT3A*, *TET1*, and *TET3* transcripts were 3-, 6-, 1.5-, and 4-fold more highly expressed in PPARg2-Pos (PPARg2-High, -Low and -Med) adipocyte factions, respectively, relative to the non-adipocyte faction.

TET2 and *AICDA* were 19- and 40-fold higher more highly expressed in the PPARg2-Pos fraction.

Second, we considered histone side chain acetylation (**Figure 4.5B**)**,** but the differences among nuclear fractions appeared less dynamic. Transcripts for two histone lysine acetyltransferases, *KAT2B* and *KAT3B*, and three histone deacetylases SIRT1, *HDAC2*, and *HDAC3*, were assayed. Only the transcripts encoding *HDAC2*, *KAT3B,* and *SIRT1* deacetylase were notably more highly expressed (e.g., ~2-fold) in PPARg2-Pos nuclei than negative nuclei, although there were also quantitative differences among the nuclear fractions for *KAT2B* and *HDAC3*.

Third, transcript levels for four factors involved in nucleosomal histone side chain methylation (**Supplemental Table 4.S4**) were quantified (**Figure 4.5C**). This included lysine-specific demethylase *KDM4A*, lysine specific methyltransferase *KMT2C*, histone H3K9 methyltransferase *SETDB1*, a cofactor that promotes histone lysine methylation *PAXIP1*, and Swi/Snf related helicase ATPase *ARID1A*, which is known to modulate H3K4me1 nucleosomes. Fourth, we examined the protein arginine methyltransferases *CARM1 and PRMT5* and demethylases, including histone arginine demethylase *JMJD6*. The transcripts of these last two classes of genes were 6- to 65-fold more highly expressed in PPARg2-Pos nuclei than PPARg2-Neg nuclei (**Figure 4.5D**). Clearly, for the PPARg2-Pos nuclei there were much higher levels of factors involved in histone methylation than factors involved in histone acetylation.

IFM analysis of chromatin modifications in isolated nuclei

Because strong differential expression of transcripts encoding proteins involved in DNA and histone methylation was observed, one DNA and two histone modification products were

assayed. First, the TET catalyzed oxidation of 5mC to 5hmC and 5hmC levels themselves are often dynamically regulated in the development of stem cells, germ cells, T cells, and neurons (Lister and others, 2013a; Rose and others, 2014; Tsagaratou and others, 2014). Therefore, we performed an immunofluorescence microscopy (IFM) analysis of 5hmC among the various fractions of VAT nuclei. Preliminary experiments showed 5hmC was concentrated in large decondensed nuclei (**Figure 4.6**)**.** When we examined the co-distribution of PPARg2 protein with 5hmC, nearly all nuclei staining most strongly for PPARg2 also stained most strongly for 5hmC (**White Arrows, Figure 4.6A**)**.** The coordinate expression of PPARg2 and 5hmC was examined further by FNC (**Figures 4.6B and 4.6C**)**.** The cytometer resolved a wide, nearly 100-fold, range of positive staining for both markers. Nuclei stained with the secondary antibody alone used to detect 5hmC helped define background fluorescence. As PPARg2 also defined nuclear size (**Figure 4.3H**), perhaps this correlation of 5hmC with PPARg2 levels should not be surprising, considering the evidence that 5hmC marks decondensed euchromatin (Ficz and others, 2011; Kubiura and others, 2012).

Levels and gene-region distribution of 5hmC

In view of the large differences in expression levels of factors controlling DNA cytosine methylation and turnover via 5hmC (**Figures 4.1 and 4.5A**) and the association of 5hmC with decondensed highly active chromatin, it seemed reasonable to consider that 5hmC levels might vary widely among the fractionated VAT nuclei and be essential to their epigenetic programming. We performed TAB-seq to evaluate 5hmC levels in three classes of VAT nuclei isolated by FANS (PPARg2-High, pooled PPARg2-Med and -Low, and PPARg2-Neg). The specificity of TET-enzymes and their cofactors, results in 98% of 5hmC being in the CG

dinucleotide context. Therefore, the data on 5hmC levels are reported as a fraction or percent of CG dinucleotides. The percent of 5hmCG ranged from 3.40%, to 3.03% to 2.22% of CG dinucleotides among these three classes of VAT nuclei (**Table 4.1**).

We compared the gene-region distribution of 5hmCs among the three classes of VAT nuclei for 25,321 genes divided into quintiles based on RNA-seq expression data in adipose tissue (Pilcher and others, 2015). Gene regions were divided into three parts: 100 kb upstream of the transcription start site (UTSS), 100 kb downstream of the transcription stop site (DTTS), and the gene body (GB) extending from TSS to TTS. 5hmC data were estimated from gene sequences divided into 20 equal bins for each region and the fraction or percent 5hmCG per CG dinucleotide was calculated. For the highest quintile of expressed genes (**5 of 5, Figure 4.7A**), the pattern of 5hmCG distribution begins with a deep valley in 5hmCG levels at the TSS, rises to a high broad plateau across the gene body, and ends with another steep valley of 5hmCG at the TTS. Across all gene regions, 5hmCG levels were the highest for PPARg2-High nuclei and lowest for PPARg2-Neg nuclei, although the pooled PPARg2-Med and -Low nuclear populations contained only slightly lower levels than that of the -High population. For the 3rd and 4th quintile expression gene groups the distribution of 5hmCG was relatively indistinct, although there was small peak in 5hmCG levels right after the TSS. Surprisingly, the 5hmC levels drop across the gene body for the lowest two quintiles (1st, 2nd) for all three classes of cellular nuclei. As far as we are aware a gene region drop in 5hmC has not been reported in any gene set. In **Figure 4.7B**, 5hmC levels are shown for all five quintiles for the PPARg2-High nuclei.

Discussion

Manipulating cellular nuclei from adipose tissue

Considerable progress was made in simplifying the isolation of total cellular nuclei from within adipose tissue as a new tool for cell-type-specific analyses. Adipocyte, endothelial cell, and lymphoid cell nuclei were easily isolated from VAT using only slight modifications to an existing rapid protocol for isolating brain cell nuclei. The method required only bench top centrifugation through a sucrose cushion and two filtration steps and did not require ultracentrifugation as in earlier established methods (Florens and others, 2008). Nuclei had sufficient purity from cytoplasmic debris to greatly simplify analysis by IFM, FNC, and FANS. The PPARg2 isoform of PPARg was adipocyte cell-type-specific and expressed strongly enough to identify adipocyte nuclei, while the PPARg1 isoform was not. The relative cell-type purity of the PPARg2-Pos adipocyte nuclear populations was validated by the quantitative assessment of cell-type-specific transcripts. Hence, PPARg2 appears to be a reasonable choice as a pan-adipocyte marker, although PPARg2 labeled nuclei from other fat deposits and from other species will have to be examined.

Quantitative assessment of nuclear transcripts in the different sorted subpopulations of VAT nuclei revealed differential expression of some important markers over more than two orders of magnitude, providing significant resolution for expression studies. This result agrees with previous RNA expression studies on isolated sub-populations of cellular nuclei from plant roots and mouse brain (Dammer and others, 2013b; Deal and Henikoff, 2010b; Lister and others, 2013a; Yu and others, 2015). We showed the utility of using PPARg2 as an adipocyte marker for IFM and FNC. More particularly, the three subsets of adipocyte nuclei that differed in ~5-fold increments in the levels of PPARg2 expression, displayed significant differences in the

expression levels of some markers, although most epigenetic markers of adipocyte identity and cell cycle activity simply distinguished adipocyte PPARg2-Pos from PPARg2-Neg nuclei.

Differential programming of distinct adipocyte populations

Our data give strong initial experimental support for the first part of our working hypothesis by showing that *adipose tissue contains subsets of adipocytes that are epigenetically distinct*. The four populations of VAT nuclei sorted based on PPARg2 protein levels differed significantly in the expression of transcripts encoding factors involved in chromatin modification and/or adipogenesis. Nineteen of the twenty-two transcripts associated with epigenetic control, pluripotency, and/or the cell cycle that were assayed showed 2- to 100-fold differences in their levels of expression among the four populations. Transcript levels were particularly distinct between PPARg2-Pos adipocyte nuclei and PPARg2-Neg non-adipocyte nuclei. IHH is the only hedgehog morphogen known to be expressed in preadipocytes, where it inhibits adipogenesis and promotes chondrocyte differentiation, proliferation, and maturation. Transcripts for IHH were far more highly expressed in non-adipocyte PPARg2-Neg nuclei than in adipocyte nuclei. IHH should not be expressed in maturing or mature adipocytes, and hence, served to confirm the identity of sorted nuclear populations of preadipocytes. We found 2- to 50-fold differences in the expression of genes specifically associated with different stages of adipogenesis including *ADIPOQ, SREBF1, GATA2, ERG3,* and *FABP4.* Three markers of pluripotency and cell cycle potential, *KLF4, MYC*, and *PCNA*, were 2- to 6-fold more highly expressed in adipocyte populations, suggesting perhaps there is reasonable developmental potential among diverse classes of adipocytes.

This discussion will focus briefly on the observed differential expression of three factors controlling H3K4me1 and H4K9me1 levels among classes of VAT nuclei: ARID1A, KMT2C, and PAXIP1 (Gupta and others, 2012). ARID1A is the large Swi/Snf ATPase subunit defining many BAF remodeling complexes including complexes that methylate H3K4 to H3K4me1 (Joshi, 2014; Singh and Archer, 2014). ARID1A complexes regulate pluripotency genes and are essential to the conversion of ES cells into adipocytes (Gao and others, 2008). KMT2C is a histone lysine methyltransferase that methylates H3K4 to H3K4me1 and me2 (Geutjes and others, 2012; Lee and others, 2013) and is physically associated with the lineage-specific enhancers and cell-type-specific factors including *PPARg* and *FABP4* (Lee and others, 2013). *KMT2C* mutant mice have less white fat and are defective in adipogenesis (Lee and others, 2008). PAXIP1 binds to histone 3 lysine 4 methyltransferases to influence the conversion of H3K4me1 to H3K4me3 in nucleosomes associated with the promoter regions of *PPARg* and *C/EBPa.* PAXIP1 is essential to their induced expression, and hence, essential to adipogenesis (Cho and others, 2009), but its activity acts in opposition to ARID1A and KTM2C because it reduces H3K4me1 levels, whereas the latter increase it. Considering that all three factors are essential to adipogenesis and that PPARg is essential to this process, it is not surprising that PPARg2-Pos adipocyte nuclei express these remodelers at much higher levels than non-adipocytes. Because turnover rates for chromatin modifications are a function of their synthesis and decay (i.e., removal) rates (Meagher, 2014), the coordinately higher expression of these factors with opposite activities in adipocytes relative to non-adipocytes suggests more rapid turnover rates for H3K4me1.

Next, we consider the two factors regulating the levels of nucleosomal H3K9me1, SETDB1 and KDM4A. SETDB1 is a H3K9 methyltransferase that represses PPARg

transactivation via nucleosomal histone methylation at PPARg target genes. SETDB1 methylates H3K9 and H3K9me1 to H3K9me3, a modification associated with transcriptional repression (Takada and others, 2009). Conversely, KDM4A is a lysine-specific demethylase that directly demethylates H3K9me3 to H3K9me1/2 (Tan and others, 2011; Zhang and others, 2014). Very early in the differentiation of 3T3-L1 preadipocytes levels of the repressive H3K9me3 mark increase 2- to 3-fold, "licensing" preadiopcytes to differentiate into mature adipocytes (Guo and others, 2009). KDM4A is essential to recruiting PPARg to the many target genes expressed during adipocyte development (Cardamone and others, 2014). It is reasonable to consider that KDM4A-catalyzed conversion of H3K9me3 to H3K9me1 directs adipogenesis to proceed. The higher levels of these two opposing activities in PPARg2-Pos adipocyte nuclei may result in an increased turnover rate for H3K9 related methylation.

TET expression and 5hmC

We began with a preliminary examination of the levels TET expression and 5hmC levels in nuclei fractionated based on PPARg2 levels. PPARg2 is the major transcription factor driving adipogenesis and lipid synthesis in mature adipocytes. It acts via its binding to PPARg enhancers (PPAREs). Using IFM we found that all three TETs proteins (TET1, 2, 3) were present at significantly higher levels in PPARg2-High adipocyte nuclei than in most adipocyte nuclei staining moderately for PPARg2 or PPARg2-Neg non-adipocytes. Based on cytometry, total 5hmC appeared proportional to PPARg2 levels in nuclei. However, qRT-PCR data only showed moderate differences in TET RNA expression among fractionated nuclei and only TET2 and TET3 levels were significantly higher in PPARg2-High nuclei. DNMT1 transcript levels were relatively higher in all three classes of PPARg2-Pos nuclei compared to PPARg2-Neg, but the

lowest level among these was seen in the PPARg2-High samples, perhaps reflecting the decline in DNMT1 reported for fully mature adipocytes (Londono Gentile and others, 2013).

Similarly, we found exceptionally high levels of 5hmC in PPARg2-High nuclei relative to the balance of VAT nuclei by IFM and observed their coordinate expression over more than an order of magnitude by FNC. Our TAB-seq data confirmed that PPARg2-Pos nuclei had the highest levels of 5hmC, significantly higher than PPARg2-Neg nuclei. The 2.2 to 3.4% 5hmCG per CG dinucleotides observed in VAT nuclei were low as compared to the estimated 13% 5hmCG in adult brain where 5hmC levels are the highest (Wen and others, 2014), but this represents an intermediate level among estimates for many other tissue types (Globisch and others, 2010b; Li and Liu, 2011). Yet, by TAB-seq there were only slightly higher levels of 5hmC in the PPARg2-High nuclei compared to the balance of PPARg2-Low/Med nuclei. The TAB-seq method undoubtedly provides the most quantitative and unbiased assessment of the relative levels of 5hmC.

There are a few straightforward explanations for these differences among measurements made by qRT-PCR for TET RNAs, immuno-detection of 5hmC, and TAB-seq analysis of 5hmC. First, differential stability of TET RNAs and proteins might favor the accumulation of TET proteins in the PPARg2-High subset of cells, while TET RNA levels declined. Second, 5hmC is most concentrated in euchromatin in regions with decondensed structure (Ficz and others, 2011; Kubiura and others, 2012; Yamaguchi and others, 2013). We observed that PPARg2-High nuclei were extremely large and decondensed and nuclear size appears to be proportional to the levels of both PPARg2 and 5hmC detected with antibodies. Both IFM and nuclear cytometry (FNC, FANS) showed a wide dynamic range for the immunological detection of PPARg2 protein and 5hmC. Perhaps a decondensed chromatin structure provides disproportionate access to immune

reagents amplifying the difference in immunochemical staining among the nuclear fractions relative to condensed chromatin is other nuclei blocking access. While this potential artifact would prevent precise quantitative interpretation of our immunochemical data, it may have contributed to the wide dynamic ranges of PPARg2 and 5hmC staining observed and aided in separating classes of PPARg2 stained nuclei by FANS.

Gene-region distribution of 5hmC

TAB-seq analysis of three classes of VAT nuclei showed that 5hmC was concentrated in the gene bodies of the highest quintile of expressed genes, above the levels in flanking regions, and was much higher for PPARg2-Pos nuclei than PPARg2-Neg. Perhaps this relationship between PPARg2 and 5hmC may not be too surprising, considering the recent evidence that PPARg bound to PPAREs attracts TET enzymes and this results in the chromatin-localized conversion of 5mC to 5hmC (Fujiki and others, 2013). 5hmC levels increase during the development of 3T3-L1 preadipocytes into adipocytes. Small RNA silencing of any one or all three TETs prevents this part of the increase, strongly supporting the view that all three contribute to 5hmC levels in adipose tissue (Fujiki and others, 2013). Perhaps 5hmCGs program cellular memory in adipose tissues, tagging sites for demethylation or remethylation at a later time and creating a poised or potentiated state as suggested for the development of neurons in the brain and for embryonic stem cells (Choi and others, 2014; Lister and others, 2013a; Pastor and others, 2011). Constitutive CTCF enhancers that are active throughout adipogenesis and PPAREs that become active during adipogenesis are often concentrated in CG rich regions. During adipogenesis, PPARg binding is associated with a dramatic decrease in 5mC levels and an increase in 5hmC levels at both constitutive enhancers and activated PPAREs. Changes in the

methylation state of the CTCF and PPARg enhancers activates adjacent gene expression, with notable increases in expression of genes involved in glucose signaling and lipid metabolism (Oger and others, 2014). Note that reduced 5mC at these enhancers is in contrast to increases in 5mC levels at enhancers in the C/EBPalpha promoter reported previously (Guo and others, 2009). Because the standard whole genome bisulfite sequencing technology to determine 5mC does not distinguish between 5mC and 5hmC, it is reasonable to consider that some of the reported increases in 5mC included increases in promoter and gene region 5hmC. By contrast, simply lowering 5mC levels via treatment with 5-azaC down regulates PPARg and halts adipogenesis of 3T3-L1 cells. One explanation for this complexity is that hydroxymethylation of these CG-rich enhancer regions is required for their subsequent activation, suggesting a possible cause-and-effect direct relationship with 5hmC acting at a high level. TET2 protein does interact with both transcription factors, PPARg and CTCF, to promote DNA hydroxymethylation of 5mCGs at their associated enhancers, CCCTC-related sequences and PPAREs, respectively. Hence, TET activity appears to drive increases in constitutive and adipogenic gene expression during the development of 3T3-L1 preadipocytes into mature, lipid-rich adipocytes (Dubois-Chevalier and others, 2014; Dubois-Chevalier and others, 2015). The likelihood of a specific relationship between PPARg and CTCF is further evidenced by that fact that during adipogenesis, CTCF binds disproportionately to enhancer sites that are near PPAREs and at most genes induced by PPARg (Dubois-Chevalier and others, 2014). It has been suggested that 3-dimensional chromatin loops bring these two enhancers into proximity to promote coordinated activity (Dubois-Chevalier and others, 2015). The resulting specific relationship of PPARg, TET activity, and 5hmC levels in adipocytes may also help explain the lower than average levels of 5hmC we observed in the gene bodies of the lowest quintile of expressed genes. This would

occur if PPARg-associated TET activity further oxidizes 5hmCG to 5fCG and 5caCG, which would not only lower 5hmC, but could lead to higher levels of 5mCGs and gene silencing**.** Future studies will explore the more complex examination of 5hmC levels surrounding these and other enhancers.

A model for 5hmC activity

Considering our results in the light of other recent publications on 5hmC in the brain suggests a model for the role for 5hmC in regulating adipocyte gene expression and development. 5hmC levels in neurons are said to "potentiate" changes in gene expression and to prepare for rapid "on demand gene regulation," but are also proportional to steady state transcript levels (Irier and others, 2014; Lister and others, 2013a). Recall that the levels of 5hmC observed in adipocytes are several fold lower than in brain, but ranged widely with gene express level. Perhaps the levels of gene region 5hmC and the open chromatin environment they create help to "warm up" these most active gene regions for more rapid transcription, similar to warming up a gasoline engine prior to putting it in gear. In this context, 5hmC levels may act as a rheostat regulating the relative transcriptional potential and activity in different regions of chromatin. However, the rheostat may be set differently in different tissues, such that the idling speed is different. By this model the range of 5hmC-determined idling speeds would be broad in adipose tissue, but still lower than in the brain, reflecting a lower rate of chromatin turnover and a slower rate of cellular memory formation in response to environmental influences relative to neurons. By measuring the relative turnover rates for 5mC and 5hmC in adipocytes and brain, this model may be tested.

Conclusions

FNC and FANS offer the technical power to analyze cell-type-specific differences in chromatin structures for less accessible organs and tissues, such as adipose tissue. Cytometry provides vast numerical superiority to the analysis of the distribution of nuclear epitypes such as DNA cytosine or histone modification over any other existing approach. An examination of subpopulations of adipocyte and non-adipocyte nuclei derived from VAT demonstrated there is a wide variation in nuclear morphology and size, chromatin structure, progenitor status, and perhaps the potential to form cellular memories, providing initial support for our hypothesis. The extreme variation in nuclear size among adipocyte nuclei is only partially explained by exceptional transcriptional and epigenetic activities, and warrants further examination, particularly in light of the data from other systems directly correlating large decondensed nuclear morphology with progenitor cell status.

This is the first report of 5hmC levels across gene regions of adipocytes and non-adipocytes isolated from within visceral adipose tissue. We found a wide range in 5hmC levels in gene regions, 5-fold differences among genes and cell types ranked based on their quintile expression level and 4-fold within the quintile expression gene groups. This is twice the difference that has been reported between neurons and non-neurons even though the total levels of 5hmC are much lower in VAT than they are in the brain. Some of the greater differences in 5hmC levels we report here may be due to the greater resolution obtained by comparing DNA from more highly enriched cell types. Most unexpected were the extremely low levels of 5hmC observed for weakly expressed genes in their gene bodies, below the levels found in flanking sequence regions. These distinctions suggest an important role for 5hmC in adipose tissue development and/or maintenance, but the role may be very different from that in the brain.

A small number of stimulating recent studies demonstrate changes in the genome-wide and gene-specific distribution of 5mC in human adipose tissue in response to obesity, metabolic syndrome, and extended exercise (Dahlman and others, 2015; Keller and others, 2014; Ronn and Ling, 2013; Ronn and others, 2013; Turcot and others, 2012). Our results showing large differences in TET expression and 5hmC levels among classes of adipocytes suggest a complex role for the turnover of modified DNA cytosine in regulating gene expression in adipose tissues. It appears likely that distinct subpopulations of adipocyte nuclei within adipose tissue may be programmed with their own cytosine modification epitype. Each subset may respond differently to stresses in their tissue environment and contribute in different ways to metabolic health. A continued examination of subpopulations of adipose tissue nuclei should greatly improve the statistical significance of epitype data from VAT and should more accurately report epigenome-induced risk of disease.

Acknowledgements

Dr. Hang Yin and Diane Hartzell at the University of Georgia offered helpful advice as this project developed. Julie Nelson provided invaluable assistance with the cytometry at UGA's Center for Tropical and Emerging Global Diseases Flow Cytometry Core facility. Ryan Crow assisted us in obtaining fresh porcine adipose tissue from UGA's Abattoir. Emily R. Trunnell and Rhi Biddy edited the manuscript for scientific clarity. This work was supported by grants from UGA's Office of the Vice President for Research, UGA's Obesity Initiative and from NIH's National Institute of Diabetes and Digestive and Kidney Diseases (NIDDK, DK1003920 and DK096300) to RBM, NHGRI HG006827 grant to CH, the National Institutes of Health grant R00GM100000 to RJS, and a Patricia and Doyle Mote Biomedical Research Award to PY. CH is

an investigator of the Howard Hughes Medical Institute. MY is an international pre-doctoral fellow of the Howard Hughes Medical Institute.

Table 4.1.Percent 5hmCG in three classes of nuclei determined by TAB-seq and averaged across all sequences.

Nuclei	Total 5hmCG	Total CG	% 5hmCG	Scaled % 5hmCG
PPARg2-High	159,774	4,695,778	3.40%	6.36%
PPARg2-Med+Low	117,954	3,886,756	3.03%	5.79%
PPARg2-Neg	88,910	4,004,237	2.22%	5.24%

PPARg2-Med+ Low: pooled PPARg-Med and PPARg-Low populations of nuclei.

Figure 4.1. Turnover cycle for DNA cytosine modification at CG dinucleotides and its potential impact on adipose tissue (Diagram modified from Dubois-Chevalier, 2015 and Kohl, 2013). A model is suggested in which the dynamic modification cycle of DNA cytosine residues (C) is linked to ubiquitous (CTCF) and adipocyte-specific (PPARg) transcription factor enhancement of gene expression during adipogenesis and in mature adipocytes. CTCF and PPARg recruit TET enzymes to promote 5mC hydroxymethylation and activate transcription of PPARg. The lower panel shows the cyclic turnover of modified cytosine (C) residues and emphasizes that TETs catalyze the rate-limiting step of removing 5mC by oxidation to 5-hydroxymethylcytosine (5hmC). TET activity further oxidizes 5hmC to 5-formalcytosine (5fC) and 5-carboxycytosine (5caC). The essential roles of other factors include DNMTs in the methylation of C to 5-methylcytosine (5mC), thymine DNA glycosidase (TDG) and methyl-CG binding domain protein 4 (MBD4) in the excision of 5fC or 5caC by creating a single nucleotide gap, and gap repair back to a C residue by base excision repair (BER) machinery such as the GADD45s. The gene-region-specific balance of these activities determines the levels of C, 5mC, and 5hmC. The diagram was modified from those in previous publications (Dubois-Chevalier and others, 2015; Kohli and Zhang, 2013).

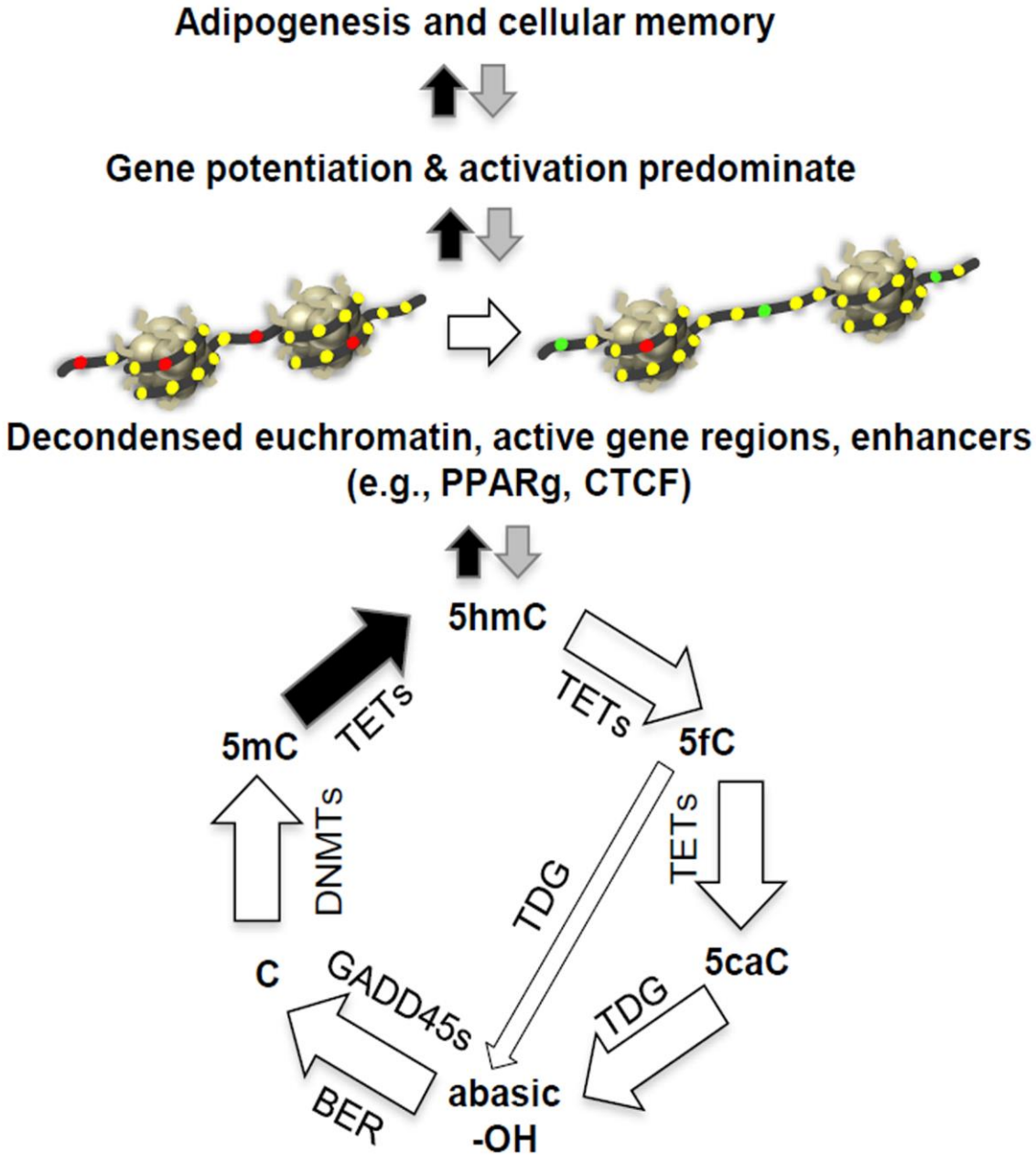
Adipogenesis and cellular memory
Gene potentiation & activation predominate
Decondensed euchromatin, active gene regions, enhancers
(e.g., PPARg, CTCF)
5hmC
TETs
5fC
TETs
5caC
TDG
abasic
-OH
BER
GADD45s
C
DNMTs
5mC
TETs
TDG

Figure 4.2. Purifying adipocyte cellular nuclei. A. Protocol for the rapid purification of cellular nuclei from adipose tissue. **B.** Phase contrast microscopic image (upper panel) and fluorescent microscopic image of DAPI staining (lower panel) of total VAT nuclei. DAPI stained for DNA (green). Phase contrast image of nuclei showed there was very little cellular debris. **C.** Western blot comparing the levels of actin and histone H3 in total *Ss*VAT homogenate (H) and purified *ss*VAT nuclear protein extracts (N). Because the protein band patterns in total cell homogenates are so distinct from the nuclear protein bands (i.e., common proteins cannot be aligned) total protein amounts could not be accurately estimated based on Coomassie stained gels run in parallel. Therefore, equal loading was predetermined by estimating Coomassie staining of equivalent samples electrophoresed into the end of stacking gel for only a brief period.

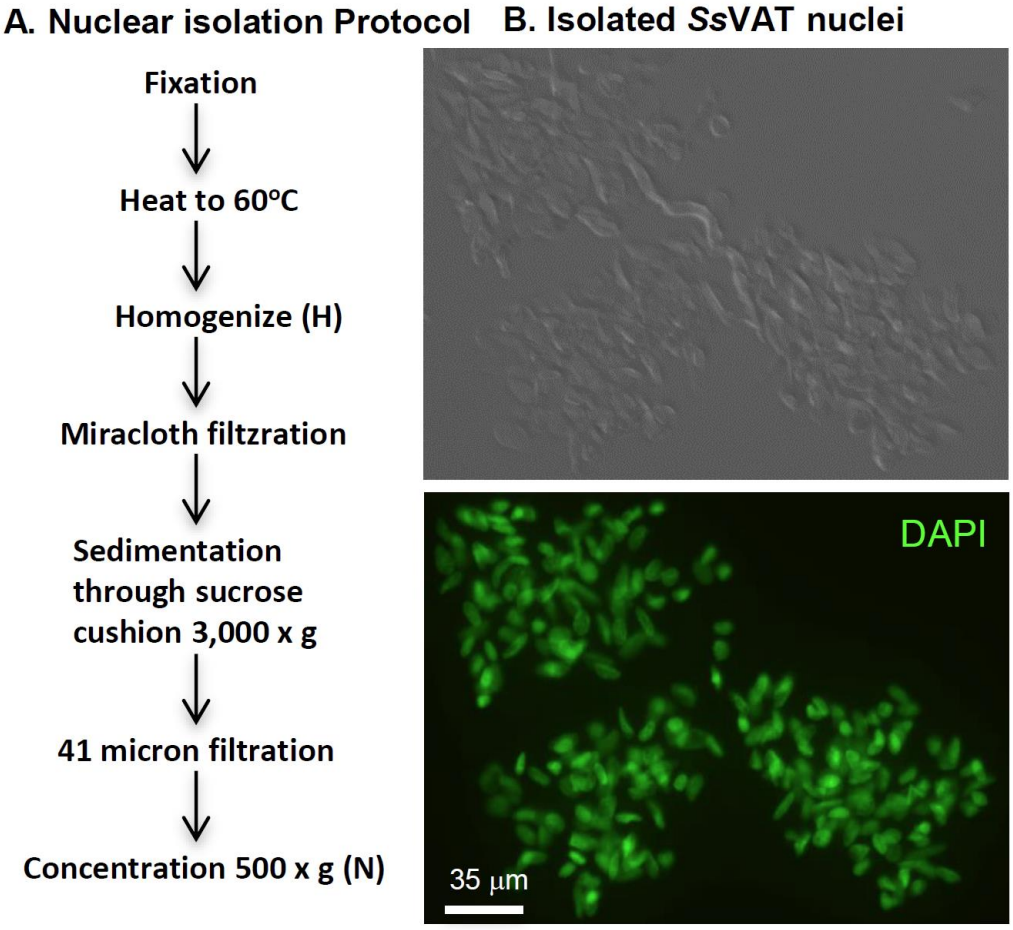
A. Nuclear isolation Protocol
B. Isolated SsVAT nuclei
Fixation
Heat to 60°C
Homogenize (H)
Miracloth filtzration
Sedimentation through sucrose cushion 3,000 x g
41 micron filtration
Concentration 500 x g (N)
DAPI
35 µm
C. Immunoblot analysis of nuclear enrichment
Actin
H
N
kDa
100-
75-
63-
48-
35-
25-
Histone H3
H
N
kDa
48-
35-
25-
20-
17-
11-
Coomassie
H
N

Figure 4.3. Fluorescence activated nuclear sorting (FANS) of three classes of visceral adipose tissue cellular nuclei immuno-stained for PPARg2. A. Histogram of PPARg2-Neg, -Low, -Med. and -High stained nuclei from sorting experiment (log scale) gated for DNA content (DAPI subset, **Supplemental Figure 4.S1B**) and forward and side light scattering (**Supplemental Figure 4.S1A**). **B**. Transcript levels of PPARg2 were assayed among the four fractions of nuclei by qRT-PCR. **C, D, E, F.** Merged immunofluorescence microscope images of four isolated fractions of nuclei without re-staining. **G.** Comparison of the average nuclear area for the four fractions from one experiment (N = 100). There were statistically significant differences between any of the two fractions of nuclear areas except for between PPARg2-Low and PPARg2-Neg fractions. A p value of $P<0.01$ is denoted by asterisk (*) and a p value of $P<0.001$ is denoted by double asterisk (**). **H.** PPARg2-High nuclei from image H showing the DAPI staining alone to reveal decondensed nuclei, however, some strongly stained PPARg2-High nuclei are small reflecting some heterogeneity in their morphology, as indicated by white arrows. For antibodies see **Supplemental Table 4.S1**.

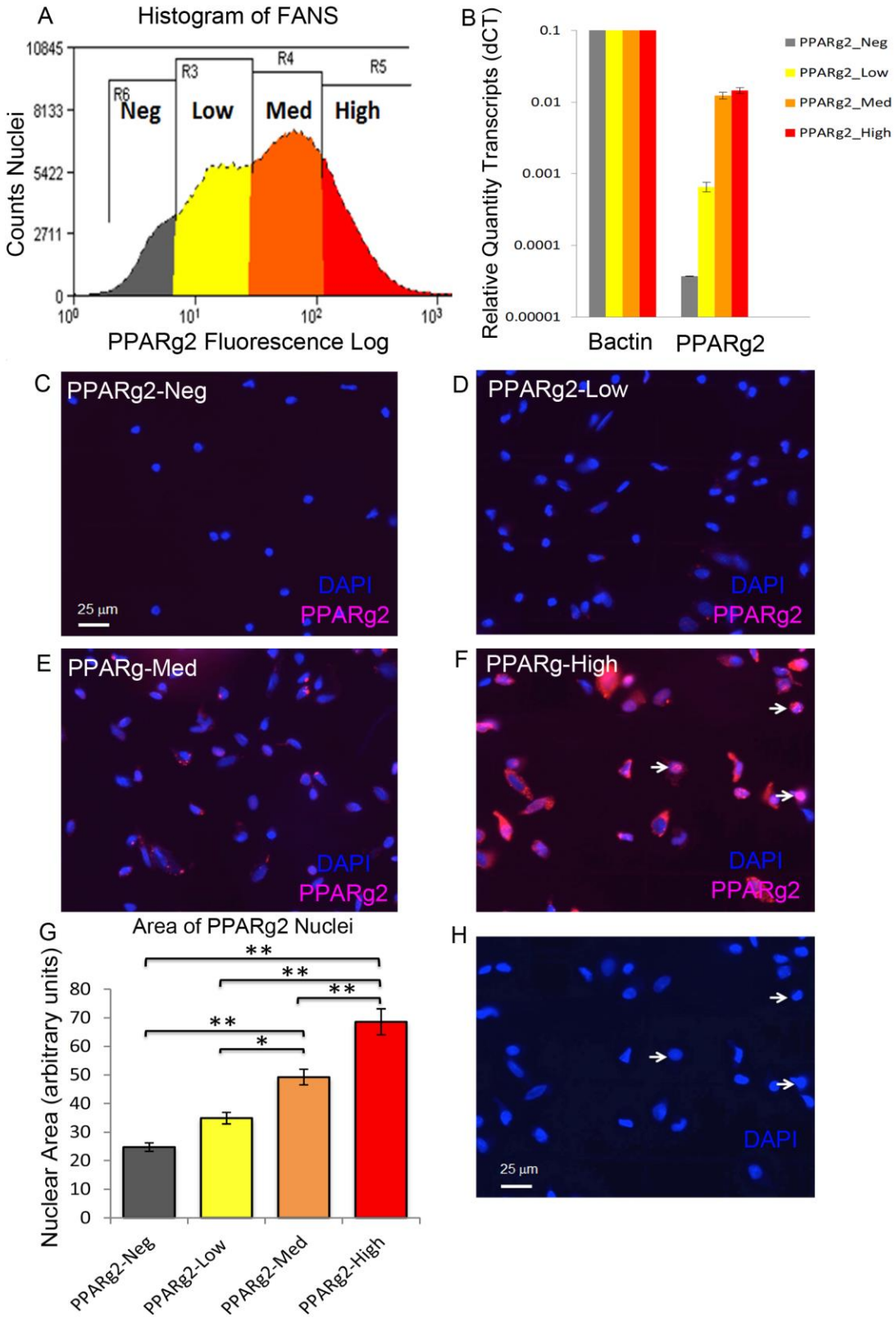
A
Histogram of FANS
Counts Nuclei
10845
8133
5422
2711
0
R6
R3
R4
R5
Neg
Low
Med
High
PPARg2 Fluorescence Log
B
Relative Quantity Transcripts (dCT)
0.1
0.01
0.001
0.0001
0.00001
PPARg2_Neg
PPARg2_Low
PPARg2_Med
PPARg2_High
Bactin
PPARg2
C
PPARg2-Neg
25 µm
DAPI
PPARg2
D
PPARg2-Low
DAPI
PPARg2
E
PPARg-Med
DAPI
PPARg2
F
PPARg-High
DAPI
PPARg2
G
Area of PPARg2 Nuclei
Nuclear Area (arbitrary units)
80
70
60
50
40
30
20
10
0
**
**
**
**
*
PPARg2-Neg
PPARg2-Low
PPARg2-Med
PPARg2-High
H
DAPI
25 µm

Figure 4.4. Transcript profiles for factors associated with cell type, pluripotency, and the cell cycle. Relative quantities (RQ) of marker transcripts among the four classes of VAT cell nuclei isolated by FANS were determined by qRT-PCR. The RQ of transcript level was calculated based on the dCT method including the standard deviation from the mean. Beta actin was used as the endogenous control. Assays were run in triplicate and standard errors are shown (See Materials and Methods). The oligonucleotide primers used and marker genes assayed are described in Supplemental **Tables 4.S2 and 4.S4,** respectively. A p value of $P<0.01$ is denoted by asterisk (*) and a p value of $P<0.001$ is denoted by double asterisk (**).

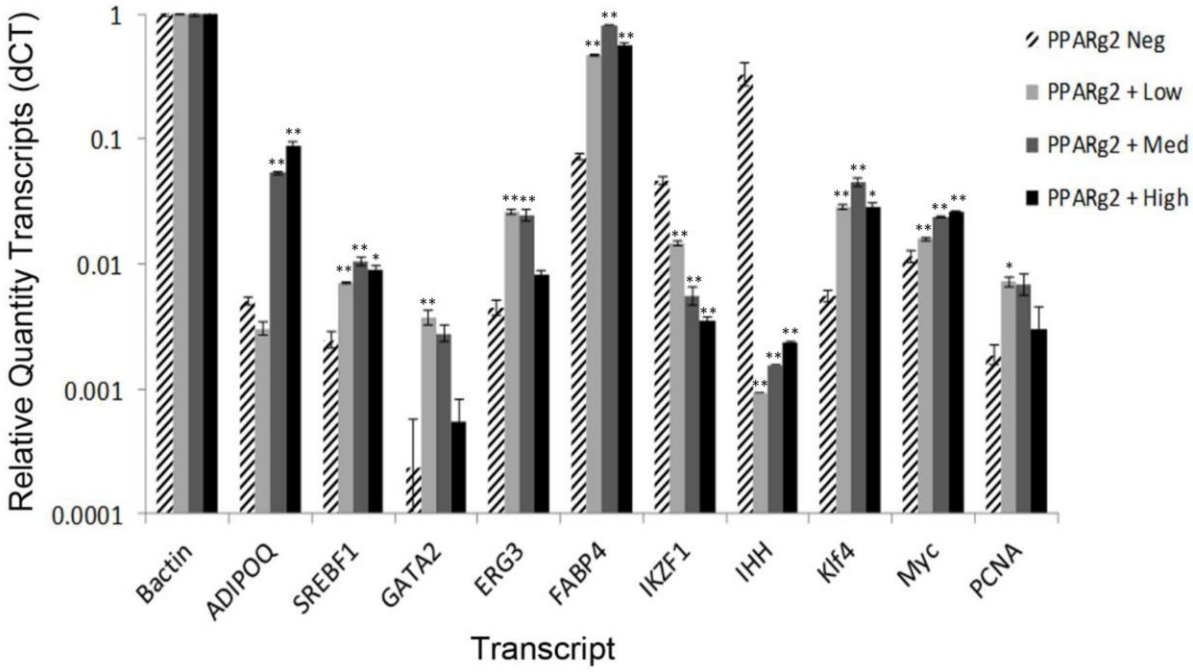
Relative Quantity Transcripts (dCT)
1
0.1
0.01
0.001
0.0001
PPARg2 Neg
PPARg2 + Low
PPARg2 + Med
PPARg2 + High
Bactin
ADIPOQ
SREBF1
GATA2
ERG3
FABP4
IKZF1
IHH
Klf4
Myc
PCNA
Transcript

Figure 4.5. Transcript profiles for factors controlling chromatin modification. Relative quantities of marker transcripts among the four classes of VAT cell nuclei isolated by FANS were determined by qRT-PCR. **A.** Factors controlling the levels of 5-methylcytosine modification of DNA (DNA cytosine methyltransferases DNMT1 and DNMT3A, methylcytosine dioxygenases (TET1, TET2, TET3), and activation-induced cytidine deaminase (AICDA)). **B.** Factors controlling acetylation of nucleosomal histones (deacetylases Sirt1, HDAC2, and HDAC3 and histone lysine transacetylases KAT2B and KAT3B). **C.** Factors involved in histone lysine methylation (ARID1A/BAF250, MLL3, and PAXIP1/PTIP impact histone H3 methylation at lysine 4, and SETDB1 and KDM4A impact histone H3 methylation at lysine 9). **D**. Factors involved in histone arginine methylation (JMJD6 is histone arginine demethylase and CARM1/PRMT4 and PRMT5 are arginine methyltransferases). See legend to Figure 4 for details of the RQ calculation. A p value of $P<0.01$ is denoted by asterisk (*) and a p value of $P<0.001$ is denoted by double asterisk (**).

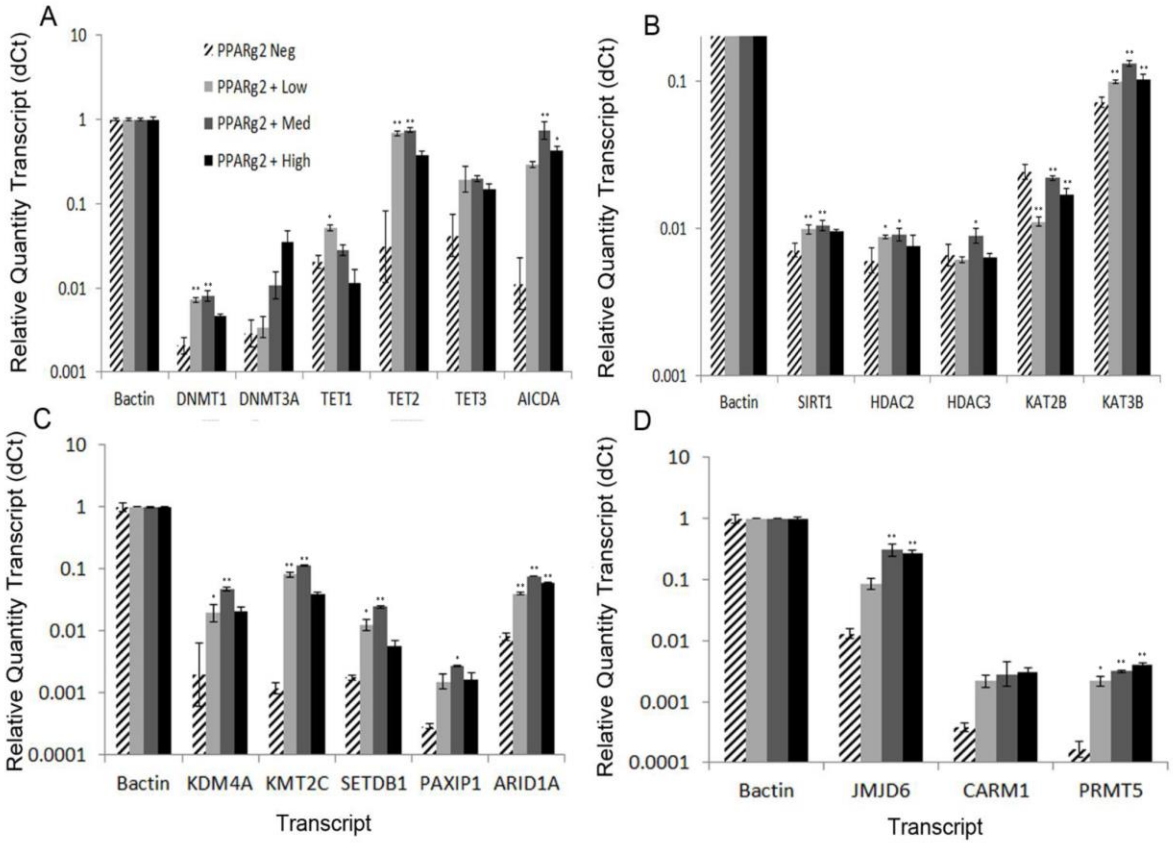
A
Relative Quantity Transcript (dCt)
PPARg2 Neg
PPARg2 + Low
PPARg2 + Med
PPARg2 + High
Bactin
DNMT1
DNMT3A
TET1
TET2
TET3
AICDA
B
Relative Quantity Transcript (dCt)
Bactin
SIRT1
HDAC2
HDAC3
KAT2B
KAT3B
C
Relative Quantity Transcript (dCt)
Bactin
KDM4A
KMT2C
SETDB1
PAXIP1
ARID1A
Transcript
D
Relative Quantity Transcript (dCt)
Bactin
JMJD6
CARM1
PRMT5
Transcript

Figure 4.6. Distribution of 5hmC among adipose tissue nuclei. IFM and FNC were used to examine 5hmC levels among visceral adipose tissue nuclei. **A.** A field of VAT nuclei examined with various combinations of DAPI staining for DNA, and immunostaining with mouse anti-PPARg2 + goat anti-mouse Alexafluor488 and rabbit anti-5hmC + goat anti-rabbit Alexafluor633. White arrows indicate those large, decondensed nuclei that are stained strongly for both 5hmC and PPARg2. **B.** Flow Cytometry of VAT nuclei immunostained as in A. **C.** Goat anti-rabbit secondary antibody used in B shows only modest background staining of nuclei. Nuclei were gated for DAPI (>2C DNA content) and size and shape by light scattering as in **Supplemental Figure 4.S1.** For antibodies see **Supplemental Table 4.S1**.

A Immunofluorescence of PPARg2 and 5hmC in isolated nuclei

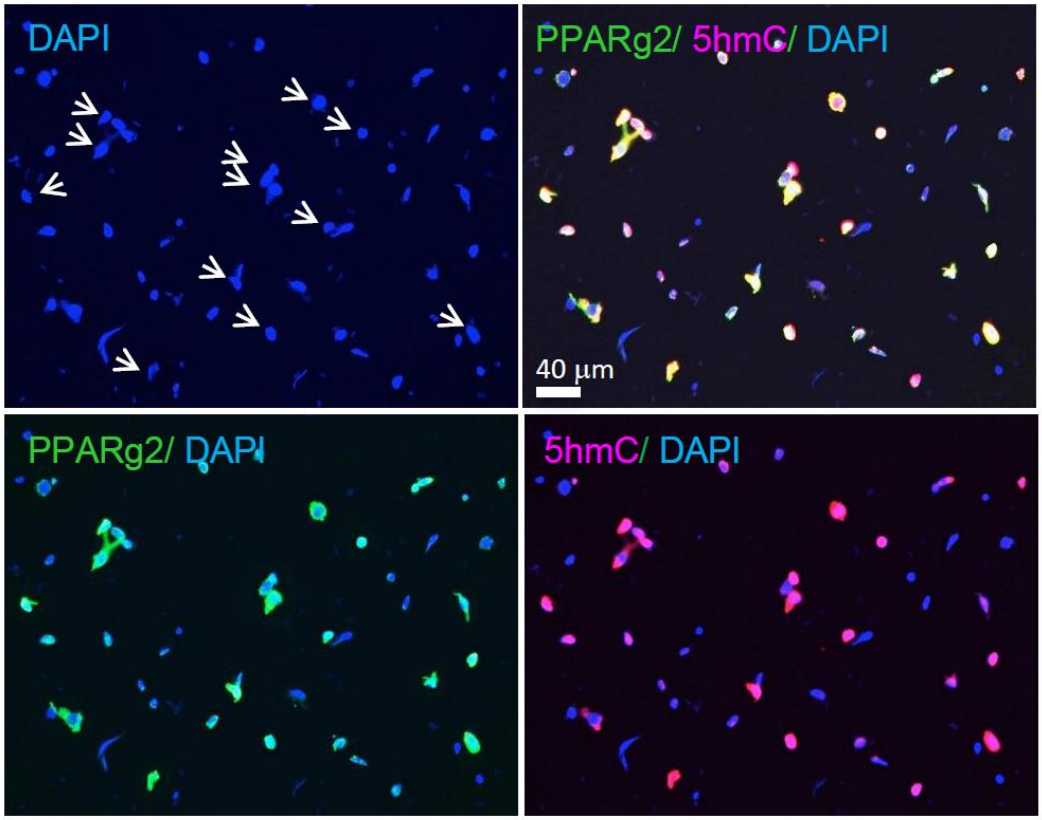

B FNC PPARg2 vs 5hmC

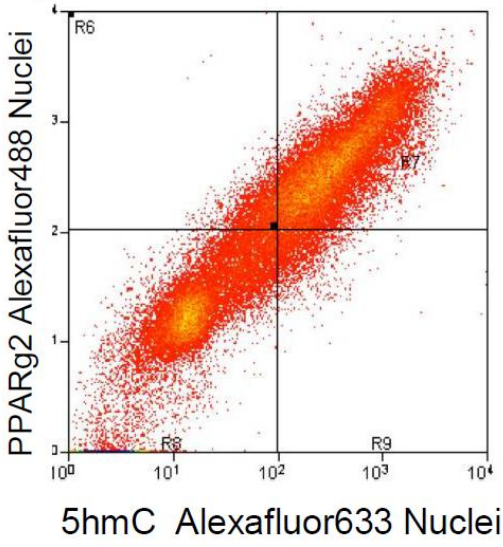

C FNC secondary antibody control

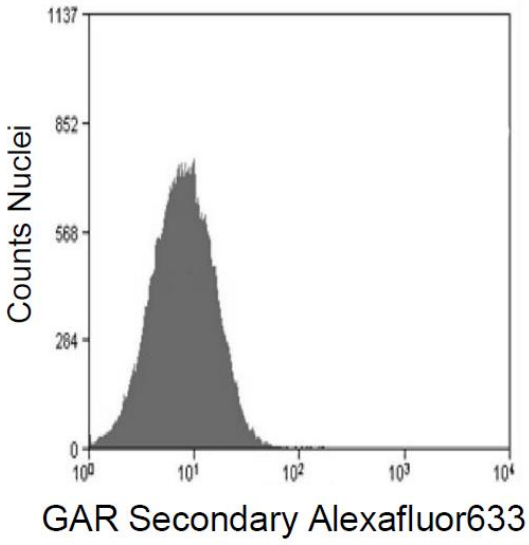

Figure 4.7. 5hmC levels vary dramatically across gene regions based on transcript levels in adipose tissue and the class of VAT nuclei. 25,321 *S. scrofa* genes were ranked into five quintiles (5,064 to 5,065 genes in each) based on the levels of adipose tissue transcript expression determined by RNAseq (1st quintile represents the lowest levels of RNA expression, 5th quintile the highest). **A.** The differences in gene region 5hmC levels for PPARg2-High, -Low, and -Neg nuclei are shown for each quintile of expressed genes. PPARg2-Neg nuclei had the lowest 5hmC levels in each quintile, while PPARg2-High nuclei had slightly higher 5hmC levels than PPARg2-Low nuclei. **B.** 5hmC levels are shown for all 5 quintiles for the PPARg2-High, PPARg2-Med+Low, and PPARg2-Neg nuclei. **A & B.** 5hmC levels were lower in the gene body relative to the flanking gene regions for the two lowest quintile expression groups of transcripts, whereas for the 3 highest transcript expression groups the pattern was reversed with 5hmC levels being the highest in the gene body. Gene regions were divided into three parts: 100 kb upstream of the transcription start site (UTSS), gene body (GB, TSS to transcription stop site (TTS)), and 100 kb downstream of the TTS (DTTS).

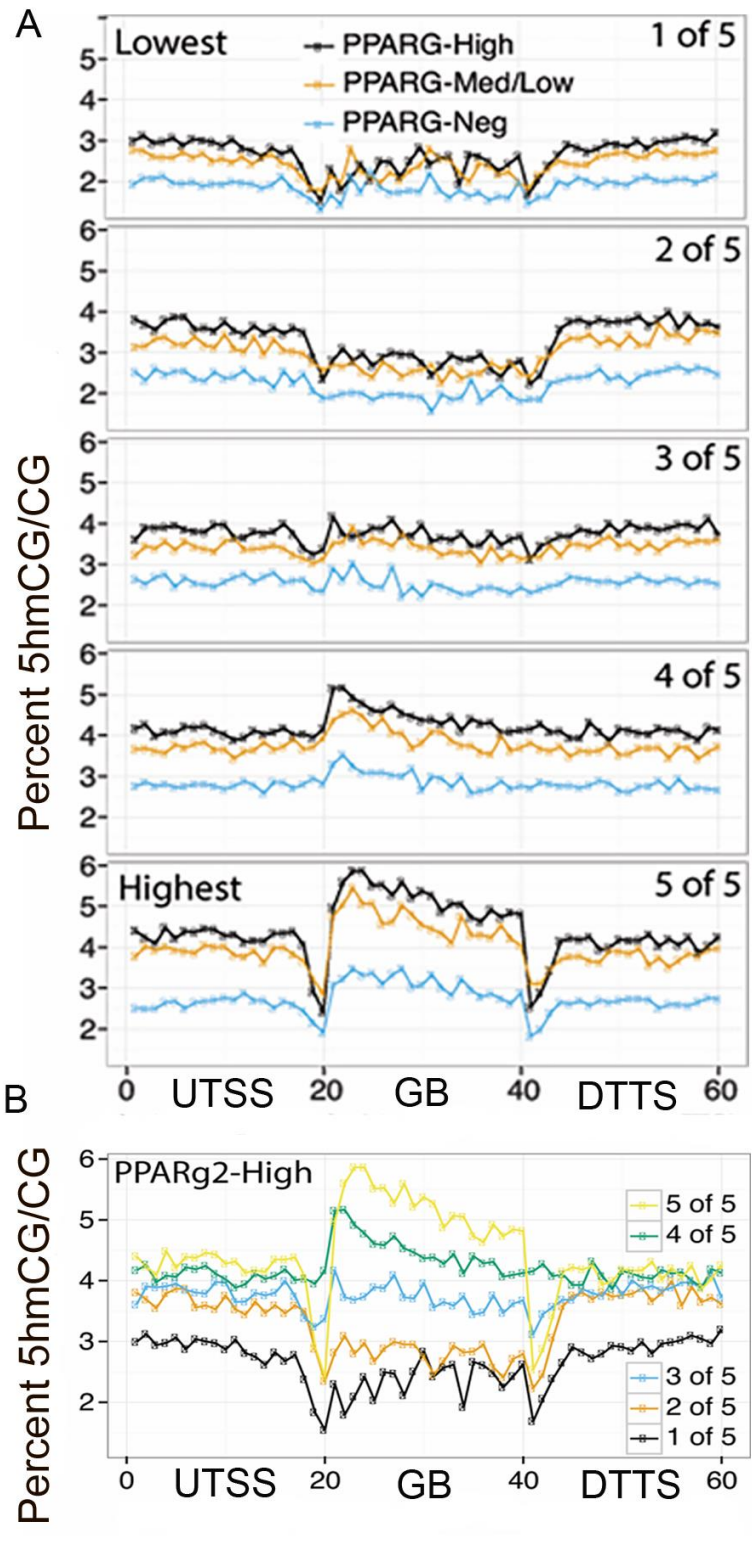
A
Lowest
PPARG-High
PPARG-Med/Low
PPARG-Neg
1 of 5
2 of 5
3 of 5
4 of 5
Highest
5 of 5
Percent 5hmCG/CG
0
UTSS
20
GB
40
DTTS
60
B
PPARg2-High
5 of 5
4 of 5
3 of 5
2 of 5
1 of 5
Percent 5hmCG/CG
0
UTSS
20
GB
40
DTTS
60

Supplemental Figure 4.S1. Additional information about *ss*VAT Nuclei sorted by FANS based on PPARg2 staining. Labeled nuclei were gated for size and shape (**A**) and DNA content (**B**) to reduce the number of contaminating particles sorted. There was no significant population of doublet nuclei was detected based on side scatter band width (**C**). **D.** Background fluorescence of PE-conjugated goat anti-rabbit secondary antibody (blue) used to label rabbit anti-PPARg2 for FANS (pink) as shown in detail in Figure 3. The low background staining levels from the secondary antibody were used to define the PPARg2-Neg class of nuclei.

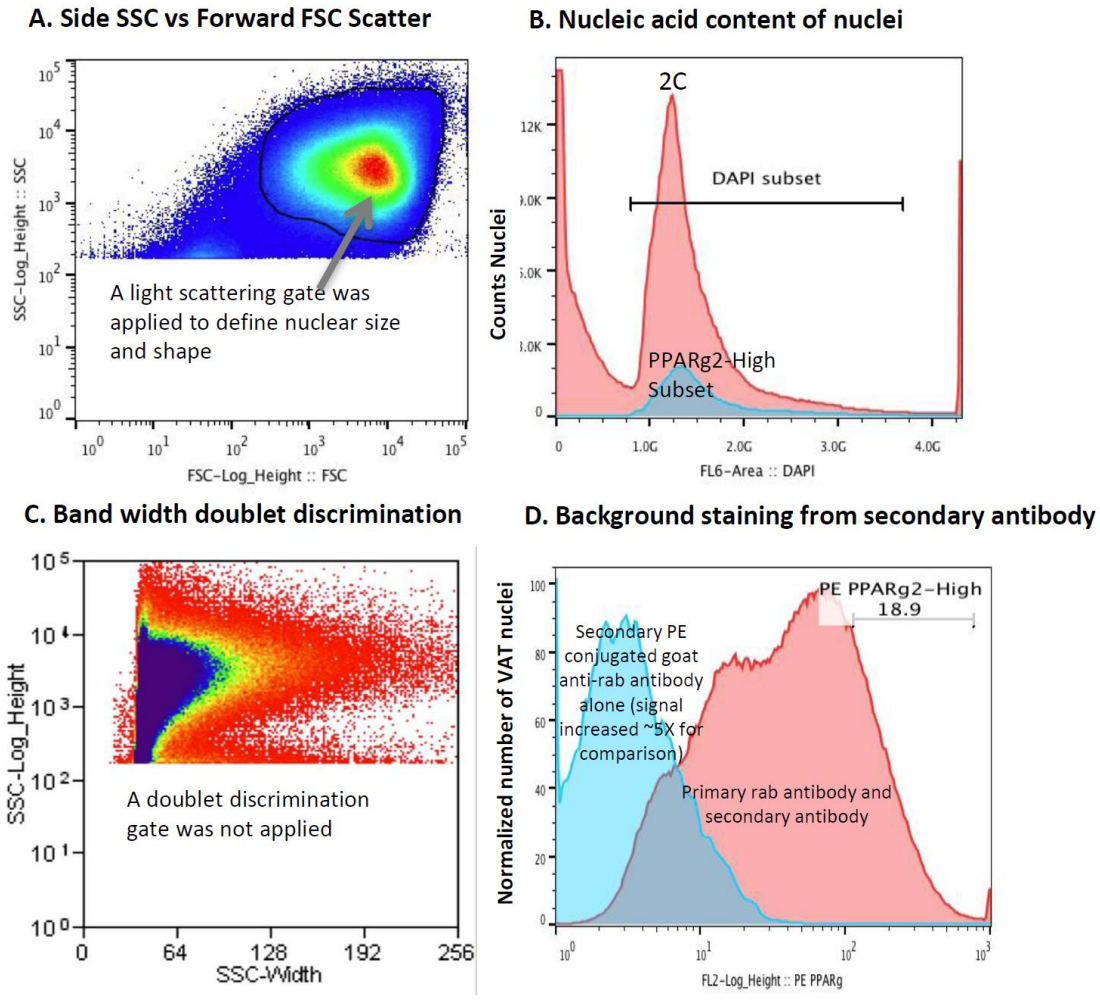

Supplemental Figure 4.S2. *Ss*VAT nuclei staining pattern for PPARg1 and PPARg2. A. Nuclei were stained with DAPI for DNA (blue) and PPARg1 (red). Nuclei were stained with monoclonal antibody to PPAR-gamma (Abcam Cat.# ab70405) and then goat anti-mouse IgG conjugated with R-PE (Invitrogen Cat.# P-852) and counter stained with DAPI (blue).**B**. Nuclei were stained with DAPI for DNA (green) and PPARg2 (red). Nuclei were stained with polyclonal antibody to PPAR gamma 2 (Abcam Cat. # ab45036) and then Alexa fluor 633 goat anti-rabbit IgG secondary antibody (Life technologies, A21070) and counter stained with DAPI (green).

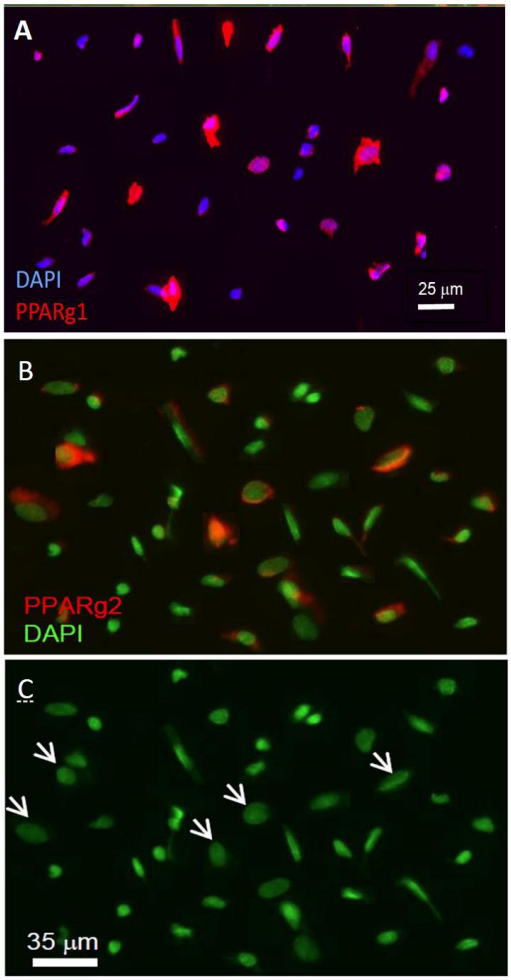

Supplemental Figure 4.S3. The level of PPARg1 was used as an immuno-marker to sort *ss*VAT nuclei. A. Histogram of PPARg1-Neg, -Low and -High stained nuclei from sorting experiment (log scale) gated for DNA content and forward and side light scattering (not shown). PPARg1 antibody (Abcam Cat.# ab70405). **B, D, E.** Histograms of three sorted nuclear fractions re-examined by cytometry to confirm their relative PPARg1 staining levels. **E, F, G**. Merged immunofluorescence microscope images of three isolated fractions of nuclei without re-staining with DAPI shown in green and PPARg1 in red.

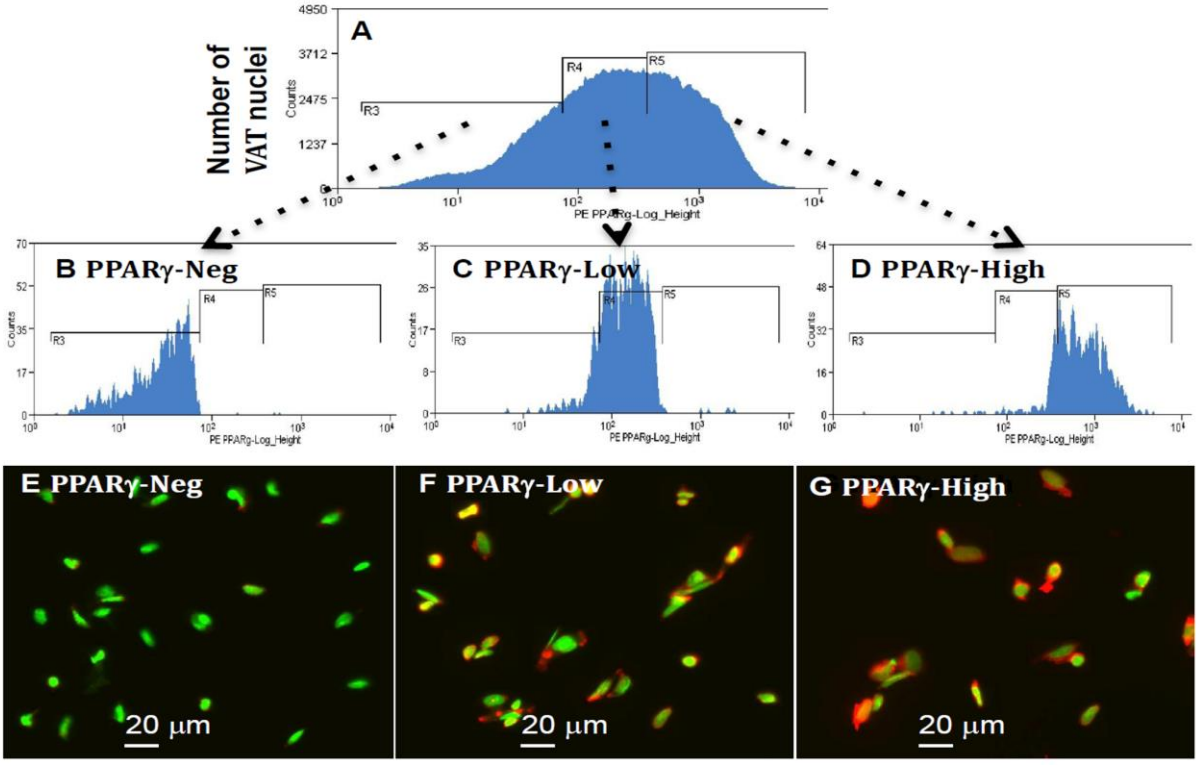

Supplemental Figure 4.S4. Nuclei sorted based on levels of immunostained PPARg1 were not well resolved from the nuclei of other cell types based on qRT-PCR analysis of cell type markers. Relative quantities of marker transcripts among the four classes of VAT cell nuclei isolated by FANS were determined by qRT-PCR. Using either *Beta actin* or *RPL13A* as endogenous controls gave similar results. Cell-type-specific markers *ADN, SREBF1, GATA2, ERG3, IKAROS,* and *CD31* were examined. The properties of maker genes and the oligonucleotide primers are described in **Supplemental Tables 4.S2 and 4.S4,** respectively.

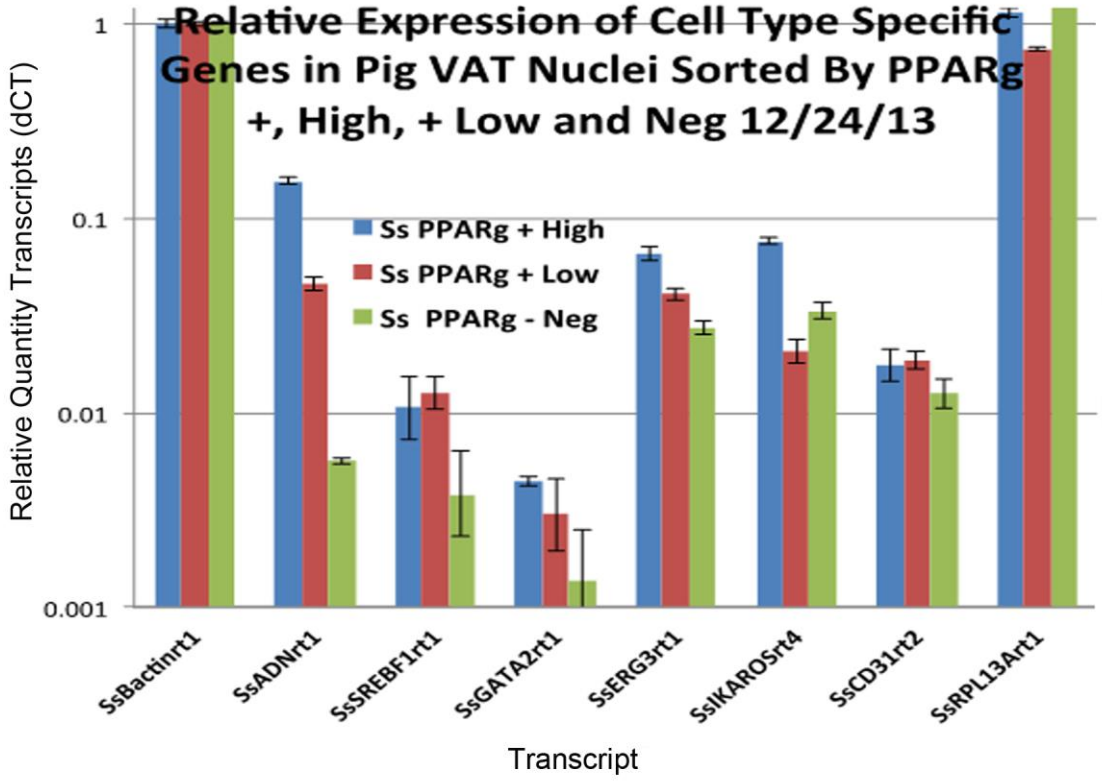

Supplemental Figure 4.S5. 5hmC metagene plots for six groups of genes from published dataset (Lister et al., 2013) with different coverage. To demonstrate that relatively low coverage don't affect 5hmC distribution for metagene plots, published dataset from Lister et al., 2013 were downloaded and 5hmC metagene plots with coverage ranging from 0.2X to 13X were made for six groups of genes. The patterns of metagene plots didn't change much even for coverage as low as 0.2X.

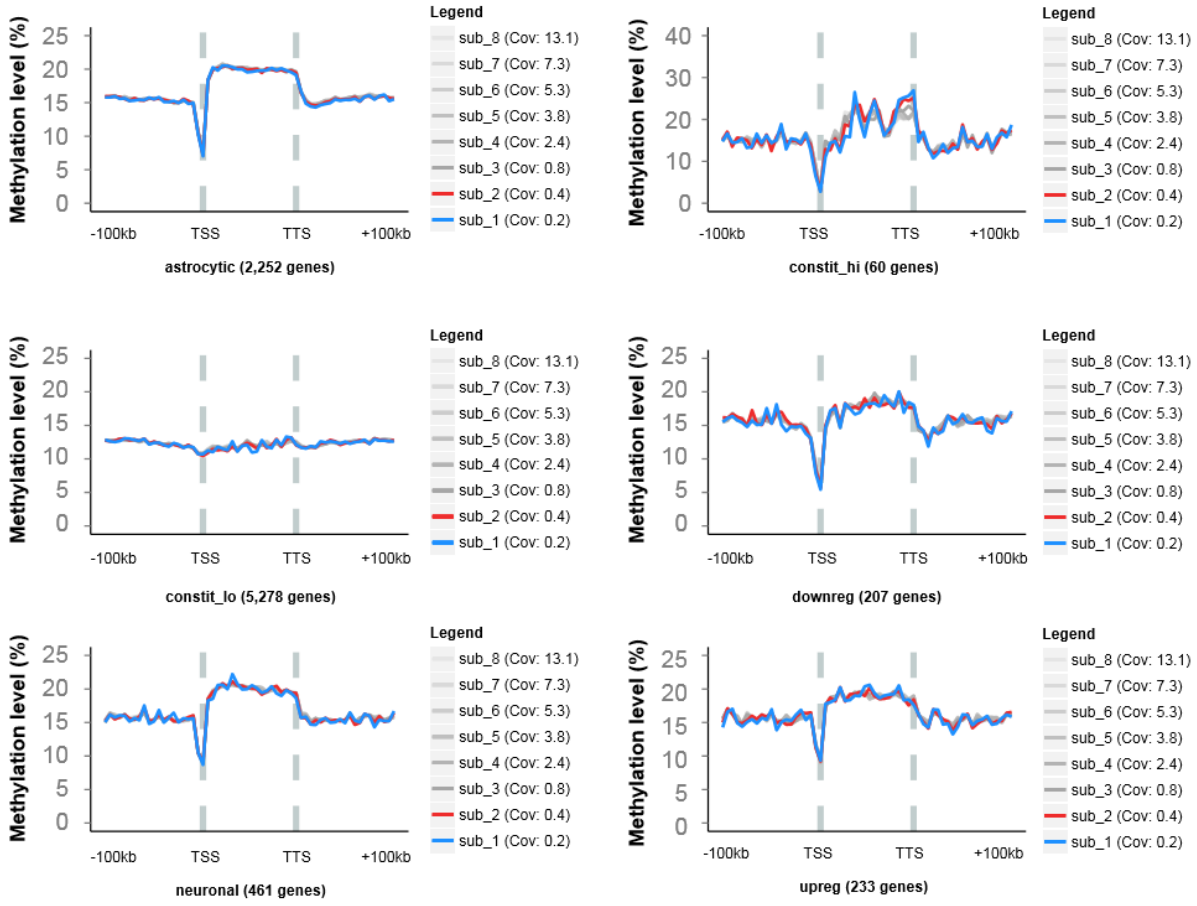

Supplemental Table 4.S1. Primary and secondary antibodies used in this paper.

Primary antibodies					
Antibody name	**Host species**	**immunogen**	**Clonality**	**Company**	**Catalogue or clone number**
Figure 2, 3					
PPAR gamma 2(Chen and others, 2011)	Rabbit	Synthetic peptide corresponding to Human PPAR gamma 2 aa 1-16. Sequence: MGETLGDSPIDPES DSC	Polyclonal	Abcam	ab45036
Actin (Kandasamy and others, 2012)	Mouse	Recombinant Arabidopsis actin protein (ACT1)	Monoclon al	Thermo Scientific	mAbGEa
Histone H3 (Yu and others, 2015)	Rabbit	Synthetic peptide within Human Histone H3 aa 100-135 (C terminal)	Polyclonal	Abcam	ab70550
Figure 6					
5hmC antibody(Thomson and others, 2015)	Rabbit	This antibody was raised against 5-hydroxymethylcytidin e conjugated to KLH and recognizes 5-hydroxymethylcytosin e.	Polyclonal	Active motif	39769
PPARg2 *	Mouse	A DNA sequence encoding the N-terminal segment (Met 1-Thr 239) of the extracellular domain of human B7-H1(NP_054862.1) was expressed with a C-terminal polyhistidine tag.	Polyclonal	Abeome	8769
Figure S2 and S3					

Anti-PPAR gamma antibody (Wolf and others, 2014)	Mouse	Recombinant fragment: KLIYDRCDLN CRIHKKSRNK CQYCRFQKCL AVGMSHNAIR FGRMPQAEKE KLLAEISSDI DQLNPESADL RALAKHLYDS YIKSFPLTKA KARAILTGKT T, corresponding t	Monoclonal	Abcam	ab70405
Figure S5					
H3K4Me1(Zhang and others, 2015)	Rabbit	Synthetic peptide within Human Histone H3 aa 1-100 (mono methyl K4) conjugated to Keyhole Limpet Haemocyanin (KLH). The exact sequence is proprietary.	Polyclonal	Abcam	ab8895
H3K9Me1(Baas and others, 2014)	Rabbit	Synthetic peptide corresponding to Human Histone H3 aa 1-100 (mono methyl K9)	Polyclonal	Abcam	ab8896

Secondary fluorescent antibodies

Name	Company	Cat. #
Goat pAb to Rb IgG (PE)	Abcam	ab97070
Alexa fluor 633 goat anti-rabbit IgG	Life technologies	A21070
Alexa fluor 488 goat anti-mouse IgG	Life technologies	A11001

* We validated PPARg2 mouse polyclonal antibody (Clone #: 8769) from Abeome company by staining *Sus scrofa* visceral adipose tissue (*Ss*VAT) nuclei (Figure 6), and we saw good staining signal on most of the large, decondensed *Ss*VAT nuclei.

Supplemental Table 4.S2. Oligonucleotide primers for qRT-PCR analysis of *Sus scrofa* transcript levels in isolated nuclei.

	Sense	Antisense	
Controls			
Beta actin	CTTCTAGGCGGACTGTTAGTTG	Beta actin	AGCCATGCCAATCTCATCTC
RPL13A	GGAGAAGGCCAAGATCCATTAC	RPL13A	CGTGAACCTGTCGATCTTCTT
Figure 4			
ADN	CAGCCTCTACAAGAAGGACAAG	ADN	CTCCAGATAGAGGAGCACAGA
SREBF1	CGGAGGCGAAGCTGAATAAA	SREBF1	CTTCTGGTTGCTCTGCTGAA
GATA2	ACGACAACCACCACCTTATG	GATA2	CATGGTCAGTGGCCTGTTTA
ERG3	CCAGAATATCGATGGGAAGGAG	ERG3	GGTAGTGGAGATGTGACAGAAG
aP2	GTGTCACGGCTACCAGAATTTA	aP2	CGGGACAATACATCCAACAGAG
IKAROS	CGGTTGGTAAACCTCACAAATG	IKAROS	CAGCGCTCTTTATGTTCCTCTA
IHH	CAGCTTGCTCTCACTACAGTT	IHH	CAGCTTGCTCTCACTACAGTT
Klf4	TCGCCTTGCTGATTGTCTATT	Klf4	TGCCAGAGATCCTTCTTCTTTG
Myc	CGCTGGATTTCCTTCGGATAG	Myc	GAGTCGTAGTCGAGGTCATAGT
PCNA	AGGAGGAAGCAGTTACCATAGA	PCNA	CTGAGTGTGACTGTAGGAGAGA
Figure 5A			
DNMT1	GCACCTCATTTGCCGAGTAT	DNMT1	CTGCAGGAACTCAACCACTATC
DNMT3A	TCCATAAAGCAGGGCAAAGA	DNMT3A	CATGTTGGAGACGTCGGTATAG
TET1	GTGTCGAGGAATCCGAAGTAAA	TET1	GAGAATAGTCCTTCACCACCAC
TET2	CAGGAGGGAAAGAATGCTAACT	TET2	TCCATGGAAGAGGCAGAAAC
TET3	CTGAAGAGCACCCATCCTTT	TET3	CTTCGGGAAACTCTGTTCTAGG
AICDA	GAGGCAGTTCCTCTACCAATTC	AICDA	TGAGAAGGAGGTGGCACTAT
Figure 5B			
SIRT1	GTGAGGCAAAGGTTCCCTATTA	SIRT1	CCCTGAAAGTAAGACCAGTAGC
HDAC2	CAACCTAGTGCTGTGGTGTTA	HDAC2	CACACATTTAGCGTGACCTTTG
HDAC3	CTGGTTACTTTCAGGGCAGTTA	HDAC3	TAGCCTTGAGAGGGAGAAGAA
KAT2B	CGGATGCCAAAGGAGTACAT	KAT2B	GGAAACAGATGCCACCAATAAC
KAT3B	GCGAAGGACTAGACTGCAAA	KAT3B	GGTTGTGGCTGTCCCATATTA
Figure 5C			
KDM4A	CCTTCGACCCAGATTCGTAAA	KDM4A	ACAGAAGTCACAATCTCCAAGG
KMT2C	GGAGTCACCGATACACAGAATAC	KMT2C	CTGCTGGTGGAGGATGATTT
SETDB1	CATGTTGACCAGCTCTTTGATG	SETDB1	CTCGGTATTGTAGTCCCAGTTTAG
PAXIP1	CTCATGGTTTCCCATCCTCTTC	PAXIP1	CCACTCATACCACACCTTCTTG
ARID1A	TGAACCGCACGGATGATATG	ARID1A	GAGGCTGAAGAGGACATGTAAG

Figure 5D			
JMJD6	TCAAGTGCGGTGAGGATAATG	JMJD6	CCGTAGCTGCTGTCAAAGAT
CARM1	GAAGGAGATTTGCACAGGATAGA	CARM1	GGACAACCACACGGTCATTA
PRMT5	CATCACACACAGAGGAGTACAG	PRMT5	GAAGGTCAGCACCAATTTCAAG
Figure S3			
CD31-S2	AGGATCAGGAGGGACAGTATTA	CD31-S2	CACTGCGATGAGTCCTTTCT

Supplemental Table 4.S3. The genome coverage achieved by our TAB-seq was listed in the last column as a fraction of our coverage to *Sus scrofa* Sscrofa10.2 (GCA_000003025.4) reference genome.

Sample	Total Mapped Reads		Lambda						Genome coverage
			CpG sites (5mC)			Non-CpG sites			
	number	%	methylated Cs	mapped Cs	%	methylated Cs	Mapped Cs	%	
PPARg2-High	7,144,386	36.18%	6,818	699,586	0.97%	14,560	2,076,320	0.70%	0.41
Pooled PPARg2-Med and Low	6,143,977	35.98%	6,962	704,566	0.99%	15,146	2,096,005	0.72%	0.35
PPARg2-Neg	6,980,655	36.45%	6,854	728,707	0.94%	14,490	2,159,023	0.67%	0.40

Provided in the table are the metrics related to the TAB-seq analysis. The genome coverage achieved by our TAB-seq meta-analysis is listed in the last column as a fraction of our coverage to the Sus scrofa reference genome Sscrofa10.2.

Supplemental Table 4.S4. Summary of the marker genes properties being assayed.

Symbol	Full Name	Description
ACTB/Bactin	Beta actin	This gene encodes one of six different actin proteins. Actins are highly conserved proteins. This actin is a major constitute of the contractile apparatus and one of the two nonmuscle cytoskeletal actin.
ADIPOQ	Adiponectin	This gene is expressed in adipose tissue exclusively. It is an important adipokine involved in the control of fat metabolism and insulin sensitivity. It is expressed in white, beige, and brown adipose tissue.
AICDA	Activation-induced cytidine deaminase	This gene encodes a RNA-editing deaminase that is a member of the cytidine deaminase family.
FABP4	Adipocyte protein 2, fatty acid binding protein 4	This gene encodes the fatty acid binding protein found in adipocytes. Its roles include fatty acid uptake, transport, and metabolism. After 10 days of 3T3-L1 differentiation, aP2 was induced 150-fold in differentiated adipocytes.
ARID1A	AT rich interactive domain 1A	This gene encodes a member of the SWI/SNF family, which have helicase and ATPase activities and are able to regulate transcription of certain genes by altering the chromatin structure around those genes. It is required for adipogenesis from ES cells. Controls Sox2, Utf1, and Oct4 expression.
CARM1	Coactivator-associated arginine methyltransferase 1	This gene belongs to the protein arginine methyltransferase (PRMT) family. It methylates histone H3 at Arg-17(H3R17me), forming H3R17me2, leading to activate transcription via chromatin remodeling.
CD31/PECAM-1	Cluster of differentiation 31	This protein is found on the surface of platelets, monocytes, neutrophils, and some types of T-cells, and makes up a large portion of endothelial cell intercellular junctions.
DNMT1	DNA methyltransferase 1	DNMT1 has a role in the establishment and regulation of tissue-specific patterns of methylated cytosine residues. DNA methyltransferases preserve the methylation pattern of the parent cell during mitosis by methylating the nonconserved strand during replication.
DNMT3A	DNA methyltransferase 3A	DNMT3A is required for genome-wide de novo methylation and is essential for the establishment of DNA methylation patterns during development.
ERG3	Early growth response protein 3	This gene encodes a transcriptional regulator that belongs to the EGR family of C2H2-type zinc-finger proteins. It plays a role in muscle development, lymphocyte development, endothelial cell growth and migration. It is a sterol C5-desaturase involved in cholesterol biosynthesis.

GATA2	GATA binding protein 2	It promotes the differentiation of MSCs into adipocytes.
HDAC2	Histone lysine deacetylase 2	It is responsible for the deacetylation of lysine residue at the N-terminal regions of core histones. It plays an important role in transcription regulation, cell cycle progression and development.
HDAC3	Histone lysine deacetylase 3	It plays a critical role in transcription regulation, cell cycle progression, and development. It has deacetylase activity and represses transcription when tethered to a promoter.
IKZF1	Ikaros family zinc finger protein 1	The gene encodes a transcription factor that belongs to the family of zinc-finger DNA-binding proteins associated with chromatin remodeling. The expression of this protein is restricted to the hemo-lymphopoietic system, and it functions as a regulator of lymphocyte differentiation.
IHH	Indian Hedgehog	IHH is present in preadipocytes and its expression decreases upon differentiation. As mesenchymal cells commit into adipocytes they lose their ability to express Ihh.
JMJD6	Jumonji Domain Containing 6	This gene encodes a nuclear protein with a JmjC domain. It is a histone arginine demethylase.
KAT2B	Lysine acetyltransferase 2B or P300/CBP-associated factor	It is a histone acetyltransferase to promote transcription activation. It has significant histone acetyltransferase activity with core histones (H3 and H4), and also with nucleosome core particles.
KAT3B	Lysine acetyltransferase P300	It functions as histone acetyltransferase that regulate transcription via chromatin remodeling.
KDM4A	Lysine-specific demethylase 4A	Histone demethylase that specifically demethylates lysine 9 and lysine 36 residues of histone H3. KDM4A generates H3K9Me from the di-and tri-methylated forms.
KLF4	Kruppel-like factor 4	It regulates the expression of key transcription factors during embryonic development. Plays an important role in maintaining embryonic stem cells, and in preventing their differentiation.
KMT2C	Lysine specific methyltransferase 2C	It is a histone lysine methyltransferase that methylate lysine 4 of histone H3. H4K4 methylation represents a specific tag for epigenetic transcription activation.
MBD4	Methyl-CpG biding domain protein 4	Mismatch-specific DNA N-glycosylase involved in DNA repair. It has thymine glycosylase activity and is specific for G:T mismatches within methylated and unmethylated CpG sites. It can also remove uracil or 5-fluorouracil in G:U mismatches.
MYC	Proto-oncogene C-	The protein encoded by this gene is a multifunctional, nuclear phosphoprotein that plays a role in cell cycle progression,

	Myc	apoptosis and cellular transformation.
PAXIP1	PAX Interacting (With Transcription-Activation Domain) Protein 1	Histone Methylation Regulator PTIP Is Required for *PPARγ* and *C/EBPα* Expression and Adipogenesis. PTIP is a protein that associates with histone H3K4 methyltransferases.
PCNA	Proliferating cellular nuclear antigen	PCNA acts as a homotrimer and helps increase the processivity of leading strand synthesis during DNA replication.
PPARg	Peroxisome proliferator-activated receptor gamma	This gene encodes a member of the peroxisome proliferator-activated receptor (PPAR) subfamily of nuclear receptors. PPAR gamma is a regulator of adipocyte differentiation.
PPARg2	Adipocyte specific 2nd isoform of peroxisome proliferator-activated receptor gamma	N-terminal domain isoform of PPARg. It has highest expression in adipose tissue than any other tissues, like muscle, spleen, heart and liver. It is more adipocyte specific. It is a nuclear receptor that binds peroxisome proliferators such as fatty acids. Once activated by a ligand, the nuclear receptor binds to DNA specific PPAR response elements (PPRE) and modulates the transcription of its target genes.
PRMT5	Protein arginine methyltransferase 5	This gene encodes a histone arginine methyltransferase 5. PRMT5 plays a high-level causal role in adipogenesis, as small RNA silencing PRMT5 expression blocks PPARg2 expression and efficiently blocks the differentiation of 3T3-L1 preadipocytes into mature lipid-containing adipocytes. PRMT5 promotes gene expression of PPARgamma2 and its target genes during adipogenesis.
SETDB1	SET domain bifurcated 1	This gene encodes a histone lysine methyltransferase. SETDB1 renders chromatin inactive through H3K9 methylation to shut off PPARg. SETDB1 is intriguing as this is the first methyl transferase for which its enzymatic function has been linked to a cell fate decision through epigenetic regulation in response to extracellular stimulation.
SIRT1	Sirtuin 1 deacetylase	It is also known as NAD-dependent deacetylase sirtuin-1. SIRT1 is a histone deacetylase.
SREBF1	Sterol regulatory element binding transcription factor 1	Transcriptional activator required for lipid homeostasis. It is expressed in adipocytes, fatty liver cells. It regulates glucose metabolism and fatty acid and lipid production and its expression is regulated by insulin.
TET1, 2, 3	Ten-eleven	TETs catalyze the conversion of 5-methylcytosine (5mC) to 5-

	translocation methylcytosine dioxygenases 1, 2, and 3	hydroxymethylcytosine (5hmC) and subsequent conversion 5hmC into 5-formylcytosine (5fC) and 5-carboxylcytosine (5caC), and plays a key role in active DNA demethylation.
TDG	Thymine-DNA Glycosylase	TDG plays a key role in active DNA demethylation. It recognizes 5fC and 5caC and mediates their excision through base-excision repair to install an unmethylated cytosine.

CHAPTER 6

CONCLUSIONS

In this dissertation I studied the cell-type-specific epigenetics from organ-derived neurons and adipocytes. The majority of previously published studies examined epigenetic profiles of samples derived from whole brain and adipose tissues with more complex mixtures of cell types. As epigenetic profiles have been shown to be different in different cell and tissue types, the data from these studies is the weighted average of the epitype of all included cell types. Thus the cell-type-specific epitype is likely to be lost in the average. Studying individual cell types instead of a mixture cells might reveal critical information to understanding the cell-type-specific features. Therefore, the studies in this dissertation dissected the cell-type-specific epigenetics of mouse brain derived neurons and pig visceral adipose tissue derived adipocytes in the context of their other constituent cell types.

Chapter 3 of this dissertation provides an efficient method for rapidly isolating mouse brain nuclei from whole mouse brain tissue. By using FANS, we identified a large number of mouse brain cell nuclei expressing the highest levels of the pan-neuronal marker NeuN (NeuN-High) had largest nuclei size and decondensed chromatin. Because the fact that decondensed chromatin is usually associated with multipotency, we hypothesized that these exceptionally large, decondensed neural cell nuclei from brain define a broad class of NPCs. Surprisingly, we found that these decondensed NeuN-High nuclei showed elevated expression levels of markers for neuronal plasticity, epigenetic machinery, cell cycle, and multipotent activities compared to neuronal NeuN-Low and mostly non-neuronal NeuN-Neg nuclei. NeuN-High nuclei have the

properties consistent with their being derived from extremely active neurons with elevated rates of chromatin modification and NPC-like cells with multi-lineage developmental potential. While our data provide strong support for this theory, and perhaps most surprising was the high percentage of nuclei (10-15%) in this category of having multipotent properties. However, other results from our investigation were also unexpected and complex, or do not fully support this working hypothesis. For example, it was perhaps not obvious that higher NeuN staining levels were associated with decondensed nuclei. Further analysis of decondensed neural cell nuclei should provide novel insights into neurobiology and neurodegenerative diseases.

In chapter 4, we evaluated 5-hydroxymethylcytosine (5hmC) levels evaluated among NeuN-High, NeuN-Low and NeuN-Neg mouse brain nuclei. TAB-seq identified NeuN-High nuclei had the highest level of 5hmC compared to the rest of nuclei types. We further profiled 5hmC levels and distribution across gene regions for 12,488 genes expressed in the brain as a function of expression level. We found genes in the highest expression quintile had the highest 5hmC levels across the whole gene region among all three classes of nuclei. Yet, the peak level of 5hmC was different for each class of nuclei. NeuN-High nuclei had the highest peak of 5hmC, generally 25% higher than the 5hmC levels in NeuN-Low and NeuN-Neg for all quintiles of transcript. Our data demonstrated that the relationship between genomic distribution of 5hmC and gene expression is neuronal cell-type-specific.

Chapter 5 of this dissertation provides a protocol for efficiently isolating nuclei from fixed adult pig visceral adipose tissue (VAT). We successfully applied modifications of this method to mouse visceral, brown, and subcutaneous adipose tissue (Ambati and others, 2016). We developed FANS of VAT nuclei using the levels of pan-adipocyte protein PPARg2, to distinguish classes of PPARg2-Positive developing or adult adipocyte nuclei from PPARg2-

Negative progenitor cell, leukocyte and endothelial cell nuclei. PPARg2-Positive nuclei were 10-fold enriched for most adipocyte marker transcripts relative to PPARg2-Negative nuclei. PPARg2-Positive nuclei showed higher levels of transcripts encoding most of the chromatin-remodeling factors assayed, which regulate the methylation of histones and DNA cytosine. PPARg2-Positive nuclei were enlarged with decondensed chromatin. TAB-seq demonstrated 5hmC levels were remarkably dynamic in gene bodies of various classes of VAT nuclei, dropping 3.8-fold from the highest quintile of expressed genes to the lowest. In short, VAT-derived adipocytes appear to be more actively remodeling their chromatin than non-adipocytes.

PPARg2-Positive mature adipocyte nuclei are larger than NeuN-High neuronal nuclei, however, they do not represent an obvious multipotent phenotype based on markers involved in multipotency, proliferation and cell cycle as did the NeuN-High nuclei. This comparison highlighted the unexplored question why these adipocyte nuclei are so large but not multipotent. Possible explanations are the following: (1) the large size of adipocyte nuclei may simply reflect more chromatin remodeling machinery and higher rates of chromatin remodeling, independent of multipotency, which is in agree with the higher levels of 5hmC in PPARg2-Positive nuclei indicating poised transcriptional active state; (2) the ages of the mouse (neuronal nuclei donor) are younger than the pig where the adipocyte nuclei come from. As the fact that stem cell niche/pool diminishes dramatically with advancing age (Rossi and others, 2007; Silva and Conboy, 2008), it is probably not surprising that the younger mouse neuronal nuclei display higher multipotency compared to the older pig adipocyte nuclei.

Collectively the data presented in Chapter 3 to 5 provides evidence for the importance and necessity of performing cell-type-specific epigenetic analysis and improved methods for characterizing specific cell types from brain and fat. Future cell-type-specific epigenetic analyses

will be enhanced by exploring the full potential of FANS and FNC technologies along with the wide variety of well-characterized markers now available.

References

Acimovic J, Korosec T, Seliskar M, Bjorkhem I, Monostory K, Szabo P, Pascussi JM, Belic A, Urleb U, Kocjan D and others. 2011. Inhibition of human sterol Delta7-reductase and other postlanosterol enzymes by LK-980, a novel inhibitor of cholesterol synthesis. Drug Metab Dispos 39(1):39-46.

Agathocleous M, Iordanova I, Willardsen MI, Xue XY, Vetter ML, Harris WA, Moore KB. 2009. A directional Wnt/beta-catenin-Sox2-proneural pathway regulates the transition from proliferation to differentiation in the Xenopus retina. Development 136(19):3289-3299.

Ahfeldt T, Schinzel RT, Lee YK, Hendrickson D, Kaplan A, Lum DH, Camahort R, Xia F, Shay J, Rhee EP and others. 2012. Programming human pluripotent stem cells into white and brown adipocytes. Nat Cell Biol 14(2):209-219.

Alvarez-Medina R, Le Dreau G, Ros M, Marti E. 2009. Hedgehog activation is required upstream of Wnt signalling to control neural progenitor proliferation. Development 136(19):3301-3309.

Ambati S, Yu P, McKinney EC, Kandasamy MK, Hartzell D, Baile CA, Meagher RB. 2016. Adipocyte nuclei captured from VAT and SAT. BMC Obes 3:35.

Aoyama T, Okamoto T, Nagayama S, Nishijo K, Ishibe T, Yasura K, Nakayama T, Nakamura T, Toguchida J. 2004. Methylation in the core-promoter region of the chondromodulin-I gene determines the cell-specific expression by regulating the binding of transcriptional activator Sp3. Journal of Biological Chemistry 279(27):28789-28797.

Archer TC, Jin J, Casey ES. 2011. Interaction of Sox1, Sox2, Sox3 and Oct4 during primary neurogenesis. Dev Biol 350(2):429-440.

Arend WP, Mehta G, Antonioli AH, Takahashi M, Takahashi K, Stahl GL, Holers VM, Banda NK. 2013. Roles of adipocytes and fibroblasts in activation of the alternative pathway of complement in inflammatory arthritis in mice. J Immunol 190(12):6423-6433.

Arendt T. 2012. Cell cycle activation and aneuploid neurons in Alzheimer's disease. Mol Neurobiol 46(1):125-135.

Aristotle. 1984. De Generatione Animalium. The Complete Works of Aristotle: Princeton University Press.

Arlotta P, Molyneaux BJ, Chen J, Inoue J, Kominami R, Macklis JD. 2005. Neuronal subtype-specific genes that control corticospinal motor neuron development in vivo. Neuron 45(2):207-221.

Arner P, Sinha I, Thorell A, Ryden M, Dahlman-Wright K, Dahlman I. 2015. The epigenetic signature of subcutaneous fat cells is linked to altered expression of genes implicated in lipid metabolism in obese women. Clin Epigenetics 7.

Azevedo FAC, Carvalho LRB, Grinberg LT, Farfel JM, Ferretti REL, Leite REP, Jacob W, Lent R, Herculano-Houzel S. 2009. Equal Numbers of Neuronal and Nonneuronal Cells Make the Human Brain an Isometrically Scaled-Up Primate Brain. Journal of Comparative Neurology 513(5):532-541.

Baas R, Lelieveld D, van Teeffelen H, Lijnzaad P, Castelijns B, van Schaik FM, Vermeulen M, Egan DA, Timmers HT, de Graaf P. 2014. A novel microscopy-based high-throughput

screening method to identify proteins that regulate global histone modification levels. J Biomol Screen 19(2):287-296.
Bardet SM, Mouriec K, Balthazart J. 2012. Birth of neural progenitors during the embryonic period of sexual differentiation in the Japanese quail brain. J Comp Neurol 520(18):4226-4253.
Barreto G, Schafer A, Marhold J, Stach D, Swaminathan SK, Handa V, Doderlein G, Maltry N, Wu W, Lyko F and others. 2007. Gadd45a promotes epigenetic gene activation by repair-mediated DNA demethylation. Nature 445(7128):671-675.
Barter MJ, Bui C, Young DA. 2012. Epigenetic mechanisms in cartilage and osteoarthritis: DNA methylation, histone modifications and microRNAs. Osteoarthritis Cartilage 20(5):339-349.
Baubec T, Colombo DF, Wirbelauer C, Schmidt J, Burger L, Krebs AR, Akalin A, Schubeler D. 2015. Genomic profiling of DNA methyltransferases reveals a role for DNMT3B in genic methylation. Nature 520(7546):243-247.
Benton MC, Johnstone A, Eccles D, Harmon B, Hayes MT, Lea RA, Griffiths L, Hoffman EP, Stubbs RS, Macartney-Coxson D. 2015. An analysis of DNA methylation in human adipose tissue reveals differential modification of obesity genes before and after gastric bypass and weight loss. Genome Biol 16.
Bhattacharya D, Talwar S, Mazumder A, Shivashankar GV. 2009. Spatio-Temporal Plasticity in Chromatin Organization in Mouse Cell Differentiation and during Drosophila Embryogenesis. Biophys J 96(9):3832-3839.
Bhave SV, Hoffman PL, Lassen N, Vasiliou V, Saba L, Deitrich RA, Tabakoff B. 2006. Gene array profiles of alcohol and aldehyde metabolizing enzymes in brains of C57BL/6 and DBA/2 mice. Alcoholism, clinical and experimental research 30(10):1659-1669.
Bilsland JG, Haldon C, Goddard J, Oliver K, Murray F, Wheeldon A, Cumberbatch J, McAllister G, Munoz-Sanjuan I. 2006a. A rapid method for the quantification of mouse hippocampal neurogenesis in vivo by flow cytometry - Validation with conventional and enhanced immunohistochemical methods. J Neurosci Meth 157(1):54-63.
Bilsland JG, Haldon C, Goddard J, Oliver K, Murray F, Wheeldon A, Cumberbatch J, McAllister G, Munoz-Sanjuan I. 2006b. A rapid method for the quantification of mouse hippocampal neurogenesis in vivo by flow cytometry. Validation with conventional and enhanced immunohistochemical methods. J Neurosci Methods 157(1):54-63.
Bird A. 2002. DNA methylation patterns and epigenetic memory. Gene Dev 16(1):6-21.
Bird AP. 1986. Cpg-Rich Islands and the Function of DNA Methylation. Nature 321(6067):209-213.
Bonaguidi MA, Song J, Ming GL, Song H. 2012a. A unifying hypothesis on mammalian neural stem cell properties in the adult hippocampus. Curr Opin Neurobiol 22(5):754-761.
Bonaguidi MA, Song J, Ming GL, Song HJ. 2012b. A unifying hypothesis on mammalian neural stem cell properties in the adult hippocampus. Curr Opin Neurobiol 22(5):754-761.
Bonaguidi MA, Wheeler MA, Shapiro JS, Stadel RP, Sun GJ, Ming GL, Song H. 2011. In vivo clonal analysis reveals self-renewing and multipotent adult neural stem cell characteristics. Cell 145(7):1142-1155.
Bonfanti L, Peretto P. 2011. Adult neurogenesis in mammals--a theme with many variations. Eur J Neurosci 34(6):930-950.

Bourlier V, Zakaroff-Girard A, Miranville A, De Barros S, Maumus M, Sengenes C, Galitzky J, Lafontan M, Karpe F, Frayn KN and others. 2008. Remodeling phenotype of human subcutaneous adipose tissue macrophages. Circulation 117(6):806-815.

Bousiges O, Neidl R, Majchrzak M, Muller MA, Barbelivien A, Pereira de Vasconcelos A, Schneider A, Loeffler JP, Cassel JC, Boutillier AL. 2013. Detection of histone acetylation levels in the dorsal hippocampus reveals early tagging on specific residues of H2B and H4 histones in response to learning. PLoS One 8(3):e57816.

Brenner C, Deplus R, Didelot C, Loriot A, Vire E, De Smet C, Gutierrez A, Danovi D, Bernard D, Boon T and others. 2005. Myc represses transcription through recruitment of DNA methyltransferase corepressor. Embo Journal 24(2):336-346.

Broide RS, Redwine JM, Aftahi N, Young W, Bloom FE, Winrow CJ. 2007. Distribution of histone deacetylases 1-11 in the rat brain. J Mol Neurosci 31(1):47-58.

Busser J, Geldmacher DS, Herrup K. 1998. Ectopic cell cycle proteins predict the sites of neuronal cell death in Alzheimer's disease brain. J Neurosci 18(8):2801-2807.

Campion J, Milagro FI, Martinez JA. 2009. Individuality and epigenetics in obesity. Obes Rev 10(4):383-392.

Cardamone MD, Tanasa B, Chan M, Cederquist CT, Andricovich J, Rosenfeld MG, Perissi V. 2014. GPS2/KDM4A pioneering activity regulates promoter-specific recruitment of PPARgamma. Cell reports 8(1):163-176.

Catalan V, Gomez-Ambrosi J, Rodriguez A, Fruhbeck G. 2012. Role of extracellular matrix remodelling in adipose tissue pathophysiology. Relevance in the development of obesity. Histol Histopathol 27(12):1515-1528.

Chahrour M, Zoghbi HY. 2007. The story of Rett syndrome: From clinic to neurobiology. Neuron 56(3):422-437.

Chen D, Fang F, Yang Y, Chen J, Xu G, Xu Y, Gao Y. 2013. Brahma-related gene 1 (Brg1) epigenetically regulates CAM activation during hypoxic pulmonary hypertension. Cardiovasc Res 100(3):363-373.

Chen H, Dzitoyeva S, Manev H. 2012. Effect of aging on 5-hydroxymethylcytosine in the mouse hippocampus. Restor Neurol Neurosci 30(3):237-245.

Chen Y, Damayanti NP, Irudayaraj J, Dunn K, Zhou FC. 2014. Diversity of two forms of DNA methylation in the brain. Front Genet 5:46.

Chen YH, Yeh FL, Yeh SP, Ma HT, Hung SC, Hung MC, Li LY. 2011. Myocyte enhancer factor-2 interacting transcriptional repressor (MITR) is a switch that promotes osteogenesis and inhibits adipogenesis of mesenchymal stem cells by inactivating peroxisome proliferator-activated receptor gamma-2. J Biol Chem 286(12):10671-10680.

Cho YW, Hong S, Jin Q, Wang L, Lee JE, Gavrilova O, Ge K. 2009. Histone methylation regulator PTIP is required for PPARgamma and C/EBPalpha expression and adipogenesis. Cell Metab 10(1):27-39.

Choi I, Kim R, Lim HW, Kaestner KH, Won KJ. 2014. 5-hydroxymethylcytosine represses the activity of enhancers in embryonic stem cells: a new epigenetic signature for gene regulation. BMC Genomics 15:670.

Chouliaras L, van den Hove DL, Kenis G, Keitel S, Hof PR, van Os J, Steinbusch HW, Schmitz C, Rutten BP. 2012. Age-related increase in levels of 5-hydroxymethylcytosine in mouse hippocampus is prevented by caloric restriction. Curr Alzheimer Res.

Craven RA, Banks RE. 2002. Use of laser capture microdissection to selectively obtain distinct populations of cells for proteomic analysis. Method Enzymol 356:33-49.

Crick F. 1984. Memory and molecular turnover. Nature 312(5990):101.
Cristancho AG, Lazar MA. 2011. Forming functional fat: a growing understanding of adipocyte differentiation. Nat Rev Mol Cell Biol 12(11):722-734.
D'Amico LA, Boujard D, Coumailleau P. 2013. The neurogenic factor NeuroD1 is expressed in post-mitotic cells during juvenile and adult Xenopus neurogenesis and not in progenitor or radial glial cells. PLoS One 8(6):e66487.
Dahlman I, Sinha I, Gao H, Brodin D, Thorell A, Ryden M, Andersson DP, Henriksson J, Perfilyev A, Ling C and others. 2015. The fat cell epigenetic signature in post-obese women is characterized by global hypomethylation and differential DNA methylation of adipogenesis genes. Int J Obes (Lond).
Dammer EB, Duong DM, Diner I, Gearing M, Feng Y, Lah JJ, Levey AI, Seyfried NT. 2013a. Neuron Enriched Nuclear Proteome Isolated from Human Brain. J Proteome Res 12(7):3193-3206.
Dammer EB, Duong DM, Diner I, Gearing M, Feng Y, Lah JJ, Levey AI, Seyfried NT. 2013b. Neuron enriched nuclear proteome isolated from human brain. J Proteome Res 12(7):3193-3206.
Darcy MJ, Calvin K, Cavnar K, Ouimet CC. 2010. Regional and subcellular distribution of HDAC4 in mouse brain. J Comp Neurol 518(5):722-740.
Davies MN, Volta M, Pidsley R, Lunnon K, Dixit A, Lovestone S, Coarfa C, Harris RA, Milosavljevic A, Troakes C and others. 2012. Functional annotation of the human brain methylome identifies tissue-specific epigenetic variation across brain and blood. Genome Biol 13(6).
Davis DM, Dyer MA. 2010a. Retinal Progenitor Cells, Differentiation, and Barriers to Cell Cycle Reentry. Invertebrate and Vertebrate Eye Development 93:175-188.
Davis DM, Dyer MA. 2010b. Retinal progenitor cells, differentiation, and barriers to cell cycle reentry. Curr Top Dev Biol 93:175-188.
Deal RB, Henikoff JG, Henikoff S. 2010a. Genome-wide kinetics of nucleosome turnover determined by metabolic labeling of histones. Science 328(5982):1161-1164.
Deal RB, Henikoff JG, Henikoff S. 2010b. Genome-Wide Kinetics of Nucleosome Turnover Determined by Metabolic Labeling of Histones. Science 328(5982):1161-1164.
Deal RB, Henikoff S. 2010a. A simple method for gene expression and chromatin profiling of individual cell types within a tissue. Dev Cell 18(6):1030-1040.
Deal RB, Henikoff S. 2010b. A Simple Method for Gene Expression and Chromatin Profiling of Individual Cell Types within a Tissue. Dev Cell 18(6):1030-1040.
Deal RB, Henikoff S. 2011. The INTACT method for cell type-specific gene expression and chromatin profiling in *Arabidopsis thaliana*. Nat Protoc 6(1):56-68.
Deaton AM, Bird A. 2011. CpG islands and the regulation of transcription. Gene Dev 25(10):1010-1022.
Deiuliis J, Shah Z, Shah N, Needleman B, Mikami D, Narula V, Perry K, Hazey J, Kampfrath T, Kollengode M and others. 2011a. Visceral adipose inflammation in obesity is associated with critical alterations in tregulatory cell numbers. PLoS One 6(1):e16376.
Deiuliis J, Shah Z, Shah N, Needleman B, Mikami D, Narula V, Perry K, Hazey J, Kampfrath T, Kollengode M and others. 2011b. Visceral Adipose Inflammation in Obesity Is Associated with Critical Alterations in Tregulatory Cell Numbers. Plos One 6(1).
Dogan N, Wu W, Morrissey CS, Chen KB, Stonestrom A, Long M, Keller CA, Cheng Y, Jain D, Visel A and others. 2015. Occupancy by key transcription factors is a more accurate

predictor of enhancer activity than histone modifications or chromatin accessibility. Epigenetics Chromatin 8:16.
Dominguez MH, Ayoub AE, Rakic P. 2013. POU-III transcription factors (Brn1, Brn2, and Oct6) influence neurogenesis, molecular identity, and migratory destination of upper-layer cells of the cerebral cortex. Cereb Cortex 23(11):2632-2643.
Dong E, Dzitoyeva SG, Matrisciano F, Tueting P, Grayson DR, Guidotti A. 2015. Brain-derived neurotrophic factor epigenetic modifications associated with schizophrenia-like phenotype induced by prenatal stress in mice. Biol Psychiatry 77(6):589-596.
Dranovsky A, Leonardo ED. 2012. Is there a role for young hippocampal neurons in adaptation to stress? Behav Brain Res 227(2):371-375.
Dredge BK, Jensen KB. 2011a. NeuN/Rbfox3 Nuclear and Cytoplasmic Isoforms Differentially Regulate Alternative Splicing and Nonsense-Mediated Decay of Rbfox2. Plos One 6(6).
Dredge BK, Jensen KB. 2011b. NeuN/Rbfox3 nuclear and cytoplasmic isoforms differentially regulate alternative splicing and nonsense-mediated decay of Rbfox2. PLoS One 6(6):e21585.
Dromard C, Bartolami S, Deleyrolle L, Takebayashi H, Ripoll C, Simonneau L, Prome S, Puech S, Tran VB, Duperray C and others. 2007. NG2 and Olig2 expression provides evidence for phenotypic deregulation of cultured central nervous system and peripheral nervous system neural precursor cells. Stem Cells 25(2):340-353.
Du Q, Luu PL, Stirzaker C, Clark SJ. 2015. Methyl-CpG-binding domain proteins: readers of the epigenome. Epigenomics:1-23.
Dubois-Chevalier J, Oger F, Dehondt H, Firmin FF, Gheeraert C, Staels B, Lefebvre P, Eeckhoute J. 2014. A dynamic CTCF chromatin binding landscape promotes DNA hydroxymethylation and transcriptional induction of adipocyte differentiation. Nucleic Acids Res.
Dubois-Chevalier J, Staels B, Lefebvre P, Eeckhoute J. 2015. The ubiquitous transcription factor CTCF promotes lineage-specific epigenomic remodeling and establishment of transcriptional networks driving cell differentiation. Nucleus 6(1):15-18.
Dupont C, Armant DR, Brenner CA. 2009. Epigenetics: Definition, Mechanisms and Clinical Perspective. Semin Reprod Med 27(5):351-357.
Durnin J. 1981. Basal metabolic rate in man. Report to Food and Agriculture Organization of the United Nations, WHO 2.2.1.
Dyrvig M, Hansen HH, Christiansen SH, Woldbye DP, Mikkelsen JD, Lichota J. 2012. Epigenetic regulation of Arc and c-Fos in the hippocampus after acute electroconvulsive stimulation in the rat. Brain Res Bull 88(5):507-513.
Dzitoyeva S, Chen H, Manev H. 2012. Effect of aging on 5-hydroxymethylcytosine in brain mitochondria. Neurobiol Aging 33(12):2881-2891.
Efroni S, Duttagupta R, Cheng J, Dehghani H, Hoeppner DJ, Dash C, Bazett-Jones DP, Le Grice S, Mckay RDG, Buetow KH and others. 2008. Global transcription in pluripotent embryonic stem cells. Cell Stem Cell 2(5):437-447.
Ehninger D, Kempermann G. 2008. Neurogenesis in the adult hippocampus. Cell Tissue Res 331(1):243-250.
Elbatarny HS, Netherton SJ, Ovens JD, Ferguson AV, Maurice DH. 2007. Adiponectin, ghrelin, and leptin differentially influence human platelet and human vascular endothelial cell functions: implication in obesity-associated cardiovascular diseases. Eur J Pharmacol 558(1-3):7-13.

Ellis P, Fagan BM, Magness ST, Hutton S, Taranova O, Hayashi S, McMahon A, Rao M, Pevny L. 2004. SOX2, a persistent marker for multipotential neural stem cells derived from embryonic stem cells, the embryo or the adult. Dev Neurosci 26(2-4):148-165.
Encinas JM, Michurina TV, Peunova N, Park JH, Tordo J, Peterson DA, Fishell G, Koulakov A, Enikolopov G. 2011. Division-Coupled Astrocytic Differentiation and Age-Related Depletion of Neural Stem Cells in the Adult Hippocampus. Cell Stem Cell 8(5):566-579.
Faiz M, Nagy A. 2013. Induced Pluripotent Stem Cells and Disorders of the Nervous System: Progress, Problems, and Prospects. Neuroscientist 19(6):567-577.
Feng J, Zhou Y, Campbell SL, Le T, Li E, Sweatt JD, Silva AJ, Fan G. 2010a. Dnmt1 and Dnmt3a maintain DNA methylation and regulate synaptic function in adult forebrain neurons. Nat Neurosci 13(4):423-430.
Feng SH, Jacobsen SE, Reik W. 2010b. Epigenetic Reprogramming in Plant and Animal Development. Science 330(6004):622-627.
Ficz G, Branco MR, Seisenberger S, Santos F, Krueger F, Hore TA, Marques CJ, Andrews S, Reik W. 2011. Dynamic regulation of 5-hydroxymethylcytosine in mouse ES cells and during differentiation. Nature 473(7347):398-402.
Florens L, Korfali N, Schirmer EC. 2008. Subcellular fractionation and proteomics of nuclear envelopes. Methods Mol Biol 432:117-137.
Folch J, Junyent F, Verdaguer E, Auladell C, Pizarro JG, Beas-Zarate C, Pallas M, Camins A. 2012. Role of cell cycle re-entry in neurons: a common apoptotic mechanism of neuronal cell death. Neurotox Res 22(3):195-207.
Foudah D, Redondo J, Caldara C, Carini F, Tredici G, Miloso M. 2013. Human mesenchymal stem cells express neuronal markers after osteogenic and adipogenic differentiation. Cell Mol Biol Lett 18(2):163-186.
Fujiki K, Shinoda A, Kano F, Sato R, Shirahige K, Murata M. 2013. PPARgamma-induced PARylation promotes local DNA demethylation by production of 5-hydroxymethylcytosine. Nat Commun 4:2262.
Fuks F, Hurd PJ, Wolf D, Nan X, Bird AP, Kouzarides T. 2003. The methyl-CpG-binding protein MeCP2 links DNA methylation to histone methylation. J Biol Chem 278(6):4035-4040.
Gao X, Tate P, Hu P, Tjian R, Skarnes WC, Wang Z. 2008. ES cell pluripotency and germ-layer formation require the SWI/SNF chromatin remodeling component BAF250a. Proc Natl Acad Sci U S A 105(18):6656-6661.
Gaspar-Maia A, Alajem A, Meshorer E, Ramalho-Santos M. 2011. Open chromatin in pluripotency and reprogramming. Nat Rev Mol Cell Biol 12(1):36-47.
Gavin DP, Chase KA, Sharma RP. 2013. Active DNA demethylation in post-mitotic neurons: a reason for optimism. Neuropharmacology 75:233-245.
Gehman LT, Meera P, Stoilov P, Shiue L, O'Brien JE, Meisler MH, Ares M, Otis TS, Black DL. 2012. The splicing regulator Rbfox2 is required for both cerebellar development and mature motor function. Gene Dev 26(5):445-460.
Geutjes EJ, Bajpe PK, Bernards R. 2012. Targeting the epigenome for treatment of cancer. Oncogene 31(34):3827-3844.
Gibbs JR, van der Brug MP, Hernandez DG, Traynor BJ, Nalls MA, Lai SL, Arepalli S, Dillman A, Rafferty IP, Troncoso J and others. 2010. Abundant Quantitative Trait Loci Exist for DNA Methylation and Gene Expression in Human Brain. Plos Genet 6(5).
Gibney ER, Nolan CM. 2010. Epigenetics and gene expression. Heredity 105(1):4-13.

Globisch D, Munzel M, Muller M, Michalakis S, Wagner M, Koch S, Bruckl T, Biel M, Carell T. 2010a. Tissue Distribution of 5-Hydroxymethylcytosine and Search for Active Demethylation Intermediates. Plos One 5(12).
Globisch D, Munzel M, Muller M, Michalakis S, Wagner M, Koch S, Bruckl T, Biel M, Carell T. 2010b. Tissue distribution of 5-hydroxymethylcytosine and search for active demethylation intermediates. PLoS One 5(12):e15367.
Goldberg AD, Allis CD, Bernstein E. 2007. Epigenetics: a landscape takes shape. Cell 128(4):635-638.
Goll MG, Bestor TH. 2005a. Eukaryotic cytosine methyltransferases. Annual Review of Biochemistry 74:481-514.
Goll MG, Bestor TH. 2005b. Eukaryotic cytosine methyltransferases. Annu Rev Biochem 74:481-514.
Gong P, Roseman J, Fernandez CG, Vetrivel KS, Bindokas VP, Zitzow LA, Kar S, Parent AT, Thinakaran G. 2011. Transgenic neuronal overexpression reveals that stringently regulated p23 expression is critical for coordinated movement in mice. Mol Neurodegener 6:87.
Gonzalez-Bosquet J, Chu Y, Chen HB, Dowdy SC, Podratz KC, Li J, Jiang SW. 2014. Development of an intracellular, DNA methyltransferase-specific, and gene-specific assay for studying dynamic DNA methylation. Curr Pharm Des 20(11):1664-1673.
Goss RJ. 1966. Hypertrophy versus hyperplasia. Science 153(3744):1615-1620.
Graff J, Rei D, Guan JS, Wang WY, Seo J, Hennig KM, Nieland TJ, Fass DM, Kao PF, Kahn M and others. 2012. An epigenetic blockade of cognitive functions in the neurodegenerating brain. Nature 483(7388):222-226.
Guan JS, Haggarty SJ, Giacometti E, Dannenberg JH, Joseph N, Gao J, Nieland TJ, Zhou Y, Wang X, Mazitschek R and others. 2009. HDAC2 negatively regulates memory formation and synaptic plasticity. Nature 459(7243):55-60.
Guo W, Zhang KM, Tu K, Li YX, Zhu L, Xiao HS, Yang Y, Wu JR. 2009. Adipogenesis licensing and execution are disparately linked to cell proliferation. Cell Res 19(2):216-223.
Gupta J, Kumar S, Li J, Krishna Murthy Karuturi R, Tikoo K. 2012. Histone H3 lysine 4 monomethylation (H3K4me1) and H3 lysine 9 monomethylation (H3K9me1): distribution and their association in regulating gene expression under hyperglycaemic/hyperinsulinemic conditions in 3T3 cells. Biochimie 94(12):2656-2664.
Guz J, Gackowski D, Foksinski M, Rozalski R, Olinski R. 2014. Comparison of the absolute level of epigenetic marks 5-methylcytosine, 5-hydroxymethylcytosine, and 5-hydroxymethyluracil between human leukocytes and sperm. Biol Reprod 91(3):55.
Hackler L, Jr., Masuda T, Oliver VF, Merbs SL, Zack DJ. 2012. Use of laser capture microdissection for analysis of retinal mRNA/miRNA expression and DNA methylation. Methods Mol Biol 884:289-304.
Hagman DK, Kuzma JN, Larson I, Foster-Schubert KE, Kuan LY, Cignarella A, Geamanu E, Makar KW, Gottlieb JR, Kratz M. 2012. Characterizing and quantifying leukocyte populations in human adipose tissue: Impact of enzymatic tissue processing. J Immunol Methods.
Hahn MA, Qiu R, Wu X, Li AX, Zhang H, Wang J, Jui J, Jin SG, Jiang Y, Pfeifer GP and others. 2013. Dynamics of 5-hydroxymethylcytosine and chromatin marks in Mammalian neurogenesis. Cell Rep 3(2):291-300.

Hahn MA, Wu X, Li AX, Hahn T, Pfeifer GP. 2011. Relationship between gene body DNA methylation and intragenic H3K9me3 and H3K36me3 chromatin marks. PLoS One 6(4):e18844.
Hahn SS, Tang Q, Zheng F, Zhao S, Wu J, Chen J. 2014. Repression of integrin-linked kinase by antidiabetes drugs through cross-talk of PPARgamma- and AMPKalpha-dependent signaling: role of AP-2alpha and Sp1. Cell Signal 26(3):639-647.
Haig D. 2004. The (dual) origin of epigenetics. Cold Spring Harb Symp Quant Biol 69:67-70.
Hajkova P, Jeffries SJ, Lee C, Miller N, Jackson SP, Surani MA. 2010. Genome-Wide Reprogramming in the Mouse Germ Line Entails the Base Excision Repair Pathway. Science 329(5987):78-82.
Handy DE, Castro R, Loscalzo J. 2011. Epigenetic modifications: basic mechanisms and role in cardiovascular disease. Circulation 123(19):2145-2156.
Harrison IF, Dexter DT. 2013. Epigenetic targeting of histone deacetylase: therapeutic potential in Parkinson's disease? Pharmacol Ther 140(1):34-52.
Hashimoto H, Hong S, Bhagwat AS, Zhang X, Cheng X. 2012. Excision of 5-hydroxymethyluracil and 5-carboxylcytosine by the thymine DNA glycosylase domain: its structural basis and implications for active DNA demethylation. Nucleic Acids Res 40(20):10203-10214.
Hawkins RD, Hon GC, Lee LK, Ngo Q, Lister R, Pelizzola M, Edsall LE, Kuan S, Luu Y, Klugman S and others. 2010. Distinct Epigenomic Landscapes of Pluripotent and Lineage-Committed Human Cells. Cell Stem Cell 6(5):479-491.
Henry GL, Davis FP, Picard S, Eddy SR. 2012. Cell type-specific genomics of Drosophila neurons. Nucleic Acids Res 40(19):9691-9704.
Herculano-Houzel S. 2009. The human brain in numbers: a linearly scaled-up primate brain. Front Hum Neurosci 3:31.
Herculano-Houzel S. 2012. Neuronal scaling rules for primate brains: the primate advantage. Prog Brain Res 195:325-340.
Herculano-Houzel S, Lent R. 2005. Isotropic fractionator: a simple, rapid method for the quantification of total cell and neuron numbers in the brain. J Neurosci 25(10):2518-2521.
Herculano-Houzel S, Mota B, Lent R. 2006. Cellular scaling rules for rodent brains. Proc Natl Acad Sci U S A 103(32):12138-12143.
Hernandez-Ortega K, Quiroz-Baez R, Arias C. 2011. Cell cycle reactivation in mature neurons: a link with brain plasticity, neuronal injury and neurodegenerative diseases? Neurosci Bull 27(3):185-196.
Hezroni H, Tzchori I, Davidi A, Mattout A, Biran A, Nissim-Rafinia M, Westphal H, Meshorer E. 2011a. H3K9 histone acetylation predicts pluripotency and reprogramming capacity of ES cells. Nucleus-Austin 2(4):300-309.
Hezroni H, Tzchori I, Davidi A, Mattout A, Biran A, Nissim-Rafinia M, Westphal H, Meshorer E. 2011b. H3K9 histone acetylation predicts pluripotency and reprogramming capacity of ES cells. Nucleus 2(4):300-309.
Hohos N, Lee J, Ji L, Yu M, Kandasamy MM, Phillips BG, Baile C, He C, Schmitz R, Meagher R. Submitted for publication. DNA cytosine hydroxymethylation levels are distinct among various peripheral blood leukocytes.

Huang PS, Son JH, Abbott LC, Winzer-Serhan UH. 2011. Regulated expression of neuronal SIRT1 and related genes by aging and neuronal beta2-containing nicotinic cholinergic receptors. Neuroscience 196:189-202.
Ichiyama K, Chen T, Wang X, Yan X, Kim BS, Tanaka S, Ndiaye-Lobry D, Deng Y, Zou Y, Zheng P and others. 2015. The methylcytosine dioxygenase Tet2 promotes DNA demethylation and activation of cytokine gene expression in T cells. Immunity 42(4):613-626.
Ichiyanagi T, Ichiyanagi K, Miyake M, Sasaki H. 2013. Accumulation and loss of asymmetric non-CpG methylation during male germ-cell development. Nucleic Acids Research 41(2):738-745.
Illingworth RS, Bird AP. 2009. CpG islands - 'A rough guide'. Febs Lett 583(11):1713-1720.
Inagaki T, Iwasaki S, Matsumura Y, Kawamura T, Tanaka T, Abe Y, Yamasaki A, Tsurutani Y, Yoshida A, Chikaoka Y and others. 2015. The FBXL10/KDM2B Scaffolding Protein Associates with Novel Polycomb Repressive Complex-1 to Regulate Adipogenesis. J Biol Chem 290(7):4163-4177.
Irier H, Street RC, Dave R, Lin L, Cai C, Davis TH, Yao B, Cheng Y, Jin P. 2014. Environmental enrichment modulates 5-hydroxymethylcytosine dynamics in hippocampus. Genomics 104(5):376-382.
Ito S, D'Alessio AC, Taranova OV, Hong K, Sowers LC, Zhang Y. 2010. Role of Tet proteins in 5mC to 5hmC conversion, ES-cell self-renewal and inner cell mass specification. Nature 466(7310):1129-1133.
Javierre BM, Fernandez AF, Richter J, Al-Shahrour F, Martin-Subero JI, Rodriguez-Ubreva J, Berdasco M, Fraga MF, O'Hanlon TP, Rider LG and others. 2010. Changes in the pattern of DNA methylation associate with twin discordance in systemic lupus erythematosus. Genome Res 20(2):170-179.
Jeffries MA, Dozmorov M, Tang Y, Merrill JT, Wren JD, Sawalha AH. 2011. Genome-wide DNA methylation patterns in CD4+ T cells from patients with systemic lupus erythematosus. Epigenetics 6(5):593-601.
Jin SG, Jiang Y, Qiu R, Rauch TA, Wang Y, Schackert G, Krex D, Lu Q, Pfeifer GP. 2011a. 5-Hydroxymethylcytosine is strongly depleted in human cancers but its levels do not correlate with IDH1 mutations. Cancer Res 71(24):7360-7365.
Jin SG, Wu X, Li AX, Pfeifer GP. 2011b. Genomic mapping of 5-hydroxymethylcytosine in the human brain. Nucleic Acids Res 39(12):5015-5024.
Jones PA, Liang GN. 2009. OPINION Rethinking how DNA methylation patterns are maintained. Nat Rev Genet 10(11):805-811.
Joshi A. 2014. Mammalian transcriptional hotspots are enriched for tissue specific enhancers near cell type specific highly expressed genes and are predicted to act as transcriptional activator hubs. BMC Bioinformatics 15(1):6591.
Kaas GA, Zhong C, Eason DE, Ross DL, Vachhani RV, Ming GL, King JR, Song H, Sweatt JD. 2013. TET1 controls CNS 5-methylcytosine hydroxylation, active DNA demethylation, gene transcription, and memory formation. Neuron 79(6):1086-1093.
Kamata M, Okitsu Y, Fujiwara T, Kanehira M, Nakajima S, Takahashi T, Inoue A, Fukuhara N, Onishi Y, Ishizawa K and others. 2014. GATA2 regulates differentiation of bone marrow-derived mesenchymal stem cells. Haematologica 99(11):1686-1696.
Kandasamy MK, McKinney EC, Meagher RB. 2002. Functional nonequivalency of actin isovariants in Arabidopsis. Mol Biol Cell 13(1):251-261.

Kandasamy MK, McKinney EC, Meagher RB. 2010. Differential Sublocalization of Actin Variants Within the Nucleus. Cytoskeleton 67(11):729-743.
Kandasamy MK, McKinney EC, Roy E, Meagher RB. 2012. Plant vegetative and animal cytoplasmic actins share functional competence for spatial development with protists. Plant Cell 24(5):2041-2057.
Kaur K, Yang J, Eisenberg CA, Eisenberg LM. 2014. 5-azacytidine promotes the transdifferentiation of cardiac cells to skeletal myocytes. Cell Reprogram 16(5):324-330.
Keller M, Kralisch S, Rohde K, Schleinitz D, Dietrich A, Schon MR, Gartner D, Lohmann T, Dressler M, Tonjes A and others. 2014. Global DNA methylation levels in human adipose tissue are related to fat distribution and glucose homeostasis. Diabetologia 57(11):2374-2383.
Khalyfa A, Mutskov V, Carreras A, Khalyfa AA, Hakim F, Gozal D. 2014. Sleep fragmentation during late gestation induces metabolic perturbations and epigenetic changes in adiponectin gene expression in male adult offspring mice. Diabetes 63(10):3230-3241.
Kim D, Frank CL, Dobbin MM, Tsunemoto RK, Tu W, Peng PL, Guan JS, Lee BH, Moy LY, Giusti P and others. 2008. Deregulation of HDAC1 by p25/Cdk5 in neurotoxicity. Neuron 60(5):803-817.
Kim KK, Adelstein RS, Kawamoto S. 2009. Identification of Neuronal Nuclei (NeuN) as Fox-3, a New Member of the Fox-1 Gene Family of Splicing Factors. Journal of Biological Chemistry 284(45):31052-31061.
Kim KK, Nam J, Mukouyama YS, Kawamoto S. 2013a. Rbfox3-regulated alternative splicing of Numb promotes neuronal differentiation during development. J Cell Biol 200(4):443-458.
Kim KK, Nam J, Mukouyama YS, Kawamoto S. 2013b. Rbfox3-regulated alternative splicing of Numb promotes neuronal differentiation during development. J Cell Biol 200(4):443-458.
Kintscher U, Hartge M, Hess K, Foryst-Ludwig A, Clemenz M, Wabitsch M, Fischer-Posovszky P, Barth TF, Dragun D, Skurk T and others. 2008. T-lymphocyte infiltration in visceral adipose tissue: a primary event in adipose tissue inflammation and the development of obesity-mediated insulin resistance. Arterioscler Thromb Vasc Biol 28(7):1304-1310.
Kohli RM, Zhang Y. 2013. TET enzymes, TDG and the dynamics of DNA demethylation. Nature 502(7472):472-479.
Korfali N, Fairley EA, Swanson SK, Florens L, Schirmer EC. 2009. Use of sequential chemical extractions to purify nuclear membrane proteins for proteomics identification. Methods Mol Biol 528:201-225.
Kouzarides T. 2007. Chromatin modifications and their function. Cell 128(4):693-705.
Kramer JM. 2013. Epigenetic regulation of memory: implications in human cognitive disorders. Biomol Concepts 4(1):1-12.
Krejci J, Uhlirova R, Galiova G, Kozubek S, Smigova J, Bartova E. 2009. Genome-Wide Reduction in H3K9 Acetylation During Human Embryonic Stem Cell Differentiation. J Cell Physiol 219(3):677-687.
Kriaucionis S, Heintz N. 2009. The nuclear DNA base 5-hydroxymethylcytosine is present in Purkinje neurons and the brain. Science 324(5929):929-930.
Kubiura M, Okano M, Kimura H, Kawamura F, Tada M. 2012. Chromosome-wide regulation of euchromatin-specific 5mC to 5hmC conversion in mouse ES cells and female human somatic cells. Chromosome Res 20(7):837-848.

Ladd-Acosta C, Pevsner J, Sabunciyan S, Yolken RH, Webster MJ, Dinkins T, Callinan PA, Fan JB, Potash JB, Feinberg AP. 2007. DNA methylation signatures within the human brain. Am J Hum Genet 81(6):1304-1315.
Ladewig J, Koch P, Brustle O. 2013a. Leveling Waddington: the emergence of direct programming and the loss of cell fate hierarchies. Nat Rev Mol Cell Bio 14(4):225-236.
Ladewig J, Koch P, Brustle O. 2013b. Leveling Waddington: the emergence of direct programming and the loss of cell fate hierarchies. Nat Rev Mol Cell Biol 14(4):225-236.
Lai K, Kaspar BK, Gage FH, Schaffer DV. 2003. Sonic hedgehog regulates adult neural progenitor proliferation in vitro and in vivo. Nat Neurosci 6(1):21-27.
Lee J, Saha PK, Yang QH, Lee S, Park JY, Suh Y, Lee SK, Chan L, Roeder RG, Lee JW. 2008. Targeted inactivation of MLL3 histone H3-Lys-4 methyltransferase activity in the mouse reveals vital roles for MLL3 in adipogenesis. Proc Natl Acad Sci U S A 105(49):19229-19234.
Lee JE, Wang C, Xu S, Cho YW, Wang L, Feng X, Baldridge A, Sartorelli V, Zhuang L, Peng W and others. 2013. H3K4 mono- and di-methyltransferase MLL4 is required for enhancer activation during cell differentiation. eLife 2:e01503.
Lewis JR, McNab TJ, Liew LJ, Tan J, Hudson P, Wang JZ, Prince RL. 2013. DNA methylation within the I.4 promoter region correlates with CYPl19A1 gene expression in human ex vivo mature omental and subcutaneous adipocytes. BMC Med Genet 14:87.
Li L, Cheung T, Chen J, Herrup K. 2011. A comparative study of five mouse models of Alzheimer's disease: cell cycle events reveal new insights into neurons at risk for death. Int J Alzheimers Dis 2011:171464.
Li T, Yang D, Li J, Tang Y, Yang J, Le W. 2015. Critical role of Tet3 in neural progenitor cell maintenance and terminal differentiation. Mol Neurobiol 51(1):142-154.
Li W, Liu M. 2011. Distribution of 5-hydroxymethylcytosine in different human tissues. J Nucleic Acids 2011:870726.
Li X, Baker-Andresen D, Zhao Q, Marshall V, Bredy TW. 2014. Methyl CpG binding domain ultra-sequencing: a novel method for identifying inter-individual and cell-type-specific variation in DNA methylation. Genes Brain Behav 13(7):721-731.
Lind D, Franken S, Kappler J, Jankowski J, Schilling K. 2005a. Characterization of the neuronal marker NeuN as a multiply phosphorylated antigen with discrete subcellular localization. Journal of Neuroscience Research 79(3):295-302.
Lind D, Franken S, Kappler J, Jankowski J, Schilling K. 2005b. Characterization of the neuronal marker NeuN as a multiply phosphorylated antigen with discrete subcellular localization. J Neurosci Res 79(3):295-302.
Lister R, Ecker JR. 2009. Finding the fifth base: genome-wide sequencing of cytosine methylation. Genome Res 19(6):959-966.
Lister R, Mukamel EA. 2015. Turning over DNA methylation in the mind. Front Neurosci 9:252.
Lister R, Mukamel EA, Nery JR, Urich M, Puddifoot CA, Johnson ND, Lucero J, Huang Y, Dwork AJ, Schultz MD and others. 2013a. Global epigenomic reconfiguration during mammalian brain development. Science 341(6146):1237905.
Lister R, Mukamel EA, Nery JR, Urich M, Puddifoot CA, Johnson ND, Lucero J, Huang Y, Dwork AJ, Schultz MD and others. 2013b. Global Epigenomic Reconfiguration During Mammalian Brain Development. Science 341(6146):629-+.

Lister R, Pelizzola M, Dowen RH, Hawkins RD, Hon G, Tonti-Filippini J, Nery JR, Lee L, Ye Z, Ngo QM and others. 2009. Human DNA methylomes at base resolution show widespread epigenomic differences. Nature 462(7271):315-322.
Liu H, Hu Q, Kaufman A, D'Ercole AJ, Ye P. 2008. Developmental expression of histone deacetylase 11 in the murine brain. J Neurosci Res 86(3):537-543.
Livak KJ, Schmittgen TD. 2001. Analysis of relative gene expression data using real-time quantitative PCR and the 2(-Delta Delta C(T)) Method. Methods 25(4):402-408.
Londono Gentile T, Lu C, Lodato PM, Tse S, Olejniczak SH, Witze ES, Thompson CB, Wellen KE. 2013. DNMT1 is regulated by ATP-citrate lyase and maintains methylation patterns during adipocyte differentiation. Mol Cell Biol 33(19):3864-3878.
Lopez-Sanchez N, Frade JM. 2013. Genetic evidence for p75NTR-dependent tetraploidy in cortical projection neurons from adult mice. J Neurosci 33(17):7488-7500.
Lubin FD, Roth TL, Sweatt JD. 2008. Epigenetic regulation of BDNF gene transcription in the consolidation of fear memory. J Neurosci 28(42):10576-10586.
Lugert S, Basak O, Knuckles P, Haussler U, Fabel K, Gotz M, Haas CA, Kempermann G, Taylor V, Giachino C. 2010. Quiescent and active hippocampal neural stem cells with distinct morphologies respond selectively to physiological and pathological stimuli and aging. Cell Stem Cell 6(5):445-456.
Lugert S, Taylor V. 2011. Neural Stem Cells: Disposable, End-State Glia? Cell Stem Cell 8(5):464-465.
Lujan E, Chanda S, Ahlenius H, Sudhof TC, Wernig M. 2012. Direct conversion of mouse fibroblasts to self-renewing, tripotent neural precursor cells. Proc Natl Acad Sci U S A 109(7):2527-2532.
Lumeng CN, Liu J, Geletka L, Delaney C, Delproposto J, Desai A, Oatmen K, Martinez-Santibanez G, Julius A, Garg S and others. 2011a. Aging Is Associated with an Increase in T Cells and Inflammatory Macrophages in Visceral Adipose Tissue. J Immunol.
Lumeng CN, Liu JH, Geletka L, Delaney C, Delproposto J, Desai A, Oatmen K, Martinez-Santibanez G, Julius A, Garg S and others. 2011b. Aging Is Associated with an Increase in T Cells and Inflammatory Macrophages in Visceral Adipose Tissue. J Immunol 187(12):6208-6216.
Lumeng CN, Saltiel AR. 2011a. Inflammatory links between obesity and metabolic disease. J Clin Invest 121(6):2111-2117.
Lumeng CN, Saltiel AR. 2011b. Inflammatory links between obesity and metabolic disease. J Clin Invest 121(6):2111-2117.
Luo W, Li S, Peng B, Ye Y, Deng X, Yao K. 2013. Embryonic stem cells markers SOX2, OCT4 and Nanog expression and their correlations with epithelial-mesenchymal transition in nasopharyngeal carcinoma. PLoS One 8(2):e56324.
Luthe DS, Quatrano RS. 1980. Transcription in Isolated Wheat Nuclei: I. ISOLATION OF NUCLEI AND ELIMINATION OF ENDOGENOUS RIBONUCLEASE ACTIVITY. Plant Physiol 65(2):305-308.
Ma DK, Jang MH, Guo JU, Kitabatake Y, Chang ML, Pow-Anpongkul N, Flavell RA, Lu B, Ming GL, Song H. 2009. Neuronal activity-induced Gadd45b promotes epigenetic DNA demethylation and adult neurogenesis. Science 323(5917):1074-1077.
Margueron R, Reinberg D. 2010. Chromatin structure and the inheritance of epigenetic information. Nat Rev Genet 11(4):285-296.

Maric D, Barker JL. 2005. Fluorescence-based sorting of neural stem cells and progenitors. Curr Protoc Neurosci Chapter 3:Unit 3 18.
Marschallinger J, Krampert M, Couillard-Despres S, Heuchel R, Bogdahn U, Aigner L. 2014. Age-dependent and differential effects of Smad7DeltaEx1 on neural progenitor cell proliferation and on neurogenesis. Exp Gerontol 57:149-154.
Marz M, Chapouton P, Diotel N, Vaillant C, Hesl B, Takamiya M, Lam CS, Kah O, Bally-Cuif L, Strahle U. 2010. Heterogeneity in progenitor cell subtypes in the ventricular zone of the zebrafish adult telencephalon. Glia 58(7):870-888.
Matsumoto T, Kano K, Kondo D, Fukuda N, Iribe Y, Tanaka N, Matsubara Y, Sakuma T, Satomi A, Otaki M and others. 2008. Mature adipocyte-derived dedifferentiated fat cells exhibit multilineage potential. J Cell Physiol 215(1):210-222.
Mattout A, Biran A, Meshorer E. 2011. Global epigenetic changes during somatic cell reprogramming to iPS cells. J Mol Cell Biol 3(6):341-350.
Maunakea AK, Nagarajan RP, Bilenky M, Ballinger TJ, D'Souza C, Fouse SD, Johnson BE, Hong C, Nielsen C, Zhao Y and others. 2010. Conserved role of intragenic DNA methylation in regulating alternative promoters. Nature 466(7303):253-257.
Maxeiner S, Glassmann A, Kao HT, Schilling K. 2014. The molecular basis of the specificity and cross-reactivity of the NeuN epitope of the neuron-specific splicing regulator, Rbfox3. Histochem Cell Biol 141(1):43-55.
Maya-Vetencourt JF, Origlia N. 2012. Visual cortex plasticity: a complex interplay of genetic and environmental influences. Neural Plast 2012:631965.
Mayer W, Niveleau A, Walter J, Fundele R, Haaf T. 2000. Embryogenesis - Demethylation of the zygotic paternal genome. Nature 403(6769):501-502.
Meagher RB. 2014. 'Memory and molecular turnover,' 30 years after inception. Epigenetics Chromatin 7(1):37.
Melcer S, Hezroni H, Rand E, Nissim-Rafinia M, Skoultchi A, Stewart CL, Bustin M, Meshorer E. 2012a. Histone modifications and lamin A regulate chromatin protein dynamics in early embryonic stem cell differentiation. Nat Commun 3:910.
Melcer S, Hezroni H, Rand E, Nissim-Rafinia M, Skoultchi A, Stewart CL, Bustin M, Meshorer E. 2012b. Histone modifications and lamin A regulate chromatin protein dynamics in early embryonic stem cell differentiation. Nat Commun 3.
Melcer S, Meshorer E. 2010a. Chromatin plasticity in pluripotent cells. Essays Biochem 48:245-262.
Melcer S, Meshorer E. 2010b. Chromatin plasticity in pluripotent cells. Essays Biochem 48(1):245-262.
Mellen M, Ayata P, Dewell S, Kriaucionis S, Heintz N. 2012. MeCP2 Binds to 5hmC Enriched within Active Genes and Accessible Chromatin in the Nervous System. Cell 151(7):1417-1430.
Merbs SL, Khan MA, Hackler L, Jr., Oliver VF, Wan J, Qian J, Zack DJ. 2012a. Cell-specific DNA methylation patterns of retina-specific genes. PLoS One 7(3):e32602.
Merbs SL, Khan MA, Hackler L, Oliver VF, Wan J, Qian J, Zack DJ. 2012b. Cell-Specific DNA Methylation Patterns of Retina-Specific Genes. Plos One 7(3).
Meshorer E, Yellajoshula D, George E, Scambler PJ, Brown DT, Mistell T. 2006. Hyperdynamic plasticity in pluripotent embryonic of chromatin proteins stem cells. Dev Cell 10(1):105-116.

Miller CA, Sweatt JD. 2007. Covalent modification of DNA regulates memory formation. Neuron 53(6):857-869.
Mo A, Mukamel EA, Davis FP, Luo C, Henry GL, Picard S, Urich MA, Nery JR, Sejnowski TJ, Lister R and others. 2015. Epigenomic Signatures of Neuronal Diversity in the Mammalian Brain. Neuron 86(6):1369-1384.
Molyneaux BJ, Arlotta P, Menezes JR, Macklis JD. 2007. Neuronal subtype specification in the cerebral cortex. Nat Rev Neurosci 8(6):427-437.
Moore DL, Blackmore MG, Hu Y, Kaestner KH, Bixby JL, Lemmon VP, Goldberg JL. 2009. KLF family members regulate intrinsic axon regeneration ability. Science 326(5950):298-301.
Morey C, Da Silva NR, Perry P, Bickmore WA. 2007a. Nuclear reorganisation and chromatin decondensation are conserved, but distinct, mechanisms linked to Hox gene activation. Development 134(5):909-919.
Morey C, Da Silva NR, Perry P, Bickmore WA. 2007b. Nuclear reorganisation and chromatin decondensation are conserved, but distinct, mechanisms linked to Hox gene activation. Development 134(5):909-919.
Morte MI, Carreira BP, Machado V, Carmo A, Nunes-Correia I, Carvalho CM, Araujo IM. 2013. Evaluation of proliferation of neural stem cells in vitro and in vivo. Curr Protoc Stem Cell Biol Chapter 2:Unit 2D 14.
Mosch B, Morawski M, Mittag A, Lenz D, Tarnok A, Arendt T. 2007. Aneuploidy and DNA replication in the normal human brain and Alzheimer's disease. Journal of Neuroscience 27(26):6859-6867.
Mulero M, Perroy J, Federici C, Cabello G, Ollendorff V. 2013. Analysis of RXR/THR and RXR/PPARG2 heterodimerization by bioluminescence resonance energy transfer (BRET). PLoS One 8(12):e84569.
Mullen RJ, Buck CR, Smith AM. 1992a. Neun, a Neuronal Specific Nuclear-Protein in Vertebrates. Development 116(1):201-211.
Mullen RJ, Buck CR, Smith AM. 1992b. NeuN, a neuronal specific nuclear protein in vertebrates. Development 116(1):201-211.
Muller T, Gessi M, Waha A, Isselstein LJ, Luxen D, Freihoff D, Freihoff J, Becker A, Simon M, Hammes J and others. 2012. Nuclear exclusion of TET1 is associated with loss of 5-hydroxymethylcytosine in IDH1 wild-type gliomas. Am J Pathol 181(2):675-683.
Munzel M, Globisch D, Bruckl T, Wagner M, Welzmiller V, Michalakis S, Muller M, Biel M, Carell T. 2010. Quantification of the Sixth DNA Base Hydroxymethylcytosine in the Brain. Angew Chem Int Edit 49(31):5375-5377.
Nanney DL. 1958. Epigenetic Control Systems. Proc Natl Acad Sci U S A 44(7):712-717.
Neri F, Incarnato D, Krepelova A, Rapelli S, Anselmi F, Parlato C, Medana C, Dal Bello F, Oliviero S. 2015. Single-Base Resolution Analysis of 5-Formyl and 5-Carboxyl Cytosine Reveals Promoter DNA Methylation Dynamics. Cell reports.
Nestor CE, Ottaviano R, Reddington J, Sproul D, Reinhardt D, Dunican D, Katz E, Dixon JM, Harrison DJ, Meehan RR. 2012. Tissue type is a major modifier of the 5-hydroxymethylcytosine content of human genes. Genome Res 22(3):467-477.
Nguyen' S, Meletis K, Fu DD, Jhaveri S, Jaenisch R. 2007. Ablation of de novo DNA methyltransferase dnmt3a in the nervous system leads to neuromuscular defects and shortened lifespan. Dev Dynam 236(6):1663-1676.

Nguyen HX, Nekanti U, Haus DL, Funes G, Moreno D, Kamei N, Cummings BJ, Anderson AJ. 2014. Induction of early neural precursors and derivation of tripotent neural stem cells from human pluripotent stem cells under xeno-free conditions. J Comp Neurol 522(12):2767-2783.

Nilsson E, Jansson P, Perilyev A, Pedersen M, Svensson MK, Poulsen P, Ribel-Madsen R, Pedersen NL, Almgren P, Fadista J and others. 2014. Altered DNA methylation and differential expression of genes influencing metabolism and inflammation in adipose tissue from subjects with type 2 diabetes. Diabetologia 57:S152-S152.

Nomura J, Hisatsune A, Miyata T, Isohama Y. 2007. The role of CpG methylation in cell type-specific expression of the aquaporin-5 gene. Biochem Bioph Res Co 353(4):1017-1022.

Oger F, Dubois-Chevalier J, Gheeraert C, Avner S, Durand E, Froguel P, Salbert G, Staels B, Lefebvre P, Eeckhoute J. 2014. Peroxisome proliferator-activated receptor gamma regulates genes involved in insulin/insulin-like growth factor signaling and lipid metabolism during adipogenesis through functionally distinct enhancer classes. J Biol Chem 289(2):708-722.

Oh S, Huang X, Liu J, Litingtung Y, Chiang C. 2009. Shh and Gli3 activities are required for timely generation of motor neuron progenitors. Dev Biol 331(2):261-269.

Okada S, Saiwai H, Kumamaru H, Kubota K, Harada A, Yamaguchi M, Iwamoto Y, Ohkawa Y. 2011a. Flow cytometric sorting of neuronal and glial nuclei from central nervous system tissue. J Cell Physiol 226(2):552-558.

Okada S, Saiwai H, Kumamaru H, Kubota K, Harada A, Yamaguchi M, Iwamoto Y, Ohkawa Y. 2011b. Flow Cytometric Sorting of Neuronal and Glial Nuclei From Central Nervous System Tissue. J Cell Physiol 226(2):552-558.

Ostrup O, Petrovicova I, Strejcek F, Morovic M, Lucas-Hahn A, Lemme E, Petersen B, Niemann H, Laurincik J, Maddox-Hyttel P. 2009a. Nuclear and Nucleolar Reprogramming during the First Cell Cycle in Bovine Nuclear Transfer Embryos. Cloning Stem Cells 11(3):367-375.

Ostrup O, Petrovicova I, Strejcek F, Morovic M, Lucas-Hahn A, Lemme E, Petersen B, Niemann H, Laurincik J, Maddox-Hyttel P. 2009b. Nuclear and nucleolar reprogramming during the first cell cycle in bovine nuclear transfer embryos. Cloning Stem Cells 11(3):367-375.

Otani J, Arita K, Kato T, Kinoshita M, Kimura H, Suetake I, Tajima S, Ariyoshi M, Shirakawa M. 2013. Structural Basis of the Versatile DNA Recognition Ability of the Methyl-CpG Binding Domain of Methyl-CpG Binding Domain Protein 4. Journal of Biological Chemistry 288(9):6351-6362.

Park CS, Rehrauer H, Mansuy IM. 2013a. Genome-wide analysis of H4K5 acetylation associated with fear memory in mice. BMC Genomics 14:539.

Park SH, Park SH, Kook MC, Kim EY, Park S, Lim JH. 2004. Ultrastructure of human embryonic stem cells and spontaneous and retinoic acid-induced differentiating cells. Ultrastruct Pathol 28(4):229-238.

Park TI, Waldvogel HJ, Montgomery JM, Mee EW, Bergin PS, Faull RL, Dragunow M, Curtis MA. 2013b. Identifying neural progenitor cells in the adult human brain. Methods Mol Biol 1059:195-225.

Pastor WA, Pape UJ, Huang Y, Henderson HR, Lister R, Ko M, McLoughlin EM, Brudno Y, Mahapatra S, Kapranov P and others. 2011. Genome-wide mapping of 5-hydroxymethylcytosine in embryonic stem cells. Nature 473(7347):394-397.

Perera A, Eisen D, Wagner M, Laube SK, Kunzel AF, Koch S, Steinbacher J, Schulze E, Splith V, Mittermeier N and others. 2015. TET3 is recruited by REST for context-specific hydroxymethylation and induction of gene expression. Cell reports 11(2):283-294.
Perez-Cornago A, Mansego ML, Zulet MA, Martinez JA. 2014. DNA hypermethylation of the serotonin receptor type-2A gene is associated with a worse response to a weight loss intervention in subjects with metabolic syndrome. Nutrients 6(6):2387-2403.
Pilcher CM, Jones CK, Schroyen M, Severin AJ, Patience JF, Tuggle CK, Koltes JE. 2015. Transcript profiles in longissimus dorsi muscle and subcutaneous adipose tissue: a comparison of pigs with different postweaning growth rates. J Anim Sci 93(5):2134-2143.
Pirooznia SK, Sarthi J, Johnson AA, Toth MS, Chiu K, Koduri S, Elefant F. 2012. Tip60 HAT activity mediates APP induced lethality and apoptotic cell death in the CNS of a Drosophila Alzheimer's disease model. PLoS One 7(7):e41776.
Popp C, Dean W, Feng S, Cokus SJ, Andrews S, Pellegrini M, Jacobsen SE, Reik W. 2010. Genome-wide erasure of DNA methylation in mouse primordial germ cells is affected by AID deficiency. Nature 463(7284):1101-1105.
Pratt T, Tian NM, Simpson TI, Mason JO, Price DJ. 2004. The winged helix transcription factor Foxg1 facilitates retinal ganglion cell axon crossing of the ventral midline in the mouse. Development 131(15):3773-3784.
Ptashne M. 2007. On the use of the word 'epigenetic'. Curr Biol 17(7):R233-236.
Qin S, Zou YH, Zhang CL. 2013. Cross-talk between KLF4 and STAT3 regulates axon regeneration. Nature Communications 4.
Rai K, Huggins IJ, James SR, Karpf AR, Jones DA, Cairns BR. 2008. DNA demethylation in zebrafish involves the coupling of a deaminase, a glycosylase, and gadd45. Cell 135(7):1201-1212.
Raichle ME, Gusnard DA. 2002. Appraising the brain's energy budget. Proc Natl Acad Sci U S A 99(16):10237-10239.
Ram EV, Meshorer E. 2009a. Transcriptional competence in pluripotency. Genes Dev 23(24):2793-2798.
Ram EVSR, Meshorer E. 2009b. Transcriptional competence in pluripotency. Gene Dev 23(24):2793-2798.
Ramsahoye BH, Biniszkiewicz D, Lyko F, Clark V, Bird AP, Jaenisch R. 2000. Non-CpG methylation is prevalent in embryonic stem cells and may be mediated by DNA methyltransferase 3a. P Natl Acad Sci USA 97(10):5237-5242.
Reddy AT, Lakshmi SP, Kleinhenz JM, Sutliff RL, Hart CM, Reddy RC. 2012. Endothelial cell peroxisome proliferator-activated receptor gamma reduces endotoxemic pulmonary inflammation and injury. J Immunol 189(11):5411-5420.
Reddy RC, Narala VR, Keshamouni VG, Milam JE, Newstead MW, Standiford TJ. 2008. Sepsis-induced inhibition of neutrophil chemotaxis is mediated by activation of peroxisome proliferator-activated receptor-{gamma}. Blood 112(10):4250-4258.
Reinius LE, Acevedo N, Joerink M, Pershagen G, Dahlen SE, Greco D, Soderhall C, Scheynius A, Kere J. 2012a. Differential DNA methylation in purified human blood cells: implications for cell lineage and studies on disease susceptibility. PLoS One 7(7):e41361.
Reinius LE, Acevedo N, Joerink M, Pershagen G, Dahlen SE, Greco D, Soderhall C, Scheynius A, Kere J. 2012b. Differential DNA Methylation in Purified Human Blood Cells: Implications for Cell Lineage and Studies on Disease Susceptibility. Plos One 7(7).

Robertson KD. 2002. DNA methylation and chromatin - unraveling the tangled web. Oncogene 21(35):5361-5379.
Rocha VZ, Folco EJ. 2011. Inflammatory concepts of obesity. Int J Inflam 2011:529061.
Ronn T, Ling C. 2013. Effect of exercise on DNA methylation and metabolism in human adipose tissue and skeletal muscle. Epigenomics 5(6):603-605.
Ronn T, Volkov P, Davegardh C, Dayeh T, Hall E, Olsson AH, Nilsson E, Tornberg A, Dekker Nitert M, Eriksson KF and others. 2013. A six months exercise intervention influences the genome-wide DNA methylation pattern in human adipose tissue. PLoS Genet 9(6):e1003572.
Rose CM, van den Driesche S, Sharpe RM, Meehan RR, Drake AJ. 2014. Dynamic changes in DNA modification states during late gestation male germ line development in the rat. Epigenetics Chromatin 7:19.
Rossi DJ, Bryder D, Weissman IL. 2007. Hematopoietic stem cell aging: mechanism and consequence. Exp Gerontol 42(5):385-390.
Rudenko A, Dawlaty MM, Seo J, Cheng AW, Meng J, Le T, Faull KF, Jaenisch R, Tsai LH. 2013. Tet1 is critical for neuronal activity-regulated gene expression and memory extinction. Neuron 79(6):1109-1122.
Rudenko A, Tsai LH. 2014. Epigenetic regulation in memory and cognitive disorders. Neuroscience 264:51-63.
Sarnat HB, Nochlin D, Born DE. 1998. Neuronal nuclear antigen (NeuN): a marker of neuronal maturation in early human fetal nervous system. Brain Dev 20(2):88-94.
Schipper HS, Prakken B, Kalkhoven E, Boes M. 2012. Adipose tissue-resident immune cells: key players in immunometabolism. Trends Endocrinol Metab 23(8):407-415.
Schmitz KM, Schmitt N, Hoffmann-Rohrer U, Schafer A, Grummt I, Mayer C. 2009. TAF12 recruits Gadd45a and the nucleotide excision repair complex to the promoter of rRNA genes leading to active DNA demethylation. Mol Cell 33(3):344-353.
Schultz MD, Schmitz RJ, Ecker JR. 2012. 'Leveling' the playing field for analyses of single-base resolution DNA methylomes. Trends Genet 28(12):583-585.
Seo J, Jo SA, Hwang S, Byun CJ, Lee HJ, Cho DH, Kim D, Koh YH, Jo I. 2013. Trichostatin A epigenetically increases calpastatin expression and inhibits calpain activity and calcium-induced SH-SY5Y neuronal cell toxicity. FEBS J 280(24):6691-6701.
Serandour AA, Avner S, Oger F, Bizot M, Percevault F, Lucchetti-Miganeh C, Palierne G, Gheeraert C, Barloy-Hubler F, Le Peron C and others. 2012a. Dynamic hydroxymethylation of deoxyribonucleic acid marks differentiation-associated enhancers. Nucleic Acids Research 40(17):8255-8265.
Serandour AA, Avner S, Oger F, Bizot M, Percevault F, Lucchetti-Miganeh C, Palierne G, Gheeraert C, Barloy-Hubler F, Peron CL and others. 2012b. Dynamic hydroxymethylation of deoxyribonucleic acid marks differentiation-associated enhancers. Nucleic Acids Res 40(17):8255-8265.
Shen L, Wu H, Diep D, Yamaguchi S, D'Alessio AC, Fung HL, Zhang K, Zhang Y. 2013. Genome-wide Analysis Reveals TET- and TDG-Dependent 5-Methylcytosine Oxidation Dynamics. Cell 153(3):692-706.
Shen LJ, Nam HS, Song P, Moore H, Anderson SA. 2006. FoxG1 haploinsufficiency results in impaired neurogenesis in the postnatal hippocampus and contextual memory deficits. Hippocampus 16(10):875-890.

Shi Y, Desponts C, Do JT, Hahm HS, Scholer HR, Ding S. 2008. Induction of pluripotent stem cells from mouse embryonic fibroblasts by Oct4 and Klf4 with small-molecule compounds. Cell Stem Cell 3(5):568-574.
Siegfried Z, Simon I. 2010. DNA methylation and gene expression. Wiley Interdiscip Rev Syst Biol Med 2(3):362-371.
Silva H, Conboy IM. 2008. Aging and stem cell renewal. StemBook. Cambridge (MA).
Sims D, Sudbery I, Ilott NE, Heger A, Ponting CP. 2014. Sequencing depth and coverage: key considerations in genomic analyses. Nat Rev Genet 15(2):121-132.
Singh AP, Archer TK. 2014. Analysis of the SWI/SNF chromatin-remodeling complex during early heart development and BAF250a repression cardiac gene transcription during P19 cell differentiation. Nucleic Acids Res 42(5):2958-2975.
Smith K, Dalton S. 2010. Myc transcription factors: key regulators behind establishment and maintenance of pluripotency. Regenerative Medicine 5(6):947-959.
Song CX, Szulwach KE, Dai Q, Fu Y, Mao SQ, Lin L, Street C, Li YJ, Poidevin M, Wu H and others. 2013. Genome-wide Profiling of 5-Formylcytosine Reveals Its Roles in Epigenetic Priming. Cell 153(3):678-691.
Song CX, Szulwach KE, Fu Y, Dai Q, Yi C, Li X, Li Y, Chen CH, Zhang W, Jian X and others. 2011a. Selective chemical labeling reveals the genome-wide distribution of 5-hydroxymethylcytosine. Nat Biotechnol 29(1):68-72.
Song CX, Szulwach KE, Fu Y, Dai Q, Yi CQ, Li XK, Li YJ, Chen CH, Zhang W, Jian X and others. 2011b. Selective chemical labeling reveals the genome-wide distribution of 5-hydroxymethylcytosine. Nature Biotechnology 29(1):68-72.
Song CX, Yi C, He C. 2012. Mapping recently identified nucleotide variants in the genome and transcriptome. Nat Biotechnol 30(11):1107-1116.
Song N, Kou L, Lu XW, Sugawara A, Shimizu Y, Wu MK, Du L, Wang H, Sato S, Shen JF. 2015. The perivascular phenotype and behaviors of dedifferentiated cells derived from human mature adipocytes. Biochem Biophys Res Commun 457(3):479-484.
Spencer M, Unal R, Zhu B, Rasouli N, McGehee RE, Jr., Peterson CA, Kern PA. 2011. Adipose tissue extracellular matrix and vascular abnormalities in obesity and insulin resistance. J Clin Endocrinol Metab 96(12):E1990-1998.
Spruijt CG, Gnerlich F, Smits AH, Pfaffeneder T, Jansen PWTC, Bauer C, Munzel M, Wagner M, Muller M, Khan F and others. 2013. Dynamic Readers for 5-(Hydroxy)Methylcytosine and Its Oxidized Derivatives. Cell 152(5):1146-1159.
Suh H, Consiglio A, Ray J, Sawai T, D'Amour KA, Gage FH. 2007. In vivo fate analysis reveals the multipotent and self-renewal capacities of Sox2(+) neural stem cells in the adult hippocampus. Cell Stem Cell 1(5):515-528.
Sultan FA, Wang J, Tront J, Liebermann DA, Sweatt JD. 2012. Genetic deletion of Gadd45b, a regulator of active DNA demethylation, enhances long-term memory and synaptic plasticity. J Neurosci 32(48):17059-17066.
Surzenko N, Crowl T, Bachleda A, Langer L, Pevny L. 2013. SOX2 maintains the quiescent progenitor cell state of postnatal retinal Muller glia. Development 140(7):1445-1456.
Suzuki MM, Bird A. 2008. DNA methylation landscapes: provocative insights from epigenomics. Nat Rev Genet 9(6):465-476.
Sweatt JD. 2013. The emerging field of neuroepigenetics. Neuron 80(3):624-632.
Sylvester JB, Rich CA, Yi C, Peres JN, Houart C, Streelman JT. 2013. Competing signals drive telencephalon diversity. Nature Communications 4.

Szulwach KE, Li X, Li Y, Song CX, Wu H, Dai Q, Irier H, Upadhyay AK, Gearing M, Levey AI and others. 2011a. 5-hmC-mediated epigenetic dynamics during postnatal neurodevelopment and aging. Nat Neurosci 14(12):1607-1616.

Szulwach KE, Li XK, Li YJ, Song CX, Han JW, Kim S, Namburi S, Hermetz K, Kim JJ, Rudd MK and others. 2011b. Integrating 5-Hydroxymethylcytosine into the Epigenomic Landscape of Human Embryonic Stem Cells. Plos Genetics 7(6).

Szulwach KE, Li XK, Li YJ, Song CX, Wu H, Dai Q, Irier H, Upadhyay AK, Gearing M, Levey AI and others. 2011c. 5-hmC-mediated epigenetic dynamics during postnatal neurodevelopment and aging. Nature Neuroscience 14(12):1607-U1150.

Tahiliani M, Koh KP, Shen Y, Pastor WA, Bandukwala H, Brudno Y, Agarwal S, Iyer LM, Liu DR, Aravind L and others. 2009. Conversion of 5-methylcytosine to 5-hydroxymethylcytosine in mammalian DNA by MLL partner TET1. Science 324(5929):930-935.

Takada I, Kouzmenko AP, Kato S. 2009. Molecular switching of osteoblastogenesis versus adipogenesis: implications for targeted therapies. Expert Opin Ther Targets 13(5):593-603.

Tan MK, Lim HJ, Harper JW. 2011. SCF(FBXO22) regulates histone H3 lysine 9 and 36 methylation levels by targeting histone demethylase KDM4A for ubiquitin-mediated proteasomal degradation. Mol Cell Biol 31(18):3687-3699.

Tanious FA, Veal JM, Buczak H, Ratmeyer LS, Wilson WD. 1992. DAPI (4',6-diamidino-2-phenylindole) binds differently to DNA and RNA: minor-groove binding at AT sites and intercalation at AU sites. Biochemistry 31(12):3103-3112.

Taranova OV, Magness ST, Fagan BM, Wu Y, Surzenko N, Hutton SR, Pevny LH. 2006. SOX2 is a dose-dependent regulator of retinal neural progenitor competence. Genes Dev 20(9):1187-1202.

Taupin P. 2009. Adult neurogenesis, neural stem cells and Alzheimer's disease: developments, limitations, problems and promises. Curr Alzheimer Res 6(6):461-470.

Terragni J, Bitinaite J, Zheng Y, Pradhan S. 2012. Biochemical characterization of recombinant beta-glucosyltransferase and analysis of global 5-hydroxymethylcytosine in unique genomes. Biochemistry 51(5):1009-1019.

Terragni J, Zhang G, Sun Z, Pradhan S, Song L, Crawford GE, Lacey M, Ehrlich M. 2014. Notch signaling genes: myogenic DNA hypomethylation and 5-hydroxymethylcytosine. Epigenetics 9(6):842-850.

Thomson JP, Fawkes A, Ottaviano R, Hunter JM, Shukla R, Mjoseng HK, Clark R, Coutts A, Murphy L, Meehan RR. 2015. DNA immunoprecipitation semiconductor sequencing (DIP-SC-seq) as a rapid method to generate genome wide epigenetic signatures. Sci Rep 5:9778.

Tian NM, Pratt T, Price DJ. 2008. Foxg1 regulates retinal axon pathfinding by repressing an ipsilateral program in nasal retina and by causing optic chiasm cells to exert a net axonal growth-promoting activity. Development 135(24):4081-4089.

Tontonoz P, Hu E, Graves RA, Budavari AI, Spiegelman BM. 1994. mPPAR gamma 2: tissue-specific regulator of an adipocyte enhancer. Genes Dev 8(10):1224-1234.

Tsagaratou A, Aijo T, Lio CW, Yue X, Huang Y, Jacobsen SE, Lahdesmaki H, Rao A. 2014. Dissecting the dynamic changes of 5-hydroxymethylcytosine in T-cell development and differentiation. Proc Natl Acad Sci U S A 111(32):E3306-3315.

Turcot V, Tchernof A, Deshaies Y, Perusse L, Belisle A, Marceau S, Biron S, Lescelleur O, Biertho L, Vohl MC. 2012. LINE-1 methylation in visceral adipose tissue of severely obese individuals is associated with metabolic syndrome status and related phenotypes. Clin Epigenetics 4(1):10.
Urich MA, Nery JR, Lister R, Schmitz RJ, Ecker JR. 2015. MethylC-seq library preparation for base-resolution whole-genome bisulfite sequencing. Nat Protoc 10(3):475-483.
Vandesompele J, De Preter K, Pattyn F, Poppe B, Van Roy N, De Paepe A, Speleman F. 2002. Accurate normalization of real-time quantitative RT-PCR data by geometric averaging of multiple internal control genes. Genome Biol 3(7):RESEARCH0034.
Varlakhanova NV, Cotterman RF, deVries WN, Morgan J, Donahue LR, Murray S, Knowles BB, Knoepfler PS. 2010. myc maintains embryonic stem cell pluripotency and self-renewal. Differentiation 80(1):9-19.
Waddington CH. 1942. The epigenotype Endeavour 1:18-20

Waddington CH. 1957. The strategy of the genes: A Discussion of Some Aspects of Theoretical Biology George Allen & Unwin.
Wang L, Xu S, Lee JE, Baldridge A, Grullon S, Peng W, Ge K. 2013. Histone H3K9 methyltransferase G9a represses PPARgamma expression and adipogenesis. EMBO J 32(1):45-59.
Wang W, Bu B, Xie M, Zhang M, Yu Z, Tao D. 2009. Neural cell cycle dysregulation and central nervous system diseases. Prog Neurobiol 89(1):1-17.
Weber M, Hellmann I, Stadler MB, Ramos L, Paabo S, Rebhan M, Schubeler D. 2007. Distribution, silencing potential and evolutionary impact of promoter DNA methylation in the human genome. Nature Genetics 39(4):457-466.
Wei S, Du M, Jiang Z, Duarte MS, Fernyhough-Culver M, Albrecht E, Will K, Zan L, Hausman GJ, Elabd EM and others. 2013. Bovine dedifferentiated adipose tissue (DFAT) cells: DFAT cell isolation. Adipocyte 2(3):148-159.
Wen L, Li X, Yan L, Tan Y, Li R, Zhao Y, Wang Y, Xie J, Zhang Y, Song C and others. 2014. Whole-genome analysis of 5-hydroxymethylcytosine and 5-methylcytosine at base resolution in the human brain. Genome Biol 15(3):R49.
Wen L, Tang F. 2014. Genomic distribution and possible functions of DNA hydroxymethylation in the brain. Genomics 104(5):341-346.
Westra JW, Rivera RR, Bushman DM, Yung YC, Peterson SE, Barral S, Chun J. 2010a. Neuronal DNA content variation (DCV) with regional and individual differences in the human brain. J Comp Neurol 518(19):3981-4000.
Westra JW, Rivera RR, Bushman DM, Yung YC, Peterson SE, Barral S, Chun J. 2010b. Neuronal DNA Content Variation (DCV) With Regional and Individual Differences in the Human Brain. Journal of Comparative Neurology 518(19):3981-4000.
Weyer A, Schilling K. 2003. Developmental and cell type-specific expression of the neuronal marker NeuN in the murine cerebellum. J Neurosci Res 73(3):400-409.
Wheldon LM, Abakir A, Ferjentsik Z, Dudnakova T, Strohbuecker S, Christie D, Dai N, Guan S, Foster JM, Correa IR, Jr. and others. 2014. Transient accumulation of 5-carboxylcytosine indicates involvement of active demethylation in lineage specification of neural stem cells. Cell reports 7(5):1353-1361.
Wickham H. 2009. ggplot2: Elegant Graphics for Data Analysis. Gentleman R, Hornik K, Parmigiani G, editors. New York, NY: Springer. 1-212 p.

Williams K, Christensen J, Pedersen MT, Johansen JV, Cloos PA, Rappsilber J, Helin K. 2011a. TET1 and hydroxymethylcytosine in transcription and DNA methylation fidelity. Nature 473(7347):343-348.
Williams K, Christensen J, Pedersen MT, Johansen JV, Cloos PAC, Rappsilber J, Helin K. 2011b. TET1 and hydroxymethylcytosine in transcription and DNA methylation fidelity. Nature 473(7347):343-U472.
Wittmann W, Schimmang T, Gunhaga L. 2014. Progressive effects of N-myc deficiency on proliferation, neurogenesis, and morphogenesis in the olfactory epithelium. Dev Neurobiol 74(6):643-656.
Wohlfert EA, Nichols FC, Nevius E, Clark RB. 2007. Peroxisome proliferator-activated receptor gamma (PPARgamma) and immunoregulation: enhancement of regulatory T cells through PPARgamma-dependent and -independent mechanisms. J Immunol 178(7):4129-4135.
Wolf D, Tseng N, Seedorf G, Roe G, Abman SH, Gien J. 2014. Endothelin-1 decreases endothelial PPARgamma signaling and impairs angiogenesis after chronic intrauterine pulmonary hypertension. Am J Physiol Lung Cell Mol Physiol 306(4):L361-371.
Wolf HK, Buslei R, Schmidt-Kastner R, Schmidt-Kastner PK, Pietsch T, Wiestler OD, Blumcke I. 1996. NeuN: a useful neuronal marker for diagnostic histopathology. J Histochem Cytochem 44(10):1167-1171.
Wolf ME, Kapatos G. 1989a. Flow cytometric analysis and isolation of permeabilized dopamine nerve terminals from rat striatum. J Neurosci 9(1):106-114.
Wolf ME, Kapatos G. 1989b. Flow cytometric analysis of rat striatal nerve terminals. J Neurosci 9(1):94-105.
Wolf ME, Kapatos G. 1989c. Stimulation of D2 dopamine receptors decreases intracellular calcium levels in rat anterior pituitary cells but not striatal synaptosomes: a flow cytometric study using indo-1. Synapse 4(4):353-370.
Wozniak SE, Gee LL, Wachtel MS, Frezza EE. 2009a. Adipose Tissue: The New Endocrine Organ? A Review Article. Digest Dis Sci 54(9):1847-1856.
Wozniak SE, Gee LL, Wachtel MS, Frezza EE. 2009b. Adipose tissue: the new endocrine organ? A review article. Dig Dis Sci 54(9):1847-1856.
Wu H, Coskun V, Tao JF, Xie W, Ge WH, Yoshikawa K, Li E, Zhang Y, Sun YE. 2010. Dnmt3a-Dependent Nonpromoter DNA Methylation Facilitates Transcription of Neurogenic Genes. Science 329(5990):444-448.
Wu H, D'Alessio AC, Ito S, Wang ZB, Cui KR, Zhao KJ, Sun YE, Zhang Y. 2011. Genome-wide analysis of 5-hydroxymethylcytosine distribution reveals its dual function in transcriptional regulation in mouse embryonic stem cells. Gene Dev 25(7):679-684.
Wu H, Zhang Y. 2014. Reversing DNA Methylation: Mechanisms, Genomics, and Biological Functions. Cell 156(1-2):45-68.
Wu SC, Zhang Y. 2010. Active DNA demethylation: many roads lead to Rome. Nat Rev Mol Cell Bio 11(9):607-620.
Xin YJ, Yuan B, Yu B, Wang YQ, Wu JJ, Zhou WH, Qiu Z. 2015. Tet1-mediated DNA demethylation regulates neuronal cell death induced by oxidative stress. Sci Rep 5:7645.
Xu GL, Walsh CP. 2014. Enzymatic DNA oxidation: mechanisms and biological significance. BMB reports.

Xu Y, Wu F, Tan L, Kong L, Xiong L, Deng J, Barbera AJ, Zheng L, Zhang H, Huang S and others. 2011. Genome-wide regulation of 5hmC, 5mC, and gene expression by Tet1 hydroxylase in mouse embryonic stem cells. Mol Cell 42(4):451-464.
Xu Y, Xu C, Kato A, Tempel W, Abreu JG, Bian C, Hu Y, Hu D, Zhao B, Cerovina T and others. 2012. Tet3 CXXC domain and dioxygenase activity cooperatively regulate key genes for Xenopus eye and neural development. Cell 151(6):1200-1213.
Yam PT, Charron F. 2013. Signaling mechanisms of non-conventional axon guidance cues: the Shh, BMP and Wnt morphogens. Curr Opin Neurobiol 23(6):965-973.
Yamada T, Urano-Tashiro Y, Tanaka S, Akiyama H, Tashiro F. 2013. Involvement of Crosstalk between Oct4 and Meis1a in Neural Cell Fate Decision. Plos One 8(2).
Yamaguchi S, Hong K, Liu R, Inoue A, Shen L, Zhang K, Zhang Y. 2013. Dynamics of 5-methylcytosine and 5-hydroxymethylcytosine during germ cell reprogramming. Cell Res 23(3):329-339.
Yang F, Baumann C, Viveiros MM, De La Fuente R. 2012. Histone hyperacetylation during meiosis interferes with large-scale chromatin remodeling, axial chromatid condensation and sister chromatid separation in the mammalian oocyte. Int J Dev Biol 56(10-12):889-899.
Yao ZG, Zhang L, Huang L, Zhu H, Liu Y, Ma CM, Sheng SL, Qin C. 2013. Regional and cell-type specific distribution of HDAC2 in the adult mouse brain. Brain Struct Funct 218(2):563-573.
Yildirim O, Li RW, Hung JH, Chen PB, Dong XJ, Ee LS, Weng ZP, Rando OJ, Fazzio TG. 2011. Mbd3/NURD Complex Regulates Expression of 5-Hydroxymethylcytosine Marked Genes in Embryonic Stem Cells. Cell 147(7):1498-1510.
Yu M, Hon GC, Szulwach KE, Song CX, Jin P, Ren B, He C. 2012a. Tet-assisted bisulfite sequencing of 5-hydroxymethylcytosine. Nat Protoc 7(12):2159-2170.
Yu M, Hon GC, Szulwach KE, Song CX, Zhang L, Kim A, Li X, Dai Q, Shen Y, Park B and others. 2012b. Base-resolution analysis of 5-hydroxymethylcytosine in the mammalian genome. Cell 149(6):1368-1380.
Yu M, Hon GC, Szulwach KE, Song CX, Zhang L, Kim A, Li XK, Dai Q, Shen Y, Park B and others. 2012c. Base-Resolution Analysis of 5-Hydroxymethylcytosine in the Mammalian Genome. Cell 149(6):1368-1380.
Yu P, Ji L, Lee KJ, Yu M, He C, Ambati S, McKinney EC, Jackson C, Baile CA, Schmitz RJ and others. 2016. Subsets of Visceral Adipose Tissue Nuclei with Distinct Levels of 5-Hydroxymethylcytosine. PLoS One 11(5):e0154949.
Yu P, McKinney EC, Kandasamy MM, Albert AL, Meagher RB. 2015. Characterization of brain cell nuclei with decondensed chromatin. Dev Neurobiol 75(7):738-756.
Zhang J, Dominguez-Sola D, Hussein S, Lee JE, Holmes AB, Bansal M, Vlasevska S, Mo T, Tang H, Basso K and others. 2015. Disruption of KMT2D perturbs germinal center B cell development and promotes lymphomagenesis. Nat Med.
Zhang RP, Shao JZ, Xiang LX. 2011. GADD45A protein plays an essential role in active DNA demethylation during terminal osteogenic differentiation of adipose-derived mesenchymal stem cells. J Biol Chem 286(47):41083-41094.
Zhang RR, Cui QY, Murai K, Lim YC, Smith ZD, Jin S, Ye P, Rosa L, Lee YK, Wu HP and others. 2013. Tet1 regulates adult hippocampal neurogenesis and cognition. Cell Stem Cell 13(2):237-245.

Zhang ZC, Liu Y, Li SF, Guo L, Zhao Y, Qian SW, Wen B, Tang QQ, Li X. 2014. Suv39h1 mediates AP-2alpha-dependent inhibition of C/EBPalpha expression during adipogenesis. Mol Cell Biol 34(12):2330-2338.

Zheng Y, Begum S, Zhang C, Fleming K, Masumura C, Zhang M, Smith P, Darlington C. 2011. Increased BrdU incorporation reflecting DNA repair, neuronal de-differentiation or possible neurogenesis in the adult cochlear nucleus following bilateral cochlear lesions in the rat. Exp Brain Res 210(3-4):477-487.

Zhu Y, Qi C, Korenberg JR, Chen XN, Noya D, Rao MS, Reddy JK. 1995. Structural organization of mouse peroxisome proliferator-activated receptor gamma (mPPAR gamma) gene: alternative promoter use and different splicing yield two mPPAR gamma isoforms. Proc Natl Acad Sci U S A 92(17):7921-7925.

Zinin N, Adameyko I, Wilhelm M, Fritz N, Uhlen P, Ernfors P, Henriksson MA. 2014. MYC proteins promote neuronal differentiation by controlling the mode of progenitor cell division. EMBO Rep 15(4):383-391.

Zovkic IB, Guzman-Karlsson MC, Sweatt JD. 2013. Epigenetic regulation of memory formation and maintenance. Learn Mem 20(2):61-74.

Zych J, Stimamiglio MA, Senegaglia AC, Brofman PR, Dallagiovanna B, Goldenberg S, Correa A. 2013. The epigenetic modifiers 5-aza-2'-deoxycytidine and trichostatin A influence adipocyte differentiation in human mesenchymal stem cells. Braz J Med Biol Res 46(5):405-416.